# Peridynamic Models in Multi-Physics Applications on Bounded and Unbounded Domains

Vom Promotionsausschuss der
Technischen Universität Hamburg

zur Erlangung des akademischen Grades

Doktor-Ingenieur (Dr.-Ing.)

genehmigte Dissertation (Monografie)

von
**Alexander Hermann**

aus
Odessa, Ukraine

2024

1. Gutachter: Prof. Dr.-Ing. Christian J. Cyron
2. Gutachter: Prof. Dr.-med. Roland C. Aydin

Tag der mündlichen Prüfung: 22. November 2024

DOI: https://doi.org/10.15480/882.13738
ORCiD: https://orcid.org/0000-0002-9731-3286

To my mother

# Acknowledgements

This doctoral thesis stands as a testament not only to my personal efforts but significantly to the encouragement and wisdom imparted by several key individuals whose contributions have been indispensable and are acknowledged here. First and foremost, I extend my deepest gratitude to my doctoral supervisor, Prof. Dr.-Ing. Christian J. Cyron, head of the Institute of Material Systems Modeling at the Helmholtz Centre Hereon in Geesthacht and the Institute for Continuum and Material Mechanics at the Hamburg University of Technology. His support, the discussions we had, and the highly scientific yet pleasant environment he fostered at the institute have been transformative in my life. His unwavering support and insightful scientific advice have been instrumental in pursuing new ideas, thus making the contributions of this thesis possible. I am also profoundly grateful to Prof. Dr.-med. Roland C. Aydin, who co-supervised this thesis and whose guidance and support throughout the journey have been invaluable. I am immensely thankful to my friend and mentor, Dr. Arman Shojaei, who first introduced me to the field of Peridynamics. His clear vision and steadfast guidance have been a major driving force in my academic journey, providing honest assessments I could always rely on. Beyond his mentorship, I am eternally happy for the friendship we have built, which has been a source of constant motivation and joy. Further appreciation goes to Dr.-Ing. Dirk Steglich, the senior scientist at the Institute of Material Systems Modeling. His extensive experience, dedication, and witty demeanor have not only added substantial value to my work but have also made my time at the institute a joyful and memorable experience. I would like to express my sincere gratitude to Prof. Farshid Mossaiby, who, at the time, was a visiting researcher at the Helmholtz Centre in our institute, and whose kind and joyful nature made him a pleasure to work with and spend time around. His invaluable help with technical and scientific problems, coupled with his clear and lean approach to computational modeling, has profoundly shaped and influenced my own methods. My heartfelt thanks go to Dr. Pablo Seleson at Oak Ridge National Laboratories, whose diligence, precision, and clarity in research have profoundly shaped my understanding of what clean, meticulous scientific work entails. I am also deeply grateful to Dr. Stewart A. Silling from Sandia National Laboratories, the originator of the theory of Peridynamics, who has kindly supported us during the project and the work surrounding this thesis with clear assessment and guidance. My heartfelt thanks go to my family, especially my mother, whose endless care and hard work laid the foundation for this thesis. Without her selfless sacrifice, none of this would have been possible. At last, I am eternally grateful to my dear spouse, Kerstin, for her unwavering support and belief in my capabilities. Her love and emotional support have been a constant source of strength and encouragement.

# Table of Contents

# Acronyms

| | |
|---|---|
| **ABCs** | Absorbing Boundary Conditions |
| **BV** | Butler-Volmer |
| **CANNs** | Constitutive Artificial Neural Networks |
| **CCM** | Classical Continuum Mechanics |
| **CDM** | Continuum Damage Mechanics |
| **CFL** | Courant-Friedrichs-Lewy |
| **DCL** | Diffusive Corrosion Layer |
| **DL** | Deep Learning |
| **DR** | Degradation Rate |
| **EBFs** | Exponential Basis Functions |
| **ED** | Experimental Design |
| **FEM** | Finite Element Method |
| **FPM** | Finite Point Method |
| **FSI** | Fluid-Structure Interaction |
| **Gd** | Gadolinium |
| **GMRES** | Generalized Minimal Residual Method |
| **GPBM** | Generalized Prototype Brittle Material |
| **GPU** | Graphics Processing Unit |
| **HPC** | High-Performance Computing |
| **LEFM** | Linear Elastic Fracture Mechanics |
| **LHS** | Latin Hypercube Sampling |
| **LPS** | Linear Peridynamic Solid |
| **MAE** | Mean Absolute Error |

| | |
|---|---|
| **MD** | Molecular Dynamics |
| **Mg** | Magnesium |
| **ML** | Machine Learning |
| **MPI** | Message Passing Interface |
| **NLFM** | Nonlinear Fracture Mechanics |
| **NNPP** | Nonlocal Nernst-Planck-Poisson |
| **OCP** | Open Circuit Potential |
| **PD** | Peridynamics |
| **PDEs** | Partial Differential Equations |
| **PDFEM** | Peridynamic Finite Element Method |
| **PML** | Perfectly Matched Layer |
| **PSO** | Particle Swarm Optimization |
| **QoI** | Quantity of Interest |
| **RKPM** | Reproducing Kernel Particle Methods |
| **SBF** | Simulated Body Fluid |
| **SHE** | Standard Hydrogen Electrode |
| **SPH** | Smoothed Particle Hydrodynamics |
| **WLS** | Weighted Least Squares |
| **X-FEM** | Extended Finite Element Method |

# List of Figures

# List of Tables

# Abstract

The following dissertation concerns with elevating the role of nonlocal peridynamic continuum models in real-world engineering and material applications by establishing efficient and robust numerical techniques and providing comprehensive model descriptions that aim to accurately represent the underlying physical properties. A number of versatile numerical discretization schemes are thoroughly evaluated for both bond-based peridynamic models in brittle fracture modeling as well as nonlocal diffusion-type models for up to three-dimensional problems. These schemes can adaptively refine the computational grid around areas of interest, are asymptotically compatible, computationally efficient, and easy to implement. Efficient solution schemes are further provided for unbounded domain problems, based on residual-free exponential basis functions, which may be used in a collocation scheme to obtain Dirichlet-type boundary conditions to approximate the far-field domain solution over a truncating boundary. The feasibility and improved capability of the proposed numerical schemes are demonstrated on the complex multi-physics simulation of the biodegradation of magnesium-based bone implant screws under physiological conditions on (nearly) unbounded three-dimensional domains, utilizing the standard bi-material peridynamic corrosion model with an efficient constitutive model of the corrosion kinetics that directly links to the experimentally easy-to-measure macroscopic volume loss. In order to augment the capabilities of standard peridynamic models towards the description of multi-ionic mass transport of electromigration, a generalized peridynamic framework of nonlocal Nernst-Planck-Poisson equations is proposed, which effectively models the diffusion-electromigration-reaction and moving boundary problems of corrosion models with arbitrary constitutive corrosion kinetics.

# Chapter 1

# Introduction

Mathematical modeling of mechanical damage and fracture in materials requires a multi-scale approach to accurately describe these phenomena across various length scales. A significant challenge is reconciling atomistic methods, such as Molecular Dynamics (MD), with the principles of Classical Continuum Mechanics (CCM) that apply at the macroscale [92]. Quantum mechanics can model certain damage phenomena, such as chemical reactions or phase changes at very small scales (see e.g., [78]), but extending these descriptions to larger macroscopic systems incurs excessive computational costs, making such approaches impractical for large-scale applications. This gap between the micro- and macroscale is exacerbated by the inherent limitations of continuum mechanics, which assumes the continuity and differentiability of state variables. These assumptions break down in the presence of discontinuities such as cracks or voids, which are fundamental to understanding and predicting material failure.

Models based on CCM can effectively solve for displacements and strain fields given the external loads, boundary conditions, and constitutive assumptions of a material, ranging from linear elasticity to visco-plasticity. However, when spatial discontinuities form in any state variables, the mathematical foundations of CCM become invalid in those regions. To address this, homogenization methods, such as Continuum Damage Mechanics (CDM), were proposed to account for the macroscopic material response in the presence of micro-cracks or voids [159, 29]. However, CDM does not provide a comprehensive description of damage at the macroscale [8, 77]. Methods based on classical Linear Elastic Fracture Mechanics (LEFM) or Nonlinear Fracture Mechanics (NLFM) are also limited, as they can only be applied to simple structures with predefined cracks and do not consider spontaneous crack initiation [132]. Dynamic fracture modeling, therefore, necessitates numerical approaches that accurately describe crack formation, propagation, branching, and coalescence on a macroscopic scale. Numerical methods, such as the Extended Finite Element Method (X-FEM), have been shown to provide reasonably accurate solutions to engineering problems [70]. However, their major drawbacks include poor numerical stability and mesh dependency, often rendering these models impractical for real-world engineering applications [139]. Additionally, these models do not adequately address crack formation and branching, resulting in *ad hoc* descriptions of crack-tip dynamics [77]. Consequently, there is a need for a modeling system that can integrate different scales of material behavior, incorporating accurate descriptions at lower length scales compared to the continuum level, without the excessive computational costs typically associated with such approaches for macroscopic structural systems.

Traditionally in multi-scale modeling, domain decomposition and coupling approaches between models at different scales are employed [117, 9, 11, 102]. However, coupling atomistic

or molecular scale models to CCM models presents challenges. CCM models are local and use spatial derivatives in the physical material description, whereas atomistic models are nonlocal. In atomistic models, material points within a certain finite interaction distance can establish bond connections, and determining the state at a particular point in time requires information from distinct neighboring points in space. Due to the inherently different physical descriptions between classical local and atomistic nonlocal models, numerical coupling and domain decomposition methods suffer from various spurious effects, necessitating additional numerical stabilization approaches [34, 120].

Peridynamics (PD) has been proposed as a nonlocal generalization of CCM and a multi-scale framework to address these challenges. Evidently, it has seen exponential growth in scientific usage and within the research community in recent years. Introduced by Stewart A. Silling in the early 2000s, PD moves away from the local interactions fundamental to CCM and instead adopts a nonlocal structure where the forces between separate points in a material are defined over finite distances, known as the peridynamic *horizon* [128]. This shift replaces differential equations, which require the differentiability of displacement fields to obtain meaningful mathematical solutions and guarantee well-posedness, with integro-differential equations. Since integral equations can be formulated even in the presence of sharp discontinuities, they inherently account for damage and fracture phenomena, such as crack propagation, while still being valid. The very name *peridynamics*, composed of the Greek *peri* for "near" and *dynamic* for "force," emphasizes the core of this theory: the dynamic interaction between points within a finite distance, i.e., the horizon, beyond which the nonlocal material point interactions are considered negligible. Through the integro-differential formulation of nonlocal bond interactions, computational models based on PD overcome the limitations of coupled atomistic and classical continuum models, as well as the mathematical limitations of purely local continuum models in applications involving evolving material discontinuities. This enables the modeling of damage and fracture phenomena ranging from the atomistic to the structural level in a consistent nonlocal multi-scale framework [117, 118, 7]. Moreover, the emergence of PD has catalyzed the development of nonlocal calculus as a new branch of mathematics, generalizing traditional calculus and thus underpinning the theoretical foundations of PD and enhancing its applicability in various areas of materials science [3, 36, 10, 35].

Given the integro-differential formalism, PD provides a comprehensive set of mathematical modeling opportunities across a wide range of damage mechanisms and has been widely exploited as an effective computational tool to model, among other phenomena, spontaneous crack nucleation [131], dynamic crack propagation, growth and branching [53, 107, 142], impact damage [61, 4], and failure and damage in concrete [24], composites [32], polycrystals [164], ice craters [160], as well as many other brittle and ductile materials. PD has advanced the state of the art for modeling material failure and is now considered an established mathematical framework and computational tool in mechanical fracture.

More recently, the nonlocal peridynamic formalism has been extended to broader fields of application, such as heat and mass transport [101, 13, 161], as well as corrosion damage modeling [25, 63, 62, 65, 80, 27]. These extensions have attracted considerable attention in the literature by presenting reliable and computationally effective methods for various relevant corrosion phenomena in engineering problems. These problems involve diffusion-type processes in coupled metal and electrolyte environments where the solid metallic phase gradually undergoes a phase change. Traditionally, classical continuum-based models that sought to model this effect of mass transport across a time-dependent corrosion interface layer faced difficulties in accurately capturing the evolution of the phase boundary. Formulations to address this, within the context of classical

computational methods, usually involve transport equations solved through Finite Element Method (FEM), but are often cumbersome to implement and computationally demanding. Peridynamic models can largely bypass this problem, as they can naturally capture the evolution of moving interfaces (where the Stefan conditions are satisfied) as part of the solution process. Another distinct feature is that peridynamic models offer a complete description of corrosion damage, including mechanical damage in the corroding layer, since in peridynamic models, corrosion is viewed as a type of damage induced in a solid coupled with a diffusion problem in an electrolyte [27].

To date, a major drawback of peridynamic models is their limited applicability to real-world engineering and structural design problems. This limitation stems from the fact that numerical modeling for peridynamic models is still relatively under-researched compared to the decades of research, testing, and employment of well-established numerical methods for CCM models, such as the FEM, when it comes to macroscopic structures relevant in engineering problems. Despite the appealing consistently nonlocal, multi-scale formulation, current numerical methods for peridynamic models remain computationally more demanding than comparative methods for classical theories when modeling and parameterizing computational models based on experimental data sets [79]. The problem mainly arises from the nonlocal nature of the theory and the associated nonlocal integration procedures. Thus, at the moment, numerical peridynamic models largely lack the efficient and robust implementations needed for practical problems in engineering applications, which is why well-established methods such as the FEM are so widely used. This makes coupling techniques between PD and FEM an important area for significantly improving computational efficiency [72, 94, 99].

In addition, most studies on PD published so far focus on solutions in bounded domains and the accurate imposition of boundary conditions, either Dirichlet or Neumann type. However, in many fields such as mechanical engineering, seismology, and coastal engineering, numerical models need to approximate solutions in unbounded domains. Numerical schemes to approximate solutions in unbounded domains for peridynamic systems are still in their early stages of research. Applying many established numerical approaches developed for local theories and equations to nonlocal peridynamic systems is not trivial, since peridynamic interactions are nonlocal and peridynamic operators are generally associated with volume-constrained boundary conditions [37, 162]. Moreover, techniques to numerically simulate unbounded domain problems typically involve Laplace transforms into the frequency domain, making the calculation of nonlocal kernel functions from these routines challenging and less accurate. In summary, while the theory of PD as a consistently nonlocal multi-scale framework has been thriving in the academic community for almost three decades, the application of nonlocal peridynamic models to complex real-world problems in engineering, structural, and material design remains sparse.

The objectives of this dissertation are to address the critical issues in the current state of the art in peridynamic modeling and to enhance its role as a competitive tool in engineering. This work includes a detailed description of the development of novel, efficient numerical discretization and quadrature schemes for peridynamic equations, and demonstrates their application to various benchmark problems in elasticity and mass transfer in one (1D), two (2D), and three dimensions (3D). Furthermore, we aim to discuss novel, fully nonlocal boundary conditions to handle unbounded domains, which can be applied to both peridynamic models and classical local models, emphasizing their versatility. To demonstrate the capabilities of peridynamic models along with the proposed improvements in numerical solution techniques, we present a multi-physical case study on an unbounded domain. This case study involves the multi-physical modeling of corrosion-driven volume loss of biodegradable binary alloy implants based on Magnesium (Mg)

and Gadolinium (Gd). Such implants are a vibrant field of research in biomedical engineering and already serve in clinical applications, promoting a promising and profitable branch of future implant design. Classical methods like FEM, based on classical local theories, face considerable difficulties in capturing the intricate multi-physics problems in corrosion, which involve damage and potentially fracture on complex 3D implant geometries. Therefore, we will demonstrate very efficient modeling approaches based on PD, specifically peridynamic corrosion models, which can be effectively used for 3D applications in biomedical implant material design. These models can replicate the macroscopic behavior of easily measurable lab data, such as percentage-wise volume loss, and serve as a chain-link in the holistic life-cycle simulation process. This process can work alongside established FEM models for residual mechanical damage analysis, where sufficiently reliable and trusted methods exist.

This dissertation is structured as follows: In Chapter 2, we review the general formulations of peridynamic models in elasticity, wave propagation, and mass transfer. We start with the state-based peridynamic model of elasticity, derive the bond-based peridynamic model, and discuss the Generalized Prototype Brittle Material (GPBM) constitutive model as a special case. We also revisit the nonlocal formulation of scalar field equations, including the peridynamic wave equation, the peridynamic diffusion model, and the diffusion-based bi-material corrosion model, generalizing to the Nonlocal Nernst-Planck-Poisson (NNPP) system of equations. Chapter 3 provides a comprehensive discussion on numerical solution strategies in peridynamic modeling, including standard approaches and proposed improvements in spatial discretization and numerical quadrature schemes. We introduce the meshfree Weighted Least Squares (WLS) collocation approach to enhance numerical integration performance and convergence, combined with the standard discretization method in PD. This combination adaptively tracks crack patterns in brittle fracture and corrosion experiments, culminating in a *multi-adaptive scheme* that improves spatial resolution and computational performance. In Chapter 4, we discuss nonlocal models in both classical local theories and PD. We derive fully nonlocal Absorbing Boundary Conditions (ABCs) based on residual-free semi-analytical Exponential Basis Functions (EBFs), applicable to bond-based peridynamic models of elasticity, wave propagation, and diffusion-type problems in up to 3D domains. Chapter 5 demonstrates the applicability and numerical performance of the proposed techniques through a multi-physical simulation of biodegradable Mg-based bone implants. We simulate a headless bone implant screw's *in vitro* biocorrosion, followed by a damage plasticity analysis using FEM over six months of simulated immersion. We also apply the NNPP corrosion system to simulate the multi-ionic electromigration of Mg-based bone implant geometries in 3D, providing detailed information on the distribution of species and the effects of precipitate formations across the corrosion surface. Furthermore, we demonstrate how the peridynamic corrosion model can be employed as the basis for efficient surrogate model approaches, effectively bridging the gap toward predictive *in vivo* corrosion modeling. The dissertation concludes in Chapter 6, with a brief outlook on ongoing research and potential future research prospects presented in Chapter 7.

# Chapter 2

# Peridynamic Models: An Overview

In this chapter, we review the nonlocal formulations of peridynamic models of elasticity and mass transfer. First, we discuss the general state-based formulation of peridynamic models, using the Linear Peridynamic Solid (LPS) model as a common example. Assuming pairwise equal and opposite force functions, we derive the bond-based peridynamic formulation as a special case, which imposes a restriction on Poisson's ratio. We then explore nonlocal scalar field equations, which can be broadly divided into hyperbolic and parabolic equations with nonlocal operators, analogous to Partial Differential Equations (PDEs). This includes the hyperbolic-type nonlocal peridynamic scalar wave equation, a nonlocal generalization of the classical acoustic wave equation, and the parabolic-type peridynamic diffusion equation governing both heat and mass transport. Unlike their classical counterparts, these nonlocal equations exhibit nonlinear dispersion relations. We also discuss the application of the peridynamic diffusion equation in the bi-material corrosion model, efficiently modeling the electrochemically driven dissolution process of metallic materials into surrounding liquid electrolytes in general corrosion scenarios. Finally, we formulate the complete NNPP system for describing electromigration and multi-ionic mass transport, constituting a generalization of peridynamic constitutive corrosion modeling. The derivations in Section 2.1 and Section 2.2 follow standard textbook descriptions (see e.g., [15]) with schematic figures from our previous publication in [122]. The formulation and definition of the peridynamic scalar wave in Section 2.3.1 were thoroughly studied and published in [59]. The peridynamic diffusion equation from Section 2.3.2 and the bi-material peridynamic corrosion model in Section 2.3.3 were examined and published in [60]. The proposed NNPP system of corrosion equations from Section 2.3.4, along with the schematic figures, has been submitted as a preprint [58].

## 2.1 State-Based Peridynamics

Let us suppose a generic body $\Omega$ that occupies a region in the Euclidean space $\Omega \subset \mathbb{R}^{n_d}$, with $n_d = 1, 2$ or 3 and is composed of material points located at the spatial positions $\mathbf{x}$ in the reference configuration. The general *state-based* formulation of the peridynamic model in continuum mechanics states that the deformation at a point depends collectively on the deformation of all points connected to this point within a finite distance, called *neighborhood*. It is commonly assumed that the neighborhood $\mathcal{H}_{\mathbf{x}}$ of point $\mathbf{x} \in \Omega$ is given by

$$\mathcal{H}_{\mathbf{x}} := \left\{ \mathbf{x}' \in \Omega : \|\mathbf{x}' - \mathbf{x}\| \leq \delta \right\}, \tag{2.1}$$

which represents a sphere, disc, or line segment in 3D, 2D, and 1D, respectively, and where the parameter $\delta > 0$ is called the *horizon*. The governing PD equation of motion is

$$\rho(\mathbf{x})\ddot{\mathbf{u}}(\mathbf{x},t) = \int_{\mathcal{H}_\mathbf{x}} \left\{ \underline{\mathbf{T}}[\mathbf{x},t]\left\langle \mathbf{x}'-\mathbf{x}\right\rangle - \underline{\mathbf{T}}[\mathbf{x}',t]\left\langle \mathbf{x}-\mathbf{x}'\right\rangle \right\} \mathrm{d}V_{\mathbf{x}'} + \mathbf{b}(\mathbf{x},t), \tag{2.2}$$

where $\rho(\mathbf{x})$ is the mass density, $\ddot{\mathbf{u}}$ is the second time derivative of the displacement field, $\mathcal{H}_\mathbf{x}$ is the neighborhood centered at $\mathbf{x}$, the operator $\underline{\mathbf{T}}[\mathbf{x},t]\left\langle \mathbf{x}'-\mathbf{x}\right\rangle$ is the *force vector state* at point $\mathbf{x}$ and time $t$, which is explained below, $\mathrm{d}V_{\mathbf{x}'}$ is the infinitesimal volume associated with point $\mathbf{x}'$ and $\mathbf{b}(\mathbf{x},t)$ is a prescribed body force density field.

Conceptually, states can be understood as mathematical operators providing a generalization of tensors. For instance, a *scalar state* represents an operator whose image is a scalar, while a *vector state*, akin to a second-order tensor, maps to vectors. One example of the latter is the force vector state $\underline{\mathbf{T}}[\mathbf{x},t]\left\langle \mathbf{x}'-\mathbf{x}\right\rangle$, which maps the bond vector $\mathbf{x}'-\mathbf{x}$ to the force vector state field, expressed in units of force per unit volume squared. In the existing literature, the notation commonly employed indicates that the square brackets denote the location and time, i.e. $[\mathbf{x},t]$, at which the force vector state is evaluated, and the angle brackets, i.e. $\langle \mathbf{x}'-\mathbf{x}\rangle$, specify the bond vector upon which the state operates. Furthermore, an underline notation is used by convention to represent states, i.e., $\underline{\mathbf{T}}[\mathbf{x},t]\left\langle \mathbf{x}'-\mathbf{x}\right\rangle$. For the sake of convenience and if possible, we drop the dependency on $\mathbf{x}$ and $t$ in the notation of a state as well as the bonds on which the states operate, thus $\underline{\mathbf{T}}[\mathbf{x},t]\left\langle \mathbf{x}'-\mathbf{x}\right\rangle$ is simply written as $\underline{\mathbf{T}}$. However, we occasionally include angle brackets in the notation to emphasize the particular vector on which a given state operates. Given the definition of a point product between states, we shall restrict our view to force vector states that may be expressed as

$$\underline{\mathbf{T}} = \underline{t}\,\underline{\mathbf{M}}, \tag{2.3}$$

where $\underline{t}$ is the *force scalar state* and $\underline{\mathbf{M}}$ is the *deformed direction vector state*. Let the *deformation vector state* $\underline{\mathbf{Y}}$ be

$$\underline{\mathbf{Y}} = \mathbf{y}(\mathbf{x}+\boldsymbol{\xi},t) - \mathbf{y}(\mathbf{x},t), \qquad \forall \boldsymbol{\xi} \in \mathcal{H}, \tag{2.4}$$

where $\boldsymbol{\xi} := \mathbf{x}'-\mathbf{x}$ is the bond vector connecting the points $\mathbf{x}'$ and $\mathbf{x}$ and $\mathcal{H}$ is the neighborhood centered around the origin. Thus, the deformed direction vector state may be expressed as

$$\underline{\mathbf{M}} = \begin{cases} \dfrac{\underline{\mathbf{Y}}}{\|\underline{\mathbf{Y}}\|}, & \|\underline{\mathbf{Y}}\| \neq 0, \\ \mathbf{0}, & \text{otherwise.} \end{cases} \tag{2.5}$$

Since $\underline{t}$ is a scalar state, the product in (2.3) represents scalar multiplication between the force scalar state field $\underline{t}$ and the deformed direction vector state field $\underline{\mathbf{M}}$. The material models described by (2.3) are known as *ordinary* materials. In the broader category of *non-ordinary* material models, this assumption is relaxed, allowing force vector states between two material points of the bond vector $\boldsymbol{\xi}$ to have arbitrary orientations. However, the discussion of these models is beyond the scope of this text. Furthermore, it can be shown that on any bounded body $\Omega$, force vector states of ordinary material models satisfy the balance of linear momentum

$$\int_\Omega \rho(\mathbf{x})\ddot{\mathbf{u}}(\mathbf{x},t)\,\mathrm{d}V_\mathbf{x} = \int_\Omega \mathbf{b}(\mathbf{x},t)\,\mathrm{d}V_\mathbf{x}, \quad \forall t \geq 0, \tag{2.6}$$

as well as the balance of angular momentum

$$\int_{\Omega} \mathbf{y}(\mathbf{x},t) \times \rho(\mathbf{x})\ddot{\mathbf{u}}(\mathbf{x},t)\, \mathrm{d}V_{\mathbf{x}} = \int_{\Omega} \mathbf{y}(\mathbf{x},t) \times \mathbf{b}(\mathbf{x},t)\, \mathrm{d}V_{\mathbf{x}}, \quad \forall t \geq 0. \tag{2.7}$$

A material model is called *simple*, if $\underline{\mathbf{T}}$ depends constitutively on the collective deformation of the neighborhood of $\mathbf{x}$

$$\underline{\mathbf{T}} = \underline{\mathbf{T}}(\underline{\mathbf{Y}}), \quad \forall \xi \in \mathcal{H}. \tag{2.8}$$

Moreover, a simple material is said to be *elastic*, if there exists a *strain energy density function* $W$, such that

$$\underline{\mathbf{T}}(\underline{\mathbf{Y}}) = \nabla_{\underline{\mathbf{Y}}} W(\underline{\mathbf{Y}}), \quad \forall \xi \in \mathcal{H}, \tag{2.9}$$

where $\nabla_{\underline{\mathbf{Y}}}$ is the Fréchet derivative of $W$ with respect to $\underline{\mathbf{Y}}$. An example of an ordinary material model in PD widely used in the literature is the LPS model represented by the strain energy density function given by

$$W_{\mathrm{LPS}} = \frac{K\theta^2}{2} + \frac{15G}{2\bar{m}} \int_{\mathcal{H}} \underline{\omega} \left( \underline{e}\langle \xi \rangle - \frac{\theta \|\xi\|}{3} \right)^2 \mathrm{d}V_{\xi}, \tag{2.10}$$

where each component is explained in the following. Respectively, $K$ and $G$ are the bulk and shear modulus. The spherical neighborhood with horizon $\delta$ centered around the origin is denoted as $\mathcal{H}$. The nonnegative scalar state $\underline{\omega}[\mathbf{x},t]\langle \mathbf{x}' - \mathbf{x} \rangle$, called *influence function*, is defined on $\mathcal{H}$ and is called *spherical*, if it depends only on the norm of a bond vector $\|\xi\| := \|\mathbf{x}' - \mathbf{x}\|$, thus $\underline{\omega}\langle \xi \rangle = \underline{\omega}\langle \|\xi\| \rangle$. Typically, we assume a spherical influence function in the form of

$$\underline{\omega}\langle \|\xi\| \rangle = \frac{\omega(\|\xi\|)}{\|\xi\|}, \tag{2.11}$$

where $\omega(\|\xi\|)$ is a spherical scalar-valued function. It can take different forms, and two common ones for peridynamic models in literature are the *constant* and *linear* ones denoted by $\omega_0$ and $\omega_1$, respectively (see Fig. 2.1). Here, $\omega_0$ is independent of the bond length,

$$\omega_0(\|\xi\|) := \begin{cases} 1, & \|\xi\| \leq \delta, \\ 0, & \|\xi\| > \delta, \end{cases} \tag{2.12}$$

whereas $\omega_1$ linearly depends on the bond length,

$$\omega_1(\|\xi\|) := \begin{cases} 1 - \dfrac{\|\xi\|}{\delta}, & \|\xi\| \leq \delta, \\ 0, & \|\xi\| > \delta. \end{cases} \tag{2.13}$$

Influence functions play a crucial role in peridynamic constitutive modeling, offering various benefits and applications [116]. They serve as a mechanism for selecting the bonds involved in force calculations and can be dynamically adjusted to remove bonds during simulations, especially in cases of bond-breaking processes. Furthermore, influence functions enable the connection between different families of peridynamic constitutive models and provide a means to control the strength of nonlocal interactions. They can accommodate non-homogeneity and time-dependence, making them suitable for systems where the peridynamic horizon varies across different points

within a body [118]. Thus, given the definition of the influence function and the *extension scalar state*

$$\underline{e}[\mathbf{x},t]\langle\boldsymbol{\xi}\rangle := \|\underline{\mathbf{Y}}[\mathbf{x},t]\langle\boldsymbol{\xi}\rangle\| - \|\boldsymbol{\xi}\|, \tag{2.14}$$

the nonlocal *dilatation* $\theta$ in PD is defined by

$$\theta := \frac{3}{\bar{m}}\int_{\mathcal{H}} \underline{\omega}\langle\|\boldsymbol{\xi}\|\rangle\,\|\boldsymbol{\xi}\|\underline{e}\langle\boldsymbol{\xi}\rangle\,\mathrm{d}V_{\boldsymbol{\xi}}, \qquad \bar{m} := \int_{\mathcal{H}} \underline{\omega}\langle\|\boldsymbol{\xi}\|\rangle\,\|\boldsymbol{\xi}\|^2\,\mathrm{d}V_{\boldsymbol{\xi}}, \tag{2.15}$$

where $\bar{m}$ is the *weighted volume*. For a fully spherical neighborhood, the weighted volume in (2.15) may be calculated as

$$\bar{m} = \begin{cases} \dfrac{4\pi\delta^5}{5}, & \omega = \omega_0, \\ \dfrac{2\pi\delta^5}{15}, & \omega = \omega_1. \end{cases} \tag{2.16}$$

According to the strain energy density function in (2.10) and the Fréchet derivative in (2.9), the force scalar state for the LPS constitutive model is derived as

$$\underline{t} = \frac{3K\theta}{\bar{m}}\underline{\omega}\langle\|\boldsymbol{\xi}\|\rangle\,\|\boldsymbol{\xi}\| + \frac{15G}{\bar{m}}\underline{\omega}\langle\|\boldsymbol{\xi}\|\rangle\left(\underline{e}\langle\boldsymbol{\xi}\rangle - \frac{\theta\|\boldsymbol{\xi}\|}{3}\right). \tag{2.17}$$

For a small change $\mathrm{d}\underline{\mathbf{Y}}$ in the deformation vector state, the LPS constitutive model may further be linearized near the reference configuration assuming a vanishing force vector state in the reference configuration. For a peridynamic model given by the *linearized* LPS constitutive model [129], the force vector state is obtained as

$$\underline{\mathbf{T}}[\mathbf{x},t]\langle\boldsymbol{\xi}\rangle = \frac{3K-5G}{\bar{m}}\omega(\|\boldsymbol{\xi}\|)\theta^{\mathrm{lin}}(\mathbf{x},t)\boldsymbol{\xi} + \frac{15G}{\bar{m}}\omega(\|\boldsymbol{\xi}\|)\frac{\boldsymbol{\xi}\otimes\boldsymbol{\xi}}{\|\boldsymbol{\xi}\|^2}\left(\mathbf{u}(\mathbf{x}+\boldsymbol{\xi},t)-\mathbf{u}(\mathbf{x},t)\right), \tag{2.18}$$

where $\theta^{\mathrm{lin}}$ is the *linearized* nonlocal dilatation given by

$$\theta^{\mathrm{lin}}(\mathbf{x},t) = \frac{3}{\bar{m}}\int_{\mathcal{H}} \omega(\|\boldsymbol{\xi}\|)\boldsymbol{\xi}\cdot\left(\mathbf{u}(\mathbf{x}+\boldsymbol{\xi},t)-\mathbf{u}(\mathbf{x},t)\right)\,\mathrm{d}V_{\boldsymbol{\xi}}. \tag{2.19}$$

It can be shown that for a quadratic displacement field $\mathbf{u}(\mathbf{x},t)$, the linearized nonlocal dilatation in (2.19) reduces to the dilatation in classical elasticity [115].

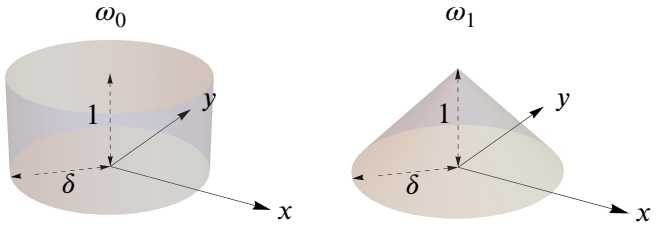


Figure 2.1: The constant and the linear influence functions, $\omega_0$ and $\omega_1$, respectively, for a neighborhood with horizon $\delta$. Reproduced from [122].

## 2.2 Bond-Based Peridynamics

The bond-based peridynamic model was first introduced in [128] and represents a special case of the general state-based PD formulation in (2.2) for a particular choice of the Poisson's ratio. According to bond-based PD, the governing equation of motion for point $\mathbf{x} \in \Omega$ in a bounded body $\Omega$ at time $t \geq 0$ is

$$\rho(\mathbf{x})\ddot{\mathbf{u}}(\mathbf{x},t) = \int_{\mathcal{H}_\mathbf{x}} \mathbf{f}\left(\mathbf{u}(\mathbf{x}',t) - \mathbf{u}(\mathbf{x},t), \mathbf{x}' - \mathbf{x}\right) \mathrm{d}V_{\mathbf{x}'} + \mathbf{b}(\mathbf{x},t), \tag{2.20}$$

where $\mathbf{f}$ is the *pairwise force function*, which represents the force per unit volume squared, also called the *micro-force density*, that the neighboring point $\mathbf{x}'$ exerts on point $\mathbf{x}$. It contains all the constitutive information of the given material and vanishes outside of the neighborhood of point $\mathbf{x}$, thus

$$\mathbf{f}(\boldsymbol{\eta}, \boldsymbol{\xi}) = \mathbf{0}, \quad \forall \mathbf{x}' \notin \mathcal{H}_\mathbf{x}, \tag{2.21}$$

where $\boldsymbol{\eta} := \mathbf{u}(\mathbf{x}',t) - \mathbf{u}(\mathbf{x},t)$ denotes the relative displacement of $\mathbf{x}$ and $\mathbf{x}'$ at time $t$. In the following, we restrict our view to pairwise force functions $\mathbf{f}$ that satisfy the linear admissibility condition,

$$\mathbf{f}(-\boldsymbol{\eta}, -\boldsymbol{\xi}) = -\mathbf{f}(\boldsymbol{\eta}, \boldsymbol{\xi}), \tag{2.22}$$

which is the analogue of Newton's third law of motion, and ensures the balance of linear momentum. The balance of angular momentum is guaranteed by the angular admissibility condition,

$$(\boldsymbol{\xi} + \boldsymbol{\eta}) \times \mathbf{f}(\boldsymbol{\eta}, \boldsymbol{\xi}) = \mathbf{0}. \tag{2.23}$$

Fig. 2.2 illustrates the term $\boldsymbol{\xi} + \boldsymbol{\eta}$, which represents the relative position of $\mathbf{x}$ and $\mathbf{x}'$ in the current (deformed) configuration. The condition stated in (2.23) mandates that the force vector between $\mathbf{x}$ and $\mathbf{x}'$ must align with the relative position vector in the deformed configuration. Consequently, under the conditions outlined in (2.22) and (2.23), the interacting forces between the points must possess equal magnitudes, opposite directions, and collinearity with their respective relative position vectors in the deformed configuration. Thus, the bond can be understood as a spring that transfers a force between the two points. To this end, the pairwise force function $\mathbf{f}$ takes the form

$$\mathbf{f}(\boldsymbol{\eta}, \boldsymbol{\xi}) = f(\boldsymbol{\eta}, \boldsymbol{\xi}) \frac{\boldsymbol{\xi} + \boldsymbol{\eta}}{\|\boldsymbol{\xi} + \boldsymbol{\eta}\|}, \tag{2.24}$$

where $f$ is a symmetric scalar-valued function, meaning that $f(\boldsymbol{\eta}, \boldsymbol{\xi}) = f(-\boldsymbol{\eta}, -\boldsymbol{\xi})$. The specific definition of $f$ depends on the material type involved. Note that $f$ is a special case of the force scalar state in (2.3). where the bond-based peridynamic model does not necessitate the general state notation. In order to model elastic materials, a specific class of peridynamic materials known as *microelastic* is introduced in [128]. In this class, the pairwise force function $\mathbf{f}$ is derived from a differentiable scalar-valued function $w$, referred to as the *pairwise potential function*. The relationship between $\mathbf{f}$ and $w$ is expressed as

$$\mathbf{f}(\boldsymbol{\eta}, \boldsymbol{\xi}) = \frac{\partial w(\boldsymbol{\eta}, \boldsymbol{\xi})}{\partial \boldsymbol{\eta}}. \tag{2.25}$$

Additionally, the *macroelastic energy density* in the GPBM constitutive model at position $\mathbf{x}$ and time $t \geq 0$ is defined as

$$W_{\mathrm{GPBM}} = \frac{1}{2} \int_{\mathcal{H}\mathbf{x}} w(\boldsymbol{\eta}, \boldsymbol{\xi}) \, \mathrm{d}V_{\mathbf{x}'}, \tag{2.26}$$

where the factor $\frac{1}{2}$ is included since the elastic energy associated with each bond is shared equally between its two endpoints. By exclusively employing pairwise potentials, a notable consequence arises in the resulting material models: for an isotropic, linear, and microelastic material, the effective Poisson's ratio $\nu$ is $\frac{1}{3}$ in 2D and plane stress conditions and $\frac{1}{4}$ in plane strain conditions and 3D problems [135]. The aforementioned limitation stems from the fact that the pairwise force function in bond-based PD defines the interaction of each pair of points solely through a central force. This constraint is overcome in the general state-based PD formulation. Nevertheless, bond-based PD remains a suitable choice for numerous applications, particularly in the context of brittle fracture modeling.

As a brief note on boundary conditions, it is important to highlight that the imposition of boundary conditions in PD differs from classical theory. The variational formulation of the peridynamic governing equation does not naturally lead to Neumann (traction) boundary conditions as in CCM [128]. Instead, surface forces are applied as body forces within a volumetric layer beneath the surface, typically with a thickness of $\delta$ in bond-based PD. Similarly, displacement (Dirichlet) boundary conditions are prescribed within a layer of thickness $\delta$ beneath the constrained surface. The specific boundary conditions used in the numerical studies are be discussed in the respective sections in this dissertation.

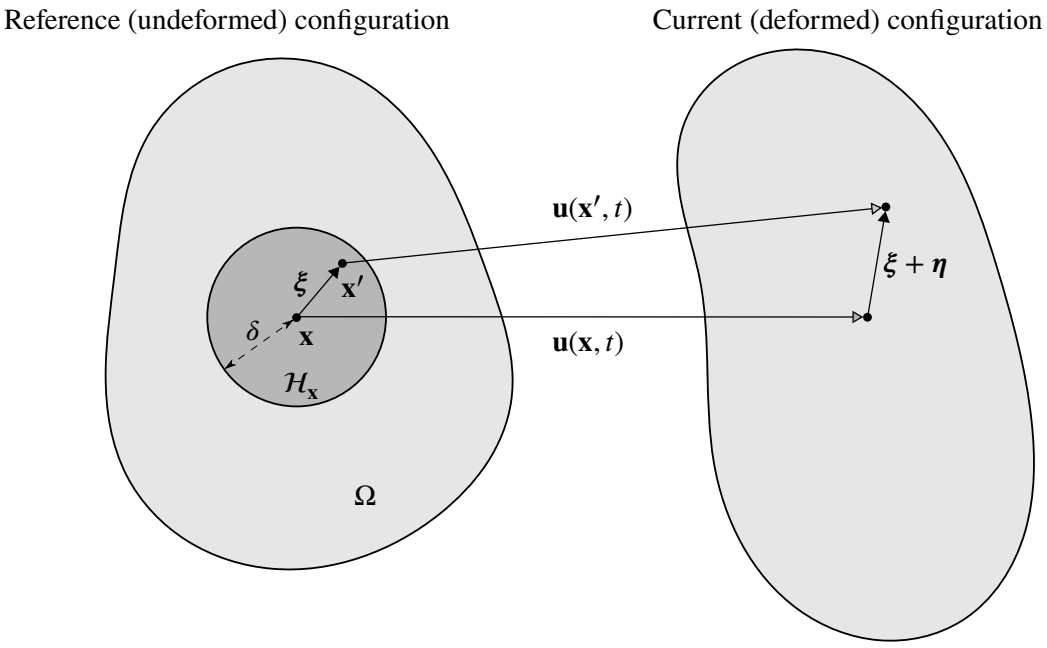


Figure 2.2: Reference and current peridynamic domain, depicting the material point $\mathbf{x}$ interacting with the neighboring point $\mathbf{x}'$ within the neighborhood $\mathcal{H}_{\mathbf{x}}$ through nonlocal bonds. Reproduced from [122].

The first prototype brittle material model was introduced in [130] and was later extended to the class of GPBM constitutive models in [116]. In the GPBM model, $w$ is defined by

$$w(\boldsymbol{\eta}, \boldsymbol{\xi}) = \frac{\omega(\|\boldsymbol{\xi}\|) c s^2 \|\boldsymbol{\xi}\|}{2}, \tag{2.27}$$

where $s$ is the *pairwise stretch function* of a bond defined by

$$s = \frac{\|\boldsymbol{\xi} + \boldsymbol{\eta}\| - \|\boldsymbol{\xi}\|}{\|\boldsymbol{\xi}\|}, \tag{2.28}$$

and $c$ is the *micromodulus* constant that determines the bond elastic stiffness and $\omega(\|\boldsymbol{\xi}\|)$ is the influence function. Given the conditions in (2.22) and (2.23), the interaction forces between two neighboring points are equal, opposite, and collinear with the relative position vector in the current configuration. The pairwise force function in (2.24) for the GPBM material model can thus be derived as

$$\mathbf{f}(\boldsymbol{\eta}, \boldsymbol{\xi}) = f(\boldsymbol{\eta}, \boldsymbol{\xi}) \frac{\boldsymbol{\xi} + \boldsymbol{\eta}}{\|\boldsymbol{\xi} + \boldsymbol{\eta}\|}, \tag{2.29}$$

where the scalar-valued function $f$ in (2.24) is given by

$$f(\boldsymbol{\eta}, \boldsymbol{\xi}) = \omega(\|\boldsymbol{\xi}\|) c s. \tag{2.30}$$

By equating the macroelastic energy density defined in (2.26) with the strain energy density of CCM for homogeneous deformations, it is possible to determine the micromodulus constant $c$ in terms of the CCM constants, namely Young's modulus $E$ and Poisson's ratio $\nu$. A detailed explanation of the procedure to obtain $c$ in terms of these classical constants can be found in [114]. Specifically, for plane stress conditions, the relationship can be established as

$$c = \begin{cases} \dfrac{9E}{\pi \delta^3}, & \omega = \omega_0, \\ \dfrac{36E}{\pi \delta^3}, & \omega = \omega_1. \end{cases} \tag{2.31}$$

Similar to (2.18) in Section 2.1, the bond-based PD formulation of the pairwise force function in (2.29) may further be linearized [128, 114]. Assuming small deformations, i.e., $\|\boldsymbol{\eta}\| \ll \delta$, the linearized form of (2.29) is given by

$$\begin{aligned} \mathbf{f}(\boldsymbol{\eta}, \boldsymbol{\xi}) =& \omega(\|\boldsymbol{\xi}\|) c \frac{\boldsymbol{\xi} \otimes \boldsymbol{\xi}}{\|\boldsymbol{\xi}\|^3} \boldsymbol{\eta} \\ :=& \mathbf{C}(\boldsymbol{\xi}) \boldsymbol{\eta}, \end{aligned} \tag{2.32}$$

where $\mathbf{C}(\boldsymbol{\xi})$ is the *micromodulus function* of the linearized system, which is a second-order tensor that depends on $\boldsymbol{\xi}$. In the work of [130], a simple approach to introducing failure in peridynamic models is presented. This is achieved through the GPBM model, where a Boolean-valued history-dependent function $\mu$ is incorporated into the (nonlinear) pairwise force function $\mathbf{f}$ in equation (2.29). The expression for $\mathbf{f}$ can be written as

$$\mathbf{f}(\boldsymbol{\eta}, \boldsymbol{\xi}) = \mu(\boldsymbol{\xi}, t) \omega(\|\boldsymbol{\xi}\|) c s \frac{\boldsymbol{\xi} + \boldsymbol{\eta}}{\|\boldsymbol{\xi} + \boldsymbol{\eta}\|}, \tag{2.33}$$

where the function $\mu(\boldsymbol{\xi}, t)$ is defined as

$$\mu(\boldsymbol{\xi}, t) = \begin{cases} 1, & s(\bar{t}) < s_0,\ 0 < \bar{t} < t, \\ 0, & \text{otherwise.} \end{cases} \tag{2.34}$$

In this formulation, $s_0$ is referred to as the *critical stretch* for bond failure. Consequently, the function $\mu$ allows a bond to break when its stretch exceeds the predefined critical stretch $s_0$. Once bond breakage occurs, the model becomes history-dependent, as there is no sustained tensile force. The constitutive relation of the GPBM model is illustrated in Fig. 2.3.

As suggested in [130], a relationship can be established between the critical stretch $s_0$ and the fracture energy $G_0$ of the material. Specifically, for plane stress conditions, the connection can be expressed as

$$s_0 = \begin{cases} \sqrt{\dfrac{4\pi G_0}{9E\delta}}, & \omega = \omega_0, \\ \sqrt{\dfrac{5\pi G_0}{9E\delta}}, & \omega = \omega_1. \end{cases} \tag{2.35}$$

The concept of damage, introduced at the bond level, allows us to define the damage state at a point $\mathbf{x}$ and time $t \geq 0$. This is quantified by the damage function $\varphi(\mathbf{x}, t)$, which is defined as

$$\varphi(\mathbf{x}, t) := 1 - \frac{\int_{\mathcal{H}_\mathbf{x}} \mu(\boldsymbol{\xi}, t) \mathrm{d}V_{\mathbf{x}'}}{\int_{\mathcal{H}_\mathbf{x}} \mathrm{d}V_{\mathbf{x}'}}. \tag{2.36}$$

The damage function $\varphi(\mathbf{x}, t)$ is defined within the range $0 \leq \varphi \leq 1$. When $\varphi = 0$, it represents an undamaged state at point $\mathbf{x}$, indicating that no damage is present. Conversely, when $\varphi = 1$, it indicates complete disconnection of point $\mathbf{x}$ from all its initially interacting neighboring points, signifying severe damage where all bonds are fully broken.

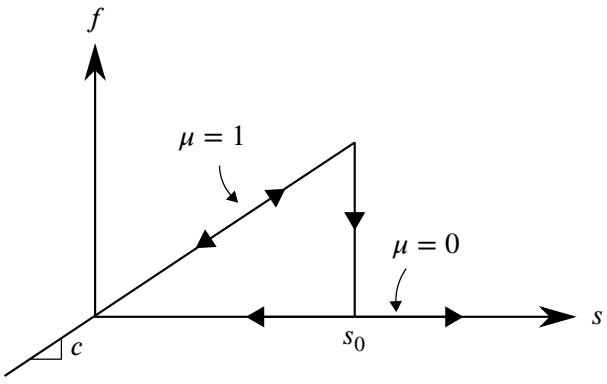


Figure 2.3: A schematic diagram illustrating the constitutive law of the GPBM model assuming the constant influence function $\omega_0$. Reproduced from [122].

## 2.3 Nonlocal Scalar Fields

Nonlocal scalar fields can be seen as a generalization of classical local field equations where the governing field variable is a scalar value that changes over time and space according to a governing equation. In this dissertation, nonlocal scalar fields encompass the nonlocal peridynamic extensions of the classical scalar wave equation, the diffusion equation, and the Nernst-Planck-Poisson system of scalar equations. Here, spatial gradients are replaced with nonlocal integral formulations that correspond, in the leading terms of the Taylor series expansion, to the definitions of their classical local counterparts. The peridynamic bi-material corrosion equation is derived from the peridynamic diffusion equation and is considered as a two-phase material system, treated as a separate model in this context. As we will see in Section 2.3.4, the NNPP system can be viewed as a generalization of the standard bi-material peridynamic corrosion model, accounting for electromigration and reaction terms.

### 2.3.1 The Nonlocal Peridynamic Scalar Wave Equation

In this section, we focus on the nonlocal peridynamic scalar wave equation, which can be seen as a generalization of the classical equation [91, 143]. We begin by reviewing the classical (local) scalar wave equation, which describes wave propagation in a viscous and isotropic medium that may contain physical objects such as baffles and sources. Considering a 2D domain, $\Omega \in \mathbb{R}^2$, the scalar wave equation is formulated for the domain and is given by

$$\ddot{u}(\mathbf{x},t) = \chi^2 \nabla^2 u(\mathbf{x},t) - 2d\dot{u}(\mathbf{x},t) + b(\mathbf{x},t), \quad \mathbf{x} \in \Omega, \quad t > 0, \tag{2.37}$$

where, $u(\mathbf{x},t)$ represents the field variable at point $\mathbf{x} = (x,y)^{\mathrm{T}}$ and time $t$, and $\dot{u}(\mathbf{x},t)$ and $\ddot{u}(\mathbf{x},t)$ denote the first and second time derivatives of $u(\mathbf{x},t)$, respectively. The parameter $\chi^2$ represents the wave propagation speed, $d$ is the damping coefficient, and $b(\mathbf{x},t)$ is a given source (or force) function. The Laplace operator, denoted as $\nabla^2$, is used to express the spatial derivatives in the equation. By convention, we incorporate the factor 2 in the damping term for convenience in subsequent calculations. The surface of the physical objects (scatterers) within the domain $\Omega$ requires the imposition of appropriate Dirichlet and Neumann boundary conditions, which are given by

$$\begin{aligned} u(\mathbf{x},t) &= b_D(\mathbf{x},t), \quad \mathbf{x} \in \Gamma_D, \\ \mathbf{n} \cdot \nabla u(\mathbf{x},t) &= b_N(\mathbf{x},t), \quad \mathbf{x} \in \Gamma_N, \end{aligned} \tag{2.38}$$

where $\mathbf{n} = (n_x, n_y)$ represents the outward unit vector normal to the boundary surface, and $b_D(\mathbf{x},t)$ and $b_N(\mathbf{x},t)$ are functions specifying the values of the boundary conditions at the Dirichlet and Neumann boundaries $\Gamma_D$ and $\Gamma_N$, respectively. The governing equation in (2.37) is augmented with initial conditions given by:

$$\begin{aligned} u(\mathbf{x},0) &= u_0(\mathbf{x}), \quad \mathbf{x} \in \Omega, \\ \dot{u}(\mathbf{x},0) &= \dot{u}_0(\mathbf{x}), \quad \mathbf{x} \in \Omega, \end{aligned} \tag{2.39}$$

where $u_0(\mathbf{x})$ and $\dot{u}_0(\mathbf{x})$ are given functions specifying the first and second kind of initial conditions, respectively. Next, we generalize the classical local model in (2.37) to the nonlocal peridynamic scalar wave equation. Unlike the classical wave equation, the peridynamic wave equation captures dispersive effects, thus encompassing a broader range of possible solutions. In Section 4.2.1 of this dissertation, we demonstrate that the peridynamic model includes the classical wave equation as a

special case when nonlocal interactions vanish by deriving fundamental solutions from harmonic EBFs. We begin by considering a circular neighborhood $\mathcal{H}_{\mathbf{x}}$, as defined in (2.1), around the material point $\mathbf{x}$ in 2D with a peridynamic horizon $\delta$. The point $\mathbf{x}$ interacts nonlocally with its neighboring points $\mathbf{x}'$ within the region $\mathcal{H}_{\mathbf{x}}$, as was schematically illustrated in Fig. 2.2. For a point $\mathbf{x} \in \Omega$ at time $t > 0$, the governing peridynamic scalar wave equation can be expressed as

$$\ddot{u}(\mathbf{x}, t) = \int_{\mathcal{H}_{\mathbf{x}}} c_s \omega(\|\mathbf{x}' - \mathbf{x}\|) \frac{u(\mathbf{x}', t) - u(\mathbf{x}, t)}{\|\mathbf{x}' - \mathbf{x}\|^p} \, \mathrm{d}V_{\mathbf{x}'} - 2d\dot{u}(\mathbf{x}, t) + b(\mathbf{x}, t), \tag{2.40}$$

where $c_s$ is the micromodulus constant of the peridynamic scalar wave equation, $\omega$ is the scalar-valued influence function, parameter $p$ in the peridynamic scalar wave equation is typically chosen as an integer value from the set $\{0, 1, 2, 3\}$ (see e.g., [99]). As discussed in Section 2.1, the influence function in the peridynamic scalar wave-type equation is commonly defined as either constant (*cf.* (2.12)) or linear (*cf.* (2.13)) within the neighborhood $\mathcal{H}_{\mathbf{x}}$ (see e.g., [16]). The choice of influence function significantly affects the spatial decay and range of the nonlocal interactions in (2.40).

The micromodulus constant $c_s$, which generally depends on the horizon $\delta$, must be determined in relation to the chosen influence function. This ensures that the peridynamic scalar wave-type equation (2.40) converges to the classical equation (2.37) as the nonlocal interactions vanish ($\delta \to 0$), assuming appropriate regularity conditions for the field variable $u$.

### 2.3.2 The Nonlocal Peridynamic Diffusion Equation

In the context of diffusion-type problems, the peridynamic governing equation can be formulated to describe the transport of concentration [13, 14]. According to the peridynamic diffusion formulation, each point $\mathbf{x}$ at time $t$ is associated with a concentration value $C(\mathbf{x}, t)$. The neighboring points $\mathbf{x}' \in \mathcal{H}_{\mathbf{x}}$ within a peridynamic horizon $\delta$ are connected to $\mathbf{x}$ through *diffusion bonds*, which can be conceptualized as pipe-like conductors. These bonds, represented by the vector $\boldsymbol{\xi}$, facilitate the transfer of concentration between the connected points, similar to buckets connected by pipes. In the bond-based version of peridynamic diffusion the transport of concentration in each bond is independent of other bonds. The governing peridynamic equation for diffusion at point $\mathbf{x}$ and time $t \geq 0$ is given by

$$\dot{C}(\mathbf{x}, t) = \int_{\mathcal{H}_{\mathbf{x}}} \boldsymbol{J} \left( C(\mathbf{x}', t) - C(\mathbf{x}, t), \mathbf{x}' - \mathbf{x} \right) \mathrm{d}V_{\mathbf{x}'} + S(\mathbf{x}, t), \tag{2.41}$$

where $\dot{C}$ is the first time derivative of the concentration field, $S$ is a given source function, and $\boldsymbol{J}$ is the *concentration flow density* given by

$$\boldsymbol{J}(\Theta, \boldsymbol{\xi}) = \begin{cases} \kappa \omega(\|\boldsymbol{\xi}\|) \dfrac{\Theta}{\|\boldsymbol{\xi}\|^q}, & \|\boldsymbol{\xi}\| \leq \delta, \\ 0, & \|\boldsymbol{\xi}\| > \delta, \end{cases} \tag{2.42}$$

where $\Theta := C(\mathbf{x}', t) - C(\mathbf{x}, t)$, and $\boldsymbol{\xi} = \mathbf{x}' - \mathbf{x}$, and $\omega$ is the influence function (typically selected from (2.12) or (2.13)). The shape of the concentration flow density $\boldsymbol{J}$ is determined by the parameter $q$, often chosen as an integer value from the set of $\{0, 1, 2, 3\}$ (see e.g., [26]). The micro-diffusivity constant $\kappa$ depends on the peridynamic horizon $\delta$ and can be derived in terms of the diffusion coefficient $\boldsymbol{D}$ in the classical local diffusion equation. This is usually achieved by equating the peridynamic flux to that of the local diffusion equation in certain steady-state cases [13, 123].

Depending on the particular choice of the influence function, in 2D peridynamic diffusion with $q = 2$ we obtain

$$\kappa = \begin{cases} \dfrac{4D}{\pi\delta^2}, & \omega = \omega_0, \\ \dfrac{12D}{\pi\delta^2}, & \omega = \omega_1. \end{cases} \tag{2.43}$$

For peridynamic diffusion models, boundary conditions are typically imposed within a volumetric layer of thickness $\delta$ on the domain. Boundary conditions of Neumann-type are included in the source term $S(\mathbf{x}, t)$ of (2.41). More details on the selection and modeling of these boundary conditions can be found in [26, 140, 162].

### 2.3.3 The Peridynamic Bi-Material Corrosion Model

In this section, we extend the peridynamic diffusion model discussed earlier to incorporate corrosion modeling. Unlike traditional corrosion models that focus solely on diffusion in the electrolyte, peridynamic corrosion models consider corrosion as a damage process resulting from dissolution within the solid material. This approach accounts for microstructure and heterogeneities, providing a more realistic representation of the corrosion phenomenon. Peridynamic corrosion models offer a comprehensive understanding of corrosion damage by integrating metal ion diffusion, phase changes caused by dissolution, and mechanical damage in the corroding layer. These models have been successful in capturing corrosion-induced phenomena and elucidating the complex interplay between dissolution, mechanical damage, and material microstructure. For more details and comprehensive numerical studies on corrosion models, refer, for example, to [25, 63, 64].

Nonlocal peridynamic diffusion equations are valuable for modeling electrochemical corrosion and anodic dissolution due to their ability to provide a homogenized representation of interface kinetics. These models efficiently capture phenomena such as surface conversion, layer deposition, and wetting of solid metal surfaces, considering factors like microcracks, pores, and precipitates. By utilizing a solid-liquid interface description, the peridynamic corrosion models offer a comprehensive approach to address the various aspects of Mg-Gd degradation, including other mechanisms that influence the process [25, 153].

In the following discussion, we introduce a Diffusive Corrosion Layer (DCL) where gradual changes in chemical composition and mechanical properties occur. The transport of metal ions across the solid-liquid interface is represented by an effective diffusivity. To model this ion transport within the DCL and into the electrolyte, a bi-material peridynamic diffusion approach is employed. The focus is on the *efficient diffusion* across the DCL due to its significantly higher flux density compared to the solid bulk material. To understand the underlying assumptions of the peridynamic corrosion model, we first examine the fluxes across the DCL from the perspective of the classical diffusion equation. We consider a generic domain $\Omega \subset \mathbb{R}^{n_d}$, where $n_d$ is the spatial dimension. Both the bulk material and the surrounding electrolyte medium are assumed to be isotropic. Within the liquid medium, at a point $\mathbf{x}$, the governing equation in the classical local theory is expressed as

$$\dot{C}(\mathbf{x}, t) = \nabla \cdot \boldsymbol{J}(C, t), \quad \mathbf{x} \in \Omega, \quad t > 0, \tag{2.44}$$

where $C(\mathbf{x}, t)$ represents the (molar) concentration of the diffusing material at point $\mathbf{x}$ and time $t$, $\boldsymbol{J}$ denotes the flux, and $\nabla\cdot$ is the divergence operator. To solve (2.44), appropriate boundary con-

ditions need to be specified. Typically, Dirichlet and Neumann conditions are employed as

$$\begin{aligned} C &= C^*(\mathbf{x}, t), \quad \mathbf{x} \in \Gamma_D \\ \mathbf{n} \cdot \boldsymbol{J} &= q^*(\mathbf{x}, t), \quad \mathbf{x} \in \Gamma_N, \end{aligned} \tag{2.45}$$

where $C^*$ represents the prescribed concentration value on the Dirichlet boundary $\Gamma_D$, while $q^*$ denotes the prescribed flux value along the outward normal vector $\mathbf{n}$ on the Neumann boundary $\Gamma_N$. The bi-material approach considers two distinct fluxes within the classical Fickian constitutive law as

$$\boldsymbol{J}(C, t) = \begin{cases} D_S(\eta) \nabla C, & \text{solid (DCL)} \\ D_L \nabla C, & \text{liquid (electrolyte),} \end{cases} \tag{2.46}$$

where $D_L > 0$ represents the metal ion diffusivity within the electrolyte medium, and $D_S(\eta) > 0$ represents the diffusivity within the solid DCL, which is also referred to as the (anodic) *dissolution affinity*. Fig. 2.4 provides a schematic representation of the bi-material effective diffusion approach, depicting the flux in the solid and liquid parts of the domain, $\boldsymbol{J}_S$ and $\boldsymbol{J}_L$, respectively.

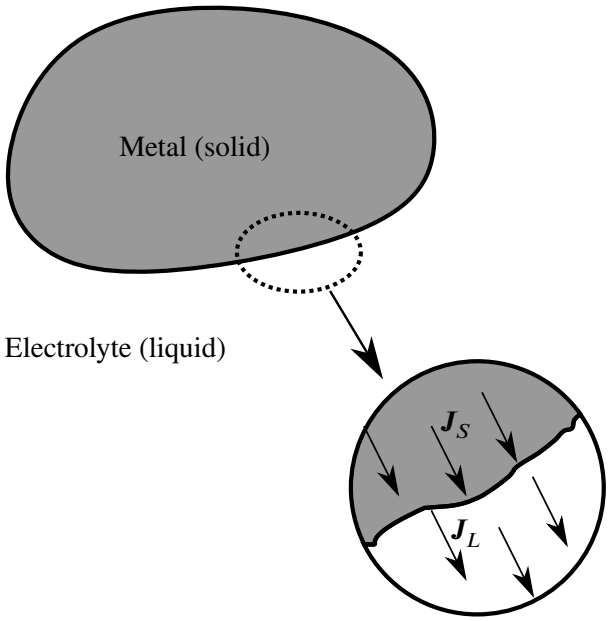


Figure 2.4: The schematic illustration of the bi-material effective diffusion approach used for corrosion modeling depicting the framework of two distinct materials: a solid metal component and a surrounding electrolyte medium. Reproduced from [60].

The dissolution affinity $D_S(\eta)$ depends on the electrochemical overpotential $\eta$ and is obtained from a Tafel-like expression as

$$D_S(\eta) = D_0\, 10^{\left(\frac{\eta}{\beta_a}\right)}, \tag{2.47}$$

where $D_0$ is the dissolution affinity at the Open Circuit Potential (OCP), and $\beta_a$ is the anodic Tafel slope, which are typically calibrated based on the Tafel plot specific to the electrochemical corrosion system. While the anodic Tafel description is not universally applicable to corrosive materials [45], it can still be used as an empirical formulation for dissolution experiments. Model parameters can be calibrated through numerical optimization and surrogate modeling techniques using experimental immersion test data. Chapter 5 of this dissertation explores a multi-physics application focusing on the bio-corrosion and mechanical bio-degradation of binary alloy Mg-Gd bone implant screws. This study demonstrates the practical implementation of peridynamic corrosion models and emphasizes the numerical parameterization aspect. The respective sections provide detailed explanations and discussions on the numerical calibration and determination of model parameters based on experimental dissolution data for accurate corrosion prediction in the context of Mg-Gd bone implant screws.

In the classical local model, diffusion behavior is described by a flux continuity condition at the solid-liquid interface, assuming Fickian diffusion. However, this model has limitations in representing the anomalous diffusion behavior often encountered in corrosion problems. In contrast, the peridynamic corrosion model, formulated within the framework of bond-based PD, offers a more versatile approach. It eliminates the need for flux continuity conditions and allows for the representation of various types of diffusion, including anomalous diffusion. By implicitly capturing the movement of boundaries in the governing equations, the peridynamic corrosion model provides a more comprehensive and realistic representation of general corrosion phenomena. The peridynamic bi-material corrosion equation describes the concentration dynamics at a material point $\mathbf{x}$ in the body $\Omega$ at time $t > 0$, and is given by

$$\dot{C}(\mathbf{x}, t) = \int_{\mathcal{H}} J_q(\Theta, \boldsymbol{\xi}, t)\, \mathrm{d}V_{\boldsymbol{\xi}}, \tag{2.48}$$

where $\mathcal{H}$ represents the neighborhood centered around the origin with horizon $\delta$. The bond vector is given by $\boldsymbol{\xi} := \mathbf{x}' - \mathbf{x}$, and $\Theta := C(\mathbf{x} + \boldsymbol{\xi}, t) - C(\mathbf{x}, t)$. The concentration flow density, also known as the kernel function of the integral operator, is represented as $J_q(\Theta, \boldsymbol{\xi}, t)$ in the context of the peridynamic corrosion system. The constitutive model of the system may explicitly incorporate a time dependence. The concentration flow density characterizes the dissolution process of ionic metal concentration and is given by

$$J_q(\Theta, \boldsymbol{\xi}, t) = \begin{cases} \omega(\|\boldsymbol{\xi}\|)\kappa(\boldsymbol{\xi}, t)\, \dfrac{\Theta}{\|\boldsymbol{\xi}\|^{n_d+2q}}, & \|\boldsymbol{\xi}\| \le \delta, \\ 0, & \|\boldsymbol{\xi}\| > \delta, \end{cases} \tag{2.49}$$

where $\delta$ is the horizon and $p \in (-1, \infty)$ is a scalar value. Unlike in previous approaches, we introduce a continuous factor $n_d + 2q$ in the kernel function. This allows us to customize the kernel to fit specific corrosion systems based on experimental data. The modified kernel captures anomalous diffusion behavior associated with anodic dissolution. Notably, when $q$ falls between 0 and 1, the kernel function resembles fractional Laplacian models. In Chapter 5, specifically

Section 5.2.2, we apply the peridynamic corrosion model to simulate the bio-corrosion process of Mg-Gd bone implant screws. In this context, we treat the parameter $q$ as an unknown model and system parameter and estimate its value through numerical parameter optimization. Similarly to the previous sections, the influence function $\omega(\|\boldsymbol{\xi}\|)$ is defined either as constant (*cf.* (2.12)) or linear (*cf.* (2.13)) within the neighborhood.

The micro-diffusivity $\kappa(\boldsymbol{\xi}, t)$ in the peridynamic bi-material corrosion model is governed by the constitutive assumptions of the corrosion system and can vary depending on the bond $\boldsymbol{\xi}$ and possibly with time [25]. For bonds within the bulk medium, away from the corrosion surface, and under steady-state conditions, the micro-diffusivity can be related to the diffusion coefficient $D_L$ of the electrolyte medium. However, when bonds extend into the DCL, the micro-diffusivity incorporates the interface kinetics of the specific corrosion system. It can be expressed using a Tafel-like expression, similar to the relation (2.47), and thus depends on the electrochemical overpotential. In this context, achieving model correspondence is essential to calibrate the peridynamic corrosion model parameters from experimental degradation data. Moreover, the phase change parameter $\varphi$ determines the micro-diffusivity. A phase transition from metal to liquid occurs when the metal ion concentration $C_{\text{metal}}(\mathbf{x}, t)$ falls below the saturation concentration $C_{\text{sat}}$, with $\varphi(\mathbf{x}, t)$ set to 1 if $C_{\text{metal}}(\mathbf{x}, t) \geq C_{\text{sat}}$ and 0 if $C_{\text{metal}}(\mathbf{x}, t) < C_{\text{sat}}$, and this phase change mechanism is applied throughout the numerical examples in this dissertation.

### 2.3.4 The Nonlocal Nernst-Planck-Poisson System

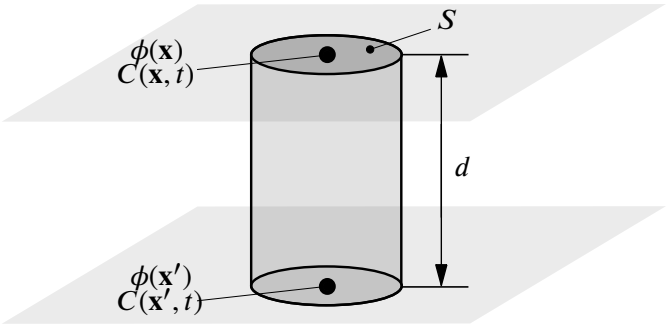


Figure 2.5: Transport of concentration within a cylindrical tube confined by two parallel planes, each characterized by different concentration and electrostatic potential values. Reproduced from [58].

To conclude this chapter, we introduce and derive the general form of the NNPP system in 3D, proposed as a consistent nonlocal generalization of the classical peridynamic bi-material corrosion model to incorporate multi-ionic electromigration. An initial attempt at this nonlocal extension was proposed by [80], which adopted a nonlocal Nernst-Planck electromigration model to include various electroneutrality constraints in 1D; however, it did not provide rigorous derivations for their equations. We extend the nonlocal equations of electromigration to 3D spaces, ensuring a corrected formulation that guarantees convergence in the nonlocal to local limit. Although the original system in [80] introduced a nonlocal electromigration term by averaging ion concentrations between two neighboring material points, our derivations suggest that a minor adjustment, specifically a factor of 2, is necessary to ensure proper convergence to classical local equations.

The derivation begins by extending the peridynamic approach to transient heat conduction, as detailed in [13, 14], to generalize and account for multi-ionic electromigration. We consider two points, $\mathbf{x}$ and $\mathbf{x}'$, situated on two parallel planes separated by a distance $d$. These planes exhibit different concentration values, with $C(\mathbf{x}', t) > C(\mathbf{x}, t)$, as illustrated in Fig. 2.5. The transfer of concentration between two planes across a surface area $S$ is governed by

$$S(J_d' - J_d) = SD\frac{C(\mathbf{x}', t) - C(\mathbf{x}, t)}{d}, \tag{2.50}$$

where $J_d'$ and $J_d$ are the diffusion-related fluxes per unit time and area at $\mathbf{x}'$ and $\mathbf{x}$, respectively, and $D$ is the diffusion coefficient of the medium. Additionally, we consider the electromigration-related flow densities $J_e$ and $J_e'$, representing the number of ions crossing a surface area perpendicular to their motion at the respective points as

$$\begin{aligned} J_e' &= v'C(\mathbf{x}', t), \\ J_e &= vC(\mathbf{x}, t), \end{aligned} \tag{2.51}$$

where v' and v are the velocities at the respective spatial positions. With the planes kept at different electric potentials, $\phi(\mathbf{x}')$ and $\phi(\mathbf{x})$, the forces exerted by a homogeneous electric field, denoted as $F_e$ and $F_e'$, due to the potential difference over the distance $d$, multiplied by the mobility $\mu$, give the velocities as

$$\begin{aligned} v' &= \mu F_e' = -\mu zF\frac{\phi(\mathbf{x}) - \phi(\mathbf{x}')}{d}, \\ v &= \mu F_e = -\mu zF\frac{\phi(\mathbf{x}') - \phi(\mathbf{x})}{d}, \end{aligned} \tag{2.52}$$

where $z$ represents the valence of the charge and $F$ is Faraday's constant. We now introduce $C_a$ as the average concentration within a cylindrical volume defined by a cross-sectional area $S$ and length $d$ between points $\mathbf{x}'$ and $\mathbf{x}$. The rate of change in concentration, $C_a$, is given by

$$d\frac{\partial C_a}{\partial t} \approx \left(J_d' + J_e'\right) - \left(J_d + J_e\right) = D\frac{C(\mathbf{x}', t) - C(\mathbf{x}, t)}{d} + \mu zF\frac{\phi(\mathbf{x}') - \phi(\mathbf{x})}{d}\left(C(\mathbf{x}', t) + C(\mathbf{x}, t)\right). \tag{2.53}$$

The electrical mobility $\mu$ is related to the medium's diffusion coefficient $D$ through the Einstein relation as

$$\mu = \frac{D}{RT}, \tag{2.54}$$

where $R$ is the gas constant and $T$ is the temperature. As $d$ approaches zero, (2.53) transitions to a spatial gradient representation, thus converging to the classical Nernst-Planck formulation. However, for the nonlocal electromigration model, we assume $d$ remains finite. Under this assumption, we explore a configuration of material points within a 3D space $\Omega$, each linked to its neighbors through bond connections within a finite radius defined by the peridynamic horizon, $\delta$. Electromigration is modeled along these bonds, treated as insulated conduits, with $\mathbf{e}$ representing the unit vector along the bond vector between $\mathbf{x}'$ and $\mathbf{x}$. The nonlocal Nernst-Planck equation for a bond between $(\mathbf{x}', \mathbf{x})$ along $\mathbf{e}$ is then formulated as

$$(\mathbf{x}' - \mathbf{x})\cdot\mathbf{e}\frac{\partial C_a(\mathbf{x}', \mathbf{x}, t)}{\partial t} = D\left(\frac{C(\mathbf{x}', t) - C(\mathbf{x}, t)}{(\mathbf{x}' - \mathbf{x})\cdot\mathbf{e}} + \frac{zF}{RT}\frac{\phi(\mathbf{x}') - \phi(\mathbf{x})}{(\mathbf{x}' - \mathbf{x})\cdot\mathbf{e}}\left(C(\mathbf{x}', t) + C(\mathbf{x}, t)\right)\right), \tag{2.55}$$

where $C_a(\mathbf{x}', \mathbf{x}, t)$ denotes the average concentration along the bond $(\mathbf{x}', \mathbf{x})$. Assuming a constant and isotropic diffusion coefficient $D$ across the neighborhood $\mathcal{H}_\mathbf{x}$, dividing both sides of (2.55) by

the distance $(\mathbf{x}' - \mathbf{x}) \cdot \mathbf{e}$ and integrating over the neighborhood, $\mathcal{H}_\mathbf{x}$, yields

$$\int_{\mathcal{H}_\mathbf{x}} \frac{\partial C_a(\mathbf{x}', \mathbf{x}, t)}{\partial t} \mathrm{d}V_{\mathbf{x}'} = \int_{\mathcal{H}_\mathbf{x}} D \left( \frac{C(\mathbf{x}', t) - C(\mathbf{x}, t)}{\|\mathbf{x}' - \mathbf{x}\|^2} + \frac{zF}{RT} \frac{\phi(\mathbf{x}') - \phi(\mathbf{x})}{\|\mathbf{x}' - \mathbf{x}\|^2} \left( C(\mathbf{x}', t) + C(\mathbf{x}, t) \right) \right) \mathrm{d}V_{\mathbf{x}'}. \tag{2.56}$$

It can be shown, that the rate of change in concentration at a point $\mathbf{x}$ over time, $C(\mathbf{x}, t)$, correlates with the average change concentration, $C_a(\mathbf{x}', \mathbf{x}, t)$, for all neighboring points within its vicinity, thus

$$\int_{\mathcal{H}_\mathbf{x}} \frac{\partial c_a(\mathbf{x}', \mathbf{x}, t)}{\partial t} \mathrm{d}V_{\mathbf{x}'} = \frac{\partial c(\mathbf{x}, t)}{\partial t} V_{\mathcal{H}_\mathbf{x}}, \tag{2.57}$$

where $V_{\mathcal{H}_\mathbf{x}}$ denotes the volume of the neighborhood, $\mathcal{H}_\mathbf{x}$, centered at the material point $\mathbf{x}$. Consequently, the integral form in (2.56) simplifies to

$$\frac{\partial C(\mathbf{x}, t)}{\partial t} = \int_{\mathcal{H}_\mathbf{x}} \kappa \left( \frac{C(\mathbf{x}', t) - C(\mathbf{x}, t)}{\|\mathbf{x}' - \mathbf{x}\|^2} + \frac{zF}{RT} \frac{\phi(\mathbf{x}') - \phi(\mathbf{x})}{\|\mathbf{x}' - \mathbf{x}\|^2} \left( C(\mathbf{x}', t) + C(\mathbf{x}, t) \right) \right) \mathrm{d}V_{\mathbf{x}'}, \tag{2.58}$$

with $\kappa = D/V_{\mathcal{H}_\mathbf{x}}$ representing the micro-diffusivity constant. In scenarios involving $N$ species, the concentrations at $\mathbf{x}$ and time $t$ for each component $k$ are denoted by $C_k(\mathbf{x}, t)$, where each species participates in chemical reactions either as a reactant or product. The cumulative reaction term for the $k$th species at $\mathbf{x}$ is represented by $R_k(\mathbf{x}, t)$. Therefore, the nonlocal Nernst-Planck system for each species, integrating diffusion, electromigration, and chemical reactions, is formulated as

$$\begin{aligned} \frac{\partial C_k(\mathbf{x}, t)}{\partial t} = & \int_{\mathcal{H}_\mathbf{x}} \kappa_k(\mathbf{x}', \mathbf{x}, t) \left( \frac{C_k(\mathbf{x}', t) - C_k(\mathbf{x}, t)}{\|\mathbf{x}' - \mathbf{x}\|^2} + \frac{z_k F}{RT} \frac{\phi(\mathbf{x}') - \phi(\mathbf{x})}{\|\mathbf{x}' - \mathbf{x}\|^2} \left( C_k(\mathbf{x}', t) + C_k(\mathbf{x}, t) \right) \right) \mathrm{d}V_{\mathbf{x}'} \\ & + R_k(\mathbf{x}, t), \end{aligned} \tag{2.59}$$

where the micro-diffusivity $\kappa(\mathbf{x}', \mathbf{x}, t)$ can generally vary over time and space, as typically assumed in peridynamic constitutive corrosion modeling. To complete the $N$-component nonlocal Nernst-Planck system with the electrostatic potential $\phi$ as an additional unknown, we incorporate the Poisson-Boltzmann equation, which describes the electric field generated by the spatial distribution of the ionic species and is given by

$$-\nabla \cdot \sigma(\mathbf{x}) \nabla \phi(\mathbf{x}) = F \sum_{k=1}^{N} z_k C_k(\mathbf{x}, t), \tag{2.60}$$

where $\sigma(\mathbf{x})$ represents the electrical conductivity at the material point $\mathbf{x}$. Assuming a constant and isotropic electrical conductivity, we complete the $N$ nonlocal Nernst-Planck equations with the nonlocal counterpart of the Poisson equation

$$-\int_{\mathcal{H}_\mathbf{x}} \epsilon \frac{\phi(\mathbf{x}') - \phi(\mathbf{x})}{\|\mathbf{x}' - \mathbf{x}\|^2} \mathrm{d}V_{\mathbf{x}'} = F \sum_{k=1}^{N} z_k C_k(\mathbf{x}, t), \tag{2.61}$$

where $\epsilon$ represents the *micro-conductivity* of the medium. The integration of the nonlocal Poisson equation provides a comprehensive model that incorporates diffusion, electromigration, as well as chemical reactions. If non-negligible external flow fields are present, it could further include an advective integral term on the right-hand side of the nonlocal Nernst-Planck equation

$$\begin{aligned} \frac{\partial C_k(\mathbf{x}, t)}{\partial t} = \int_{\mathcal{H}_\mathbf{x}} \Big( & \kappa_k(\mathbf{x}', \mathbf{x}, t) \frac{C_k(\mathbf{x}', t) - C_k(\mathbf{x}, t)}{\|\mathbf{x}' - \mathbf{x}\|^2} - \nu_k(\mathbf{x}', \mathbf{x}, t) \frac{C_k(\mathbf{x}', t) - C_k(\mathbf{x}, t)}{\|\mathbf{x}' - \mathbf{x}\|} + \\ & \kappa_k(\mathbf{x}', \mathbf{x}, t) \frac{z_k F}{RT} \frac{\phi(\mathbf{x}') - \phi(\mathbf{x})}{\|\mathbf{x}' - \mathbf{x}\|^2} \left( C_k(\mathbf{x}', t) + C_k(\mathbf{x}, t) \right) \Big) \mathrm{d}V_{\mathbf{x}'} + R_k(\mathbf{x}, t), \end{aligned} \tag{2.62}$$

where $v_k(\mathbf{x}', \mathbf{x}, t)$ signifies the *micro-velocity* for the bond between $\mathbf{x}'$ and $\mathbf{x}$ related to the $k$th ionic species. This micro-velocity, like micro-diffusivity, can vary over time and space. While (2.62) and (2.62) were initially derived using specific kernel functions and bond norms, we now consider a more general nonlocal Nernst-Planck equation, expressed as

$$\frac{\partial C_k(\mathbf{x}, t)}{\partial t} = \int_{\mathcal{H}_\mathbf{x}} \Bigg( K_1 \omega(\|\boldsymbol{\xi}\|) D_k \frac{C_k(\mathbf{x}', t) - C_k(\mathbf{x}, t)}{\|\boldsymbol{\xi}\|^{n_d + 2q_1}} + K_2 \omega(\|\boldsymbol{\xi}\|) D_k \frac{z_k F}{RT} \frac{\phi(\mathbf{x}') - \phi(\mathbf{x})}{\|\boldsymbol{\xi}\|^{n_d + 2q_2}} \left( C_k(\mathbf{x}', t) + C_k(\mathbf{x}, t) \right) \Bigg) \mathrm{d}V_{\mathbf{x}'} + R_k(\mathbf{x}, t), \tag{2.63}$$

where $K_1$ and $K_2$ are the proportionality constants, $n_d$ is the spatial dimension, and $q_1$ and $q_2$ are the shape factors for the diffusion and electromigration kernels, respectively. $D_k$ is the Fickian diffusion coefficient for the $k$th species, $z_k$ is the valence, $F$, $R$, and $T$ represent Faraday's constant, the gas constant, and temperature, respectively. This general form (2.63) allows for a broader range of kernel functions, providing greater flexibility in modeling diverse electrochemical dissolution phenomena. The field variables $C_k(\mathbf{x}', t)$, $C_k(\mathbf{x}, t)$, and $\phi(\mathbf{x}')$, $\phi(\mathbf{x})$ indicate the molar concentration and electrostatic potential at the material points $\mathbf{x}'$ and $\mathbf{x}$, respectively. The reaction terms $R_k$ encompass the chemical reactions involving the $k$th species, both as reactants and products. The nonlocal Poisson equation is also adapted to various kernel functions, formulated as

$$-\int_{\mathcal{H}_\mathbf{x}} K_3 \omega(\|\boldsymbol{\xi}\|) \sigma \frac{\phi(\mathbf{x}') - \phi(\mathbf{x})}{\|\boldsymbol{\xi}\|^{n_d + 2q_3}} \mathrm{d}V_{\mathbf{x}'} = F \sum_{i=1}^{N} z_k C_k(\mathbf{x}, t), \tag{2.64}$$

where $K_3$ is a proportionality constant, $q_3$ is the kernel shape exponent, and $\sigma$ is the electrical conductivity.

**Nonlocal to Local Limit Convergence Behavior**

In this section, we introduce a comprehensive class of NNPP systems in 3D and demonstrate the nonlocal to local convergence behavior as the peridynamic horizon $\delta \to 0$ approaches zero. The generalized form of the nonlocal Nernst-Planck equation for the $k$th species is given in (2.63). Note that for (2.63), if $\omega(\|\boldsymbol{\xi}\|) \equiv 1$, with $p_1 = p_2 = -1/2$ and $K_1 = K_2 = 1/V_{\mathcal{H}_\mathbf{x}}$, the system reduces to the specific case in (2.59), showing it as a particular instance of the broader form in (2.63). The nonlocal Poisson equation is similarly expanded to include different kernel functions as shown in (2.64). We aim to demonstrate that as nonlocal interactions vanish with $\delta$ approaching zero, the system described by (2.63) and (2.64) converges to the classical local Nernst-Planck-Poisson equations. The proof involves using Taylor series expansions for the nonlocal fluxes and setting proportionality constants so that the leading terms match their classical counterparts, as elaborated in references such as [114, 15]. We define a spherical subregion $\mathcal{B}^{0,\delta}$ within a bounded body $\mathcal{B}$ as

$$\mathcal{B}^{0,\delta} := \{\mathbf{x} \in \mathcal{B} : \mathcal{H}_\mathbf{x} \subset \mathcal{B}\}. \tag{2.65}$$

For a material point $\mathbf{x}$ within $\mathcal{B}^{0,\delta}$, we assume a smoothly varying concentration field $C_k(\mathbf{x}, t)$. For bond vectors satisfying $\|\boldsymbol{\xi}\| \leq \delta$, the concentration field can be expanded in the form of a Taylor series as

$$C_k(\mathbf{x}', t) = C_k(\mathbf{x}, t) + (\boldsymbol{\xi} \cdot \nabla) C_k(\mathbf{x}, t) + \frac{1}{2} (\boldsymbol{\xi} \cdot \nabla)(\boldsymbol{\xi} \cdot \nabla) C_k(\mathbf{x}, t) + \mathcal{O}\left(\|\boldsymbol{\xi}\|^3\right). \tag{2.66}$$

When incorporating the upper expansion in (2.66) into the first term of the integrand from (2.63), and employing the Einstein summation convention for repeated indices, we get

$$\begin{aligned}\int_{\mathcal{H}_{\mathbf{x}}} K_1\omega(\|\boldsymbol{\xi}\|)D_k\frac{C_k(\mathbf{x}',t)-C_k(\mathbf{x},t)}{\|\boldsymbol{\xi}\|^{n_d+2q_1}}\mathrm{d}V_{\mathbf{x}'} &= \left(\int_{\mathcal{H}} K_1\omega(\|\boldsymbol{\xi}\|)D_k\frac{\xi_i}{\|\boldsymbol{\xi}\|^{n_d+2q_1}}\mathrm{d}V_{\boldsymbol{\xi}}\right)\frac{\partial C_k(\mathbf{x},t)}{\partial x_i}\\ &+\frac{1}{2}\left(\int_{\mathcal{H}} K_1\omega(\|\boldsymbol{\xi}\|)D_k\frac{\xi_i\xi_j}{\|\boldsymbol{\xi}\|^{n_d+2q_1}}\mathrm{d}V_{\boldsymbol{\xi}}\right)\frac{\partial^2 C_k(\mathbf{x},t)}{\partial x_i\partial x_j}+\mathcal{O}\left(\delta^2\right),\end{aligned} \tag{2.67}$$

where $\mathcal{H}$ represents the spherical neighborhood with radius $\delta$ around the origin. The symmetric ranges of the integration in (2.67) eliminate all antisymmetric terms, highlighting the second-order partial derivatives as the first elements in the expansion, while the fourth-order derivatives contribute to the truncation error. For the 3D case, we express the bond vector $\boldsymbol{\xi}$ in spherical coordinates as $\boldsymbol{\xi} = \left(\xi_x, \xi_y, \xi_z\right) = r(\cos\theta\sin\varphi, \sin\theta\sin\varphi, \cos\varphi)$. This allows for the coefficients of the second-order derivatives to be succinctly expressed in matrix form as

$$\begin{aligned}\mathbf{M} = \frac{1}{2}\int_0^{\pi}\int_0^{2\pi}\int_0^{\delta} K_1\omega(r)&\begin{bmatrix}\cos^2\theta\sin^2\varphi & \sin\theta\cos\theta\sin^2\varphi & \cos\theta\sin\varphi\cos\varphi\\ \sin\theta\cos\theta\sin^2\varphi & \sin^2\theta\sin^2\varphi & \sin\theta\sin\varphi\cos\varphi\\ \cos\theta\sin\varphi\cos\varphi & \sin\theta\sin\varphi\cos\varphi & \cos^2\varphi\end{bmatrix}\cdot\\ &\frac{D_k}{r^{n_d+2q_1}}r^4\sin\varphi\,\mathrm{d}r\,\mathrm{d}\theta\,\mathrm{d}\varphi.\end{aligned} \tag{2.68}$$

As the integration spans the full spherical ranges, non-diagonal elements of $\mathbf{M}$ disappear, leaving equal diagonal values. By defining the proportionality constant $K_1$ as

$$K_1 = 2\left(\int_0^{\pi}\int_0^{2\pi}\int_0^{\delta}\omega(r)\frac{r^4}{r^{n_d+2q_1}}\cos^2\varphi\sin\varphi\,\mathrm{d}r\,\mathrm{d}\theta\,\mathrm{d}\varphi\right)^{-1}, \tag{2.69}$$

the matrix $\mathbf{M}$ simplifies to

$$M_{ij} = D_k\delta_{ij}, \tag{2.70}$$

where $\delta_{ij}$ is the Kronecker delta. As $\delta \to 0$, the following limit demonstrates the convergence to the local Fickian diffusion term as

$$\lim_{\delta\to 0} M_{ij}\frac{\partial^2 C_k(\mathbf{x},t)}{\partial x_i\partial x_j} + \mathcal{O}(\delta^2) = D_k\frac{\partial^2 C_k(\mathbf{x},t)}{\partial x_j\partial x_j}. \tag{2.71}$$

Assuming a uniform influence function $\omega(\|\boldsymbol{\xi}\|)$ given by (2.12), and the 3D scenario, we can derive an analytical expression for $K_1$ as

$$K_1 = \frac{3(1-p_1)}{\pi\delta^{2-2s_1}}, \quad p_1 < 1. \tag{2.72}$$

Next, we analyze the convergence behavior of the second integrand in (2.63). Using the Taylor series expansion in (2.66) for the concentration $C_k(\mathbf{x},t)$ and the electrostatic potential $\phi(\mathbf{x})$ at a material point $\mathbf{x} \in \mathcal{B}^{0,\delta}$, and inserting these into the second integrand, we derive

$$\begin{aligned}&\int_{\mathcal{H}_{\mathbf{x}}} K_2\omega(\|\boldsymbol{\xi}\|)D_k\frac{z_kF}{RT}\frac{\phi(\mathbf{x}')-\phi(\mathbf{x})}{\|\boldsymbol{\xi}\|^{n_d+2q_2}}\left(C_k(\mathbf{x}',t)+C_k(\mathbf{x},t)\right)\mathrm{d}V_{\mathbf{x}'}\\ &= \int_{\mathcal{H}_{\mathbf{x}}} K_2\omega(\|\boldsymbol{\xi}\|)D_k\frac{z_kF}{RT}\frac{1}{\|\boldsymbol{\xi}\|^{n_d+2q_2}}\left(2C_k(\mathbf{x},t)+(\boldsymbol{\xi}\cdot\nabla)C_k(\mathbf{x},t)+\frac{1}{2}(\boldsymbol{\xi}\cdot\nabla)(\boldsymbol{\xi}\cdot\nabla)C_k(\mathbf{x},t)+\dots\right)\cdot\\ &\qquad\left((\boldsymbol{\xi}\cdot\nabla)\phi(\mathbf{x})+\frac{1}{2}(\boldsymbol{\xi}\cdot\nabla)(\boldsymbol{\xi}\cdot\nabla)\phi(\mathbf{x})+\dots\right)\mathrm{d}V_{\mathbf{x}'}.\end{aligned} \tag{2.73}$$

Given the symmetry of the integration domain, antisymmetric terms in (2.73) are eliminated. Following the Einstein summation convention, the resulting equation simplifies to

$$\begin{aligned}&\int_{\mathcal{H}_{\mathbf{x}}} K_2\omega(\|\boldsymbol{\xi}\|)D_k\frac{z_kF}{RT}\frac{\phi(\mathbf{x}')-\phi(\mathbf{x})}{\|\boldsymbol{\xi}\|^{n_d+2q_2}}\left(C_k(\mathbf{x}',t)+C_k(\mathbf{x},t)\right)\mathrm{d}V_{\mathbf{x}'}\\&=\int_{\mathcal{H}} K_2\omega(\|\boldsymbol{\xi}\|)D_k\frac{z_kF}{RT}\frac{\xi_i\xi_j}{\|\boldsymbol{\xi}\|^{n_d+2q_2}}\mathrm{d}V_{\boldsymbol{\xi}}\left(C_k(\mathbf{x},t)\frac{\partial^2\phi(\mathbf{x})}{\partial x_i\partial x_j}+\frac{\partial C_k(\mathbf{x},t)}{\partial x_i}\frac{\partial\phi(\mathbf{x})}{\partial x_j}\right)+\mathcal{O}(\delta^2).\end{aligned} \tag{2.74}$$

For the 3D case, the coefficients related to the second-order derivatives are collected in matrix form, paralleling the approach of (2.68), ensuring that due to symmetric integration ranges, non-diagonal terms are nullified and diagonal entries are equated. Therefore, defining the proportionality constant $K_2$ as

$$K_2=\left(\int_0^{\pi}\int_0^{2\pi}\int_0^{\delta}\omega(r)\frac{r^4}{r^{n_d+2q_2}}\cos^2\varphi\sin\varphi\,\mathrm{d}r\,\mathrm{d}\theta\,\mathrm{d}\varphi\right)^{-1}, \tag{2.75}$$

aligns the second integrand in (2.63) with the electromigration fluxes of the classical Nernst-Planck model. Note that, when $p_1 = p_2$, the proportionality constants $K_1 = K_2$ coincide. As $\delta \to 0$ approaches zero in the limit, we obtain

$$\begin{aligned}&\lim_{\delta\to 0}\left(\int_{\mathcal{H}} K_2\omega(\|\boldsymbol{\xi}\|)D_k\frac{z_kF}{RT}\frac{\xi_i\xi_j}{\|\boldsymbol{\xi}\|^{n_d+2q_2}}\mathrm{d}V_{\boldsymbol{\xi}}\right)\left(C_k(\mathbf{x},t)\frac{\partial^2\phi(\mathbf{x})}{\partial x_i\partial x_j}+\frac{\partial C_k(\mathbf{x},t)}{\partial x_i}\frac{\partial\phi(\mathbf{x})}{\partial x_j}\right)+\mathcal{O}(\delta^2)\\&\qquad=D_k\frac{z_kF}{RT}\left(C_k(\mathbf{x},t)\frac{\partial^2\phi(\mathbf{x})}{\partial x_j\partial x_j}+\frac{\partial C_k(\mathbf{x},t)}{\partial x_j}\frac{\partial\phi(\mathbf{x})}{\partial x_j}\right).\end{aligned} \tag{2.76}$$

Assuming a uniform influence function from (2.12), an analytical expression in 3D is derived for the proportionality constant $K_2$ as

$$K_2=\frac{3(1-p_2)}{\pi\delta^{2-2p_2}},\quad p_2<1. \tag{2.77}$$

The analytical approach used for the nonlocal Nernst-Planck equation is equally applicable to the nonlocal Poisson equation as described in (2.64), which is omitted here for the sake of brevity.

### Constitutive Peridynamic Corrosion Modeling

The NNPP system outlined in (2.63) and (2.64) provides a nonlocal approach for simulating the electrochemical corrosion of metals in aqueous environments, extending the standard peridynamic bi-material corrosion model, which is based solely on an effective diffusion term. To capture the corrosion dynamics of a system under consideration, the NNPP system has to incorporate specific constitutive assumptions about the interface kinetics. As discussed in Section 2.3.3, the standard peridynamic bi-material corrosion model employs a homogenization approach for the solid-liquid interface, efficiently describing processes like anodic dissolution and layer deposition [25, 100]. The computational domain divides into a metallic phase ($\varphi = 1$) and a surrounding liquid electrolyte ($\varphi = 0$), facilitating the representation of the DCL at the interface. This layer, defined by a $2\delta$ boundary around the phase line as shown in Fig. 2.6, marks the transition zone where ionic

metal transport into the electrolyte occurs. Within the peridynamic neighborhood with a horizon of $\delta$, material points establish nonlocal bond interactions across these phases, distinguishing between solid-solid, liquid-liquid, and interface bonds, as depicted in Fig. 2.6.

The domain separation in the NNPP system is designed to mirror the approach used in peridynamic bi-material corrosion models. Bonds act as channels between *concentration buckets*, each with distinct properties that influence species transport. These properties address the dynamics of solid metal surface wetting and the effects of microstructural defects such as microcracks, pores, and precipitates on material degradation, as outlined in [25, 153]. For peridynamic corrosion modeling, a specific constitutive relation is used at the bond level, primarily through defining the Fickian diffusion coefficient $D_{k,ij}(t)$ for each species $k$ associated with a bond vector $\boldsymbol{\xi} := \mathbf{x}_j - \mathbf{x}_i$ as

$$D_{k,ij}(t) = \begin{cases} D_{k,l}, & \varphi(\mathbf{x}_j, t) = 0 \wedge \varphi(\mathbf{x}_i, t) = 0 \\ D_{k,i}(t), & \varphi(\mathbf{x}_j, t) = 1 \oplus \varphi(\mathbf{x}_i, t) = 1 \\ D_{k,s}, & \varphi(\mathbf{x}_j, t) = 1 \wedge \varphi(\mathbf{x}_i, t) = 1 \end{cases}, \tag{2.78}$$

where $D_{k,l}$ and $D_{k,s}$ represent the diffusion coefficients for liquid-liquid and solid-solid bonds, respectively, and are assumed constant. The interface diffusivity $D_{k,i}(t)$ is adjusted to reflect the specific corrosion system dynamics being studied. Additionally, the electrical conductivity $\sigma$ within the nonlocal Poisson equation must also be parameterized to accurately depict the dissolution of metallic ions and the distribution of electrostatic potential in the electrolyte. Although the NNPP system is adaptable to various corrosion scenarios, it is crucial to note that diffusion coefficients and the electrical conductivity are influenced by the phase change parameter $\varphi$, necessitating an appropriate phase change mechanism in the model. Following the peridynamic bi-material corrosion model, a phase transition from metal to liquid occurs if the metal ion concentration falls below the saturation concentration, indicated by the phase variable

$$\varphi(\mathbf{x}, t) = \begin{cases} 1, & C_{\text{metal}}(\mathbf{x}, t) \geq C_{\text{sat}} \\ 0, & C_{\text{metal}}(\mathbf{x}, t) < C_{\text{sat}} \end{cases}, \tag{2.79}$$

where $C_{\text{sat}}$ is the saturation concentration of metal ions in the liquid electrolyte, and $C_{\text{metal}}(\mathbf{x}, t)$ represents the concentration of metal ions at material point $\mathbf{x}$ and time $t$. This mechanism is employed throughout the numerical examples of this dissertation.

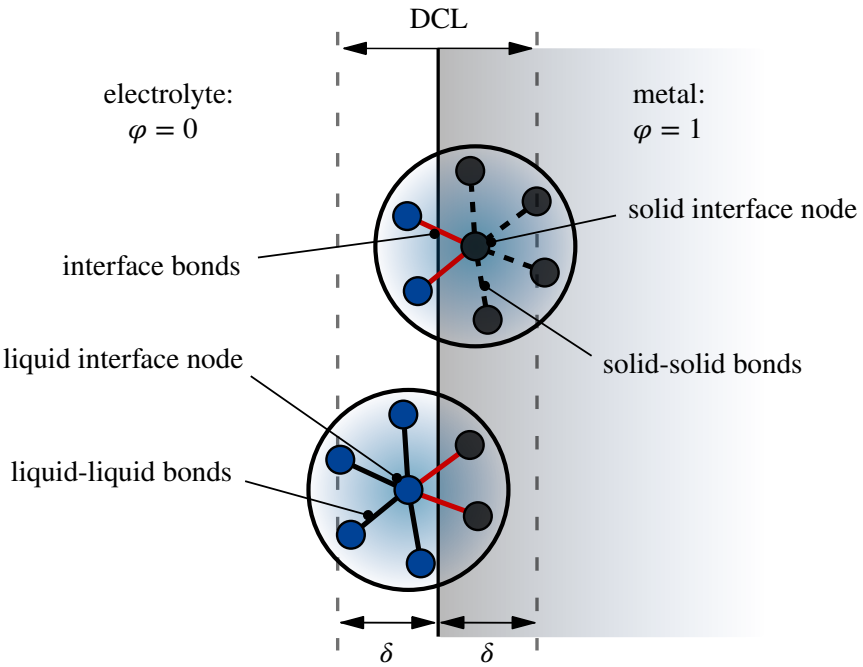


Figure 2.6: A schematic representation of the diffusive corrosion layer and spherical neighborhoods with different bond types across the corrosion interface. Reproduced from [58].

# Chapter 3

# Numerical Solution Strategies for Peridynamic Models

This chapter focuses on numerical discretization techniques for bond-based peridynamic brittle fracture models and nonlocal scalar field equations, with examples in up to 3D. Since crack propagation in brittle fracture problems often occurs on millisecond or nanosecond time scales, we emphasize explicit time marching techniques. However, we also demonstrate numerical solution strategies for implicit and semi-implicit time discretization schemes, which are more relevant for scalar field equations like the peridynamic diffusion and the derived peridynamic corrosion equation, where mass transport may occur over hours or weeks. First, we revisit the standard particle-based meshfree discretization scheme for peridynamic models, originally proposed in [130]. This scheme, combined with an appropriate volume correction method for partially covered cell volumes within the horizon radius, is widely used in peridynamic models due to its simplicity and ability to handle material separation. However, it exhibits poor convergence properties and is not asymptotically compatible [134]. Therefore, we discuss a meshfree WLS approach, which provides improved convergence properties and requires fewer family (or collocation) nodes, making it computationally more efficient, especially in 3D problems. We also discuss the advantages of a multi-grid approach with refined computational grids around regions of interest, such as crack formation or phase transitions, where the standard meshfree method is typically used. We demonstrate the benefits of these numerical improvements through various examples of the so-called *multi-adaptive scheme*. The results of this chapter have been published in several academic journals. Specifically, Section 3.1 includes material and descriptions similar to those in [122, 58]. The results of Section 3.2 and Section 3.3 were published in [122], while Section 3.4 contains results published in [100, 60, 58] and a supervised student thesis [33]. Section 3.5 includes results published in [100].

## 3.1 The Standard Discretization Scheme

Various discretization methods have been proposed for the peridynamic governing equations [39]. The most widely used approach is the meshfree (particle-based) scheme introduced in [130], which discretizes the strong form of the peridynamic equation. This scheme discretizes the strong form of the peridynamic equation and is well-suited for addressing problems involving discontinuities such as crack propagation and corrosion and is highly regarded for its simplicity of implementation. In the standard discretization scheme, the domain is divided into a cubic lattice of nodes forming a uniform grid with spacing $\Delta x$, see Fig. 3.1. Each node $\mathbf{x}_i$ has an associated *volume* $\Delta V_i$ (volume $(\Delta x)^3$ in 3D, area $(\Delta x)^2$ in 2D, and length $\Delta x$ in 1D), and the source node $\mathbf{x}_i$ interacts with neighboring family nodes $\mathbf{x}_j$. The set of *family nodes* is denoted as $\mathcal{F}_i$, and the neighborhood of $\mathbf{x}_i$ is $\mathcal{H}_{\mathbf{x}_i}$. In this scheme, a uniform horizon $\delta = m\Delta x$ is assumed for all nodes, where $\Delta x$ is the grid spacing and $m \in \mathbb{N}$ represents a positive integer factor. Furthermore, time is discretized into a sequence of instants denoted as $t^0, t^1, \ldots, t^n, t^{n+1}, \ldots$.

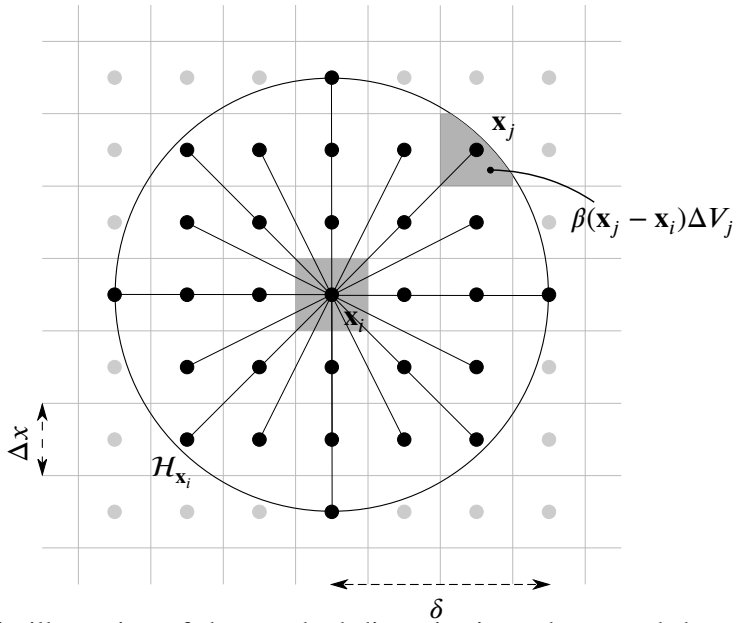


Figure 3.1: Schematic illustration of the standard discretization scheme and the neighborhood associated with node $\mathbf{x}_i$. Reproduced and adjusted from [122].

The integral over each neighborhood is computed by decomposing it into a sum over neighboring cells. A modified one-point Gaussian quadrature rule is used, with quadrature points and weights determined by the intersections between the neighborhood and cells. In the linearized bond-based PD equation of motion, where the pairwise force function $\mathbf{f}$ is given in (2.32), the standard discretization scheme replaces the integral at node $\mathbf{x}_i$ and time step $t^n$ with a finite sum as

$$\rho_i \ddot{\mathbf{u}}_i^n = \sum_{j \in \mathcal{F}_i} c\omega(\|\mathbf{x}_j - \mathbf{x}_i\|) \frac{(\mathbf{x}_j - \mathbf{x}_i) \otimes (\mathbf{x}_j - \mathbf{x}_i)}{\|(\mathbf{x}_j - \mathbf{x}_i)\|^3} (\mathbf{u}_j^n - \mathbf{u}_i^n) \beta\left(\mathbf{x}_j - \mathbf{x}_i\right) \Delta V_j + \mathbf{b}_i^n, \tag{3.1}$$

where $\rho_i := \rho(\mathbf{x}_i)$, $\ddot{\mathbf{u}}_i^n := \ddot{\mathbf{u}}(\mathbf{x}_i, t^n)$, $\mathbf{u}_i^n := \mathbf{u}(\mathbf{x}_i, t^n)$, $\mathbf{b}_i^n := \mathbf{b}(\mathbf{x}_i, t^n)$ denote the density, acceleration, displacement, and source term at node $\mathbf{x}_i$ and time step $t^n$, respectively. The function $\beta\left(\mathbf{x}_j - \mathbf{x}_i\right)$ in (3.1) is known as the *volume reduction factor* (see, e.g. [148]). It approximates the portion of

$\Delta V_j$ covered by the neighborhood $\mathcal{H}_{\mathbf{x}_i}$ (see Fig. 3.1) and is defined as

$$\beta(\boldsymbol{\xi}) = \begin{cases} 1, & \|\boldsymbol{\xi}\| \leq \delta - 0.5\Delta x, \\ \dfrac{\delta + 0.5\Delta x - \|\boldsymbol{\xi}\|}{\Delta x}, & \delta - 0.5\Delta x < \|\boldsymbol{\xi}\| < \delta + 0.5\Delta x, \\ 0, & \|\boldsymbol{\xi}\| \geq \delta + 0.5\Delta x. \end{cases} \tag{3.2}$$

Originally, the standard scheme used $\beta = 1$. However, later implementations, such as PDLAMMPS and PERIDIGM, introduced the use of a volume reduction factor to approximate the covered portion of $V_j$ by the neighborhood $\mathcal{H}_{\mathbf{x}_i}$. Further details can be found in [148, 103, 105, 104]. In this dissertation, we will consistently utilize the volume reduction factor given by (3.2) in the standard discretization scheme. Additionally, alternative methods for determining the quadrature weights by approximating the intersections between neighbor cells and the neighborhood of a specific point, such as the calculation of partial volumes in 3D, partial areas in 2D, and partial lengths in 1D, are discussed in more detail in references [112, 115, 110].

The standard discretization scheme for the peridynamic scalar wave equation can be expressed as

$$\ddot{u}_i^n = \sum_{j \in \mathcal{F}_i} c_s \omega(\|\mathbf{x}_j - \mathbf{x}_i\|) \frac{u_j^n - u_i^n}{\|\mathbf{x}_j - \mathbf{x}_i\|^p} \beta(\mathbf{x}_j - \mathbf{x}_i) \Delta V_j - 2d\dot{u}_i^n + b_i^n, \tag{3.3}$$

where $\ddot{u}_i^n := \ddot{u}(\mathbf{x}_i, t^n)$, $\dot{u}_i^n := \dot{u}(\mathbf{x}_i, t^n)$, $u_i^n := u(\mathbf{x}_i, t^n)$ and $b_i^n := b(\mathbf{x}_i, t^n)$ represent the acceleration, velocity, displacement, and source term at node $\mathbf{x}_i$ and time step $t^n$, respectively. Similarly, the standard discretization scheme for the diffusion equation in (2.41) is given by

$$\dot{C}_i^n = \sum_{j \in \mathcal{F}_i} \kappa \omega(\|\mathbf{x}_j - \mathbf{x}_i\|) \frac{C_j^n - C_i^n}{\|\mathbf{x}_j - \mathbf{x}_i\|^q} \beta\left(\mathbf{x}_j - \mathbf{x}_i\right) \Delta V_j + S_i^n, \tag{3.4}$$

where $\dot{C}_i^n := \dot{C}(\mathbf{x}_i, t^n)$, $C_i^n := C(\mathbf{x}_i, t^n)$, $S_i^n := S(\mathbf{x}_i, t^n)$ represent the time derivative of concentration, concentration, and source term at node $\mathbf{x}_i$ and time step $t^n$, respectively. Note that both the proportionality constant $c_s$ in (3.3) and the micro-diffusivity $\kappa$ in (3.4) may generally be time- and space-dependent, or, in the discretized form, dependent on the bond vector $\boldsymbol{\xi} = \mathbf{x}_j - \mathbf{x}_i$.

### 3.1.1 Explicit Time Marching Schemes

Both Explicit or implicit methods can be employed for time marching in discrete peridynamic equations. However, the choice of method depends on the time scales involved in the specific application. In peridynamic elasticity models, where dynamic processes occur on extremely short time scales, explicit time-stepping algorithms are often preferred. On the other hand, peridynamic corrosion simulations may involve significantly longer time scales spanning weeks or months, necessitating the use of implicit algorithms [60]. In this dissertation, we utilize two commonly used algorithms for explicit time marching in peridynamic models. For elasticity problems, we employ the velocity-Verlet algorithm, which is represented by

$$\begin{aligned} \dot{\mathbf{u}}_i^{n+\frac{1}{2}} &= \dot{\mathbf{u}}_i^n + \frac{\Delta t}{2} \ddot{\mathbf{u}}_i^n, \\ \mathbf{u}_i^{n+1} &= \mathbf{u}_i^n + \Delta t \dot{\mathbf{u}}_i^{n+\frac{1}{2}}, \\ \dot{\mathbf{u}}_i^{n+1} &= \dot{\mathbf{u}}_i^{n+\frac{1}{2}} + \frac{\Delta t}{2} \ddot{\mathbf{u}}_i^{n+1}, \end{aligned} \tag{3.5}$$

where $\Delta t$ represents the time step, which is typically chosen to be constant. In this case, $\Delta t = t^{n+1} - t^n$ for any time step index $n \in \mathbb{Z}$, and $t^n = t^0 + n\Delta t$. Given the nodal values of $\mathbf{x}_i$ at time instant $t^n$, $\mathbf{u}_i^n$, $\dot{\mathbf{u}}_i^n$, and $\ddot{\mathbf{u}}_i^n$, the solver computes the displacement at the next time instant using the velocity-Verlet algorithm by

$$\mathbf{u}_i^{n+1} = \mathbf{u}_i^n + \Delta t \dot{\mathbf{u}}_i^n + \frac{\Delta t^2}{2} \ddot{\mathbf{u}}_i^n, \tag{3.6}$$

thus providing the updated displacement $\mathbf{u}_i^{n+1}$ at time $t^{n+1}$. To ensure the numerical stability of the explicit time-stepping algorithm, it is necessary to estimate the maximum allowable time step size $\Delta t_{\text{crit}}$ before selecting the time step size $\Delta t \leq \Delta t_{\text{crit}}$. A means of estimating the critical time step in peridynamic models was proposed in [130], which can be generalized to any spatial dimension. This estimation method involves performing a standard von Neumann stability analysis in the 1D case of the linearized GPBM model by considering the time evolution of a Fourier mode in the form of

$$u_i^n = \lambda^n \exp\left(\iota \alpha x_i\right), \tag{3.7}$$

where $\lambda^n$ is a complex-valued amplification factor, $\alpha$ is a positive real number, and $\iota^2 := -1$. The maximum time step (in up to 3D cases) can then be determined through iterating over all material points $\mathbf{x}_i \in \Omega$ in the body $\Omega$ by

$$\Delta t_{\text{crit}} = \min_{\forall \mathbf{x}_i \in \Omega} \sqrt{\frac{2\rho_i}{\sum_{j \in \mathcal{F}_i} \|\mathbf{C}(\mathbf{x}_j - \mathbf{x}_i)\| V_j}}, \tag{3.8}$$

where $\|\mathbf{C}(\mathbf{x}_j - \mathbf{x}_i)\|$ represents an appropriate matrix norm of the micromodulus function between the given material point $\mathbf{x}_i$ and its neighbor $\mathbf{x}_j$. This approach allows for the estimation of the critical time step based on the local material properties and the interaction forces with neighboring points. Additionally, alternative methods based on the well-known Courant-Friedrichs-Lewy (CFL) condition can also be employed to estimate the maximum critical time step, as described in [85]. However, this approach provides rather conservative estimates for peridynamic models [15].

For the peridynamic scalar wave equation, likewise to (3.5) the velocity-Verlet algorithm may be applied, thus, given the nodal values $u_i^n$, $\dot{u}_i^n$ at $\mathbf{x}_i$ at the current time instant $t^n$ and $\ddot{u}_i^{n+1}$ at time $t^{n+1}$ (which may be expressed in terms of $u_i^n$ and $\dot{u}_i^n$) the field variable and its first time derivative at node $\mathbf{x}_i$ at time $t^{n+1}$ may be calculated as

$$\begin{aligned} u_i^{n+1} &= u_i^n + \Delta t \dot{u}_i^n + \frac{\Delta t^2}{2} \ddot{u}_i^n, \\ \dot{u}_i^{n+1} &= \dot{u}_i^n + \frac{\Delta t}{2} \left(\ddot{u}_i^n + \ddot{u}_i^{n+1}\right). \end{aligned} \tag{3.9}$$

Similar as in the case of elasticity, a maximum critical time step may also be estimated on the basis of a von Neumann stability analysis. Finally, for diffusion-type problems involving the first time derivative of the concentration field, we can use the explicit forward Euler algorithm. Given the nodal values $C_i^n$ and $\dot{C}_i^n$ at node $\mathbf{x}_i$ at time $t^n$, the concentration at the next time step is computed by

$$C_i^{n+1} = C_i^n + \Delta t \dot{C}_i^n. \tag{3.10}$$

The stability condition described in (3.8) may be utilized to determine the maximum critical time step, or alternatively, the CFL condition can be applied.

### 3.1.2 Implicit Time Marching with Newton-Raphson Iteration Scheme

In this section, we explore implicit time marching schemes, particularly suited for the peridynamic bi-material and NNPP corrosion systems. Given that corrosion processes may span several days or weeks of immersion, implicit techniques offer more efficient simulation capabilities. Although the literature has examined implicit approaches for quasi-static crack propagation problems in PD, methods such as the Newton-Raphson iteration scheme often fail to address snap-back instabilities caused by material or geometrical nonlinearities [119]. This dissertation, however, focuses on dynamic crack propagation issues, and thus, we employ the implicit framework for peridynamic diffusion-based problems only.

We next detail the discrete formulation of the NNPP governing equations, from (2.63) and (2.64), and introduce an effective numerical scheme for 3D problems. It is important to note that the NNPP system includes the peridynamic diffusion model as a particular case of a single-component system where the electrostatic potential is negligible, allowing the derivations here to also apply to the peridynamic diffusion and diffusion-based bi-material corrosion models when the electrostatic potential, $\phi$, is zero. We employ a time-implicit discretization for the nonlocal Nernst-Planck equation concerning the field variable $C_k(\mathbf{x}, t)$, while treating the electrostatic potential $\phi(\mathbf{x})$ and the nonlinear interactions through reaction terms explicitly. This semi-implicit strategy reduces the computational complexity by decreasing the number of unknowns required for the update of the $k$th species, providing both enhanced accuracy and numerical stability compared to explicit approaches. The integral term is approximated using a modified one-point Gaussian summation rule, i.e., the standard discretization in peridynamic modeling. Consequently, the governing equation in its discretized residual form is expressed as

$$\begin{aligned} F_{C,i}(C_{k,i}^{n+1}) :=& \frac{C_{k,i}^{n+1} - C_{k,i}^{n}}{\Delta t} - \sum_{j \in \mathcal{F}_i} \Bigg( K_1 \omega(\|\mathbf{x}_j - \mathbf{x}_i\|) D_{k,ij}^{n} \frac{C_{k,j}^{n+1} - C_{k,i}^{n+1}}{\|\mathbf{x}_j - \mathbf{x}_i\|^{n_d + 2q_1}} \\ &+ K_2 \omega(\|\mathbf{x}_j - \mathbf{x}_i\|) D_{k,ij}^{n} \frac{z_k F}{RT} \frac{\phi_j - \phi_i}{\|\mathbf{x}_j - \mathbf{x}_i\|^{n_d + 2q_2}} \left( C_{k,j}^{n+1} + C_{k,i}^{n+1} \right) \Bigg) \Delta \mathrm{V}_j - R_{k,i}^{n+1} = 0, \end{aligned} \tag{3.11}$$

where $C_{k,i}^{n+1} := C_k(\mathbf{x}_i, t^{n+1})$ represents the $k$th species concentration with the time step marked by the upper index and spatial location by the lower indices. Note that the comma index notation is purely for spatial indication and does not imply differentiation. In (3.11), $D_{k,ij}^{n}$ specifies the Fickian diffusion coefficient for the $k$th species across the bond $\boldsymbol{\xi} = \mathbf{x}_j - \mathbf{x}_i$ at time $t^n$, which may change across both time and space. $\Delta V_j$ is the volume of the cell surrounding the neighbor point $\mathbf{x}_j$ within the local neighborhood, $\mathcal{F}_i$, of point $\mathbf{x}_i$. The term $R_{k,i}^{n+1}$ contains the reactions of the $k$th species at $\mathbf{x}_i$, managing the dependencies on the $k$th concentration value implicitly over time, while contributions from other species are addressed explicitly. To solve the algebraic equation presented in (3.11), the Newton-Raphson method is employed, necessitating an initial linearization of the equation as

$$\mathbf{F}_C(\mathbf{C}_k^{n+1}) \approx \mathbf{F}_C(\mathbf{C}_k^{n}) + \mathbf{K}_C(\mathbf{C}_k^{n}) \Delta \mathbf{C} = \mathbf{0}, \tag{3.12}$$

where $\mathbf{K}_C(\mathbf{C}_k^{n})$ is the Jacobian matrix, $\Delta \mathbf{C}$ is the incremental change, and the global vector, $\mathbf{C}_k^{n+1}$,

of nodal concentrations of the $k$th species is given by

$$\mathbf{C}_k^{n+1} := \begin{pmatrix} C_{k,1}^{n+1} \\ C_{k,2}^{n+1} \\ \vdots \\ C_{k,i}^{n+1} \\ \vdots \\ C_{k,N_p}^{n+1} \end{pmatrix}, \tag{3.13}$$

with $N_p$ representing the total count of nodal points, and $\mathbf{F}_C(\mathbf{C}_k^{n+1})$ referring to the aggregate residual vector relating to the $k$th species across all nodal points for the timestep $t^{n+1}$. At each timestep, the entries of the Jacobian matrix are set as

$$\begin{aligned} K_{C,ii} = \frac{\partial F_{C,i}(C_{k,i}^{n+1})}{\partial C_{k,i}^{n+1}} = \frac{1}{\Delta t} - \sum_{j \in \mathcal{F}_i} \Bigg( & - K_1 \omega(\|\mathbf{x}_j - \mathbf{x}_i\|) \frac{D_{k,ij}^n}{\|\mathbf{x}_j - \mathbf{x}_i\|^{n_d+2q_1}} \\ & + K_2 \omega(\|\mathbf{x}_j - \mathbf{x}_i\|) D_{k,ij}^n \frac{z_k F}{RT} \frac{\phi_j - \phi_i}{\|\mathbf{x}_j - \mathbf{x}_i\|^{n_d+2q_2}} \Bigg) \Delta V_j - \frac{\partial R_{k,i}^{n+1}}{\partial C_{k,i}^{n+1}}, \end{aligned} \tag{3.14}$$

$$\begin{aligned} K_{C,ij} = \frac{\partial F_{C,i}(C_{k,i}^{n+1})}{\partial c_{k,j}^{n+1}} = -\Bigg( & - K_1 \omega(\|\mathbf{x}_j - \mathbf{x}_i\|) \frac{D_{k,ij}^n}{\|\mathbf{x}_j - \mathbf{x}_i\|^{n_d+2q_1}} \\ & + K_2 \omega(\|\mathbf{x}_j - \mathbf{x}_i\|) D_{k,ij}^n \frac{z_k F}{RT} \frac{\phi_j - \phi_i}{\|\mathbf{x}_j - \mathbf{x}_i\|^{n_d+2q_2}} \Bigg) \Delta V_j, \end{aligned} \tag{3.15}$$

where $K_{C,ii}$ and $K_{C,ij}$ denote the diagonal and off-diagonal elements of the Jacobian matrix, $\mathbf{K}_C$. For the initial step of the Newton-Raphson iteration, the starting guess for the concentration vector, $\mathbf{C}_k^{n+1,m=0}$, is aligned with the values from the previous timestep

$$\mathbf{C}_k^{n+1,m=0} = \mathbf{C}_k^{n+1,0} = \mathbf{C}_k^n, \tag{3.16}$$

using index $m$ to mark iterations within the Newton-Raphson method. During each iteration step, the concentration vector is updated by solving the linear system defined as

$$\begin{aligned} \Delta \mathbf{C} &= -\mathbf{K}_C^{-1}(\mathbf{C}_k^{n,0}) \mathbf{F}_C(\mathbf{C}_k^{n+1,m}) \\ \mathbf{C}_k^{n+1,m+1} &= \mathbf{C}_k^{n+1,m} + \lambda \Delta \mathbf{C}. \end{aligned} \tag{3.17}$$

The Jacobian matrix $\mathbf{K}_C$ is computed at the start of the iteration process and is assumed to remain constant thereafter. The relaxation factor $\lambda$, chosen to be within the range $(0, 1]$, is set as $\lambda = 1$ for all reported numerical results in this dissertation. Following the modeling techniques used for the nonlocal Nernst-Planck equation, the nonlocal Poisson equation described in (2.64) is spatially discretized using the standard discretization approach of peridynamic modeling. The resultant residual formulation at point $\mathbf{x}_i$ is

$$F_{\phi,i}(\phi_i) := - \sum_{j \in \mathcal{F}_i} \left( K_3 \omega(\|\mathbf{x}_j - \mathbf{x}_i\|) \frac{\sigma_{ij}^n}{\|\mathbf{x}_j - \mathbf{x}_i\|^{n_d+2q_3}} \left(\phi_j - \phi_i\right) \right) \Delta V_j - F \sum_{k=1}^{N} z_k C_{k,i}^n = 0, \tag{3.18}$$

where $\sigma_{ij}^n$ stands for the electrical conductivity of the bond $\boldsymbol{\xi} = \mathbf{x}_j - \mathbf{x}_i$ at the current timestep $t^n$, which may vary with space and time. The linear system to solve at each timestep is given as

$$\boldsymbol{\phi} = \mathbf{K}_\phi^{-1}\mathbf{b}_\phi, \tag{3.19}$$

where $\boldsymbol{\phi}$ denotes the global vector of electrostatic potential at the nodes, and $\mathbf{b}_\phi$ is the vector on the right-hand side, computed by

$$\mathbf{b}_\phi = F\begin{pmatrix} \sum_{k=1}^N z_k C_{k,1}^n \\ \sum_{k=1}^N z_k C_{k,2}^n \\ \vdots \\ \sum_{k=1}^N z_k C_{k,j}^n \\ \vdots \\ \sum_{k=1}^N z_k C_{k,N_p}^n \end{pmatrix}, \tag{3.20}$$

and $\mathbf{K}_\phi^{-1}$ represents the inverse of the conductance matrix. The components of the Jacobian matrix are initiated at each step as

$$\begin{aligned} K_{\phi,ii} &= \sum_{j\in\mathcal{F}_i}\left(K_3\omega(\|\mathbf{x}_j-\mathbf{x}_i\|)\frac{\sigma_{ij}^n}{\mathbf{x}_j-\mathbf{x}_i\|^{n_d+2q_3}}\right)\Delta V_j \\ K_{\phi,ij} &= -K_3\omega(\|\mathbf{x}_j-\mathbf{x}_i\|)\frac{\sigma_{ij}^n}{\|\mathbf{x}_j-\mathbf{x}_i\|^{n_d+2q_3}}\Delta V_j. \end{aligned} \tag{3.21}$$

To incorporate boundary conditions, whether Dirichlet or Neumann, into (3.17) and (3.19) requires modifications to both the system matrices $\mathbf{K}_C$ and $\mathbf{K}_\phi$, and the vectors $\mathbf{F}_C$ and $\mathbf{b}_\phi$. Further methodological details for embedding boundary conditions are provided in [60] and are discussed in Chapter 4. However, the integration of Neumann-type boundary conditions in nonlocal models is still a topic of active discussion, with additional insights available in the literature [123, 101, 140].

## 3.2 Meshfree Weighted Least Squares Collocation Scheme

In the following section, we present an integration scheme for peridynamic models that aims to improve computational efficiency as well as convergence rates compared to the standard discretization in PD. This scheme is based on the WLS approximation, a widely used technique in the Finite Point Method (FPM) [98, 95]. For a more in-depth understanding of the WLS approximation, refer to [86]. The WLS approximation allows for the local approximation of a general function $g(\mathbf{x})$ within a subdomain centered at node $\mathbf{x}_i$ known as the *cloud*, which is equivalent to the spherical neighborhood $\mathcal{H}_{\mathbf{x}_i}$ in the context of peridynamic models. By establishing a local coordinate system with the cloud center as the origin, we can express the approximation $\hat{g}(\mathbf{x})$ for a general function $g : \mathcal{H}_{\mathbf{x}_i} \subseteq \mathbb{R}^3 \to \mathbb{R}, \mathbf{x} \mapsto g(\mathbf{x})$ by

$$g(\mathbf{x}) \approx \hat{g}_i(\mathbf{x}-\mathbf{x}_i) = \sum_{j=1}^{n_p} a_j p_j(\mathbf{x}-\mathbf{x}_i) = \mathbf{p}(\mathbf{x}-\mathbf{x}_i)\boldsymbol{a}_i, \quad \forall \mathbf{x} \in \mathcal{H}_{\mathbf{x}_i}, \tag{3.22}$$

where $\mathbf{x} = (x, y, z)^\mathrm{T}$ represents the spatial coordinates, and $\mathbf{p}(\mathbf{x})$ is a vector containing $n_p$ monomial basis functions. The vector $\boldsymbol{a}_i$ consists of the unknown coefficients, which are determined based

on the nodal values of the collocation nodes. For example, when considering a complete set of monomial bases up to the second order with $n_p = 10$, we have

$$\begin{aligned} \mathbf{p}(\mathbf{x}) &= \left(1, x, y, z, x^2, xy, xz, y^2, yz, z^2\right), \\ \boldsymbol{a}_i &= \left((a_i)_1, (a_i)_2, \dots, (a_i)_{10}\right)^{\mathrm{T}}. \end{aligned} \tag{3.23}$$

To approximate the function described in (3.22), we sample it at the collocation nodes in $C_i$, which represents the set of collocation nodes. An auxiliary Cartesian grid, represented by red circles in Fig. 3.2 (left), is utilized for selecting collocation nodes. By adjusting the grid spacing, the auxiliary grid nodes approximate the desired positions of the collocation nodes. The collocation nodes are then chosen as the closest subset of family nodes (i.e., $C_i \subseteq \mathcal{F}_i$) to the auxiliary grid nodes. This approach ensures a symmetrical and homogeneous distribution of collocation nodes within the cloud, enhancing the accuracy of the approximation. The resulting values are collected in a vector $\mathbf{G}_i$ given by

$$\mathbf{G}_i = \begin{pmatrix} g_i \\ \vdots \\ g_j \\ \vdots \end{pmatrix} \approx \begin{pmatrix} \hat{g}_i(\mathbf{x}_i - \mathbf{x}_i) \\ \vdots \\ \hat{g}_i(\mathbf{x}_j - \mathbf{x}_i) \\ \vdots \end{pmatrix} = \begin{bmatrix} \mathbf{p}(\mathbf{x}_i - \mathbf{x}_i) \\ \vdots \\ \mathbf{p}(\mathbf{x}_j - \mathbf{x}_i) \\ \vdots \end{bmatrix} \boldsymbol{a}_i = \mathbf{M}_i \boldsymbol{a}_i, \quad \forall \mathbf{x}_j \in C_i, \tag{3.24}$$

where $\mathbf{M}_i$ is the moment matrix of the approximation. Since the number of collocation nodes $n_c$ is typically greater than the number of basis functions $n_p$, the matrix $\mathbf{M}_i$ is not square. Therefore, solving the linear system of equations in (3.24) requires a WLS procedure. The solution is obtained by minimizing the weighted sum of squared residuals given by

$$\begin{aligned} \mathcal{J} &= \sum_{j \in C_i} \bar{\omega}\left(\|\mathbf{x}_j - \mathbf{x}_i\|\right)\left(g_j - \hat{g}_i\left(\mathbf{x}_j - \mathbf{x}_i\right)\right)^2 \\ &= \sum_{j \in C_i} \bar{\omega}\left(\|\mathbf{x}_j - \mathbf{x}_i\|\right)\left(g_j - \mathbf{p}\left(\mathbf{x}_j - \mathbf{x}_i\right)\boldsymbol{a}_i\right)^2, \end{aligned} \tag{3.25}$$

where $\bar{\omega}$ is a spherical weight function that influences the contribution of each collocation node based on its distance from the source node. Throughout this dissertation, we adopt the weight function proposed in [20], given by

$$\bar{\omega}(\|\mathbf{x}_j - \mathbf{x}_i\|) = \frac{1 - \exp\left(64 - 16\dfrac{\|\mathbf{x}_j - \mathbf{x}_i\|^2}{\bar{r}^2}\right)}{1 - \exp(64)}, \tag{3.26}$$

where $\bar{r}$ represents the maximum distance of a collocation node from the source node. The minimization of $\mathcal{J}$ in (3.25) leads to a linear system of equations, given by

$$\mathbf{A}_i \boldsymbol{a}_i = \mathbf{B}_i \mathbf{G}_i, \tag{3.27}$$

where the square matrix $\mathbf{A}_i \in \mathbb{R}^{n_p \times n_p}$ and the rectangular matrix $\mathbf{B}_i \in \mathbb{R}^{n_p \times |C_i|}$, where $|C_i|$ denotes the cardinality of cloud $C_i$, are given by

$$\mathbf{A}_i = \sum_{j \in C_i} \bar{\omega}\left(\|\mathbf{x}_j - \mathbf{x}_i\|\right) \mathbf{p}^{\mathrm{T}}\left(\mathbf{x}_i - \mathbf{x}_j\right) \mathbf{p}\left(\mathbf{x}_i - \mathbf{x}_j\right), \tag{3.28}$$

$$\mathbf{B}_i = \left[\bar{\omega}\left(\|\mathbf{x}_i - \mathbf{x}_i\|\right) \mathbf{p}^{\mathrm{T}}\left(\mathbf{x}_i - \mathbf{x}_i\right) \quad \cdots \quad \bar{\omega}\left(\|\mathbf{x}_j - \mathbf{x}_i\|\right) \mathbf{p}^{\mathrm{T}}\left(\mathbf{x}_j - \mathbf{x}_i\right) \quad \cdots \quad \right]. \tag{3.29}$$

Solving equation (3.27) for $\boldsymbol{a}_i$ yields

$$\boldsymbol{a}_i = \mathbf{A}_i^{-1} \mathbf{B}_i \mathbf{G}_i. \tag{3.30}$$

Substituting $\boldsymbol{a}_i$ from (3.30) into (3.22), the approximate function $\hat{g}_i$ can be written in terms of the nodal values of the collocation nodes $\mathbf{G}_i$ as

$$\hat{g}_i(\mathbf{x} - \mathbf{x}_i) = \mathbf{p}(\mathbf{x} - \mathbf{x}_i)\mathbf{Q}_i \mathbf{G}_i = \sum_{j \in C_i} N_j(\mathbf{x} - \mathbf{x}_i) g_j, \tag{3.31}$$

where $\mathbf{Q}_i = \mathbf{A}_i^{-1}\mathbf{B}_i$ and $N_j$ represents the shape function of the approximation corresponding to node $\mathbf{x}_j$ in the set of collocation nodes. Note that, the accuracy of the WLS scheme depends on the condition of $\mathbf{A}_i$, which is affected by the number and arrangement of collocation nodes [86]. Higher-order monomials require more collocation nodes to maintain good conditioning. In this dissertation, we use the minimum number of collocation nodes necessary for a well-conditioned system in the numerical examples. The optimal construction of shape functions is a topic of ongoing research and discussion [21], which is beyond the scope of this dissertation.

It is worth noting, that recent studies have aimed to improve the convergence rates of peridynamic discretization schemes. Approaches like equality constrained least squares minimization [137, 136] and meshfree Reproducing Kernel Particle Methods (RKPM) [106] have been proposed. While RKPM can enhance convergence, it is computationally expensive due to numerous quadrature points. To mitigate this, an RKPM collocation approach was introduced in [83, 82]. This dissertation aims for higher computational efficiency and better convergence by combining the WLS approximation scheme with an adaptive hybrid discretization and potentially a multi-grid approach, as discussed in Section 3.5 and related literature [122, 100].

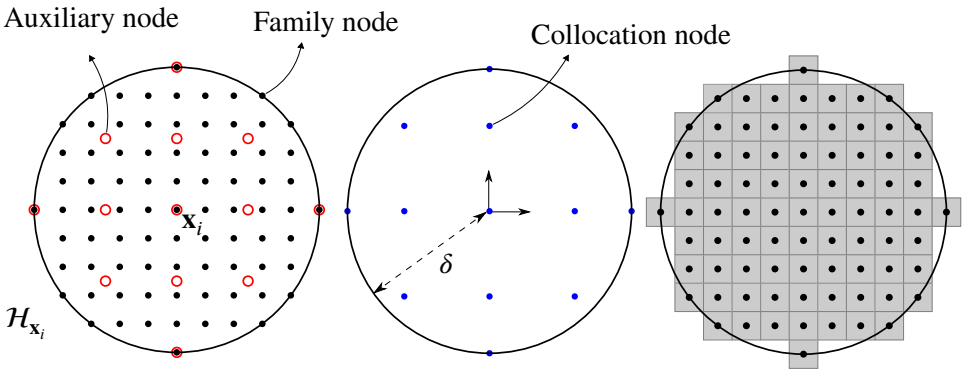


Figure 3.2: Illustration of a generic peridynamic neighborhood: (left) arrangement of family nodes within a Cartesian auxiliary grid, (center) selected collocation nodes closest to auxiliary nodes in the proposed scheme, (right) family nodes with associated background integration cells in the standard discretization scheme. Reproduced from [122].

### 3.2.1 Elasticity in Lenearized State-Based Peridynamics

In the framework of the linearized state-based PD formulation for small deformation elasticity, the proposed meshfree WLS method is used to discretize the governing equations in their strong form. The displacement field $\mathbf{u}(\mathbf{x}, t)$ is approximated within the local neighborhood $\mathcal{H}_{\mathbf{x}_i}$ at time $t$ using the WLS approach as given in (3.31). This approximation is applied to the individual components of the displacement field, specifically $\hat{u}_i$, $\hat{v}_i$, and $\hat{w}_i$, which denote the displacements in the $x$-, $y$-, and $z$- directions, respectively. The approximation of the displacement field is expressed as $\hat{\mathbf{u}}_i(\mathbf{x} - \mathbf{x}_i, t)$ and relies on the matrices $\bar{\mathbf{P}}(\mathbf{x} - \mathbf{x}_i)$, $\bar{\mathbf{Q}}_i$, and $\bar{\mathbf{U}}_i(t)$. This formulation is valid for all points $\mathbf{x} \in \mathcal{H}_{\mathbf{x}_i}$, thus

$$\mathbf{u}(\mathbf{x}, t) \approx \hat{\mathbf{u}}_i(\mathbf{x} - \mathbf{x}_i, t) = \begin{pmatrix} \hat{u}_i(\mathbf{x} - \mathbf{x}_i, t) \\ \hat{v}_i(\mathbf{x} - \mathbf{x}_i, t) \\ \hat{w}_i(\mathbf{x} - \mathbf{x}_i, t) \end{pmatrix} = \bar{\mathbf{P}}(\mathbf{x} - \mathbf{x}_i)\bar{\mathbf{Q}}_i\bar{\mathbf{U}}_i(t), \quad \forall \mathbf{x} \in \mathcal{H}_{\mathbf{x}_i}, \tag{3.32}$$

where the displacement values of the collocation nodes at time $t$ and along the $x$-, $y$-, and $z$-directions are collected in the vectors $\mathbf{U}_i(t)$, $\mathbf{V}_i(t)$, and $\mathbf{W}_i(t)$, respectively, given by

$$\mathbf{U}_i(t) = \begin{pmatrix} u_i(t) \\ \vdots \\ u_j(t) \\ \vdots \end{pmatrix}, \quad \mathbf{V}_i(t) = \begin{pmatrix} v_i(t) \\ \vdots \\ v_j(t) \\ \vdots \end{pmatrix}, \quad \mathbf{W}_i(t) = \begin{pmatrix} w_i(t) \\ \vdots \\ w_j(t) \\ \vdots \end{pmatrix}, \quad \forall \mathbf{x}_j \in C_i, \tag{3.33}$$

where $u_j(t) := u(\mathbf{x}_j, t)$, $v_j(t) := v(\mathbf{x}_j, t)$, and $w_j(t) := w(\mathbf{x}_j, t)$. The matrices $\bar{\mathbf{P}}(\mathbf{x} - \mathbf{x}_i)$ and $\bar{\mathbf{Q}}_i$ are defined in (3.34), where $\bar{\mathbf{P}}(\mathbf{x} - \mathbf{x}_i)$ is a block diagonal matrix with the monomial basis functions $\mathbf{p}(\mathbf{x} - \mathbf{x}_i)$ along the diagonal, and $\bar{\mathbf{Q}}_i$ is a block diagonal matrix composed of the matrix $\mathbf{Q}_i$ repeated along the diagonal, given as

$$\bar{\mathbf{P}}(\mathbf{x} - \mathbf{x}_i) = \begin{bmatrix} \mathbf{p}(\mathbf{x} - \mathbf{x}_i) & \mathbf{0} & \mathbf{0} \\ \mathbf{0} & \mathbf{p}(\mathbf{x} - \mathbf{x}_i) & \mathbf{0} \\ \mathbf{0} & \mathbf{0} & \mathbf{p}(\mathbf{x} - \mathbf{x}_i) \end{bmatrix}, \quad \bar{\mathbf{Q}}_i = \begin{bmatrix} \mathbf{Q}_i & \mathbf{0} & \mathbf{0} \\ \mathbf{0} & \mathbf{Q}_i & \mathbf{0} \\ \mathbf{0} & \mathbf{0} & \mathbf{Q}_i \end{bmatrix}. \tag{3.34}$$

The approximation $\mathbf{u}(\mathbf{x}, t) \approx \hat{\mathbf{u}}_i(\mathbf{x} - \mathbf{x}_i, t)$ from (3.32) is employed in the linearized state-based PD model (2.2), with the linearized force state given in (2.18) evaluated at $\mathbf{x}_i$. The force state of the linearized LPS model involves the approximation of the linearized dilatation parameter (*cf.* (2.19)) at $\mathbf{x}_i$ within the neighborhood of $\mathbf{x}_i$ at $t$, and is thus approximated as

$$\begin{aligned} \theta^{\text{lin}}(\mathbf{x}_i, t) &\approx \frac{3}{\bar{m}} \int_{\mathcal{H}} \omega(\|\boldsymbol{\xi}\|)\boldsymbol{\xi} \cdot \left(\hat{\mathbf{u}}_i(\boldsymbol{\xi}, t) - \hat{\mathbf{u}}_i(\mathbf{0}, t)\right) \mathrm{d}V_{\boldsymbol{\xi}} \\ &= \mathbf{L}_\theta \bar{\mathbf{Q}}_i \bar{\mathbf{U}}_i(t), \end{aligned} \tag{3.35}$$

where the change of variables $\boldsymbol{\xi} = \mathbf{x}' - \mathbf{x}_i$ is used and $\bar{m}$ is the weighted volume (*cf.* (2.15)). The tensor $\mathbf{L}_\theta$ may be expressed in spherical coordinates as

$$\mathbf{L}_\theta = \frac{3}{\bar{m}} \int_0^\pi \int_0^{2\pi} \int_0^\delta \omega(\mathbf{r}) \begin{pmatrix} r\cos\theta\sin\phi \\ r\sin\theta\sin\phi \\ r\cos\phi \end{pmatrix}^\top \left(\bar{\mathbf{P}}(\mathbf{r}) - \bar{\mathbf{P}}(\mathbf{0})\right) r^2 \sin\phi \mathrm{d}r\mathrm{d}\theta\mathrm{d}\phi. \tag{3.36}$$

Choosing an approximation based on a set of monomials up to second order for $\mathbf{p}$, as in (3.23), we obtain

$$\mathbf{L}_\theta = \begin{pmatrix} \mathbf{L}_{\theta,u} & \mathbf{L}_{\theta,v} & \mathbf{L}_{\theta,w} \end{pmatrix}, \tag{3.37}$$

where the comma in the notation indicates the spatial directions of displacements and does not refer to differentiation. The components are given as

$$\begin{aligned}\mathbf{L}_{\theta,u} &= \lambda_\theta\,(0,1,0,0,0,0,0,0,0,0)\,,\\ \mathbf{L}_{\theta,v} &= \lambda_\theta\,(0,0,1,0,0,0,0,0,0,0)\,,\\ \mathbf{L}_{\theta,w} &= \lambda_\theta\,(0,0,0,1,0,0,0,0,0,0)\,,\end{aligned} \tag{3.38}$$

with the proportionality constant $\lambda_\theta$ depending on the particular choice of the influence function. Assuming either a constant influence function (*cf.* (2.12)) or a linear influence function (*cf.* (2.13)), we obtain

$$\lambda_\theta = \begin{cases} \dfrac{4\pi\delta^5}{15}, & \omega = \omega_0,\\ \dfrac{2\pi\delta^5}{45}, & \omega = \omega_1. \end{cases} \tag{3.39}$$

In order to approximate the linearized dilatation parameter $\theta^{\text{lin}}$ within the neighborhood $\mathcal{H}_{\mathbf{x}_i}$, we employ the WLS collocation procedure from (3.24), thus yielding

$$\theta^{\text{lin}}(\mathbf{x},t) \approx \hat{\theta}_i^{\text{lin}}(\mathbf{x}-\mathbf{x}_i,t) = \mathbf{p}(\mathbf{x}-\mathbf{x}_i)\mathbf{Q}_i\boldsymbol{\Theta}_i(t), \quad \boldsymbol{\Theta}_i(t) = \begin{pmatrix} \theta^{\text{lin}}(\mathbf{x}_i,t)\\ \vdots \\ \theta^{\text{lin}}(\mathbf{x}_j,t)\\ \vdots \end{pmatrix}, \quad \forall \mathbf{x}_j \in C_i, \tag{3.40}$$

where $\boldsymbol{\Theta}_i(t)$ collects the linearized nonlocal dilatation values of the collocation nodes at time $t$. For the linearized LPS model, the governing equation in (2.2) can be expressed in terms of two integral components, given by

$$\rho(\mathbf{x})\ddot{\mathbf{u}}(\mathbf{x},t) = \int_{\mathcal{H}_\mathbf{x}} \left\{\underline{\mathbf{T}}[\mathbf{x},t]\left\langle \mathbf{x}'-\mathbf{x}\right\rangle - \underline{\mathbf{T}}[\mathbf{x}',t]\left\langle \mathbf{x}-\mathbf{x}'\right\rangle\right\} \mathrm{d}V_{\mathbf{x}'} + \mathbf{b}(\mathbf{x},t) = \mathbf{I}(\mathbf{x},t) + \mathbf{J}(\mathbf{x},t) + \mathbf{b}(\mathbf{x},t), \tag{3.41}$$

where the components are given by

$$\begin{aligned}\mathbf{I}(\mathbf{x},t) &= \int_{\mathcal{H}_\mathbf{x}} \frac{3K-5G}{\bar{m}}\omega(\|\boldsymbol{\xi}\|)\left(\theta^{\text{lin}}(\mathbf{x},t) + \theta^{\text{lin}}(\mathbf{x}',t)\right)\boldsymbol{\xi}\mathrm{d}V_{\mathbf{x}'},\\ \mathbf{J}(\mathbf{x},t) &= \int_{\mathcal{H}_\mathbf{x}} \frac{30G}{\bar{m}}\omega(\|\boldsymbol{\xi}\|)\frac{\boldsymbol{\xi}\otimes\boldsymbol{\xi}}{\|\boldsymbol{\xi}\|^2}\left(\mathbf{u}(\mathbf{x}+\boldsymbol{\xi},t)-\mathbf{u}(\mathbf{x},t)\right)\mathrm{d}V_{\mathbf{x}'}.\end{aligned} \tag{3.42}$$

The first term of the integral in (3.42) can be evaluated at $\mathbf{x}_i$, yielding

$$\begin{aligned}\mathbf{I}(\mathbf{x}_i,t) &\approx \int_{\mathcal{H}} \frac{3K-5G}{\bar{m}}\omega(\|\boldsymbol{\xi}\|)\left(\mathbf{p}(\mathbf{0})+\mathbf{p}(\boldsymbol{\xi})\right)\mathbf{Q}_i\boldsymbol{\Theta}_i(t)\boldsymbol{\xi}\mathrm{d}V_\xi\\ &= \mathbf{L}_I\mathbf{Q}_i\boldsymbol{\Theta}_i(t),\end{aligned} \tag{3.43}$$

where, assuming a spherical coordinate system representation of the bond vector as $\boldsymbol{\xi} \equiv \mathbf{r} = r\,(\cos\theta\sin\phi, \sin\theta\sin\phi, \cos\phi)$, the tensor $\mathbf{L}_I$ is given by

$$\mathbf{L}_I = \frac{3K-5G}{\bar{m}}\int_0^\pi\int_0^{2\pi}\int_0^\delta \omega(\mathbf{r})\begin{pmatrix} r\cos\theta\sin\phi\\ r\sin\theta\sin\phi\\ r\cos\phi\end{pmatrix}\left(\mathbf{p}(\mathbf{0})+\mathbf{p}(\mathbf{r})\right)r^2\sin\phi\mathrm{d}r\mathrm{d}\theta\mathrm{d}\phi. \tag{3.44}$$

Given a set of monomials up to second order and a weighted volume of either type from (2.16), we obtain

$$\mathbf{L}_I = \frac{3K - 5G}{3}\begin{bmatrix} 0 & 1 & 0 & 0 & 0 & 0 & 0 & 0 & 0 & 0 \\ 0 & 0 & 1 & 0 & 0 & 0 & 0 & 0 & 0 & 0 \\ 0 & 0 & 0 & 1 & 0 & 0 & 0 & 0 & 0 & 0 \end{bmatrix}. \tag{3.45}$$

The second integral term of (3.41) evaluated at $\mathbf{x}_i$ and time $t$ is approximated as

$$\begin{aligned} \mathbf{J}(\mathbf{x}_i, t) &\approx \int_{\mathcal{H}} \frac{30G}{\bar{m}} \omega(\|\xi\|) \frac{\xi \otimes \xi}{\|\xi\|^2} \left(\hat{\mathbf{u}}_i(\xi, t) - \hat{\mathbf{u}}_i(\mathbf{0}, t)\right) \mathrm{d}V_\xi \\ &= \mathbf{L}_J \bar{\mathbf{Q}}_i \bar{\mathbf{U}}_i(t), \end{aligned} \tag{3.46}$$

where $\mathbf{L}_J$ consists of three column vectors given by

$$\mathbf{L}_J = \begin{bmatrix} \mathbf{L}_{J,u} & \mathbf{L}_{J,v} & \mathbf{L}_{J,w} \end{bmatrix}. \tag{3.47}$$

Here, $\mathbf{L}_{J,u}$, $\mathbf{L}_{J,v}$, and $\mathbf{L}_{J,w}$ correspond to the displacement field along the $x$-, $y$-, and $z$-directions, respectively, and may be expressed as

$$\begin{aligned} \mathbf{L}_{J,u} &= \int_{\mathcal{H}} \frac{30G}{\bar{m}} \omega(\|\xi\|) \frac{\xi \otimes \xi}{\|\xi\|^2} \begin{bmatrix} \mathbf{p}(\xi) - \mathbf{p}(\mathbf{0}) \\ \mathbf{0} \\ \mathbf{0} \end{bmatrix} \mathrm{d}V_\xi, \\ \mathbf{L}_{J,v} &= \int_{\mathcal{H}} \frac{30G}{\bar{m}} \omega(\|\xi\|) \frac{\xi \otimes \xi}{\|\xi\|^2} \begin{bmatrix} \mathbf{0} \\ \mathbf{p}(\xi) - \mathbf{p}(\mathbf{0}) \\ \mathbf{0} \end{bmatrix} \mathrm{d}V_\xi, \\ \mathbf{L}_{J,w} &= \int_{\mathcal{H}} \frac{30G}{\bar{m}} \omega(\|\xi\|) \frac{\xi \otimes \xi}{\|\xi\|^2} \begin{bmatrix} \mathbf{0} \\ \mathbf{0} \\ \mathbf{p}(\xi) - \mathbf{p}(\mathbf{0}) \end{bmatrix} \mathrm{d}V_\xi. \end{aligned} \tag{3.48}$$

The vectors in (3.48) can be expressed in spherical coordinates, thus yielding

$$\begin{aligned} \mathbf{L}_{J,u} = \int_0^\pi \int_0^{2\pi} \int_0^\delta \frac{30G}{\bar{m}} \omega(r) &\begin{bmatrix} \cos^2\theta \sin^2\phi & \sin\theta\cos\theta\sin^2\phi & \cos\theta\sin\phi\cos\phi \\ \sin\theta\cos\theta\sin^2\phi & \sin^2\theta\sin^2\phi & \sin\theta\sin\phi\cos\phi \\ \cos\theta\sin\phi\cos\phi & \sin\theta\sin\phi\cos\phi & \cos^2\phi \end{bmatrix} \cdot \\ &\begin{bmatrix} \mathbf{p}(\mathbf{r}) - \mathbf{p}(\mathbf{0}) \\ \mathbf{0} \\ \mathbf{0} \end{bmatrix} r^2 \sin\phi \mathrm{d}r^2 \mathrm{d}\theta \mathrm{d}\phi, \\ \mathbf{L}_{J,v} = \int_0^\pi \int_0^{2\pi} \int_0^\delta \frac{30G}{\bar{m}} \omega(r) &\begin{bmatrix} \cos^2\theta \sin^2\phi & \sin\theta\cos\theta\sin^2\phi & \cos\theta\sin\phi\cos\phi \\ \sin\theta\cos\theta\sin^2\phi & \sin^2\theta\sin^2\phi & \sin\theta\sin\phi\cos\phi \\ \cos\theta\sin\phi\cos\phi & \sin\theta\sin\phi\cos\phi & \cos^2\phi \end{bmatrix} \cdot \\ &\begin{bmatrix} \mathbf{0} \\ \mathbf{p}(\mathbf{r}) - \mathbf{p}(\mathbf{0}) \\ \mathbf{0} \end{bmatrix} r^2 \sin\phi \mathrm{d}r^2 \mathrm{d}\theta \mathrm{d}\phi, \end{aligned}$$

$$\mathbf{L}_{J,w} = \int_0^{\pi}\int_0^{2\pi}\int_0^{\delta} \frac{30G}{\bar{m}}\omega(r)\begin{bmatrix} \cos^2\theta\sin^2\phi & \sin\theta\cos\theta\sin^2\phi & \cos\theta\sin\phi\cos\phi \\ \sin\theta\cos\theta\sin^2\phi & \sin^2\theta\sin^2\phi & \sin\theta\sin\phi\cos\phi \\ \cos\theta\sin\phi\cos\phi & \sin\theta\sin\phi\cos\phi & \cos^2\phi \end{bmatrix} \cdot \begin{bmatrix} \mathbf{0} \\ \mathbf{0} \\ \mathbf{p}(\mathbf{r}) - \mathbf{p}(\mathbf{0}) \end{bmatrix} r^2\sin\phi \mathrm{d}r^2\mathrm{d}\theta\mathrm{d}\phi. \tag{3.49}$$

Closed-form analytical expressions can be obtained for the integrals in (3.48) and (3.49). Given a complete set of monomials up to second order of approximation and for either choice of influence function, either constant (*cf.* (2.12)) or linear (*cf.* (2.13)), as well as their corresponding weighted volumes $\bar{m}$ (*cf.* (2.15)), the resulting matrices $\mathbf{L}_{J,u}$, $\mathbf{L}_{J,v}$, and $\mathbf{L}_{J,w}$ are given by

$$\begin{aligned} \mathbf{L}_{J,u} =& 6G\begin{bmatrix} 0 & 0 & 0 & 0 & 1 & 0 & 0 & \frac{1}{3} & 0 & \frac{1}{3} \\ 0 & 0 & 0 & 0 & 0 & \frac{1}{3} & 0 & 0 & 0 & 0 \\ 0 & 0 & 0 & 0 & 0 & 0 & \frac{1}{3} & 0 & 0 & 0 \end{bmatrix}, \\ \mathbf{L}_{J,v} =& 6G\begin{bmatrix} 0 & 0 & 0 & 0 & 0 & \frac{1}{3} & 0 & 0 & 0 & 0 \\ 0 & 0 & 0 & 0 & \frac{1}{3} & 0 & 0 & 1 & 0 & \frac{1}{3} \\ 0 & 0 & 0 & 0 & 0 & 0 & 0 & 0 & \frac{1}{3} & 0 \end{bmatrix}, \\ \mathbf{L}_{J,w} =& 6G\begin{bmatrix} 0 & 0 & 0 & 0 & 0 & 0 & \frac{1}{3} & 0 & 0 & 0 \\ 0 & 0 & 0 & 0 & 0 & 0 & 0 & 0 & \frac{1}{3} & 0 \\ 0 & 0 & 0 & 0 & \frac{1}{3} & 0 & 0 & \frac{1}{3} & 0 & 1 \end{bmatrix}. \end{aligned} \tag{3.50}$$

Note that the zeros arise from the specific choice of quadratic monomials in $\mathbf{p}$; however, their contribution to a complete set of monomials is required for an accurate WLS approximation and they cannot be omitted. Thus, the approximation of the linearized LPS model in (3.41) can be written in terms of two components, each of which requires matrix-vector multiplications, resulting in

$$\rho(\mathbf{x}_i)\ddot{\mathbf{u}}(\mathbf{x}_i,t) \approx \mathbf{I}(\mathbf{x}_i,t) + \mathbf{J}(\mathbf{x}_i,t) + \mathbf{b}(\mathbf{x}_i,t) = \mathbf{L}_I\mathbf{Q}_i\boldsymbol{\Theta}_i(t) + \mathbf{L}_J\bar{\mathbf{Q}}_i\bar{\mathbf{U}}_i(t) + \mathbf{b}(\mathbf{x}_i,t). \tag{3.51}$$

The products $\mathbf{L}_I\mathbf{Q}_i$ and $\mathbf{L}_J\bar{\mathbf{Q}}_i$ in (3.51) incorporate the quadrature weights of the proposed meshfree WLS discretization scheme, with the collocation nodes serving as the corresponding quadrature points.

### 3.2.2 Elasticity in Linearized Bond-Based Peridynamics

In the following section, the WLS approximation scheme is applied to the special case of the pairwise force function in (2.20) according to the linearized bond-based description in (2.32) for the GPBM model. Similar to the approach outlined in the previous section, we substitute the approximation $\hat{\mathbf{u}}_i$ from (3.32) into the linearized bond-based PD model evaluated at $\mathbf{x}_i$, and obtain

$$\rho(\mathbf{x}_i)\ddot{\mathbf{u}}(\mathbf{x}_i,t) \approx \int_{\mathcal{H}} \omega(\|\boldsymbol{\xi}\|)c\frac{\boldsymbol{\xi}\otimes\boldsymbol{\xi}}{\|\boldsymbol{\xi}\|^3}\left(\hat{\mathbf{u}}_i(\boldsymbol{\xi},t)-\hat{\mathbf{u}}_i(\mathbf{0},t)\right)\mathrm{d}V_{\boldsymbol{\xi}} + \mathbf{b}(\mathbf{x}_i,t). \tag{3.52}$$

The integral term in (3.52) can be expressed in terms of the displacement values of the collocation nodes, as indicated by (3.32), yielding

$$\rho(\mathbf{x}_i)\ddot{\mathbf{u}}(\mathbf{x}_i,t) \approx \bar{\mathbf{L}}\bar{\mathbf{Q}}_i\bar{\mathbf{U}}_i(t) + \mathbf{b}(\mathbf{x}_i,t), \tag{3.53}$$

where $\bar{\mathbf{L}}$ is given by

$$\bar{\mathbf{L}} = \int_{\mathcal{H}} \omega(\|\boldsymbol{\xi}\|)c\frac{\boldsymbol{\xi}\otimes\boldsymbol{\xi}}{\|\boldsymbol{\xi}\|^3}\left(\bar{\mathbf{P}}(\boldsymbol{\xi})-\bar{\mathbf{P}}(\mathbf{0})\right)\mathrm{d}V_{\boldsymbol{\xi}}. \tag{3.54}$$

In matrix form, $\bar{\mathbf{L}}$ consists of three column vectors given by

$$\bar{\mathbf{L}} = \begin{bmatrix}\mathbf{L}_u & \mathbf{L}_v & \mathbf{L}_w\end{bmatrix}, \tag{3.55}$$

where $\mathbf{L}_u$, $\mathbf{L}_v$, and $\mathbf{L}_w$ correspond to the displacement field along the $x$-, $y$-, and $z$-directions, respectively, and may be expressed as

$$\begin{aligned}
\mathbf{L}_u &= \int_{\mathcal{H}} \omega(\|\boldsymbol{\xi}\|)c\frac{\boldsymbol{\xi}\otimes\boldsymbol{\xi}}{\|\boldsymbol{\xi}\|^3}\begin{bmatrix}\mathbf{p}(\boldsymbol{\xi})-\mathbf{p}(\mathbf{0})\\ \mathbf{0}\\ \mathbf{0}\end{bmatrix}\mathrm{d}V_{\boldsymbol{\xi}},\\
\mathbf{L}_v &= \int_{\mathcal{H}} \omega(\|\boldsymbol{\xi}\|)c\frac{\boldsymbol{\xi}\otimes\boldsymbol{\xi}}{\|\boldsymbol{\xi}\|^3}\begin{bmatrix}\mathbf{0}\\ \mathbf{p}(\boldsymbol{\xi})-\mathbf{p}(\mathbf{0})\\ \mathbf{0}\end{bmatrix}\mathrm{d}V_{\boldsymbol{\xi}},\\
\mathbf{L}_w &= \int_{\mathcal{H}} \omega(\|\boldsymbol{\xi}\|)c\frac{\boldsymbol{\xi}\otimes\boldsymbol{\xi}}{\|\boldsymbol{\xi}\|^3}\begin{bmatrix}\mathbf{0}\\ \mathbf{0}\\ \mathbf{p}(\boldsymbol{\xi})-\mathbf{p}(\mathbf{0})\end{bmatrix}\mathrm{d}V_{\boldsymbol{\xi}}.
\end{aligned} \tag{3.56}$$

The vectors in (3.56) can be expressed in spherical coordinates, similar to those in (3.48). Thus, the vectors $\mathbf{L}_u$, $\mathbf{L}_v$, and $\mathbf{L}_w$ are given as

$$\mathbf{L}_u = \int_0^{\pi}\int_0^{2\pi}\int_0^{\delta} \omega(r)c\begin{bmatrix}\cos^2\theta\sin^2\phi & \sin\theta\cos\theta\sin^2\phi & \cos\theta\sin\phi\cos\phi\\ \sin\theta\cos\theta\sin^2\phi & \sin^2\theta\sin^2\phi & \sin\theta\sin\phi\cos\phi\\ \cos\theta\sin\phi\cos\phi & \sin\theta\sin\phi\cos\phi & \cos^2\phi\end{bmatrix}\cdot \begin{bmatrix}\mathbf{p}(\mathbf{r})-\mathbf{p}(\mathbf{0})\\ \mathbf{0}\\ \mathbf{0}\end{bmatrix} r\sin\phi\mathrm{d}r^2\mathrm{d}\theta\mathrm{d}\phi,$$

$$\mathbf{L}_v = \int_0^{\pi}\int_0^{2\pi}\int_0^{\delta} \omega(r)c\begin{bmatrix}\cos^2\theta\sin^2\phi & \sin\theta\cos\theta\sin^2\phi & \cos\theta\sin\phi\cos\phi\\ \sin\theta\cos\theta\sin^2\phi & \sin^2\theta\sin^2\phi & \sin\theta\sin\phi\cos\phi\\ \cos\theta\sin\phi\cos\phi & \sin\theta\sin\phi\cos\phi & \cos^2\phi\end{bmatrix}\cdot \begin{bmatrix}\mathbf{0}\\ \mathbf{p}(\mathbf{r})-\mathbf{p}(\mathbf{0})\\ \mathbf{0}\end{bmatrix} r\sin\phi\mathrm{d}r^2\mathrm{d}\theta\mathrm{d}\phi,$$

$$\mathbf{L}_w = \int_0^{\pi}\int_0^{2\pi}\int_0^{\delta} \omega(r)c \begin{bmatrix} \cos^2\theta\sin^2\phi & \sin\theta\cos\theta\sin^2\phi & \cos\theta\sin\phi\cos\phi \\ \sin\theta\cos\theta\sin^2\phi & \sin^2\theta\sin^2\phi & \sin\theta\sin\phi\cos\phi \\ \cos\theta\sin\phi\cos\phi & \sin\theta\sin\phi\cos\phi & \cos^2\phi \end{bmatrix} \cdot \begin{bmatrix} \mathbf{0} \\ \mathbf{0} \\ \mathbf{p}(\mathbf{r}) - \mathbf{p}(\mathbf{0}) \end{bmatrix} r\sin\phi \mathrm{d}r^2\mathrm{d}\theta\mathrm{d}\phi. \tag{3.57}$$

By assuming a complete spherical region for $\mathcal{H}$, closed-form analytical expressions can be obtained for the integrals in (3.56) and (3.57). Taking a complete set of monomial bases up to second order for $\mathbf{p}$ in (3.56), the resulting matrices $\mathbf{L}_u$, $\mathbf{L}_v$, and $\mathbf{L}_w$ are expressed as

$$\begin{aligned} \mathbf{L}_u =& \lambda \begin{bmatrix} 0 & 0 & 0 & 0 & 1 & 0 & 0 & \frac{1}{3} & 0 & \frac{1}{3} \\ 0 & 0 & 0 & 0 & 0 & \frac{1}{3} & 0 & 0 & 0 & 0 \\ 0 & 0 & 0 & 0 & 0 & 0 & \frac{1}{3} & 0 & 0 & 0 \end{bmatrix}, \\ \mathbf{L}_v =& \lambda \begin{bmatrix} 0 & 0 & 0 & 0 & 0 & \frac{1}{3} & 0 & 0 & 0 & 0 \\ 0 & 0 & 0 & 0 & \frac{1}{3} & 0 & 0 & 1 & 0 & \frac{1}{3} \\ 0 & 0 & 0 & 0 & 0 & 0 & 0 & 0 & \frac{1}{3} & 0 \end{bmatrix}, \\ \mathbf{L}_w =& \lambda \begin{bmatrix} 0 & 0 & 0 & 0 & 0 & 0 & \frac{1}{3} & 0 & 0 & 0 \\ 0 & 0 & 0 & 0 & 0 & 0 & 0 & 0 & \frac{1}{3} & 0 \\ 0 & 0 & 0 & 0 & \frac{1}{3} & 0 & 0 & \frac{1}{3} & 0 & 1 \end{bmatrix}, \end{aligned} \tag{3.58}$$

where the constant $\lambda$ in (3.59) depends on the choice of the influence function $\omega$, and is given by

$$\lambda = \begin{cases} \dfrac{\pi c\delta^4}{5}, & \omega = \omega_0, \\ \dfrac{\pi c\delta^4}{25}, & \omega = \omega_1. \end{cases} \tag{3.59}$$

Note that the matrices provided in (3.58) are identical in the distribution of entries to those in (3.50); only the coefficients differ. Similarly to the previous section, the product $\bar{\mathbf{L}}\bar{\mathbf{Q}}_i$ in (3.55) incorporates the quadrature weights of the proposed discretization scheme, with the collocation nodes serving as the corresponding quadrature points. Furthermore, note that the contribution from the nonlocal dilation parameter in the state-based formalism, as given in (3.51), vanishes in the linearized bond-based PD formulation since the pairwise force function assumption results in a fixed Poisson's ratio.

### 3.2.3 Peridynamic Diffusion Problems

The WLS collocation scheme is applied to nonlocal scalar field equations after deriving the formulations for vector fields, such as elasticity, in the previous section. In the context of peridynamic diffusion and corrosion problems, we utilize the proposed integration scheme to approximate the concentration field. Since the right-hand side of the peridynamic diffusion problem given in (2.41) and (2.42) shares structural similarities with the peridynamic scalar wave equation (*cf.* (2.40)), we focus our discussion on diffusion problems only. The derivation for the peridynamic scalar wave equation follows a similar procedure. In the beginning, the concentration field within $\mathcal{H}_{\mathbf{x}_i}$ at time $t$ is approximated using (3.31), yielding

$$C(\mathbf{x},t) \approx \hat{C}_i(\mathbf{x}-\mathbf{x}_i,t) = \mathbf{p}(\mathbf{x}-\mathbf{x}_i)\mathbf{Q}_i\bar{\mathbf{C}}_i(t), \quad \forall \mathbf{x} \in \mathcal{H}_{\mathbf{x}_i}, \tag{3.60}$$

where $\bar{\mathbf{C}}_i(t)$ represents the collection of concentration values of the collocation nodes at time $t$ by

$$\bar{\mathbf{C}}_i(t) = \begin{pmatrix} C_i(t) \\ \vdots \\ C_j(t) \\ \vdots \end{pmatrix}, \quad \forall \mathbf{x}_j \in C_i, \tag{3.61}$$

where $C_j(t) := C(\mathbf{x}_j,t)$. By substituting $\hat{C}_i$ from (3.60) into the governing equation (2.41) evaluated at $\mathbf{x}_i$, we obtain

$$\dot{C}(\mathbf{x}_i,t) = \int_{\mathcal{H}} \omega(\|\boldsymbol{\xi}\|)\kappa \frac{1}{\|\boldsymbol{\xi}\|^q}\left(\hat{C}_i(\boldsymbol{\xi},t) - \hat{C}_i(\mathbf{0},t)\right) \mathrm{d}V_{\boldsymbol{\xi}} + S(\mathbf{x}_i,t), \tag{3.62}$$

where $\boldsymbol{\xi} := \mathbf{x}' - \mathbf{x}_i$ with $\mathbf{x}' \in \mathcal{H}_{\mathbf{x}_i}$ and $\mathcal{H} := \{\boldsymbol{\xi} \in \mathbb{R}^{n_d} : \|\boldsymbol{\xi}\| \leq \delta\}$ with $n_d$ denoting the space dimension. The integral equation (3.62) can be expressed in terms of the concentration values of the collocation nodes as

$$\dot{C}(\mathbf{x}_i,t) = \mathbf{L}_C\mathbf{Q}_i\bar{\mathbf{C}}_i(t) + S(\mathbf{x}_i,t), \tag{3.63}$$

where $\mathbf{L}_C$ is defined as

$$\mathbf{L}_C = \int_{\mathcal{H}} \omega(\|\boldsymbol{\xi}\|)\kappa \frac{1}{\|\boldsymbol{\xi}\|^q}\left(\mathbf{p}(\boldsymbol{\xi}) - \mathbf{p}(\mathbf{0})\right) \mathrm{d}V_{\boldsymbol{\xi}}. \tag{3.64}$$

Employing the spherical coordinate system, thus, $\boldsymbol{\xi} \equiv \mathbf{r} = r(\cos\theta\sin\phi, \sin\theta\sin\phi, \cos\phi)$, we obtain

$$\mathbf{L}_C = \int_0^{\pi}\int_0^{2\pi}\int_0^{\delta} \omega(r)\kappa \frac{1}{r^{q-2}}\left(\mathbf{p}(\mathbf{r}) - \mathbf{p}(\mathbf{0})\right)\sin\phi \,\mathrm{d}r\mathrm{d}\theta\mathrm{d}\phi. \tag{3.65}$$

Assuming a complete spherical neighborhood for $\mathcal{H}_{\mathbf{x}_i}$ and using a complete set of monomial bases up to the second order for $\mathbf{p}$ in (3.56), the expression for $\mathbf{L}_C$ in (3.64) can be evaluated as

$$\mathbf{L}_C = \lambda_C \begin{pmatrix} 0 & 0 & 0 & 0 & 1 & 0 & 0 & 1 & 0 & 1 \end{pmatrix}, \tag{3.66}$$

where $\lambda_C$ is a constant coefficient that depending on the influence function $\omega$ is given by

$$\lambda_C = \begin{cases} \dfrac{4\pi\kappa\delta^{5-q}}{-3q+15}, & \omega = \omega_0, \\ \dfrac{4\pi\kappa\delta^{5-q}}{3q^2-33q+90}, & \omega = \omega_1. \end{cases} \tag{3.67}$$

In summary, the term $\mathbf{L}_C\mathbf{Q}_i$ in (3.63) incorporates the quadrature weights in the discretization scheme, with the collocation nodes serving as the corresponding quadrature points. The presence of zero values in some matrix entries in (3.67) is due to specific monomials in $\mathbf{p}$, although a complete set of monomials is still necessary for the WLS approximation.

### 3.2.4 Convergence Analysis

Convergence in the numerical approximation of peridynamic models differs from traditional FEM approaches for local problems due to the nonlocal nature of peridynamic models and their dependence on the peridynamic horizon $\delta$ (see e.g., [17]). To illustrate this, consider a 1D linear peridynamic model with the equation of motion given by (2.20). In this model, the displacement field is governed by

$$\rho(x)\ddot{u}(x,t) = \int_{x-\delta}^{x+\delta} c\omega\left(|x'-x|\right)\left(\frac{u(x',t)-u(x,t)}{|x'-x|}\right)\mathrm{d}x' + b(x,t). \tag{3.68}$$

By considering a constant influence function $\omega$ as defined in (2.12) and introducing the variable transformation $\xi = x' - x$, we can perform a Taylor expansion of $u(x',t)$ around $x$, assuming a smooth displacement field. This yields

$$\begin{aligned}
\rho(x)\ddot{u}(x,t) &= \int_{x-\delta}^{x+\delta} c\left(\frac{u(x',t)-u(x,t)}{|x'-x|}\right)\mathrm{d}x' + b(x,t)\\
&= \int_{-\delta}^{\delta} c\left(\frac{u(x+\xi,t)-u(x,t)}{|\xi|}\right)\mathrm{d}\xi + b(x,t)\\
&= \int_{-\delta}^{\delta} \frac{c}{|\xi|}\left[\frac{\partial u}{\partial x}(x,t)\xi + \frac{1}{2}\frac{\partial^2 u}{\partial x^2}(x,t)\xi^2 + \frac{1}{6}\frac{\partial^3 u}{\partial x^3}(x,t)\xi^3 + \cdots\right]\mathrm{d}\xi + b(x,t)\\
&= \left(\frac{1}{2}c\int_{-\delta}^{\delta}|\xi|\mathrm{d}\xi\right)\frac{\partial^2 u}{\partial x^2}(x,t) + \cdots + b(x,t).
\end{aligned} \tag{3.69}$$

Due to the symmetry of the integration domain, the antisymmetric terms in (3.69) vanish. By performing the necessary calculations and integrations, we can simplify the expression obtained in (3.69). The equation of motion for the displacement field in the 1D linear peridynamic model can be written as

$$\rho(x)\ddot{u}(x,t) = \frac{1}{2}c\delta^2\frac{\partial^2 u}{\partial x^2}(x,t) + \frac{1}{48}c\delta^4\frac{\partial^4 u}{\partial x^4}(x,t) + \frac{1}{2160}c\delta^6\frac{\partial^6 u}{\partial x^6}(x,t) + \cdots + b(x,t). \tag{3.70}$$

The convergence analysis of peridynamic models considers two perspectives. First, as the peridynamic horizon $\delta$ approaches zero, the influence of higher-order terms diminishes, leading to the asymptotic convergence of the peridynamic equation to the classical local model. This notion of asymptotic compatibility is achieved numerically by maintaining a constant ratio of $\delta/\Delta x$ and gradually reducing $\Delta x$ to zero, resulting in what is known as $\delta$-convergence and has been explored in various studies, e.g., [133, 134]. Thus, by neglecting higher than second order terms in the Taylor expansion of (3.70) as $\delta \to 0$, and setting $c = \frac{2E}{\delta^2}$, the equation of motion in CCM is recovered as

$$\rho(x)\ddot{u}(x,t) = E\frac{\partial^2 u}{\partial x^2}(x,t) + b(x,t). \tag{3.71}$$

Second, when the peridynamic horizon $\delta = m\Delta x = \text{const.}$, where $m \in \mathbb{N}$ represents the ratio $\delta/\Delta x$, remains constant, the numerical solution can converge to the continuum solution by considering more terms from the expansion in (3.70). This convergence, referred to as $m$-convergence, is obtained by decreasing the grid spacing $\Delta x$ while keeping $\delta$ constant. As $\Delta x$ decreases, more nodes fall within each peridynamic neighborhood, enhancing the accuracy of higher-order terms and improving the convergence towards the continuum solution. This approach has been discussed in the literature as well [17].

The meshfree WLS collocation scheme introduced in the previous sections exhibits $k$-order consistency ($C^k$), similar to traditional FEM, where $k$ represents the maximum order of the employed monomial basis. This feature enables the scheme to generate exact polynomial solutions up to order $k$. A minimum of $C^2$ consistency is required for the scheme to exhibit monotonic behavior in $\delta$-convergence. When $\delta$ is kept constant, the scheme achieves numerical solutions with accuracy determined by the order of consistency. Using higher-order monomials incorporates more terms from the expansion, leading to more accurate peridynamic integrals. However, in $m$-convergence, reducing $\Delta x$ while maintaining a constant $\delta$ does not enhance accuracy unless the order of consistency is increased. This behavior is illustrated in the numerical examples of Section 3.2.5.

### 3.2.5 1D Static Elasticity with Manufactured Solution

In this example we investigate the convergence behavior of the meshfree WLS collocation scheme in comparison to the standard discretization method. For that purpose, let us consider a 1D static elasticity problem on a domain $\Omega = (-100, 100)$, governed by the peridynamic equilibrium equation (3.72) for $x \in \Omega$ given by

$$0 = \int_{x-\delta}^{x+\delta} c \frac{1}{|x' - x|} \big(u(x') - u(x)\big)\, \mathrm{d}x' + b(x), \tag{3.72}$$

where the micromodulus is set to $c = \frac{2E}{\delta^2}$, and the Young's modulus $E$ is set to $E = 1$. In this study, a constant influence function $\omega = 1$ according to (2.12) is assumed. Dirichlet boundary conditions are imposed within a layer of length $\delta$ near the boundaries, where the displacement values are prescribed based on a manufactured solution.

We investigate the meshfree WLS collocation scheme with three different approaches, characterized by varying numbers of collocation nodes ($n_c$) and basis functions ($n_p$), representing different levels of consistency $C^k$. These approaches are summarized in Tab. 3.1, and examples of the peridynamic neighborhoods used are shown in Fig. 3.3. Equilibrium is achieved by solving a linear system of equations on a uniformly spaced grid with grid spacing $\Delta x$. The following analysis focuses on examining the convergence behavior of these approaches, specifically considering the $m$- and $\delta$-convergence.

Table 3.1: Specifications of the three scenarios employed for the meshfree WLS collocation scheme for the 1D static elasticity problem. Reproduced from [122].

| Scheme | $C^k$ | $n_p$ | $n_c$ |
|---|---|---|---|
| WLS-2 | $C^2$ | 3 | 5 |
| WLS-4 | $C^4$ | 5 | 11 |
| WLS-6 | $C^6$ | 7 | 13 |

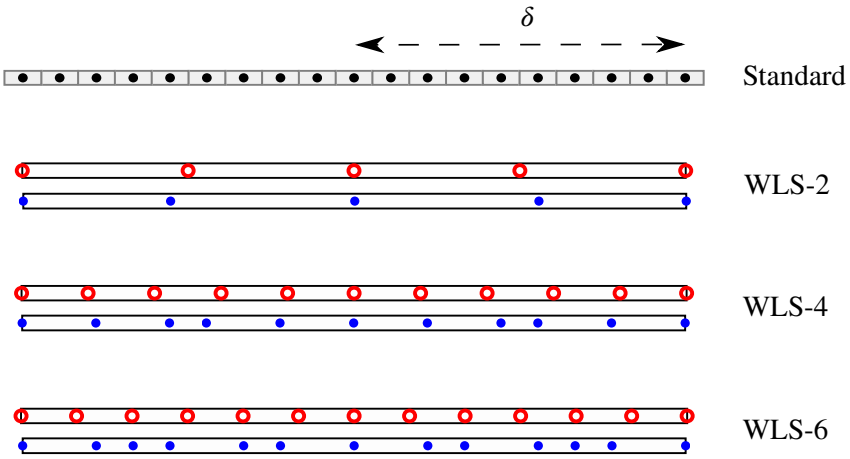


Figure 3.3: Examples of the peridynamic neighborhood used in Section 3.2.5: red circles represent auxiliary nodes, and blue dots are collocation nodes. Reproduced from [122].

### *m*-Convergence Analysis

We begin by investigating the *m*-convergence, which refers to the convergence of the numerical approximation towards the exact peridynamic continuum solution. To assess this, we consider an exact (or manufactured) solution for the 1D peridynamic elasticity problem, given by

$$u^{\mathrm{Ex}}(x) := \sin\left(\frac{x}{10}\right), \tag{3.73}$$

thus ensuring that the particular choice of this exact solution is not spanned by the monomials used in the collocation scheme. Substituting the exact solution (3.73) into the equilibrium equation (3.72), we obtain the corresponding body force density function as

$$b(x) = 2c\left[e - \mathrm{Ci}\left(\frac{\delta}{10}\right) + \ln\left(\frac{\delta}{10}\right)\right]\sin\left(\frac{x}{10}\right), \tag{3.74}$$

where Ci represents the cosine integral function, $e$ is Euler's constant, and the peridynamic horizon is arbitrarily assumed as $\delta = 6$. Displacement boundary conditions are prescribed according to the exact solution given in (3.73).

Fig. 3.4 (left) illustrates the outcomes of the *m*-convergence analysis. In the standard discretization scheme, the accuracy improves as the $\delta/\Delta x$ ratio increases while maintaining a constant value of $\delta = 6$. Meanwhile, the meshfree WLS scheme achieves a certain level of accuracy based on the order of consistency $C^k$, but further convergence to the exact solution necessitates the incorporation of higher-order monomials. Notably, even with a coarser discretization, the WLS-2 scheme surpasses the standard scheme with a finer discretization. It is noteworthy that the peridynamic neighborhood in the finest grid spacing case encompasses 67 family nodes in the standard scheme, while the WLS-2 scheme utilizes only 5 collocation nodes for integration. This significant reduction in the number of nodes employed by the WLS scheme contributes to its superior computational efficiency. The results emphasize that increasing the level of consistency $C^k$ in the WLS scheme significantly enhances the accuracy. Overall, the WLS-4 and WLS-6 schemes yield results approximately two and five orders of magnitude more accurate, respectively, than the WLS-2 scheme.

### $\delta$-Convergence Analysis

As the peridynamic horizon $\delta$ shrinks to zero ($\delta \to 0$) in the limit of vanishing nonlocal interactions, the equilibrium equation in (3.72) converges to

$$0 = \frac{\partial^2 u(x)}{\partial x^2} + b(x), \tag{3.75}$$

which presents the classical wave equation with the Young's modulus assumed to be one, $E = 1$. Substituting the exact solution from (3.73) for $u$ in (3.75), we obtain an expression for the body force density $b(x)$ given as

$$b(x) = \frac{1}{100} \sin\left(\frac{x}{10}\right). \tag{3.76}$$

In the $\delta$-convergence analysis, we follow a similar approach as the previous $m$-convergence study. We apply the displacement boundary conditions based on the exact solution and utilize the body force density given in (3.76). However, in this study, we focus on the convergence behavior with a constant ratio of $m = \delta/\Delta x$ (set to 12) for both the standard and meshfree WLS schemes. The results in Fig. 3.4 show contrasting behaviors between the two approaches. The standard scheme exhibits oscillatory patterns and fails to converge, indicating a lack of asymptotic compatibility. In contrast, all meshfree WLS schemes, regardless of the level of consistency, demonstrate monotonic convergence towards the exact solution. These findings highlight the superior convergence properties of the meshfree WLS scheme, showcasing its effectiveness in approximating the classical continuum mechanics solution.

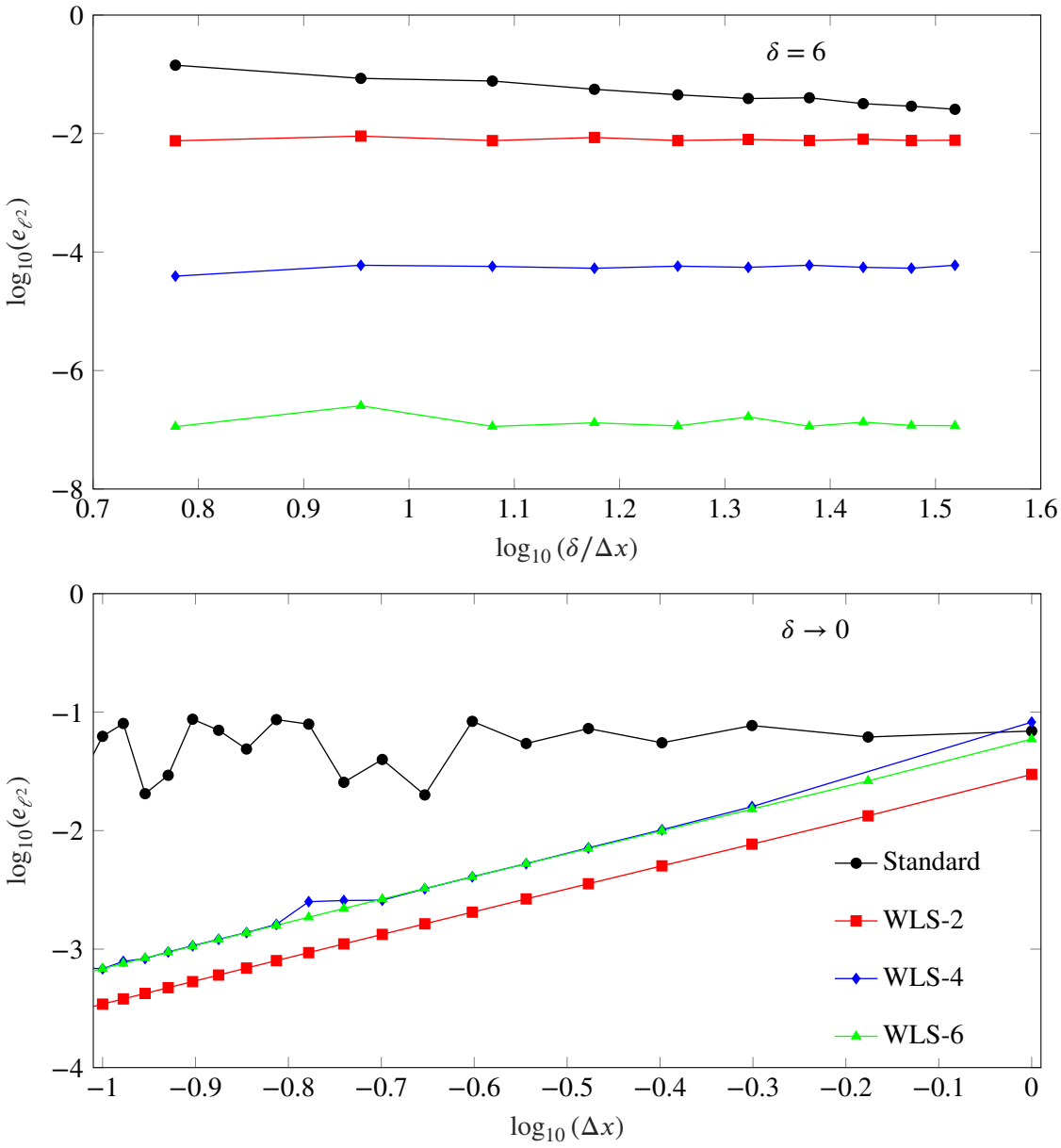


Figure 3.4: Convergence analysis for 1D static elasticity example in PD: (top) $m$-convergence analysis and (bottom) $\delta$-convergence analysis. Reproduced and adjusted from [122].

### 3.2.6 2D Peridynamic Diffusion with Manufactured Solution

We compare the accuracy of the meshfree WLS collocation scheme and the standard discretization scheme in solving a 2D transient peridynamic diffusion problem described by equation (2.42). The problem is defined on a square domain with dimensions $(-0.5, 0.5)\times(-0.5, 0.5)$, and Dirichlet boundary conditions based on the exact solution are imposed in a boundary layer near the domain boundary, as depicted in Fig. 3.5. Two discretization approaches are considered: uniform and non-uniform. Figures 3.7 and 3.8 depict examples of the peridynamic neighborhoods and auxiliary grids, respectively, for each discretization employed in the problem. The problem domain is discretized with an average grid spacing of $\Delta x = 1/39 \approx 0.0256$ with the peridynamic horizon $\delta = 5\Delta x \approx 0.1282$. In the non-uniform discretization, the coordinates of the nodes are perturbed by small random numbers within the range $[0, 0.35\Delta x]$, ensuring the validity of the assumption of identical background cells for the nodes in the standard discretization scheme.

Similar to the previous example, we utilize an exact (or manufactured) solution that cannot be represented by the monomial basis used in the WLS scheme. The exact solution is given by

$$C_{\text{ex}}(\mathbf{x}, t) = \sin(5t)\left(x^2y^2 + x^3y + x^4 + xy^3 + y^4\right), \tag{3.77}$$

whereas the corresponding source function is

$$S(\mathbf{x}, t) = 5\cos(5t)\left(x^2y^2 + x^3y + x^4 + xy^3 + y^4\right) - \frac{1}{16}\pi\delta^2\sin(5t)\left(7\delta^2 + 56x^2 + 48xy + 56y^2\right). \tag{3.78}$$

The time marching is performed using the explicit forward Euler algorithm (*cf.* (3.10)) with a time step of $\Delta t = 10^{-5}$. In this example, we utilize two different configurations of the meshfree WLS collocation scheme. The details of these configurations are provided in Tab. 3.2.

The numerical error is defined as a relative $\ell^2$-norm

$$e_{\ell^2} := \frac{\sqrt{\sum_{i=1}^{N} \|C_{\text{Num},i} - C_{\text{Ex},i}\|^2}}{\sqrt{\sum_{i=1}^{N} \|C_{\text{Ex},i}\|^2}}, \tag{3.79}$$

where $N$ is the number of nodes, $C_{\text{Num},i}$ is the field variable from the numerical solution at node $\mathbf{x}_i$, and $C_{\text{Ex},i}$ is from the exact solution, is depicted in Fig. 3.6 for various time points. It is evident that the meshfree WLS scheme consistently outperforms the standard discretization scheme in terms of accuracy. Specifically, the WLS-4 scheme, with its higher consistency order, exhibits lower errors compared to the WLS-2 scheme. Interestingly, the meshfree WLS schemes demonstrate reduced sensitivity to the non-uniformity of the spatial discretization, which is not observed in the standard scheme. At the final time instant, the relative difference in the error norm between the uniform and non-uniform standard schemes is 38.63%, while the differences for the WLS-2 and WLS-4 schemes are 6.53% and 7.09%, respectively.

Table 3.2: Specifications of the proposed WLS meshfree scheme approaches for the transient 2D peridynamic diffusion problem. Reproduced from [122].

| Scheme | $C^k$ | $n_p$ | $n_c$ |
|---|---|---|---|
| WLS-2 | $C^2$ | 6 | 29 |
| WLS-4 | $C^4$ | 15 | 49 |

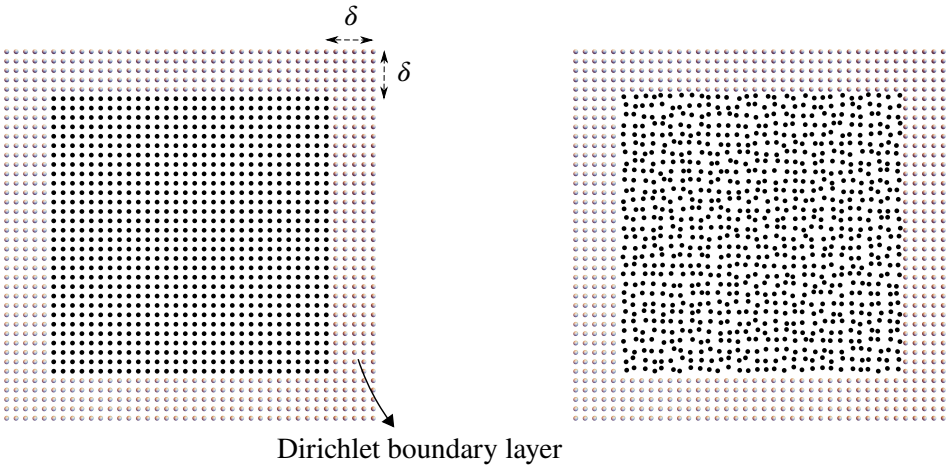


Figure 3.5: Illustration of the 2D problem domains and boundary layers using uniform and non-uniform discretization approaches. Reproduced from [122].

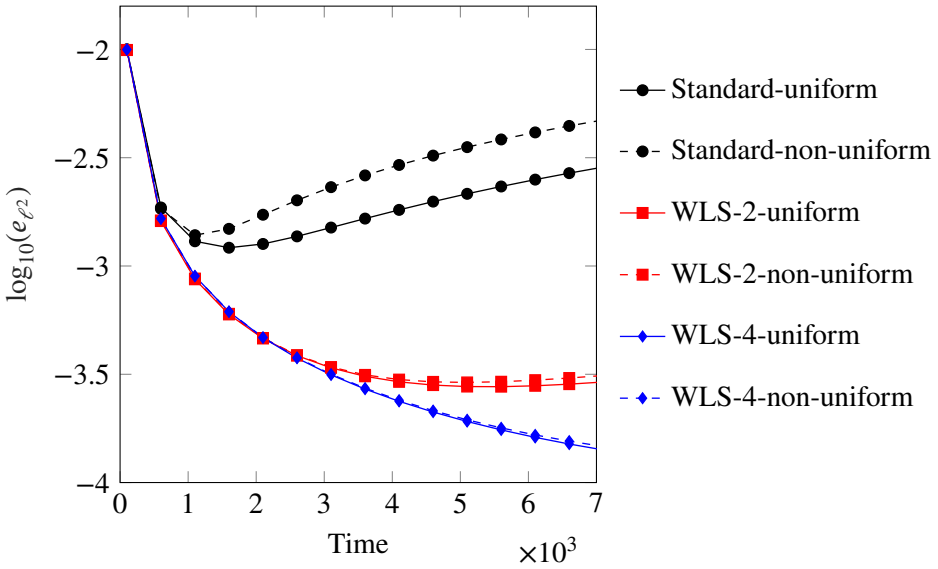


Figure 3.6: The time evolution of the error, measured by the $\ell^2$-norm, is shown for the various approaches used in the transient 2D peridynamic diffusion problem. Reproduced and adjusted from [122].

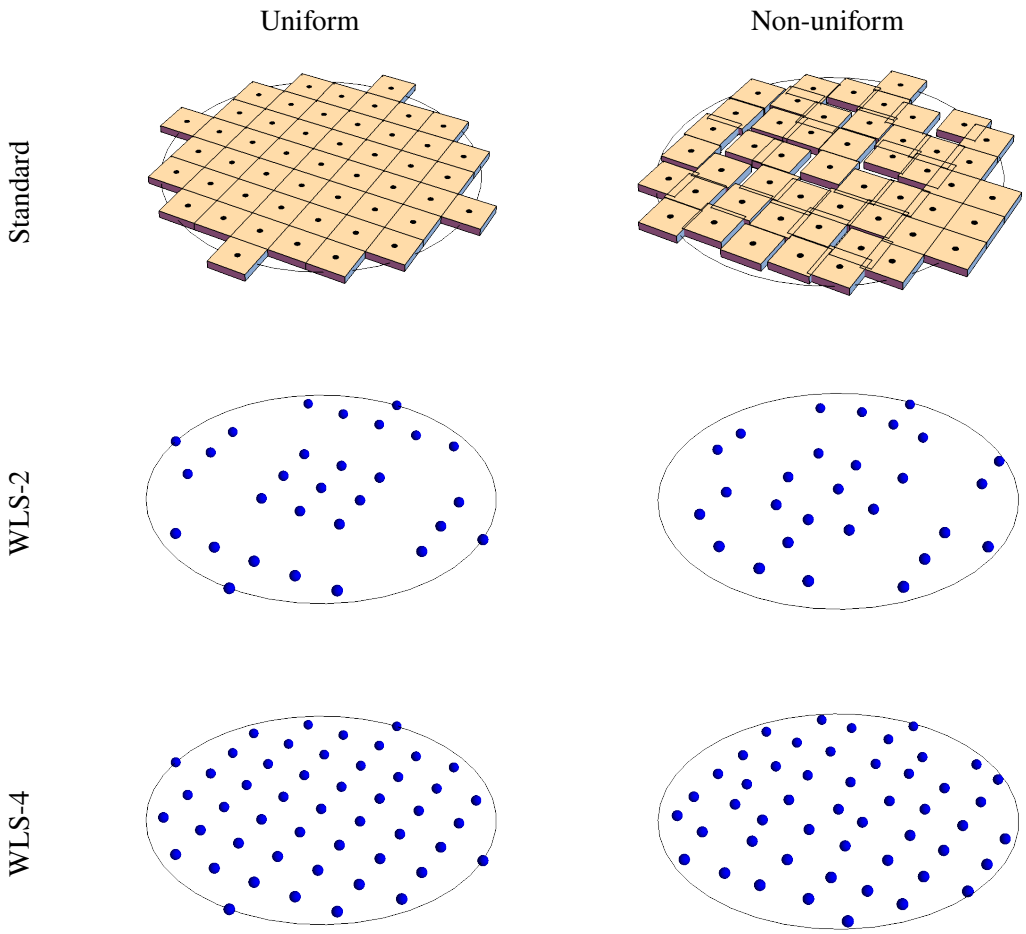


Figure 3.7: Representations of the peridynamic neighborhoods used in Section 3.2.6. The figures illustrate the peridynamic neighborhoods, where for the WLS approaches, only the collocation nodes are shown. Reproduced from [122].

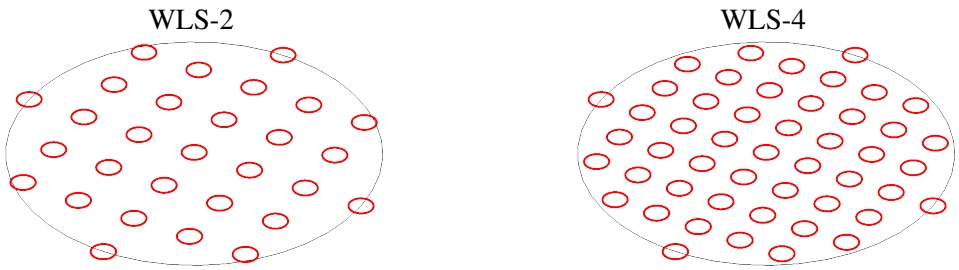


Figure 3.8: The auxiliary grids used in the configurations of the meshfree WLS collocation scheme for the transient peridynamic diffusion example. Reproduced from [122].

## 3.3 The Adaptive Hybrid Configuration

A hybrid framework is developed to optimize computational resources in damage-related problems by combining the standard discretization and meshfree WLS collocation schemes. This approach divides the domain into two regions: $\Omega_s$ and $\Omega_w$. The standard scheme is applied to $\Omega_s$, which includes critical zones and boundaries, while the meshfree WLS scheme is adaptively used for the remaining region, $\Omega_w$.

As indicated in Fig. 3.9, two hybrid configurations are considered: the *hybrid fixed configuration* and the *hybrid adaptive configuration*. In the fixed configuration, $\Omega_s$ is predetermined and remains unchanged throughout the simulation. This approach offers efficiency when the critical zones are known. In the adaptive configuration, only initial zones with known damage are included in $\Omega_s$, and an adaptive switching algorithm expands $\Omega_s$ by identifying critical zones within $\Omega_w$. This adaptive approach allows for the dynamic adaptation of $\Omega_s$ to evolving damage morphology, focusing computational resources on crucial zones. However, the adaptive strategy may introduce additional computational overhead due to the switching algorithm.

To identify the critical zones for the switching algorithm, we employ a criterion inspired by previous works such as [126, 149]. In the context of brittle crack propagation, we adopt a criterion based on the stretch of each bond within the region $\Omega_w$. Consider two neighboring nodes $\mathbf{x}_i$ and $\mathbf{x}_j$ as illustrated in Fig. 3.10. At a given time $t^n$, the bond connecting $\mathbf{x}_i$ and $\mathbf{x}_j$ is classified as critical if its stretch falls within a specific range, defined by the inequality

$$\sigma s_0 \leqslant \frac{\left|\left(\mathbf{x}_j + \mathbf{u}_j^n\right) - \left(\mathbf{x}_i + \mathbf{u}_i^n\right)\right|}{|\mathbf{x}_j - \mathbf{x}_i|} - 1 \leqslant s_0, \tag{3.80}$$

where $\sigma \in (0, 1)$ represents the margin of critical bond stretch $s_0$ that influences the expansion size of $\Omega_s$. If two nodes are identified as critical, indicating that their linking bond is critical, the union of their neighborhoods is considered a critical zone (see Fig. 3.10). At the end of the $n$th time step, before the critical zone is evaluated for damage, the discretization scheme of nodes within the critical zone is switched to the standard scheme. The value of $\sigma$ must therefore be chosen appropriately to balance the efficiency of the switching algorithm and the distance between the damage front and $\Omega_w$.

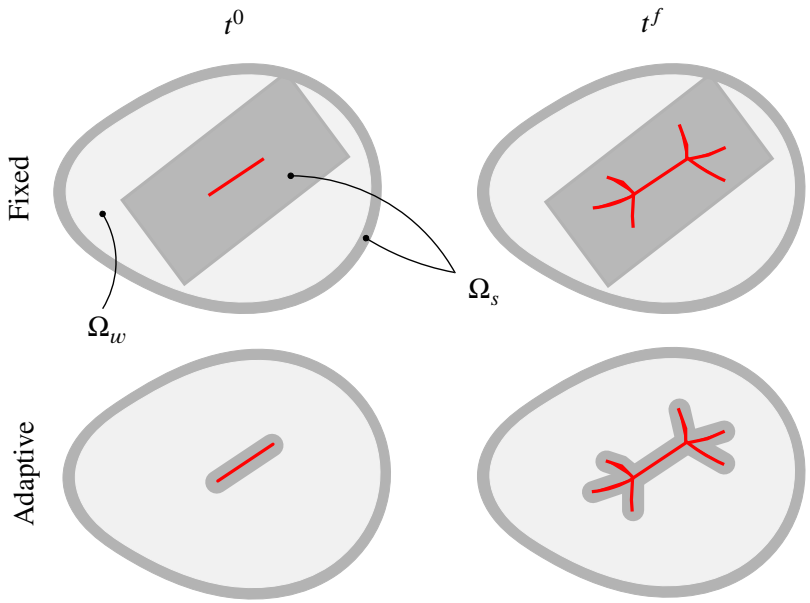


Figure 3.9: The schematic representation illustrates two hybrid configurations utilized in this study: (top) the fixed configuration, where $\Omega_s$ and $\Omega_w$ remain unchanged throughout the solution process, and (bottom) the adaptive configuration, where $\Omega_s$ evolves over time to adapt to the damage morphology. The initial and final time instants are denoted as $t^0$ and $t^f$, respectively. Reproduced from [122].

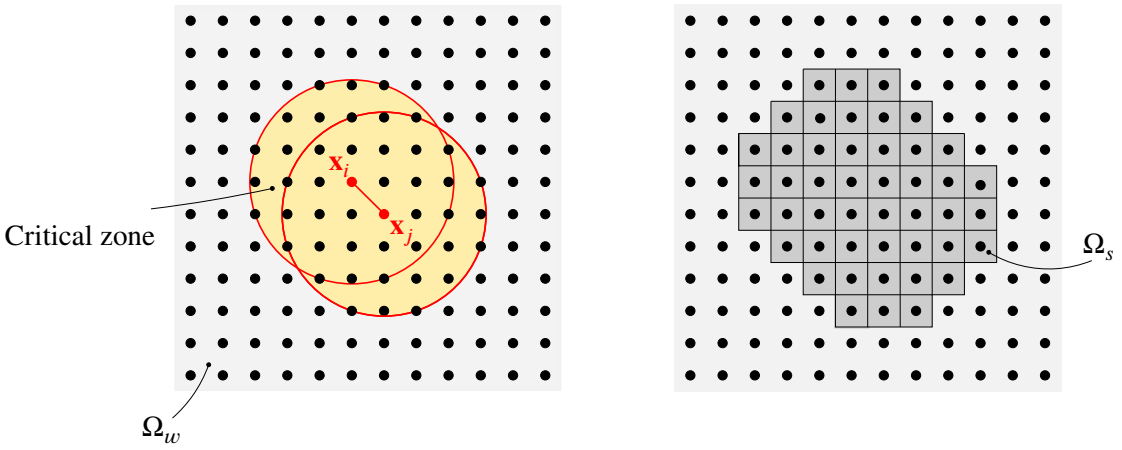


Figure 3.10: Illustration of the switching algorithm used in the hybrid adaptive configuration. On the left, the bond between $\mathbf{x}_i$ and $\mathbf{x}_j$ is identified as critical at time $t^n$. On the right, at the next time step $t^{n+1}$, the discretization scheme of the neighboring nodes corresponding to $\mathbf{x}_i$ and $\mathbf{x}_j$ is switched to the standard scheme. Reproduced from [122].

### 3.3.1 2D Kalthoff-Winkler Experiment on Hybrid Configuration

This example focuses on a hybrid approach to leverage the strengths of both the meshfree WLS scheme and the standard discretization scheme for dynamic fracture modeling of brittle materials, specifically in replicating the behavior observed in the Kalthoff-Winkler experiment [69]. The experiment involves a steel plate, specifically 18Ni1900, with two pre-cracks subjected to impact by a rigid projectile at a velocity of $32 \times 10^3$ mm/s [69]. The experimental findings indicate that at this impact speed, a brittle fracture occurs predominantly in mode I. The cracks initiate from the pre-crack tips and propagate nearly straight, forming an angle of approximately 68° with respect to the horizontal direction, until they reach the plate boundaries [69]. Notably, peridynamic models have demonstrated the ability to accurately capture the observed crack angles, as evidenced by previous studies [31, 127].

The hybrid framework utilizes the computational efficiency and accuracy of the meshfree WLS scheme throughout most of the domain, while selectively employing the standard scheme in critical regions such as crack tips and boundaries. The schematic setup and geometry of the problem are illustrated in Fig. 3.11 (left), and the hybrid approach is depicted in Fig. 3.11 (right). In the bond-based PD model of the Kalthoff-Winkler experiment, we define the mechanical properties and boundary conditions based on the values reported in [31]. Specifically, we set the Young's modulus $E = 190 \times 10^3\,\mathrm{N/mm^2}$, Poisson's ratio $\nu = 1/4$ (assuming plane strain), density $\rho = 8000 \times 10^{-9}\,\mathrm{kg/mm^3}$, and critical energy release rate $G_0 = 0.022\,170\,\mathrm{J/mm^2}$. To replicate the projectile impact, a constant velocity of $16.5 \times 10^3$ mm/s is assigned to the nodes located along the portion of the left side of the plate between the two pre-cracks, as depicted in Fig. 3.11 (left). This prescribed velocity is maintained unchanged throughout the simulation.

In this example, we examine two different discretization approaches: a standard scheme and a hybrid adaptive configuration utilizing the switching strategy explained in Section 3.3. The problem domain is discretized using a uniform grid with a spacing of $\Delta x = 0.25$ mm, resulting in a total of 321, 201 nodes. The influence function $\omega$ is assumed to be constant according to (2.12), and $\delta$ is set to 2 mm. Time integration is performed using the velocity-Verlet algorithm outlined in (3.5) and (3.6) with a time step of $\Delta t = 2 \times 10^{-9}$ s. The simulation spans a duration of $87 \times 10^{-6}$ s. In the adaptive approach, the WLS-2 scheme is employed within the $\Omega_w$ region, as depicted in Fig. 3.10. The specifications of this scheme can be found in Tab. 3.2. Samples of the peridynamic neighborhood are shown in Fig. 3.12, demonstrating that out of the total 197 nodes in the neighborhood, only 29 nodes are involved in the meshfree WLS collocation scheme.

Fig. 3.11 (right) depicts the domain decomposition employed in the adaptive approach at the start of the simulation. The domain is partitioned such that the $\Omega_s$ region, encompassing the pre-cracks and boundaries, accounts for only 9.72% of the entire domain. In this example, the critical bond stretch margin $\sigma$ is selected as 0.95.

Fig. 3.13 presents contour plots of damage obtained using both approaches at four time instants. Additionally, the evolving configuration for the adaptive approach is depicted at the same time instances. The results indicate a close agreement between the adaptive approach and the fully standard scheme. The switching algorithm effectively adapts the $\Omega_s$ region to follow the crack morphology, ensuring that it evolves only as necessary.

Fig. 3.14 is included to assess the consistency between the numerical solutions in relation to the velocity field. The contour plots depict the velocity field in the vertical direction. It is evident that there is a high degree of agreement between the solutions obtained using both approaches.

Tab. 3.3 provides a comprehensive comparison of the computational cost between the adaptive approach and the standard approach. It is noteworthy that in the adaptive approach, the region

$\Omega_s$ governed by the standard discretization scheme only constitutes 14.70% of the entire domain. The runtime analysis reveals that the adaptive approach exhibits a significant advantage, being 2.26 times faster than the standard scheme. This indicates a remarkable optimization of computational resources. Consequently, the adaptive approach achieves comparable results to the standard approach at a significantly reduced computational cost.

Table 3.3: Comparison of the CPU times as an indication of the computational resources utilized in the Kalthoff-Winkler simulation. Data available in [122].

| | **Standard** | **Adaptive** |
|---|---|---|
| Initial $\Omega_s$ portion [%] | 100 | 9.72 |
| Final $\Omega_s$ portion [%] | 100 | 14.70 |
| CPU time [s] | 53.25 | 23.59 |

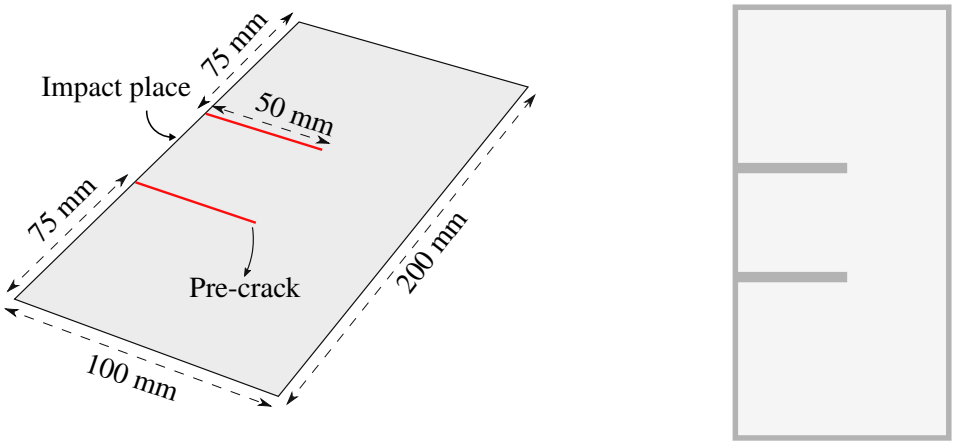


Figure 3.11: (Left) Problem domain from Section 3.3.1; (right) initial configuration of the adaptive approach, with the darker gray indicating the $\Omega_s$ region. Reproduced from [122].

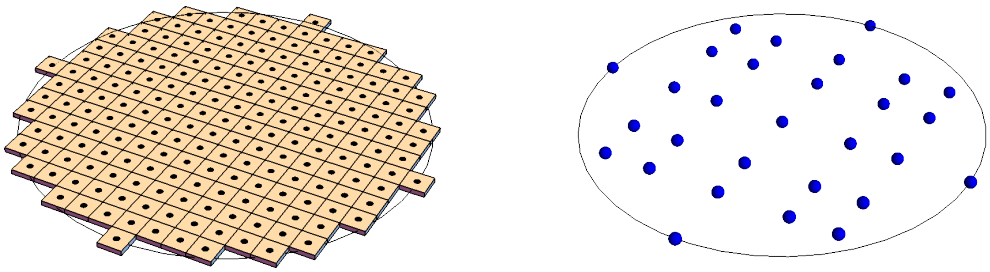

Figure 3.12: Illustration of the peridynamic neighborhood in the hybrid configuration of the Kalthoff-Winkler simulation, with the $\Omega_s$ region shown on the left, encompassing 197 family nodes, and the $\Omega_w$ region displayed on the right, comprising 29 collocation nodes. Reproduced from [122].

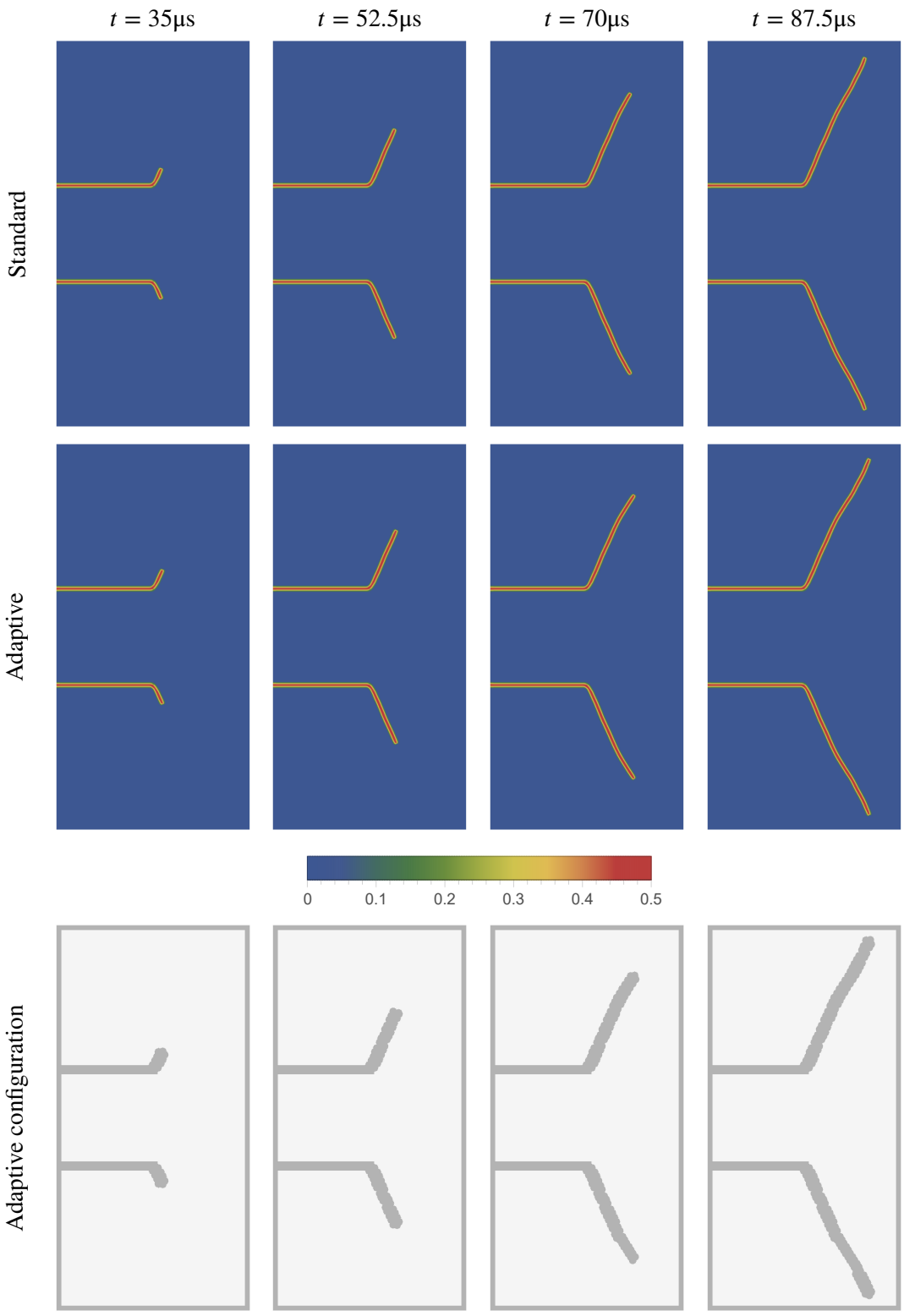


Figure 3.13: Contour plots of damage at four time instants obtained by the standard and adaptive approaches in the Kalthoff-Winkler simulation with the corresponding configuration evolution in the adaptive approach shown below; dark gray zones represent $\Omega_s$. Reproduced from [122].

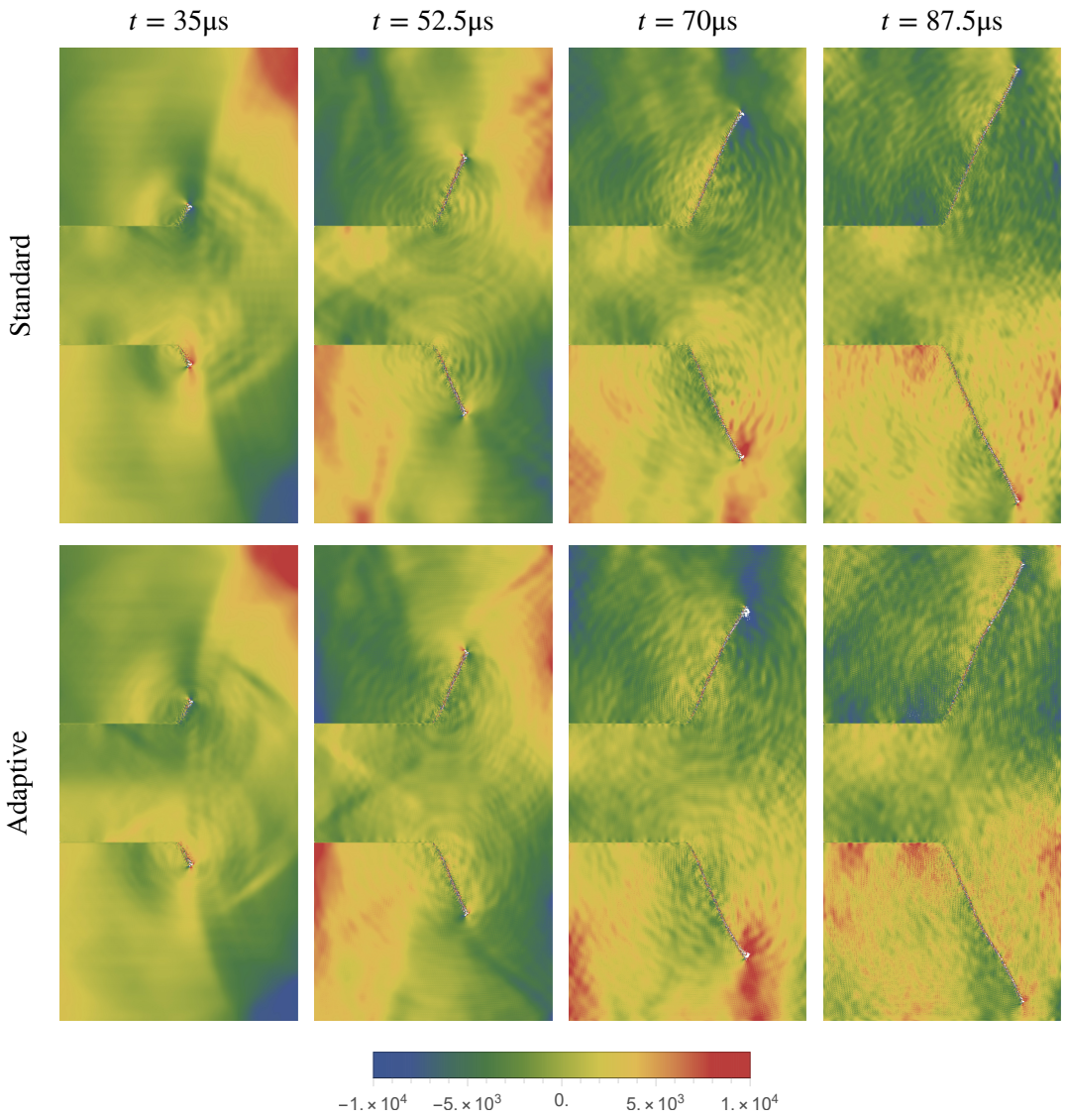


Figure 3.14: Contour plots depicting the vertical velocity field at four time instances are presented for both the standard and adaptive approaches in the Kalthoff-Winkler simulation. The velocity field is represented in units of mm/s. Reproduced from [122].

### 3.3.2 3D Peridynamic Corrosion on Hybrid Configuration

In this example, we conduct a comparative analysis between the meshfree WLS collocation scheme and the standard discretization scheme for solving a 3D peridynamic corrosion problem. The corrosion phenomenon occurs in a metallic specimen represented by the Stanford bunny geometry, which is immersed in a liquid electrolyte contained within a sphere with a radius of 9 mm (Fig. 3.15). As the corrosion progresses, the solid material gradually dissolves into the surrounding liquid medium, resulting in a reduction of the solid phase. Notably, traditional computational methods face challenges in accurately representing the dissolution flux between the phases and capturing the non-smooth concentration field with its strong discontinuities at the corrosion front. For this simulation, the metallic material is assumed to be 304SS, and the initial concentration of the intact metal is $143\,000\,\mathrm{mol/m^3}$, while the surrounding liquid has an initial concentration of $0\,\mathrm{mol/m^3}$, as reported in [25]. A constrained concentration of $0\,\mathrm{mol/m^3}$ is imposed as a boundary condition at the surface of the sphere. The explicit peridynamic diffusion solver in (3.10) is utilized to simulate the corrosion process.

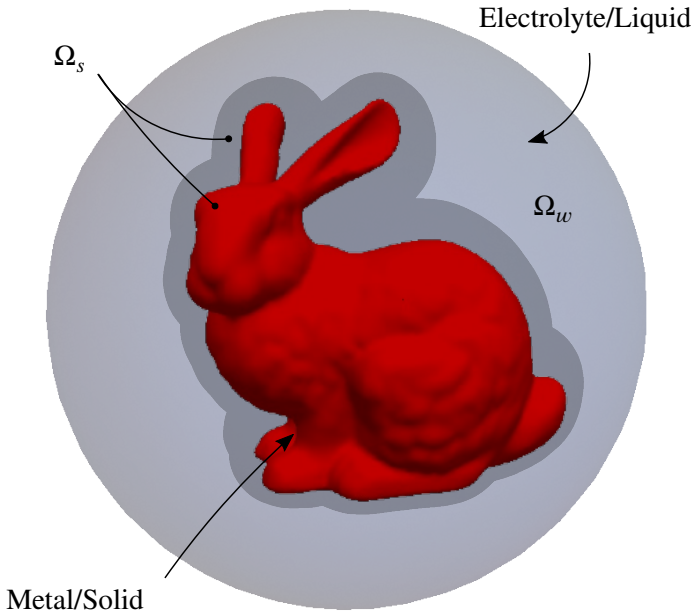


Figure 3.15: Schematic representation the domain and initial bi-material configuration in the 3D peridynamic corrosion example. Reproduced from [122].

To model the corrosion process in the peridynamic diffusion framework, we introduce two constant micro-diffusivity parameters: $\kappa_{\mathrm{int}}$ and $\kappa_{\mathrm{liq}}$ [65]. These parameters capture the interaction between the solid and liquid phases. $\kappa_{\mathrm{int}}$ represents the micro-dissolvability of interfacial peridynamic bonds between solid and liquid points, while $\kappa_{\mathrm{liq}}$ characterizes the micro-diffusivity of peridynamic bonds within the liquid phase. Mass transfer between solid points is neglected due to the significant disparity in diffusion time scales [63]. Additionally, the corrosion process is influenced by a threshold concentration, $C_{\mathrm{sat}}$, which triggers the dissolution of the solid phase. When the concentration of a solid point falls below $C_{\mathrm{sat}}$, it transitions to the liquid phase, driving the autonomous evolution of the corrosion front and gradual dissolution of the solid material.

In this example, the model parameters are configured as follows: the peridynamic horizon is set to $\delta = 0.6\,\text{mm}$, and the metallic ion solubility concentration threshold for 304SS is $C_{\text{sat}} = 5100\,\text{mol/m}^3$ [25]. The micro-diffusivities are arbitrarily chosen as $\kappa_{\text{liq}} = 0.0126\,\text{s}^{-1}\,\text{mm}^{-2}$ and $\kappa_{\text{int}} = 0.0029\,\text{s}^{-1}\,\text{mm}^{-2}$ without calibration to experimental data. Dirichlet-type boundary conditions with zero concentration are imposed near the surface of the sphere, within a distance $\delta 0$. This example compares two peridynamic schemes: the standard discretization scheme with a peridynamic neighborhood comprising 925 nodes, and the meshfree WLS collocation scheme of second-order consistency with a hybrid fixed configuration with 123 collocation nodes. Both schemes use a grid spacing of $\Delta x = 0.1\,\text{mm}$, resulting in a total of $3,053,107$ nodes. The meshfree WLS scheme divides the domain into $\Omega_s$ and $\Omega_w$ regions, with $\Omega_s$ covering the zones where diffusion occurs between different phases and representing 35.02% of the domain. The remaining zones, where the concentration field is smooth, are modeled using the meshfree WLS scheme. The time marching is performed using the explicit forward Euler algorithm with a time step of $\Delta t = 0.1\,\text{s}$, and the problem is solved for a duration of $10\,000\,\text{s}$ using $100,000$ time steps.

Fig. 3.18 showcases the concentration profiles of the metal using the standard scheme and the meshfree WLS scheme at different time points. The plots present separate visualizations of the solid and liquid phases, with a focus on three octants of the liquid phase. The results demonstrate a strong agreement between the two schemes regarding the corrosion and bulk diffusion patterns. In terms of quantitative analysis, both schemes exhibit the same corrosion rate, as depicted in Fig. 3.17. When considering computational performance, the meshfree WLS scheme surpasses the standard scheme, achieving a speedup of 3.7 times, as indicated in Tab. 3.4. In summary, the proposed scheme achieves comparable results to the standard scheme while significantly reducing computational costs.

Table 3.4: Computational resource utilization comparison in 3D peridynamic corrosion. Data available in [122].

| | **Standard** | **Hybrid** |
|---|---|---|
| Initial $\Omega_s$ portion [%] | 100 | 35.02 |
| Final $\Omega_s$ portion [%] | 100 | 35.02 |
| CPU time [s] | 177,138.06 | 47,770.09 |

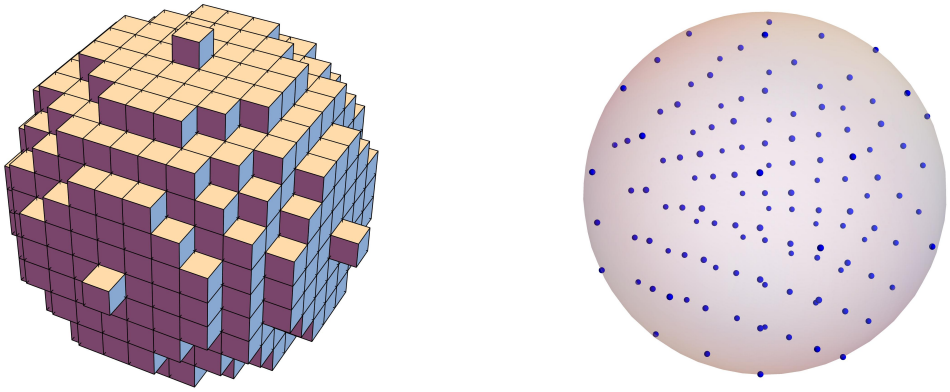

Figure 3.16: The peridynamic neighborhood in the 3D peridynamic corrosion example, showing the representation for both the standard scheme and the meshfree WLS scheme. In the standard scheme (left), the peridynamic neighborhood consists of 925 family nodes. On the other hand, the meshfree WLS scheme (right) utilizes 123 collocation nodes to define the peridynamic neighborhood. Reproduced from [122].

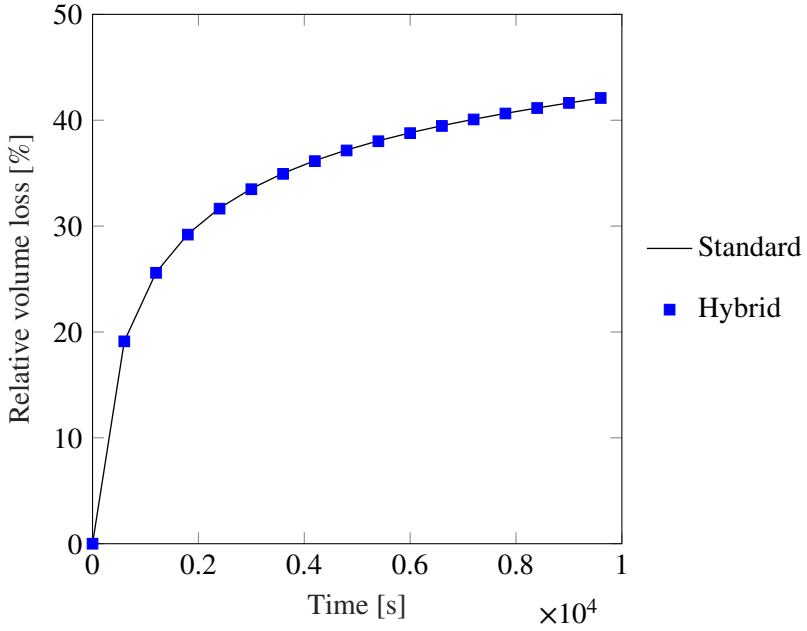


Figure 3.17: Temporal evolution of the relative volume loss of the solid phase in the 3D peridynamic corrosion example, as obtained by both schemes. Reproduced from [122].

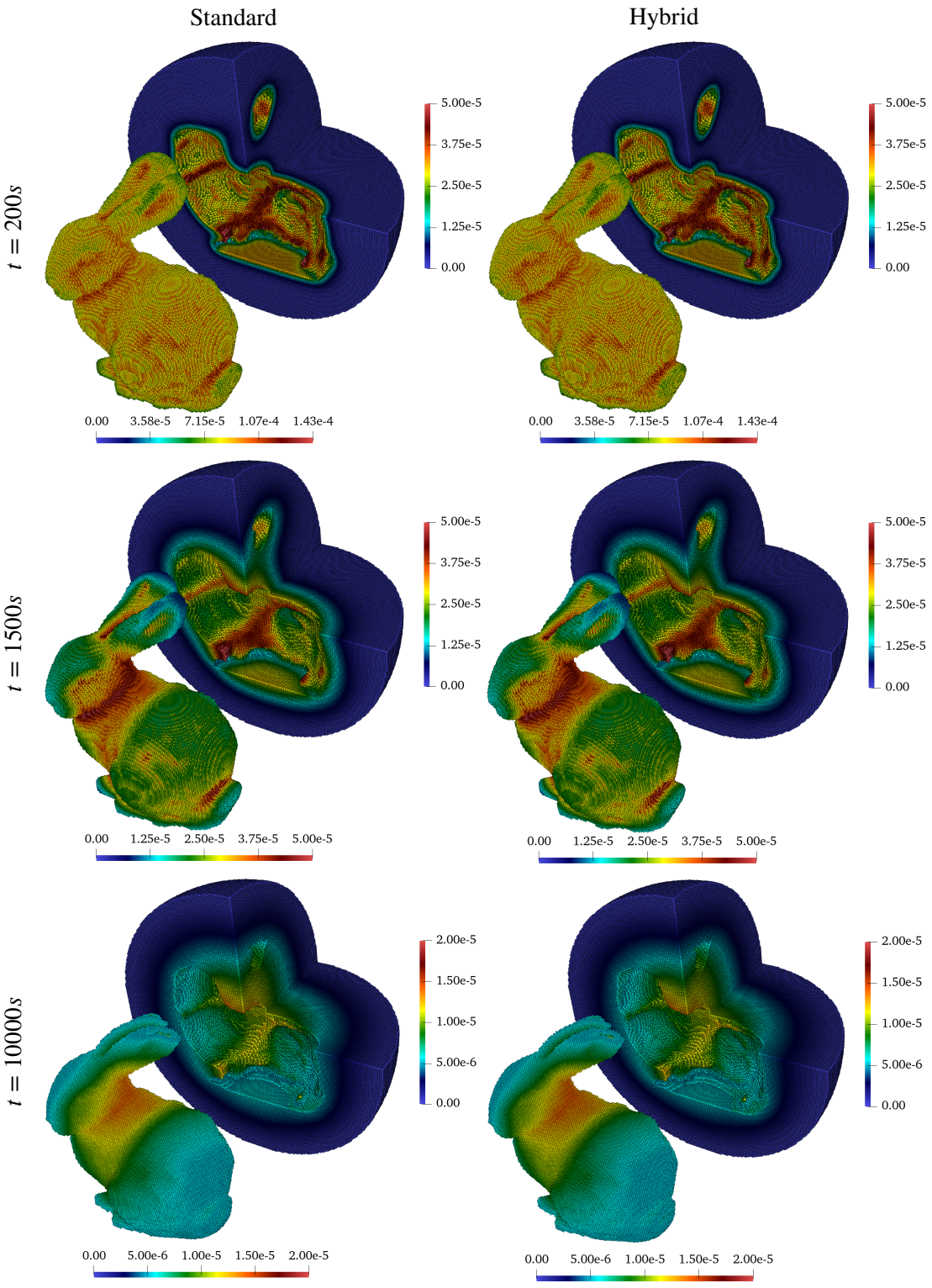


Figure 3.18: Contour plots illustrating the concentration field obtained from both schemes in the 3D peridynamic corrosion example at three different time points. The concentration values are expressed in units of mol/mm$^3$. Reproduced from [122].

## 3.4 Multi-Grid Approach for Adaptive Mesh Refinement

As previously discussed in Section 3.1, the standard discretization scheme of peridynamic models necessitates a uniform grid throughout the entire computational domain. However, this can result in unnecessary computational overhead, particularly in regions that are not of particular interest. To address this issue, a multi-grid approach was introduced in [121] to enable non-uniform spatial discretization, significantly reducing computational costs and expanding the applicability of peridynamic models to real-world geometries in both 2D and 3D. The multi-grid scheme begins by considering a generic peridynamic domain $\Omega$ with one or more discontinuities that may propagate, branch, or coalesce due to deformation. In this framework, the boundaries and critical regions surrounding the discontinuities are discretized using the standard scheme with a fine grid, while the remaining parts of the domain are discretized using a coarser grid, employing either the standard or the meshfree WLS collocation scheme.

The multi-grid approach, as introduced in [121], incorporates fictitious material points near critical regions and boundaries in both the $\Omega^+$ and $\Omega^-$ regions. These additional points serve the purpose of completing the neighborhood of other material points, ensuring the independence of the coarse and fine grids. Importantly, these fictitious points do not contribute to the total count of material points. By employing two separate solution domains, one for the peridynamic model discretized with a fine grid using the standard scheme and another for the peridynamic model discretized with a coarse grid, the grids remain independent. Within the fine grid solution domain, material points are represented by $\mathbf{x}$ while fictitious material points, denoted as $\mathbf{x}'$, are introduced to account for missing neighbors.

dThe interaction between material points $\mathbf{x}$ and $\mathbf{x}'$ in the multi-grid approach is achieved by computing the quantities associated with $\mathbf{x}'$ through interpolation from neighboring material points in the solution domain $\Omega^+$ (see Fig. 3.19). Similarly, the quantities related to fictitious material points in the coarse grid are computed by interpolating values from adjacent material points in the solution domain $\Omega^-$. This approach creates a constraint between the solution domains, where the solution outside the critical region in $\Omega^-$ is linked to its corresponding region in $\Omega^+$, and the solution within the critical region in $\Omega^+$ is constrained to its counterpart in $\Omega^-$.

The configuration of the solution domains in the multi-grid approach is illustrated in Fig. 3.19, where active and inactive regions are identified. Inactive regions represent constrained parts of the solution that are not involved in the computation, allowing for conservation of the total mass of the system. Each solution domain can be discretized independently and in advance, leading to increased efficiency in the adaptive refinement process that tracks the evolution of critical regions. By considering the same portion of the domain $\Omega$ near the border of the critical region in both the $\Omega^-$ and $\Omega^+$ solution domains, as depicted in Fig. 3.20, the discretized form of the multi-grid scheme can be easily introduced.

Within the multi-grid framework, the grid spacings $\Delta x^-$ and $\Delta x^+$ are used to discretize the $\Omega^-$ and $\Omega^+$ solution domains, respectively. Four types of nodes can be distinguished in the discretized solution domains: active and fictitious nodes in the fine grid, and active and fictitious nodes in the coarse grid. As illustrated in Fig. 3.20, an active node a in the fine grid has neighbors consisting of both active nodes, denoted as $\mathrm{a}_j$, and fictitious nodes, denoted as $\mathrm{a}_k$. Similarly, an active node B in the coarse grid has neighbors comprising both active nodes, labeled as $\mathrm{B}_j$, and fictitious nodes, marked as $\mathrm{B}_k$.

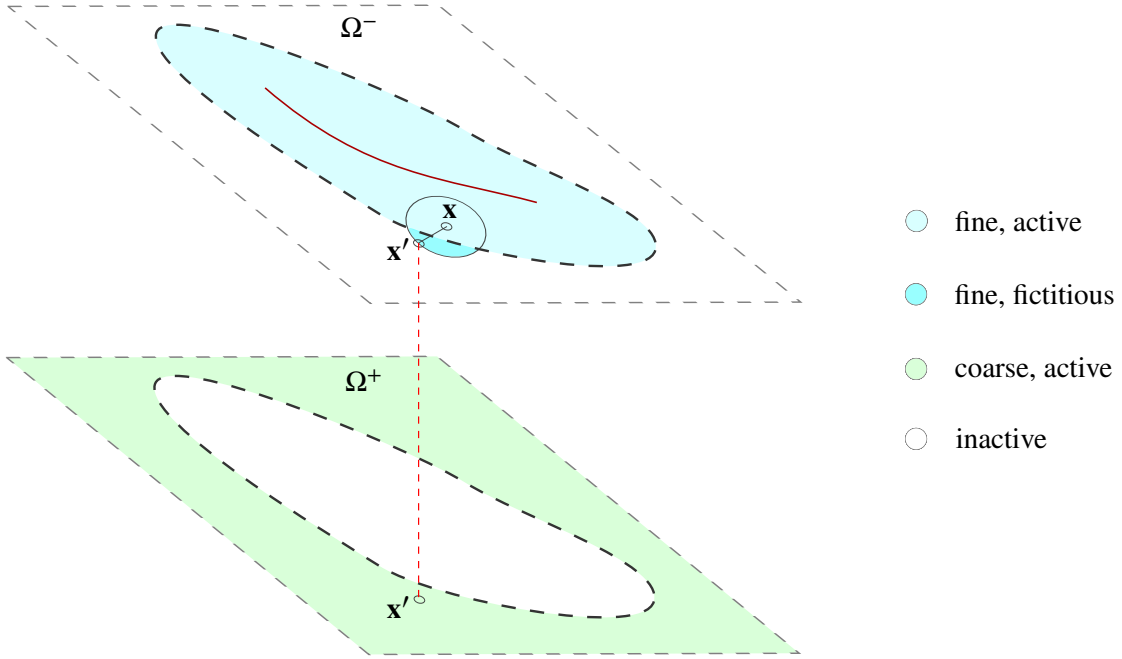


Figure 3.19: Schematic representation of fictitious material points in the proximity of a critical region and computation of the corresponding data from the counterpart active domain. Reproduced from [100].

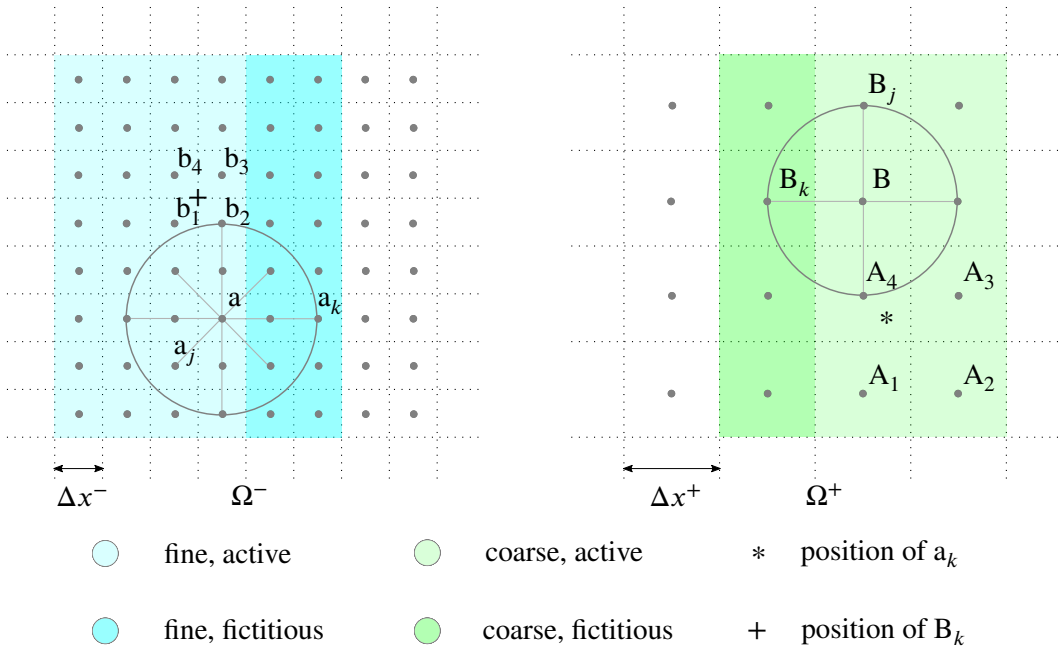


Figure 3.20: Schematic representation of the solution domain; (left) fine grid, (right) coarse grid. For clarity reasons, $m^- = \delta/\Delta x^- = 2$ is adopted in the fine region of the domain, whereas $m^+ = \delta/\Delta x^+ = 1$ is considered in the coarse portion of the domain, where $\delta$ is the horizon. Note that, $\Delta x^+ = 2\Delta x^-$ is chosen only as an example. Reproduced from [100].

Next, we describe the time marching scheme for a typical active node a in the fine grid for the bond-based peridynamic elasticity problem. The velocity-Verlet algorithm is used to discretize the equations, yielding

$$\mathbf{u}_{\mathrm{a}}^{n+1} = \mathbf{u}_{\mathrm{a}}^{n} + \Delta t \dot{\mathbf{u}}_{\mathrm{a}}^{n} + \frac{\Delta t^2}{2} \ddot{\mathbf{u}}_{\mathrm{a}}^{n}, \tag{3.81a}$$

$$\begin{aligned} \ddot{\mathbf{u}}_{\mathrm{a}}^{n+1} = \frac{1}{\rho_{\mathrm{a}}} \Big[ & \mathbf{f}\left(\mathbf{u}_{\mathrm{a}_j}^{n+1} - \mathbf{u}_{\mathrm{a}}^{n+1}, \mathbf{x}_{\mathrm{a}_j} - \mathbf{x}_{\mathrm{a}}\right) \beta \left(\mathbf{x}_{\mathrm{a}_j} - \mathbf{x}_{\mathrm{a}}\right) V_{\mathrm{a}_j} + \cdots \\ & + \mathbf{f}\left(\mathbf{u}_{\mathrm{a}_k}^{n+1} - \mathbf{u}_{\mathrm{a}}^{n+1}, \mathbf{x}_{\mathrm{a}_k} - \mathbf{x}_{\mathrm{a}}\right) \beta \left(\mathbf{x}_{\mathrm{a}_k} - \mathbf{x}_{\mathrm{a}}\right) V_{\mathrm{a}_k} + \cdots + \mathbf{b}_{\mathrm{a}}^{n+1} \Big], \end{aligned} \tag{3.81b}$$

$$\dot{\mathbf{u}}_{\mathrm{a}}^{n+1} = \dot{\mathbf{u}}_{\mathrm{a}}^{n} + \frac{\Delta t}{2} \left( \ddot{\mathbf{u}}_{\mathrm{a}}^{n} + \ddot{\mathbf{u}}_{\mathrm{a}}^{n+1} \right), \tag{3.81c}$$

where $\mathbf{f}$ represents the pairwise force function, which can be nonlinear. The equations obtained from the velocity-Verlet algorithm and the considerations regarding the coupling of different grid sizes are structurally equivalent to the peridynamic scalar wave equation described in (2.40). The only distinction lies in the scalar nature of the field variables, namely displacement, velocity, and acceleration. For the sake of brevity, the subsequent formulations will omit the specific considerations for the peridynamic scalar wave equation.

For the peridynamic diffusion problem, the explicit Euler time marching scheme (*cf.* (3.10)) for an active node 'a' in the fine grid domain is expressed as

$$\begin{aligned} C_{\mathrm{a}}^{n+1} &= C_{\mathrm{a}}^{n} + \Delta t \dot{C}_{\mathrm{a}}^{n}, \\ \dot{C}_{\mathrm{a}}^{n+1} &= J\left(C_{\mathrm{a}_j}^{n+1} - C_{\mathrm{a}}^{n+1}, \mathbf{x}_{\mathrm{a}_j} - \mathbf{x}_{\mathrm{a}}\right) \beta \left(\mathbf{x}_{\mathrm{a}_j} - \mathbf{x}_{\mathrm{a}}\right) V_{\mathrm{a}_j} + \cdots \\ &\quad + J\left(C_{\mathrm{a}_k}^{n+1} - C_{\mathrm{a}}^{n+1}, \mathbf{x}_{\mathrm{a}_k} - \mathbf{x}_{\mathrm{a}}\right) \beta \left(\mathbf{x}_{\mathrm{a}_k} - \mathbf{x}_{\mathrm{a}}\right) V_{\mathrm{a}_k} + \cdots + S_{\mathrm{a}}^{n+1}. \end{aligned} \tag{3.82}$$

In the preceding equations (*cf.* (3.81) - (3.82)), the first and second ellipses represent the contributions from other active and fictitious nodes within the neighborhood of the active node a, similar to those already defined for $\mathrm{a}_j$ and $\mathrm{a}_k$. The time marching scheme for a general active node B in the coarse grid, in the context of the bond-based PD elasticity problem, can be defined as

$$\begin{aligned} \mathbf{u}_{\mathrm{B}}^{n+1} &= \mathbf{u}_{\mathrm{B}}^{n} + \Delta t \dot{\mathbf{u}}_{\mathrm{B}}^{n} + \frac{\Delta t^2}{2} \ddot{\mathbf{u}}_{\mathrm{B}}^{n}, \\ \ddot{\mathbf{u}}_{\mathrm{B}}^{n+1} &= \frac{1}{\rho_{\mathrm{B}}} \Big[ \mathbf{f}\left(\mathbf{u}_{\mathrm{B}_j}^{n+1} - \mathbf{u}_{\mathrm{B}}^{n+1}, \mathbf{x}_{\mathrm{B}_j} - \mathbf{x}_{\mathrm{B}}\right) \beta \left(\mathbf{x}_{\mathrm{B}_j} - \mathbf{x}_{\mathrm{B}}\right) V_{\mathrm{B}_j} + \cdots \\ &\quad + \mathbf{f}\left(\mathbf{u}_{\mathrm{B}_k}^{n+1} - \mathbf{u}_{\mathrm{B}}^{n+1}, \mathbf{x}_{\mathrm{B}_k} - \mathbf{x}_{\mathrm{B}}\right) \beta \left(\mathbf{x}_{\mathrm{B}_k} - \mathbf{x}_{\mathrm{B}}\right) V_{\mathrm{B}_k} + \cdots + \mathbf{b}_{\mathrm{B}}^{n+1} \Big], \\ \dot{\mathbf{u}}_{\mathrm{B}}^{n+1} &= \dot{\mathbf{u}}_{\mathrm{B}}^{n} + \frac{\Delta t}{2} \left( \ddot{\mathbf{u}}_{\mathrm{B}}^{n} + \ddot{\mathbf{u}}_{\mathrm{B}}^{n+1} \right), \end{aligned} \tag{3.83}$$

and for the peridynamic diffusion equation as

$$\begin{aligned} C_{\mathrm{B}}^{n+1} &= C_{\mathrm{B}}^{n} + \Delta t \dot{C}_{\mathrm{B}}^{n}, \\ \dot{C}_{\mathrm{B}}^{n+1} &= J\left(C_{\mathrm{B}_j}^{n+1} - C_{\mathrm{B}}^{n+1}, \mathbf{x}_{\mathrm{B}_j} - \mathbf{x}_{\mathrm{B}}\right) \beta \left(\mathbf{x}_{\mathrm{B}_j} - \mathbf{x}_{\mathrm{B}}\right) V_{\mathrm{B}_j} + \cdots \\ &\quad + J\left(C_{\mathrm{B}_k}^{n+1} - C_{\mathrm{B}}^{n+1}, \mathbf{x}_{\mathrm{B}_k} - \mathbf{x}_{\mathrm{B}}\right) \beta \left(\mathbf{x}_{\mathrm{B}_k} - \mathbf{x}_{\mathrm{B}}\right) V_{\mathrm{B}_k} + \cdots + S_{\mathrm{B}}^{n+1}. \end{aligned} \tag{3.84}$$

The equations in (3.83) and (3.84) incorporate the contribution from neighboring active and fictitious nodes within the vicinity of the active node B. This contribution is analogous to the terms described for $\mathrm{B}_j$ and $\mathrm{B}_k$.

The interpolation scheme for evaluating the quantities associated with fictitious nodes in both the coarse and fine grids is presented after introducing the time marching schemes. In the context of elasticity and diffusion problems, the fictitious node $\mathrm{B}_k$ in the coarse grid, as shown in Fig. 3.20, obtains its associated values, such as displacement, velocity, and acceleration, through a simple interpolation. This interpolation is based on inverse distance weighting and utilizes the values of the surrounding active nodes $\mathrm{b}_1$ to $\mathrm{b}_4$ in the fine grid, given by

$$\begin{aligned}
\mathbf{u}_{\mathrm{B}_k}^{n+1} &= \frac{\sum_{j=1}^{4} \frac{1}{\|\mathbf{x}_{\mathrm{B}_k} - \mathbf{x}_{\mathrm{b}_j}\|} \mathbf{u}_{\mathrm{b}_j}^{n+1}}{\sum_{j=1}^{4} \frac{1}{\|\mathbf{x}_{\mathrm{B}_k} - \mathbf{x}_{\mathrm{b}_j}\|}}, \\
\dot{\mathbf{u}}_{\mathrm{B}_k}^{n+1} &= \frac{\sum_{j=1}^{4} \frac{1}{\|\mathbf{x}_{\mathrm{B}_k} - \mathbf{x}_{\mathrm{b}_j}\|} \dot{\mathbf{u}}_{\mathrm{b}_j}^{n+1}}{\sum_{j=1}^{4} \frac{1}{\|\mathbf{x}_{\mathrm{B}_k} - \mathbf{x}_{\mathrm{b}_j}\|}},
\end{aligned} \tag{3.85}$$

in the case of bond-based PD elasticity, and as such as

$$C_{\mathrm{B}_k}^{n+1} = \frac{\sum_{j=1}^{4} \frac{1}{\|\mathbf{x}_{\mathrm{B}_k} - \mathbf{x}_{\mathrm{b}_j}\|} C_{\mathrm{b}_j}^{n+1}}{\sum_{j=1}^{4} \frac{1}{\|\mathbf{x}_{\mathrm{B}_k} - \mathbf{x}_{\mathrm{b}_j}\|}}, \tag{3.86}$$

for peridynamic diffusion problems. It is worth noting that a similar procedure can be applied to the scalar peridynamic scalar wave problem, but it is omitted here for brevity.

In a similar manner, as illustrated in Fig. 3.20, the fictitious node $\mathrm{a}_k$ in the fine grid is introduced. To obtain the required values for this node, a straightforward interpolation technique, employing inverse distance weighting, is applied. The interpolation is performed using the values of the surrounding active nodes $\mathrm{A}_1$ to $\mathrm{A}_4$ in the coarse grid, yielding

$$\begin{aligned}
\mathbf{u}_{\mathrm{a}_k}^{n+1} &= \frac{\sum_{j=1}^{4} \frac{1}{\|\mathbf{x}_{\mathrm{a}_k} - \mathbf{x}_{\mathrm{A}_j}\|} \mathbf{u}_{\mathrm{A}_j}^{n+1}}{\sum_{j=1}^{4} \frac{1}{\|\mathbf{x}_{\mathrm{a}_k} - \mathbf{x}_{\mathrm{A}_j}\|}}, \\
\dot{\mathbf{u}}_{\mathrm{a}_k}^{n+1} &= \frac{\sum_{j=1}^{4} \frac{1}{\|\mathbf{x}_{\mathrm{a}_k} - \mathbf{x}_{\mathrm{A}_j}\|} \dot{\mathbf{u}}_{\mathrm{A}_j}^{n+1}}{\sum_{j=1}^{4} \frac{1}{\|\mathbf{x}_{\mathrm{a}_k} - \mathbf{x}_{\mathrm{A}_j}\|}},
\end{aligned} \tag{3.87}$$

for the bond-based PD elasticity problems, and

$$C_{\mathrm{a}_k}^{n+1} = \frac{\sum_{j=1}^{4} \frac{1}{\|\mathbf{x}_{\mathrm{a}_k} - \mathbf{x}_{\mathrm{A}_j}\|} C_{\mathrm{A}_j}^{n+1}}{\sum_{j=1}^{4} \frac{1}{\|\mathbf{x}_{\mathrm{a}_k} - \mathbf{x}_{\mathrm{A}_j}\|}}, \tag{3.88}$$

for peridynamic diffusion.

To incorporate the multi-grid approach for implicit time discretization schemes, we need to account for the effect of fictitious nodes in the linear system, specifically in (3.17). This requires modifying the entries of the Jacobian $\mathbf{K}_C\left(\mathbf{C}^n\right)$ and the residual $\mathbf{F}_C\left(\mathbf{C}^{n+1,k}\right)$. Therefore, we set the corresponding diagonal and off-diagonal values of the respective fictitious nodes in the coarse grid, $\mathrm{B}_k$, and in the fine grid, $\mathrm{a}_k$, as

$$\begin{aligned} K_{C,a_k a_k} &= 1, \quad K_{C,a_k A_j} = -\frac{\frac{1}{\|\mathbf{x}_{\mathrm{a}_k}-\mathbf{x}_{\mathrm{A}_j}\|}}{\sum_{j=1}^{4}\frac{1}{\|\mathbf{x}_{\mathrm{a}_k}-\mathbf{x}_{\mathrm{A}_j}\|}}, \\ K_{C,B_k B_k} &= 1, \quad K_{C,B_k b_j} = -\frac{\frac{1}{\|\mathbf{x}_{\mathrm{B}_k}-\mathbf{x}_{\mathrm{b}_j}\|}}{\sum_{j=1}^{4}\frac{1}{\|\mathbf{x}_{\mathrm{B}_k}-\mathbf{x}_{\mathrm{b}_j}\|}}. \end{aligned} \tag{3.89}$$

The associated residual is updated according to

$$\begin{aligned} F_{C,a_k}\left(C_{a_k}^{n+1,k}\right) &= C_{a_k}^{n+1,k} - \frac{\sum_{j=1}^{4}\frac{1}{\|\mathbf{x}_{\mathrm{a}_k}-\mathbf{x}_{\mathrm{A}_j}\|}C_{A_j}^{n+1,k}}{\sum_{j=1}^{4}\frac{1}{\|\mathbf{x}_{\mathrm{a}_k}-\mathbf{x}_{\mathrm{A}_j}\|}} = 0, \\ F_{C,B_k}\left(C_{B_k}^{n+1,k}\right) &= C_{B_k}^{n+1,k} - \frac{\sum_{j=1}^{4}\frac{1}{\|\mathbf{x}_{\mathrm{B}_k}-\mathbf{x}_{\mathrm{b}_j}\|}C_{b_j}^{n+1,k}}{\sum_{j=1}^{4}\frac{1}{\|\mathbf{x}_{\mathrm{B}_k}-\mathbf{x}_{\mathrm{b}_j}\|}} = 0. \end{aligned} \tag{3.90}$$

In Section 3.4.1, we further demonstrate the accuracy of the proposed multi-grid approach using a representative example in 1D. Moreover, in Chapter 5 of this dissertation, the advantages of this approach in terms of computational time reduction and accuracy are discussed in the context of a complex multi-physics example: the bio-corrosion simulation of a bone implant screw.

### 3.4.1 1D Peridynamic Corrosion using the Multi-Grid Technique

The primary objective of this section is to assess the effectiveness of the multi-grid approach in a 1D peridynamic corrosion example. In peridynamic corrosion examples, the region of interest corresponds to the vicinity of the liquid-solid interface, where a fine grid spacing with high spatial resolution is necessary. On the other hand, the liquid region, which is governed by simple diffusion, typically does not require a fine level of discretization compared to the region of interest. This discrepancy in grid resolution is also observed in the 3D multi-physics case studies presented in Chapter 5 of this dissertation, specifically in the application of the peridynamic corrosion model to the bio-corrosion and material degradation of Mg-based bone implant screws. In these case studies, the solid metal part, which includes the geometric details of the sample, necessitates a larger number of nodes for accurate representation. Conversely, the surrounding liquid domain, particularly the areas further away from the corrosion interface, can be represented with a smaller number of nodes.

In this illustrative example, we consider a 1D medium with a range of $[-50, 50]$ that includes both solid and liquid phases. The solid phase is confined to the interval $[-5, 5]$, while the liquid phase occupies the intervals $[-50, -5)$ and $(5, 50]$. The problem focuses on the corrosion of the solid phase, which gradually dissolves into the surrounding liquid medium. The initial concentration value is set to $C(x, 0) = 1$ for material points in the solid phase ($x \in [-5, 5]$) and $C(x, 0) = 0$

for the liquid phase ($x \in [-50, -5) \cup (5, 50]$). Other parameters used in the simulation include the peridynamic horizon $\delta = 1$, the saturation concentration $C_{\text{sat}} = 0.85$, the micro-diffusivity in the liquid phase $\kappa_{\text{liq}} = 2$, and the micro-diffusivity at the solid-liquid interface $\kappa_{\text{int}} = 0.1$. Homogeneous Neumann boundary conditions are imposed at the boundaries of the medium.

For comparative analysis, three different models are utilized to solve the 1D peridynamic corrosion problem. The first model, called *Coarse*, employs a uniform grid with a grid spacing of $\Delta x^+ = 0.5$, resulting in a total of 201 nodes. The second model, known as *Fine*, also utilizes a uniform grid, but with a smaller grid spacing of $\Delta x^- = 0.025$, which gives rise to 801 nodes. In the third model, referred to as *Multi-grid*, the region within $(-15.25, 15.25)$ is discretized using $\Delta x^-$, while the remaining region is discretized using $\Delta x^+$. This configuration ensures that the finer grid captures the solid phase and the critical corrosion region with higher resolution. The coupling of the regions with different grid spacing is achieved using the approach described in Section 3.4, resulting in a total of 404 nodes: 140 nodes in the coarser grid, 244 nodes in the finer grid, and 20 auxiliary nodes. A portion of the multi-grid domain is visualized in Fig. 3.21, illustrating the arrangement of the nodes and associated integration cells while conserving the total mass of the system. To advance in time, all models adopt an incremental time step of $\Delta t = 0.025$.

The accuracy of the Multi-grid model is evaluated by comparing it to the Fine model, which serves as the reference solution. In Fig. 3.22, the initial concentration levels of the solid phase are compared between the Multi-grid and Fine models across different parts of the solution domain. The evolution of the concentration over time is depicted in Fig. 3.24 for both models. The regions with concentration levels $C(x, t) \geq 0.85$ (represented by black points) correspond to the solid phase of the solution domain. The results show that the Multi-grid solution closely resembles the Fine model, with a similar pattern of solid phase reduction. The coupling approach effectively prevents spurious flux in the connecting regions of the grids. Overall, the Multi-grid approach achieves a comparable solution to the Fine model with significantly fewer computational resources and a reduced number of nodes.

Fig. 3.23 presents the volume loss of the solid phase as obtained by the different models. The results demonstrate that the Multi-grid and Fine models exhibit a similar vanishing time for the solid phase, while the Coarse model shows an earlier disappearance. This can be attributed to the fact that the Multi-grid approach employs a grid spacing identical to that of the Fine model in the corrosion region, while using a grid spacing identical to that of the Coarse model in the diffusion-dominated parts. Consequently, the Multi-grid approach effectively utilizes computational resources, achieving comparable results to the Fine model while reducing the grid resolution in non-critical regions.

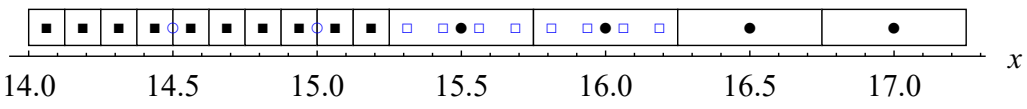


Figure 3.21: A section of the Multi-grid model in the vicinity of the coupling region. Reproduced from [60].

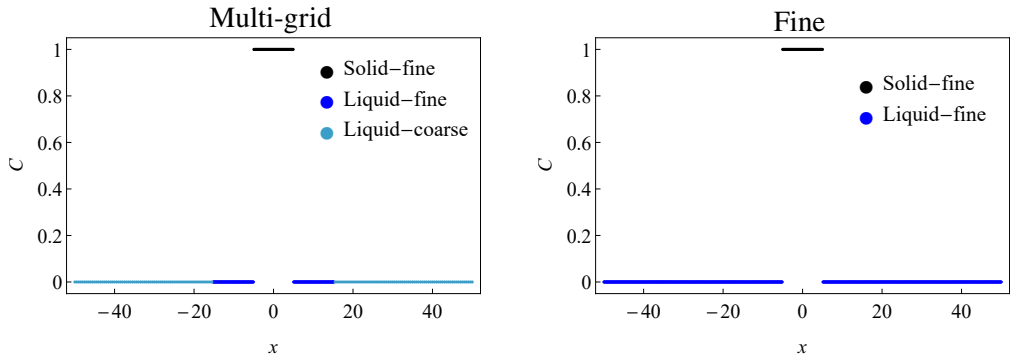


Figure 3.22: Comparison of the initial concentration levels between the Multi-grid and Fine models. The legend indicates the discretization used, with the second term specifying the grid resolution. Reproduced from [60].

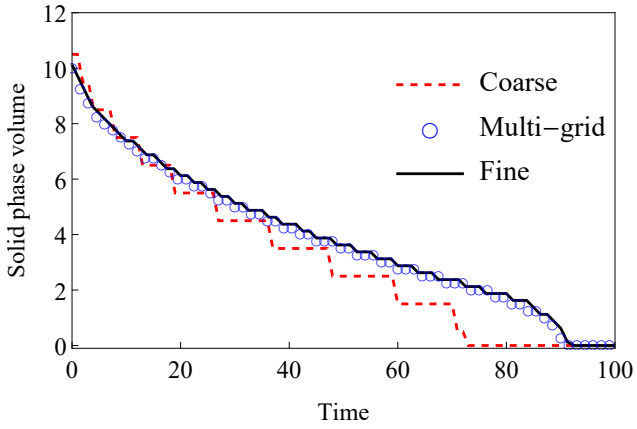


Figure 3.23: The temporal evolution of the solid phase volume is depicted for all three models. Reproduced from [60].

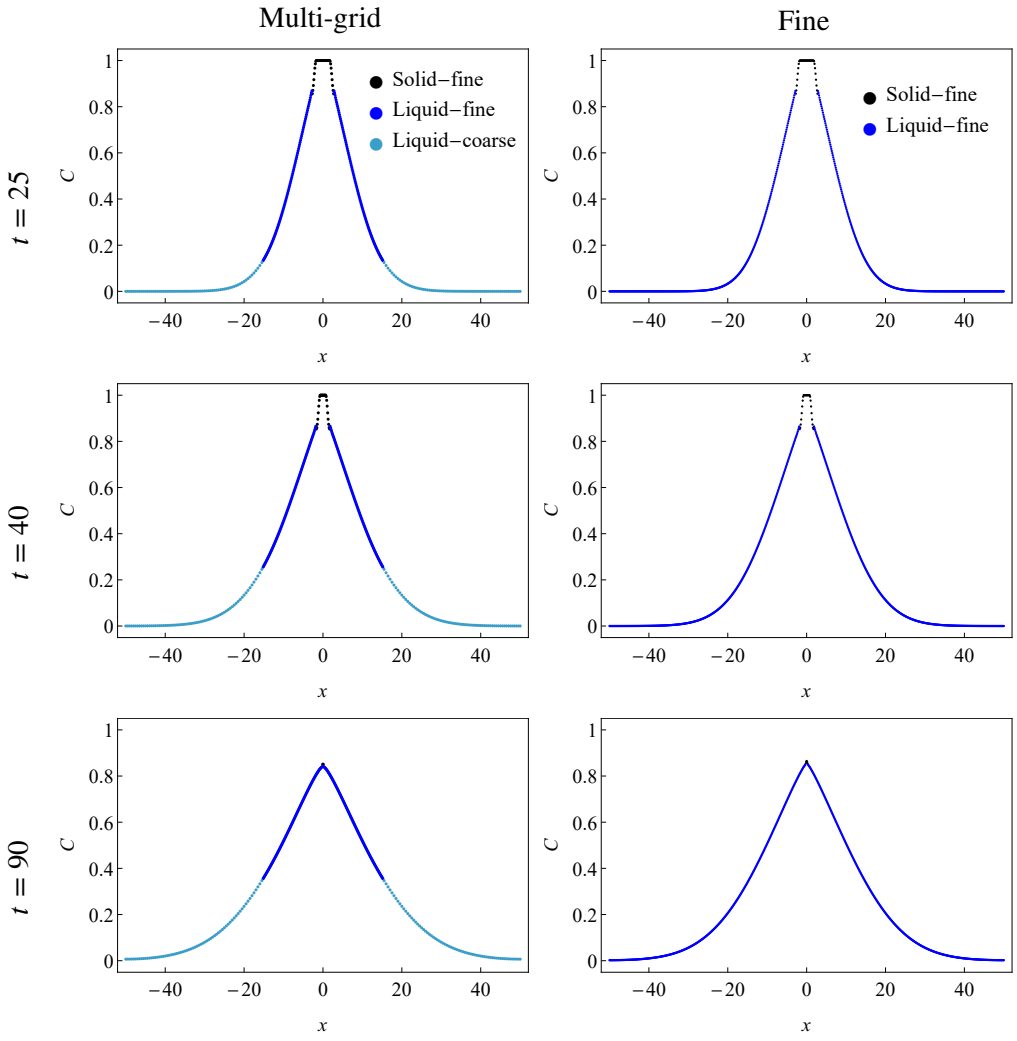


Figure 3.24: The concentration field at various time points is displayed for both the Multi-grid model (left column) and the Fine model (right column). Reproduced from [60].

### 3.4.2 3D Nonlocal Nernst-Planck-Poisson Corrosion on Multi-Grid Domain

In this section, we apply the multi-grid approach of adaptive grid refinement to a 3D problem using the NNPP corrosion formalism, provided in (2.63) and (2.64), to model the electrochemical dissolution process of a Mg-based headless M2 $\times$ 4 mm bone implant screw. Mg-based implant materials have garnered significant attention due to their favorable biomechanical and osteoconductive properties, as well as their biocompatibility. These implants degrade naturally over time through bio-corrosion, eliminating the need for a second surgical intervention for removal. Chapter 5, particularly Section 5.2 and 5.3, of this dissertation, provide a comprehensive discussion on using the peridynamic framework to establish a digital twin for numerically modeling the *in vitro* degradation behavior of Mg-based bone implants and the use of surrogate models for efficient *in vivo* corrosion predictions.

The purpose of the following numerical example is to demonstrate the computational capabilities of the full NNPP corrosion model on 3D implant geometries. This demonstration does not involve parameter calibration using experimental corrosion data and does not claim to fully represent the chemical compositions, precipitation formations, or constitutive corrosion kinetics of Mg-based alloy bio-corrosion in physiological environments. In Section 5.2, we delve into the parameter calibration of the peridynamic bi-material bio-corrosion model in more detail, and provide an example of their application in real-world multi-physics scenarios, such as the *in vitro* bio-degradation in physiological environments using Simulated Body Fluid (SBF) as the liquid electrolyte environment. The 3D problem investigated involves a metallic specimen, specifically the Mg-based bone implant screw shown in Fig. 3.25, immersed in a liquid electrolyte within a spherical domain. The dimensions of the cylindrical $\Omega^-$ solution domain are specified with a radius of 2.1 mm and a height of 6.2 mm.

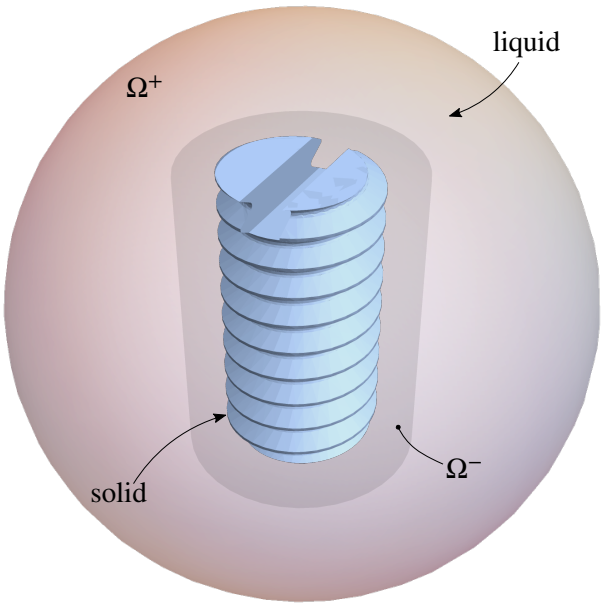


Figure 3.25: Illustration of the problem domain and initial configuration for the 3D peridynamic corrosion example utilized in the multi-adaptive scheme. Reproduced from [100].

The constitutive corrosion model for the 3D NNPP corrosion system is briefly summarized below. For this example, we use a standard corrosion system in a salty aqueous environment, assuming the formation of a single corrosion product. This experimental setup has been extensively explored in references like [41, 42] and is commonly used to benchmark numerical corrosion models [6]. We adopt this scenario to assess and evaluate the NNPP system's performance on a 3D bio-corrosion model of a bone implant screw geometry. The experimental data and system parameters align closely with the numerical corrosion study in [6] and are detailed in Tab. 3.7. The experiment simulates 3D electrochemical corrosion at 20 °C with a metal potential of 844 mV in a 1 M NaCl electrolyte solution. Following the classical Butler-Volmer (BV) equation for anodic dissolution

$$i_a = i_0 \left[ \exp\left( \frac{\alpha_a z_1 F \eta}{RT} \right) - \exp\left( -\frac{\alpha_c z_1 F \eta}{RT} \right) \right], \tag{3.91}$$

where $i_a$ is the anodic current density, $i_0$ is the exchange current density, $\alpha_a$ and $\alpha_c$ are the anodic and cathodic charge transfer coefficients, $\eta$ is the overpotential, and $z_1$ is the charge number of the metal ion. If the cathodic current in the BV relation is small, it can be omitted, reducing the relation to the well-known Tafel equation. According to [25], the anodic current described by (3.91) is linearly dependent on the effective ionic diffusivity, providing a linear correlation between the Fickian diffusion coefficient and the anodic dissolution current density. Substituting this linear relationship yields an Arrhenius-type expression for the diffusion coefficient

$$D_{\text{int}}(\eta) = D_0 \left[ \exp\left( \frac{\alpha_a z_1 F \eta}{RT} \right) - \exp\left( -\frac{\alpha_c z_1 F \eta}{RT} \right) \right], \tag{3.92}$$

with $D_0$ being the diffusion coefficient at zero overpotential. The following two cathodic reactions are proposed within the liquid electrolyte

$$2H^+(aq) + 2e^- \rightarrow H_2, \tag{3.93}$$

$$2H_2O + 2e^- \rightarrow H_2 + 2OH^-(aq), \tag{3.94}$$

where (3.93) corresponds to hydrogen discharge near the corrosion surface, and (3.94) to the water reduction process. The abbreviation (aq) denotes an aqueous phase. The hydrogen discharge reaction occurs near the corrosion interface, within a $\delta$ distance from the interface in the electrolyte phase. Thus, the peridynamic horizon $\delta$ represents a length scale that determines the corrosion and precipitation layer thickness and can be correlated with experimental findings [47, 60, 28]. In addition, two reactions occur within the electrolyte

$$Me^{z_1}(aq) + H_2O \rightleftharpoons MeOH^{z_2}(s) + H^+(aq), \tag{3.95}$$

$$H_2O \rightleftharpoons OH^(aq) - +H^+(aq), \tag{3.96}$$

which represent the oxidation of the metallic magnesium sample, leading to the formation of a precipitated hydroxide layer, and the self-dissociation of water, respectively. The abbreviation (s) denotes a solid phase. The overall NNPP electrochemical corrosion model consists of seven field variables, defined as

$$\begin{aligned} C_1 &= [Me^{z_1}], \\ C_2 &= [MeOH^{z_2}], \\ C_3 &= [Cl^{z_3}], \\ C_4 &= [Na^{z_4}], \\ C_5 &= [H^{z_5}], \\ C_6 &= [OH^{z_6}], \end{aligned} \tag{3.97}$$

where $C_1, C_2, \ldots, C_6$ denote the molar concentrations of the ionic species in the domain, and $z_1, z_2, \ldots, z_6$ are their respective charge numbers, with $\phi$ as the electrostatic potential, serving as the seventh unknown field variable. The initial values and the boundary conditions for each component are summarized in Tab. 3.5. Given the reactions outlined in (3.93) and (3.94), the reaction terms $R_{1,i}^{n+1}$ for $C_{1,i}^{n+1}$ and $R_{2,i}^{n+1}$ for $C_{2,i}^{n+1}$ at the spatial point $\mathbf{x}_i$ and time $t^{n+1}$ are defined based on [6] as

$$R_{1,i}^{n+1} = \begin{cases} -k_{1f} C_{1,i}^{n+1} + k_{1b} C_{2,i}^{n} C_{5,i}^{n}, & \varphi(\mathbf{x}_i, t^n) = 0 \vee \exists \mathbf{x} \in \mathcal{F}_i \,:\, \varphi(\mathbf{x}_i, t^n) \neq \varphi(\mathbf{x}, t^n) \\ 0, & \varphi(\mathbf{x}_i, t^n) = 1 \wedge \forall \mathbf{x} \in \mathcal{F}_i \,:\, \varphi(\mathbf{x}, t^n) = 1 \end{cases}, \tag{3.98}$$

$$R_{2,i}^{n+1} = \begin{cases} k_{1f} C_{1,i}^{n} - k_{1b} C_{2,i}^{n+1} C_{5,i}^{n}, & \varphi(\mathbf{x}_i, t^n) = 0 \vee \exists \mathbf{x} \in \mathcal{F}_i \,:\, \varphi(\mathbf{x}_i, t^n) \neq \varphi(\mathbf{x}, t^n) \\ 0, & \varphi(\mathbf{x}_i, t^n) = 1 \wedge \forall \mathbf{x} \in \mathcal{F}_i \,:\, \varphi(\mathbf{x}, t^n) = 1 \end{cases}, \tag{3.99}$$

where $k_{1f}$ and $k_{1b}$ are the forward and backward reaction rates for the reactions described in (3.95). These reaction terms are used in the semi-implicit time discretization framework and apply exclusively within the liquid electrolyte phase. Since chloride and sodium concentrations ($C_3$ and $C_4$) are non-reactive, their reaction terms are zero. The reaction terms for $C_5$ and $C_6$ are based on the reactions in (3.93) to (3.94) and (3.95) to (3.96), and are expressed as

$$R_{5,i}^{n+1} = \begin{cases} A_i^{n+1}, & \varphi(\mathbf{x}_i, t^n) = 0 \wedge \forall \mathbf{x} \in \mathcal{F}_i \,:\, \varphi(\mathbf{x}, t^n) = 0 \\ A_i^{n+1} + \dfrac{J_{50}}{z_5 F c_{\text{solid}}} \exp\left(\dfrac{\alpha_{\text{H}^+} F}{RT} \eta_i^n\right), & \exists \mathbf{x} \in \mathcal{F}_i \,:\, \varphi(\mathbf{x}_i, t^n) \neq \varphi(\mathbf{x}, t^n) \\ 0, & \varphi(\mathbf{x}_i, t^n) = 1 \wedge \forall \mathbf{x} \in \mathcal{F}_i \,:\, \varphi(\mathbf{x}, t^n) = 1 \end{cases}, \tag{3.100}$$

$$A_i^{n+1} = k_{1f} C_{1,i}^{n} - k_{1b} C_{2,i}^{n} C_{5,i}^{n+1} + k_{2f} - k_{2b} C_{5,i}^{n+1} C_{6,i}^{n},$$

where $k_{2f}$ and $k_{2b}$ represent the forward and backward reaction rates of (3.96), $J_{50}$ is the proportionality factor at zero overpotential, $C_{\text{solid}}$ denotes the initial metal solid concentration, $\alpha_{\text{H}^+}$ is the charge coefficient of the hydrogen ion, and $\eta_i^n$ is the overpotential at material point $\mathbf{x}_i$ and time $t^n$. The reaction term for the hydroxide ion concentration $C_6$ is given by

$$R_{6,i}^{n+1} = \begin{cases} B_i^{n+1}, & \varphi(\mathbf{x}_i, t^n) = 0 \wedge \forall \mathbf{x} \in \mathcal{F}_i \,:\, \varphi(\mathbf{x}, t^n) = 0 \\ B_i^{n+1} + \dfrac{J_{60}}{z_6 F c_{\text{solid}}} \exp\left(\dfrac{\alpha_{\text{OH}^-} F}{RT} \eta_i^n\right), & \exists \mathbf{x} \in \mathcal{F}_i \,:\, \varphi(\mathbf{x}_i, t^n) \neq \varphi(\mathbf{x}, t^n) \\ 0, & \varphi(\mathbf{x}_i, t^n) = 1 \wedge \forall \mathbf{x} \in \mathcal{F}_i \,:\, \varphi(\mathbf{x}, t^n) = 1 \end{cases}, \tag{3.101}$$

$$B_i^{n+1} = k_{2f} - k_{2b} C_{5,i}^{n} C_{6,i}^{n+1},$$

where $J_{60}$ is the proportionality factor at zero overpotential, and $\alpha_{\text{OH}^-}$ is the charge coefficient of the hydroxide ion. The electric overpotential $\eta_i^n$ at material point $\mathbf{x}_i$ and time $t^n$ is calculated as

$$\eta_i^n = \phi_{\text{applied}} - \phi_0 - \phi_{c,i}^n - \phi_i, \tag{3.102}$$

where $\phi_{\text{applied}}$ is the applied potential (relative to the Standard Hydrogen Electrode (SHE)) in the metallic Mg phase, $\phi_0$ is the reference potential, and $\phi_{c,i}^n$ is the concentration overpotential at point $\mathbf{x}_i$ and time $t^n$ of the solid metal phase, expressed as

$$\phi_{C,i}^n = \frac{RT}{z_1 F} \ln\left(\frac{C_{1,i}^n}{C_{\text{sat}}}\right), \tag{3.103}$$

where $C_{\text{sat}}$ denotes the equilibrium saturation concentration in the liquid electrolyte phase, specifically 1 M NaCl solution. The electrostatic potential, $\phi_i$, at point $\mathbf{x}_i$, is determined using the nonlocal Poisson equation in (2.64) at time $t^n$.

Table 3.5: Initial and Boundary Condition for 3D Bone Implant Screw Degradation. Reproduced from [58].

| Species | Initial Value in Solid | Initial Value in Liquid | Boundary Condition |
|---|---|---|---|
| $C_1$ | 1 | 0 | 0 |
| $C_2$ | 0 | $10^{-9}$ | 0 |
| $C_3$ | 0 | $1/143.1$ | $1/143.1$ |
| $C_4$ | 0 | $1/143.1$ | $1/143.1$ |
| $C_5$ | 0 | $10^{-7}/143.1$ | $10^{-7}/143.1$ |
| $C_6$ | 0 | $10^{-7}/143.1$ | $10^{-7}/143.1$ |
| $\phi$ | 0 | 0 | 0 |

The numerical simulation is executed using a custom C++ code with OpenMP for shared-memory parallelism on the High-Performance Computing (HPC) cluster node at the Helmholtz Zentrum Hereon, equipped with two 24-core 2.1 GHz Intel Xeon Scalable Platinum 8160 processors. A spatial hashing algorithm is utilized to define neighborhood point sets in the nonlocal corrosion model [81]. Simulations, each with a time step size of $\Delta t = 10.800\,\text{s}$ (3 hours), are reported for two configurations: one using 48 parallel threads and the other 12 threads (or cores) to compare the scenarios of running on an HPC node versus mimicking the computational performance of a regular desktop computer (*cf.* [100]). These configurations are analyzed across three spatial discretizations: *uniform, coarse*, with a total of 903, 939 nodes; *adaptive, multi-grid*, with 1, 736, 901 nodes; and *uniform, fine*, totaling 7, 236, 427 nodes. In the case of the adaptive, multi-grid approach, as shown in Fig. 3.25, the domain is partitioned into $\Omega^+$ and $\Omega^-$, with 834, 496 and 902, 405 nodes, and a spatial resolution of $\Delta x^+ = 100\,\mu\text{m}$ and $\Delta x^- = 50\,\mu\text{m}$ respectively. Due to the high computational demands, the uniform, fine grid simulation results cover seven days, while the uniform, coarse and adaptive, multi-grid simulations span 26 days of simulated immersion.

The results indicate that grid resolution can cause minor variations in the relative volume loss of the bone implant screw. Fig. 3.26 shows the relative volume loss per simulated day, demonstrating the similarity in results across the approaches, while noticeable differences exist between the uniform coarse grid and both the fine and multi-grid approaches. Validation against experimental data is beyond this discussion. Further comparisons between the different approaches of corrosion-induced damage and the reduction of Mg-ion concentration in the implant screw are detailed in Fig. 3.27, showing metallic degradation after one week of simulated immersion. Additionally, the simulation results for the hydroxide layer formation ($C_2$) and the distribution of electrostatic potential ($\phi$) are depicted in Fig. 3.28 and Fig. 3.29. Since the sodium and chloride components ($C_3$ and $C_4$) are non-reactive, their distribution in the liquid electrolyte solution is not displayed. From the simulation results, it can be observed that the numerical outcomes of the three approaches are similar in providing the spatial distribution of ionic components and electrostatic potential, with the adaptive, multi-grid refinement around the bone implant screw yielding macroscopic volume loss results closer to the uniform, fine reference solution at a reduced number of nodes. Noticeable differences in simulation duration are observed between the three approaches. These differences are summarized in Tab. 3.6, which includes the total simulation times for the

seven-day uniform, fine grid and the 26-day uniform, coarse and adaptive, multi-grid simulations. It is evident that the uniform coarse approach is the most computationally efficient, while the uniform fine approach is the most resource-intensive. In the first seven days of simulated immersion, the uniform fine simulation is about 35% slower than the uniform coarse one. The multi-grid approach, using two parallelization configurations, takes 4% to 5% more CPU time but maintains the accuracy of the uniform fine approach, achieving efficiency improvement with minimal overhead. The 48-core configuration significantly reduces run times compared to the 12-core, demonstrating the effectiveness of parallelization.

Table 3.6: Summary of the 3D implant screw bio-corrosion simulation run times and node numbers for different grid configurations. Data available in [33].

| | **Uniform, Coarse** | **Adaptive, Multi-grid** | | **Uniform, Fine** |
|---|---|---|---|---|
| | 48 cores | 12 cores | 48 cores | 48 cores |
| No. of active nodes | 903,939 | 1,736,901 | | 7,236,427 |
| Run time (7 days) | 14588.37s | 68178.55s | 59764.56s | 507623.1s |
| Run time (26 days) | 49496s | 251142.38s | 230965.4s | - |

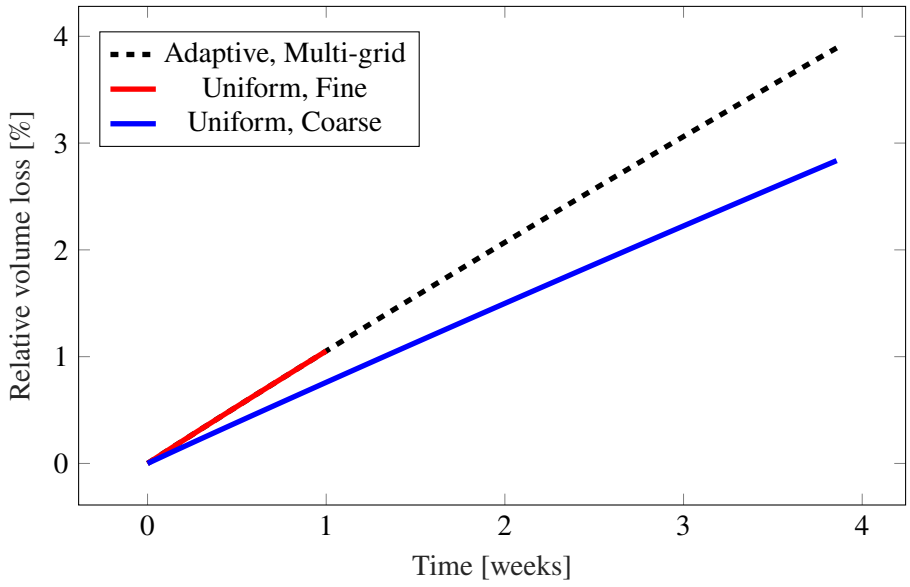


Figure 3.26: Relative volume loss for the three different grid configurations in the 3D implant screw bio-corrosion simulation. Reproduced and adjusted from [33].

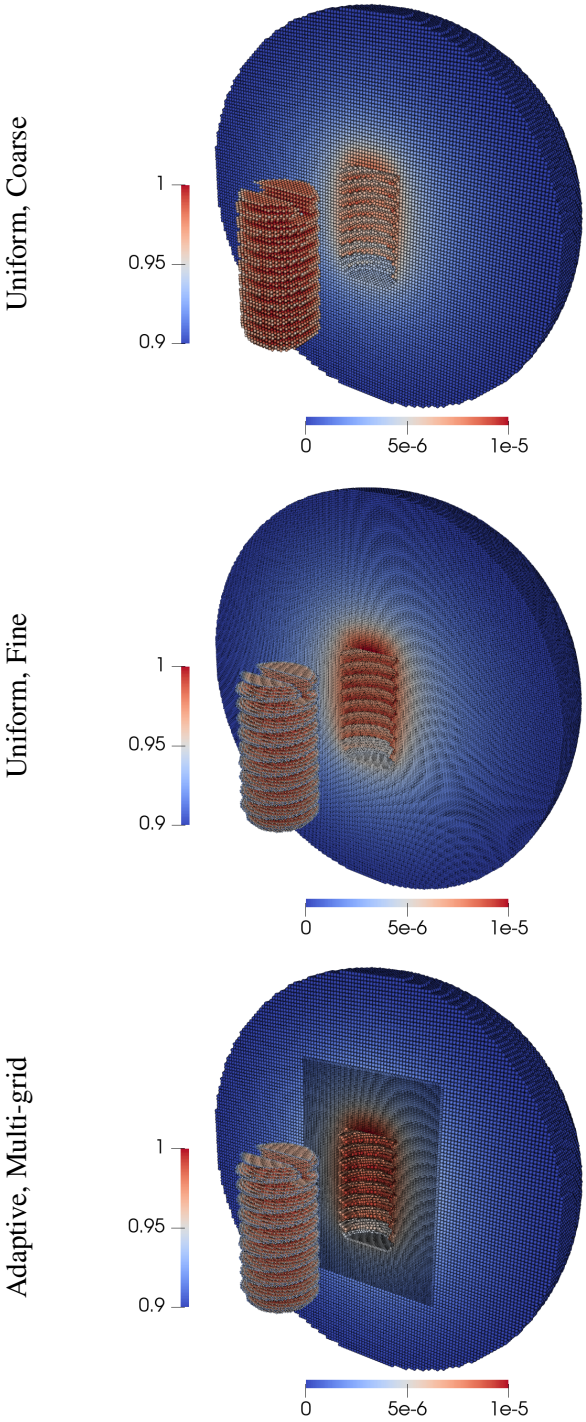


Figure 3.27: Normalized Mg ion concentration distribution, relative to $C_{\text{solid}}$, after one week of simulated corrosion for the three different grid configurations. Based on the findings presented in [33].

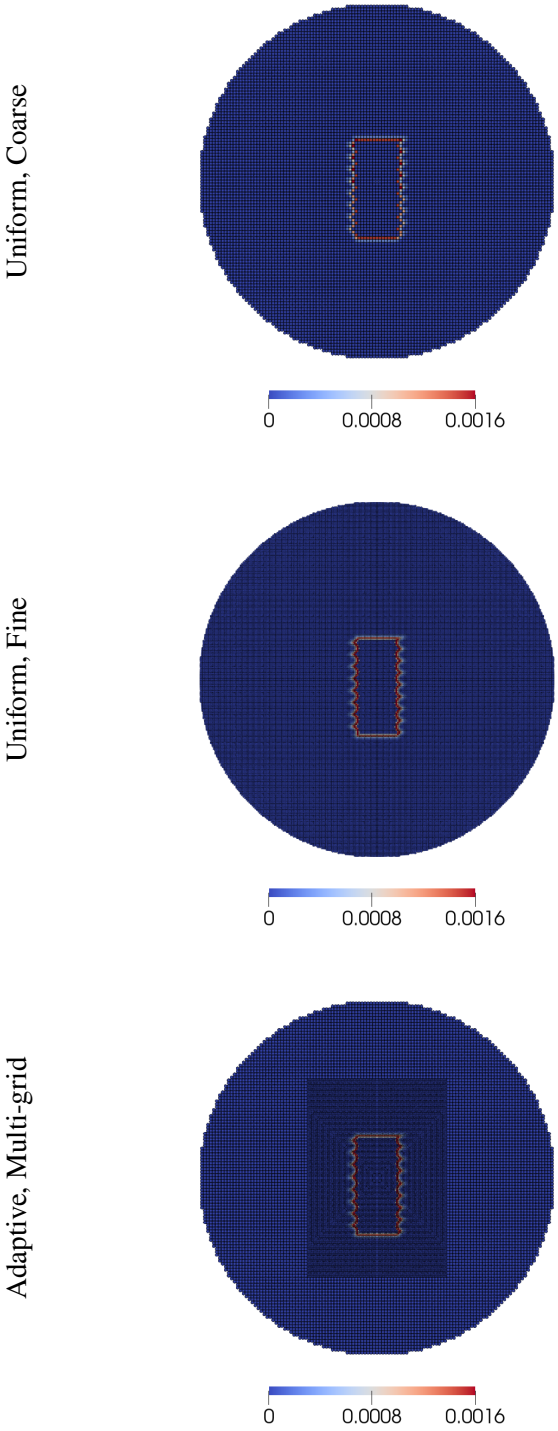


Figure 3.28: Normalized hydroxide ion concentration distribution, relative to $C_{\text{solid}}$, around the implant geometry after one week of simulated corrosion for the three different grid configurations. Based on the findings presented in [33].

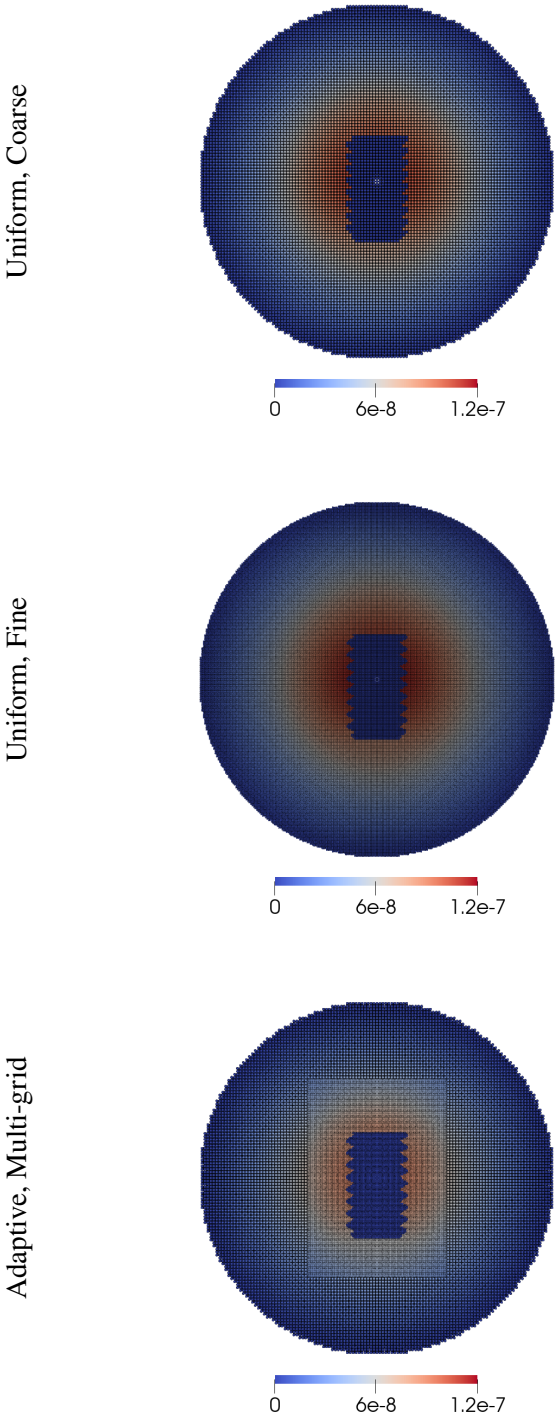


Figure 3.29: Electrostatic potential distribution in the liquid electrolyte domain after one week of simulated corrosion for the three different grid configurations. Note that the nonlocal Poisson equation is not computed within the solid Mg phase, where it is zero. The colorbar is expressed in volts (V). Based on the findings presented in [33].

Table 3.7: Model and System Parameters for 3D NNPP Corrosion Simulation of Bone Implant Screws in 1 M NaCl Solution. Data avialable in [58, 33].

| Symbol | Value | Unit | Description |
|---|---|---|---|
| $T$ | 298.15 | K | Temperature |
| $G$ | 8.3145 | $\mathrm{J\,mol^{-1}\,K^{-1}}$ | Gas constant |
| $F$ | 96485 | $\mathrm{C\,mol^{-1}}$ | Faraday's constant |
| $\delta$ | 200 | µm | Peridynamic horizon |
| $z_1$ | 2.19 | - | Charge number for $C_1$ |
| $z_2$ | 1.19 | - | Charge number for $C_2$ |
| $z_3$ | $-1$ | - | Charge number for $C_3$ |
| $z_4$ | 1 | - | Charge number for $C_4$ |
| $z_5$ | 1 | - | Charge number for $C_5$ |
| $z_6$ | $-1$ | - | Charge number for $C_6$ |
| $C_{\mathrm{solid}}$ | 143.1 | $\mathrm{mol\,L^{-1}}$ | Concentration of intact material |
| $C_{\mathrm{sat}}$ | 5.1 | $\mathrm{mol\,L^{-1}}$ | Saturation concentration |
| $D_{1,\mathrm{liq}}$ | $9.75 \times 10^{-10}$ | $\mathrm{m^2/s}$ | Diffusivity of $C_1$ for liquid-liquid bonds |
| $D_{1,\mathrm{int}}$ | $2.125 \times 10^{-19}$ | $\mathrm{m^2/s}$ | Diffusivity of $C_1$ for interface bonds |
| $D_{2,\mathrm{liq}}$ | $4.25 \times 10^{-10}$ | $\mathrm{m^2/s}$ | Diffusivity of $C_2$ for liquid-liquid bonds |
| $D_{2,\mathrm{int}}$ | $8.5 \times 10^{-13}$ | $\mathrm{m^2/s}$ | Diffusivity of $C_2$ for interface bonds |
| $D_{3,\mathrm{liq}}$ | $8.5 \times 10^{-11}$ | $\mathrm{m^2/s}$ | Diffusivity of $C_3$ for liquid-liquid bonds |
| $D_{3,\mathrm{int}}$ | $8.5 \times 10^{-12}$ | $\mathrm{m^2/s}$ | Diffusivity of $C_3$ for interface bonds |
| $D_{4,\mathrm{liq}}$ | $8.5 \times 10^{-11}$ | $\mathrm{m^2/s}$ | Diffusivity of $C_4$ for liquid-liquid bonds |
| $D_{4,\mathrm{int}}$ | $8.5 \times 10^{-12}$ | $\mathrm{m^2/s}$ | Diffusivity of $C_4$ for interface bonds |
| $D_{5,\mathrm{liq}}$ | $4.25 \times 10^{-10}$ | $\mathrm{m^2/s}$ | Diffusivity of $C_5$ for liquid-liquid bonds |
| $D_{5,\mathrm{int}}$ | $8.5 \times 10^{-12}$ | $\mathrm{m^2/s}$ | Diffusivity of $C_5$ for interface bonds |
| $D_{6,\mathrm{liq}}$ | $1.7 \times 10^{-10}$ | $\mathrm{m^2/s}$ | Diffusivity of $C_6$ for liquid-liquid bonds |
| $D_{6,\mathrm{int}}$ | $8.5 \times 10^{-12}$ | $\mathrm{m^2/s}$ | Diffusivity of $C_6$ for interface bonds |
| $\phi_{\mathrm{applied}}$ | $-300$ | mV | Applied potential on SHE |
| $\phi_0$ | $-477$ | mV | Standard electrode potential on SHE |
| $\epsilon$ | $6.1 \times 10^6$ | $\mathrm{S\,m^{-1}}$ | Electrical conductivity in liquid solution |
| $k_{f,1}$ | $5 \times 10^{-9}$ | $\mathrm{s^{-1}}$ | Forward reaction rate in (3.95) |
| $k_{b,1}$ | 0.0158 | $\mathrm{mol^{-1}\,s^{-1}}$ | Backward reaction rate in (3.95) |
| $k_{f,2}$ | $2.5 \times 10^{-8}$ | $\mathrm{mol\,s^{-1}}$ | Forward reaction rate in (3.96) |
| $k_{b,2}$ | $2.5 \times 10^{-16}$ | $\mathrm{mol^{-1}\,s^{-1}}$ | Backward reaction rate in (3.96) |
| $J_{50}$ | $-2 \times 10^{-3}$ | $\mathrm{A\,m\,mol^{-1}}$ | Proportionality factor in (3.100) |
| $J_{60}$ | $8 \times 10^{-10}$ | $\mathrm{A/m^2}$ | Proportionality factor in (3.101) |

## 3.5 The Multi-Adaptive Scheme

In this section, we explore the integration of the hybrid configuration discussed in Section 3.3 and published in [122] with the multi-grid method from Section 3.4 and published in [121, 60] to maximize the numerical performance of peridynamic models. The hybrid configuration combines the advantages of both fixed and adaptive grid strategies, allowing for a more efficient representation of the computational domain. On the other hand, the multi-grid method enables the use of different grid resolutions in different regions of interest, reducing unnecessary computational overhead. By integrating these two approaches, we aim to achieve a highly optimized numerical framework for peridynamic simulations.

The resulting framework, referred to as the *multi-adaptive* scheme, is outlined in the following sections. One of the key aspects of this scheme is the implementation of a switching strategy that dynamically adapts to the evolution of critical regions. This strategy, as discussed in Section 3.3, automatically identifies which parts of the domain require a higher grid resolution in the standard discretization scheme. By selectively refining the grid resolution in these critical regions, we can accurately capture the desired phenomena while minimizing computational costs.

#### The Switching Strategy for Multi-Adaptive Peridynamic Simulations

An adaptive algorithm is implemented to optimize the utilization of computational resources by dynamically adjusting the configuration of active regions in the solution domains $\Omega^+$ and $\Omega^-$. The goal is to track the evolution of critical regions, such as the changing morphology of damage, by switching between the meshfree WLS collocation scheme with a coarse grid and the standard scheme with a fine grid. This adaptive strategy ensures that coalescence and propagation of discontinuities occur within the active regions of $\Omega^-$. By deactivating nodes in $\Omega^+$ and activating corresponding nodes in $\Omega^-$, and employing appropriate fictitious nodes in both domains, the algorithm optimizes computational efficiency while accurately capturing the system's behavior. The switching process is depicted in Fig. 3.30.

In bond-based PD elasticity, determining the critical zones that require a configuration switch relies on a criterion based on the stretch status of each bond vector. The same criterion defined in Section 3.3, as derived and used by [126, 122, 93], is utilized in this configuration. The bond stretch, as defined in (2.28), is evaluated between two neighboring nodes $\mathbf{x}_i$ and $\mathbf{x}_j$ in the initial configuration of the system at time $t^n$. A linking bond is considered critical if its stretch value falls within the specified range. The critical bond stretch margin is determined by a switching parameter $\sigma \in (0, 1)$, which was chosen to be 0.95 based on the descriptions of Section 3.3. When a bond connecting nodes $\mathbf{x}_i$ and $\mathbf{x}_j$ is classified as critical, the neighborhoods of these nodes are designated as critical zones. As a result, the discretization scheme used for these regions is switched to the standard scheme, and the grid spacing employed to describe them is adjusted to a finer grid spacing.

The switching strategy depicted in Fig. 3.30 outlines the process of updating the configuration of $\Omega^-$ and $\Omega^+$ near a critical region at time instant $t^n$. When a critical linking bond between nodes $\mathbf{x}_1$ and $\mathbf{x}_2$ in the coarse grid is identified by the adaptive algorithm, an update is performed before advancing to the next time step $t^{n+1}$. The update involves deactivating nodes within the switching area in $\Omega^+$, which encompasses the combined neighborhood of nodes $\mathbf{x}_1$ and $\mathbf{x}_2$, and activating specific nodes within the same area in $\Omega^-$. This switching process ensures that the configuration accurately represents the critical region and facilitates the subsequent time marching calculations.

The adaptive algorithm for activating and deactivating nodes, along with the identification of fictitious nodes, is employed to update the configuration of $\Omega^-$ and $\Omega^+$ in the switching strategy.

The updated configuration at the next time step is depicted in Fig. 3.30. While the adaptive algorithm adds computational overhead, it proves to be particularly beneficial in problems involving fast and uncertain discontinuity evolution, such as dynamic crack propagation. Therefore, in the numerical examples presented in the following sections, the switching strategy is implemented only in the dynamic brittle fracture case study, while the corrosion problem maintains predefined and unchanged $\Omega^-$ and $\Omega^+$ solution domains throughout the simulation.

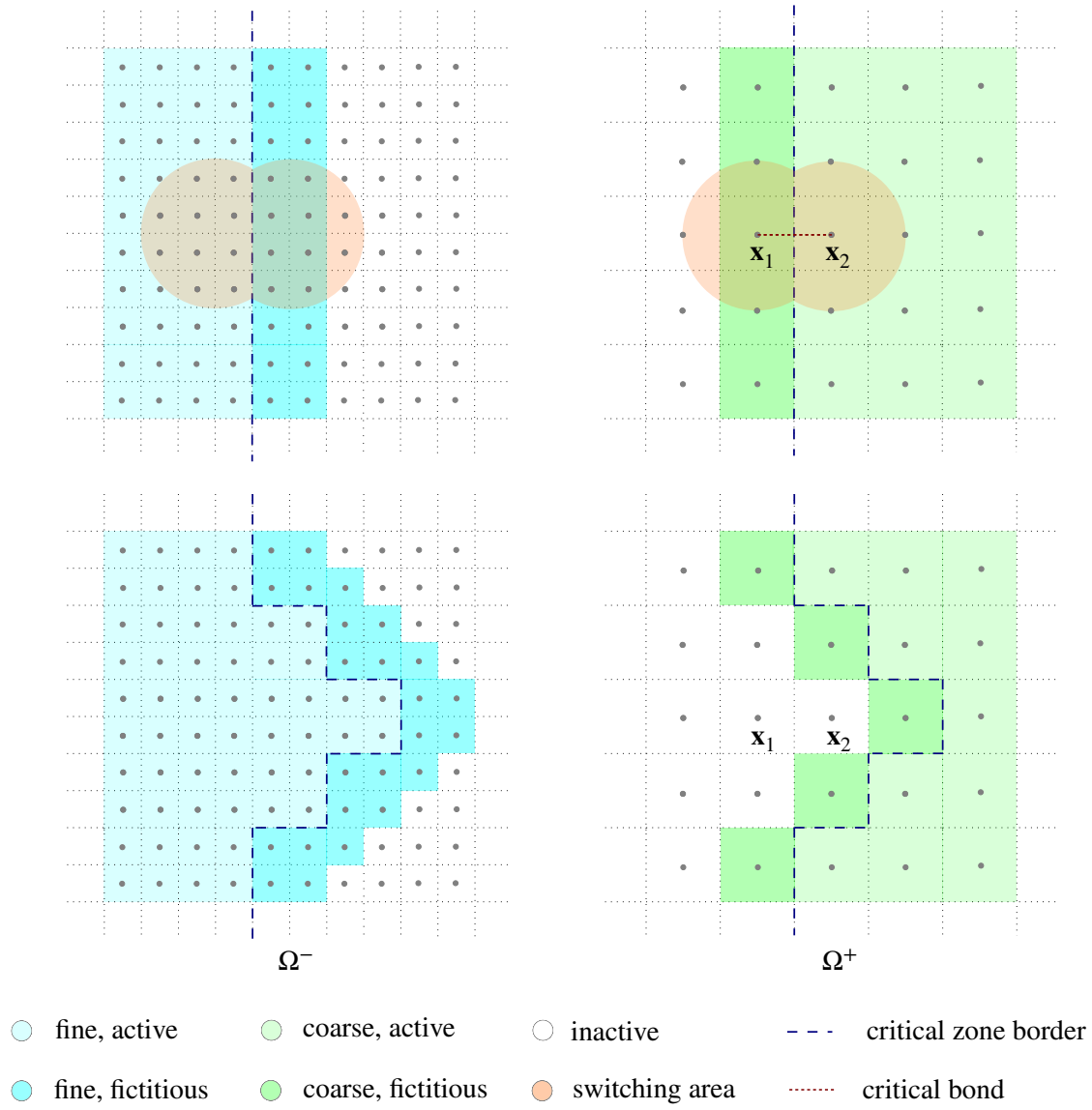


Figure 3.30: Illustration of the switching strategy for a critical region, depicting the configurations of $\Omega^-$ and $\Omega^+$ at two different time instants. The top illustration represents the configuration at time instant $t^n$, while the bottom illustration shows the configuration at time instant $t^{n+1}$. Reproduced from [100].

### 3.5.1 2D Kalthoff-Winkler Experiment on Multi-Adaptive Configuration

In this example, we revisit the well-known Kalthoff-Winkler experiment [69], which has been extensively studied for evaluating and validating computational models in the context of dynamic fracture modeling of brittle materials, particularly in the peridynamic framework [121, 149, 31]. In Section 3.3, we discussed the improved computational performance achieved by using a hybrid configuration that combines the standard discretization scheme for critical fracture regions with the meshfree WLS scheme for smooth field variable regions. Here, we investigate further improvements in computational performance by incorporating the multi-grid approach for the smooth field variable regions within the multi-adaptive configuration.

To reiterate the problem setup, Fig. 3.31 (left) depicts the schematic geometry of the problem. It consists of a rectangular steel plate with two parallel pre-cracks that undergo an impact load from a rigid projectile striking the boundary region between the pre-cracks. The experimental setup and model parameters align with those detailed in Section 3.3.1. The impact load is simulated by imposing an initial velocity of $v_0 = 16.5 \times 10^3\,\mathrm{mm\,s^{-1}}$ on the nodes located along the left side of the plate between the two pre-cracks, with the velocity directed horizontally and maintained constant throughout the simulation.

The problem is investigated using the four approaches introduced in this section, with $\Delta x^+ = 2\Delta x^- = 0.333\,\mathrm{mm}$ and $\delta = 4\,\mathrm{mm}$ ($m^+ = \delta/\Delta x^+ = 12$, $m^- = \delta/\Delta x^- = 24$). The time integration is performed using the velocity-Verlet algorithm described in Section 3.1.1 (*cf.* (3.5)-(3.6)). The simulation is carried out for a total duration of 87.5 µs with a time step of $\Delta t = 2 \times 10^{-3}\,\mu\mathrm{s}$. In the multi-adaptive scheme, the meshfree WLS collocation scheme is used for the portion of the domain discretized with monomial basis functions up to second-order, resulting in $n_p = 6$ monomials and $n_c = 49$ collocation nodes. Fig. 3.32 shows the peridynamic neighborhoods obtained using different discretization schemes, highlighting the advantage of the proposed scheme over the standard one in terms of reduced number of nodes. The configuration of the *adaptive, hybrid* and *adaptive, standard* approaches at the start of the simulation is illustrated in Fig. 3.31 (right), with the black color representing the $\Omega^-$ solution domain encompassing the pre-cracks and boundaries. In the *adaptive, hybrid* approach, $\Omega^-$ is discretized using the standard scheme while $\Omega^+$ employs the collocation scheme. In the *adaptive, standard* approach, both solution domains are discretized using the standard scheme. The critical bond stretch margin $\sigma$ in the adaptive algorithm is set to 0.95.

Fig. 3.33 showcases crack patterns and evolving configurations of the $\Omega^-$ solution domain at different time instants for the four models studied, including the two adaptive approaches. The damage contour plots exhibit similarities among all models except for the *uniform, coarse* approach, which displays slightly different crack propagation angles and speeds along with a secondary fracture on the opposite side of the impacted region. In contrast, the other models do not exhibit this secondary fracture. The *adaptive, hybrid* approach demonstrates excellent agreement with the *uniform, fine* and *adaptive, standard* approaches, confirming the effectiveness of the proposed multi-adaptive scheme for studying dynamic crack propagation. Further validation is provided in Fig. 3.34, which displays contour plots of the velocity field along the vertical direction. The *adaptive, hybrid* scheme closely aligns with the *uniform, fine* and *adaptive, standard* approaches, while the discrepancies observed in the *uniform, coarse* model are also evident in the velocity field.

The computational efficiency of the *adaptive, hybrid* model is assessed by comparing it with the *uniform, fine* and *adaptive, standard* approaches. Tab. 3.8 provides information on the number of active nodes in each solution domain, the computational run times of the models, and the speed ups achieved over the *uniform, fine* approach. Results show that when running the simulations on

12 cores, both adaptive approaches are 1.86 times faster than the *uniform, fine* approach. On the other hand, with 48 cores, the *adaptive, hybrid* scheme demonstrates the highest computational efficiency, being 1.19 times faster than the *uniform, fine* model and almost 1.09 times faster than the *adaptive, standard* scheme. The multi-adaptive scheme accurately reproduces the reference solution obtained from the *uniform, fine* approach, while significantly reducing the computational cost. The findings validate the effectiveness of the proposed scheme in achieving computational efficiency in dynamic crack propagation simulations.

To validate the effectiveness of the multi-adaptive approach, Fig. 3.35 presents the energy variation $\Pi$ of the system throughout the simulation for the four models. The energy content is computed in a circular region at the tip of the upper pre-crack. The energy plot obtained by the *adaptive, hybrid* model closely matches those of the *uniform, fine* and *adaptive, standard* approaches, indicating that the proposed scheme accurately captures crack nucleation and propagation speed. Moreover, as demonstrated in Tab. 3.8, the multi-adaptive approach outperforms the other models in terms of computational efficiency.

Table 3.8: Computational run times for the Kalthoff-Winkler experiment using grid spacings of $\Delta x^- = 0.167\,\text{mm}$ and $\Delta x^+ = 0.333\,\text{mm}$. Data available in [100].

| | number of active nodes | | | | |
|---|---|---|---|---|---|
| | **Uniform, Fine** | **Adaptive, Multi-grid** | | **Adaptive, Hybrid** | |
| | | $\Omega^+$ | $\Omega^-$ | $\Omega^+$ | $\Omega^-$ |
| $t = 0\mu\text{s}$ | 721801 | 150625 | 117000 | 150625 | 117000 |
| $t = 87.5\mu\text{s}$ | | 126859 | 212568 | 120681 | 237447 |
| Run time (12 cores) | 3796.6s | 2042.9s | | 2037.1s | |
| Run time (48 cores) | 1190.4s | 1096.0s | | 1003.8s | |
| Speed up (12 cores) | – | 1.86 | | 1.86 | |
| Speed up (48 cores) | – | 1.09 | | 1.19 | |

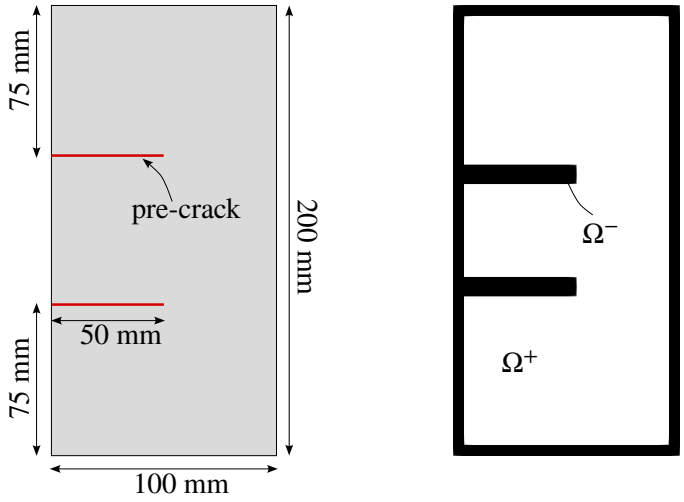


Figure 3.31: Illustration of the problem domain for the Kalthoff-Winkler experiment (left) and the initial configuration in the multi-adaptive configuration (right). Reproduced from [100].

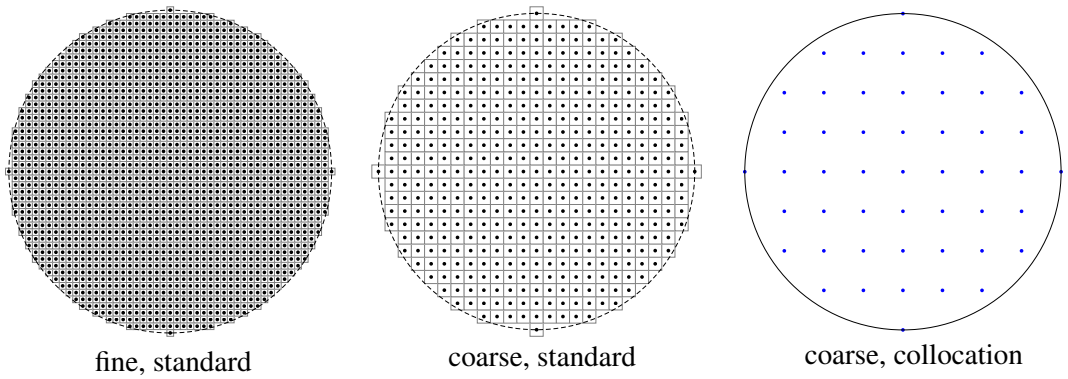


Figure 3.32: Illustration of the peridynamic neighborhood using different discretization schemes in Kalthoff-Winkler experiment on the multi-adaptive configuration. The standard scheme utilizes 1793 and 441 nodes for the peridynamic neighborhoods within the fine and coarse grids, respectively. In contrast, the hybrid discretization scheme employs only 49 collocation nodes for the peridynamic neighborhood within the coarse grid. Reproduced from [100].

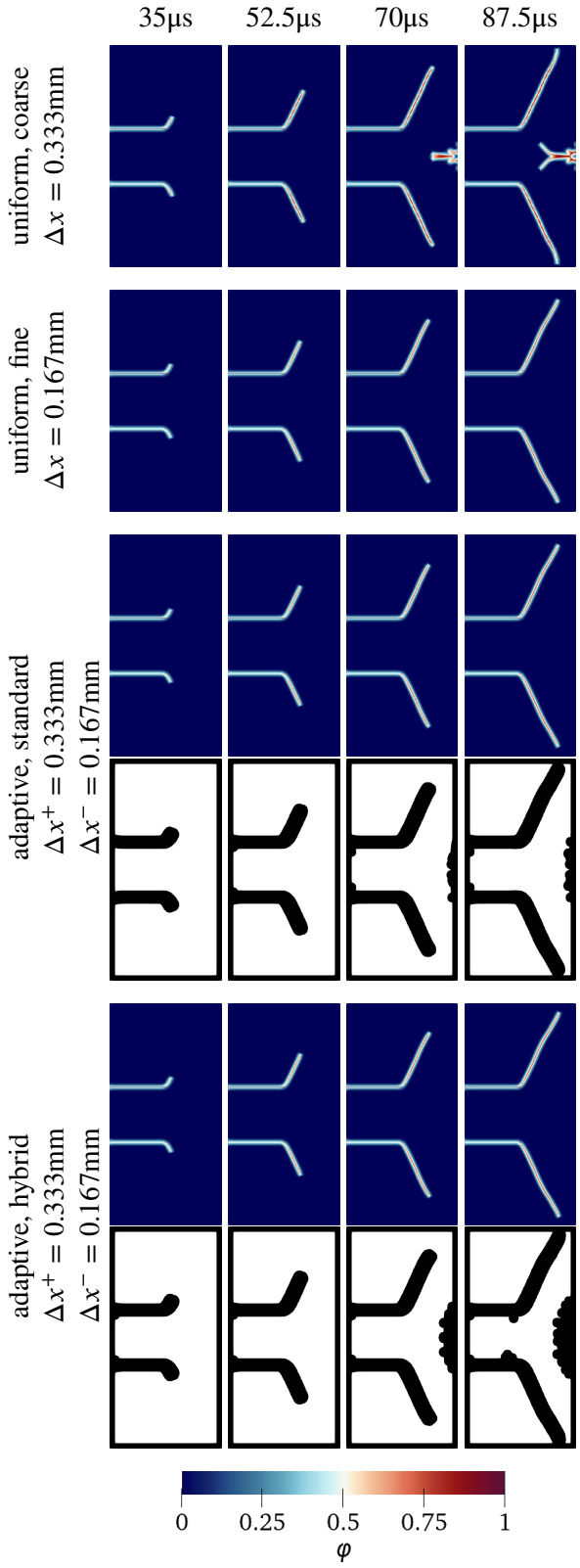


Figure 3.33: The crack patterns obtained by different models in the Kalthoff-Winkler experiment. Additionally, the evolution of the $\Omega^-$ solution domain is shown for the *adaptive standard* and *adaptive hybrid* approaches. Reproduced from [100].

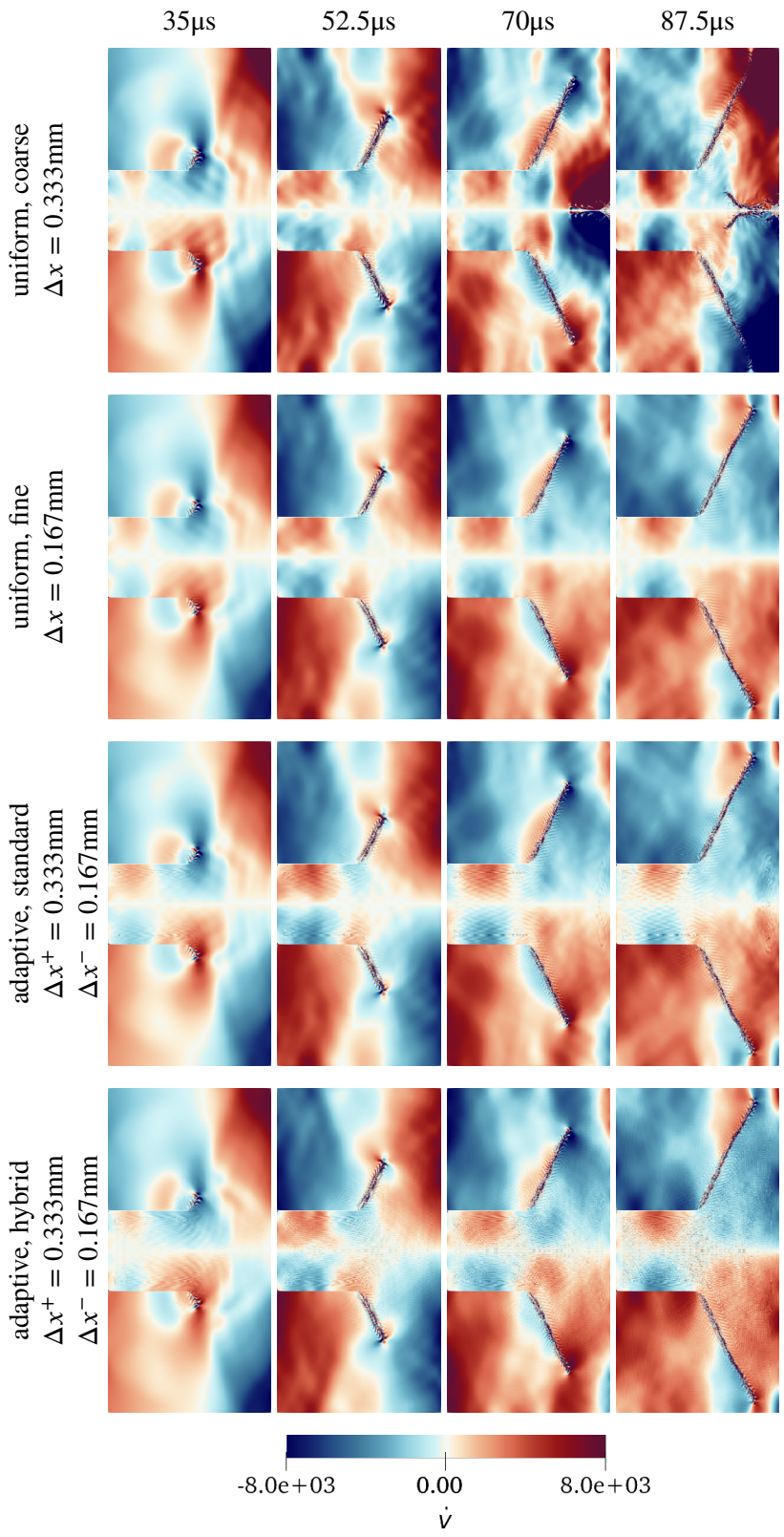


Figure 3.34: Velocity contour plots along the vertical direction at four different time instants for the four approaches: (*uniform, coarse*), (*uniform, fine*), (*adaptive, standard*), and (*adaptive, hybrid*). The color scale represents the velocity values in mm $s^{-1}$. Reproduced from [100].

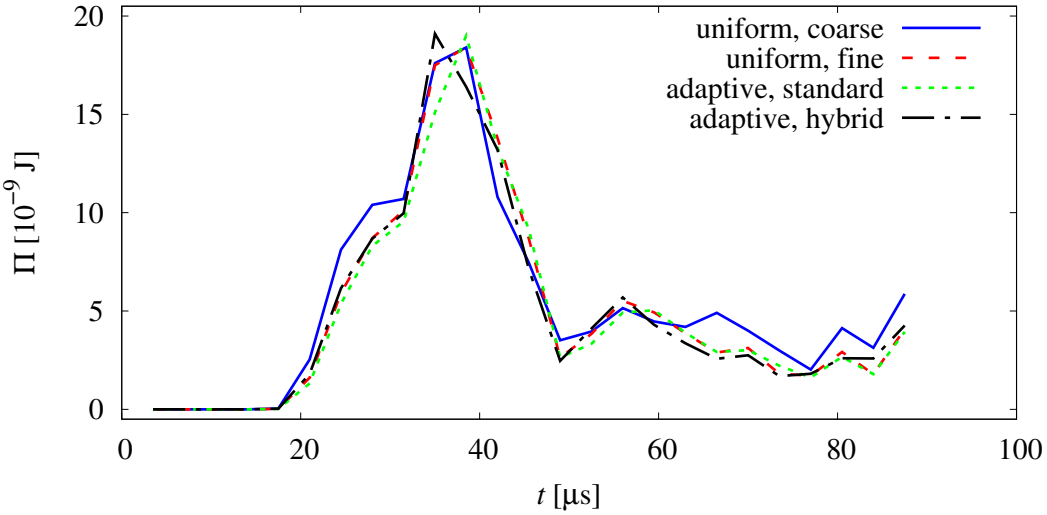


Figure 3.35: The energy content of the system is compared among the four approaches: (*uniform, coarse*), (*uniform, fine*), (*adaptive, standard*), and (*adaptive, hybrid*) in the Kalthoff-Winkler experiment. The comparison is based on the energy computed within a circular region centered at the tip of the upper pre-crack with a radius of 10 mm. Reproduced from [100].

### 3.5.2 3D Peridynamic Corrosion on Multi-Adaptive Configuration

In this example, we apply the multi-adaptive scheme to simulate the electrochemical dissolution of the 3D headless bone implant screw, as depicted in Fig. 3.25 of Section 3.4.2. The computational domain description and the partitioning of $\Omega^+$ and $\Omega^-$ remain the same as in the previous example. However, to demonstrate the efficacy of the multi-adaptive scheme, we use the standard bi-material peridynamic corrosion model with explicit time discretization instead of the full NNPP system. This choice is made because we are not interested in the electromigration of other ionic components and aim to showcase the performance of the multi-adaptive scheme for diffusion-type problems.

The corrosion kinetics are specified by means of the two constant micro-diffusivity parameters in the peridynamic bi-material corrosion model, i.e., $\kappa_{\text{liq}}$ and $\kappa_{\text{int}}$, which correspond to the bonds connecting pairs of material points belonging to the liquid phase and to the interfacial bonds connecting material points in the solid phase with material points in the liquid phase, respectively. In the solid phase, no flux between pairs of material points is considered. The threshold concentration parameter $C_{\text{sat}}$ is used to determine the concentration of the solid phase during the dissolution process. It plays a role in determining when the concentration reaches a level that indicates complete dissolution of the solid phase. Following the phase-changing mechanism, when the concentration at a material point in the solid phase drops below a certain threshold value, the phase of that material point transitions from solid to liquid.

The model parameters of the peridynamic corrosion model are chosen as follows: the micro-diffusivity for the liquid bulk medium is $\kappa_{\text{liq}} = 7.98 \times 10^{-5}\ \text{s}^{-1}\text{mm}^{-2}$, the interfacial micro-diffusivity for bonds between the solid metallic and the liquid electrolyte medium is $\kappa_{\text{int}} = 2.81 \times 10^{-6}\ \text{s}^{-1}\text{mm}^{-2}$, the saturation concentration of magnesium ions in the bulk solution is $C_{\text{sat}} = 6.26 \times 10^{-10}\ \text{mol/mm}^3$, and the exponent of the kernel function is $q = 1$. These parameter values are selected to produce a volume loss and corrosion rate within the observed ranges in experimental studies and numerical parameter calibrations (*cf.* (2.42)). The problem is investigated using the multi-adaptive scheme, specifically the (*uniform, fine*) and (*adaptive, hybrid*) models, with grid spacings of $\Delta x^+ = 0.075$ mm and $\Delta x^- = 0.0375$ mm, respectively. The horizon $\delta$ is set to 0.45 mm, resulting in a ratio of $m^+ = 6$ for the coarse portion of the domain and $m^- = 12$ for the fine portion. Zero Dirichlet-type boundary conditions are imposed on all nodes within a distance of $\delta$ from the surface of the sphere.

In this example, the multi-adaptive scheme, also referred to as (*adaptive, hybrid*), is utilized. However, unlike in previous cases, the adaptive algorithm is not triggered during the corrosion simulation. The configuration of the solution domains, $\Omega^-$ and $\Omega^+$, depicted in Fig. 3.25, is predefined and remains unchanged throughout the simulation. The $\Omega^-$ domain, discretized using the standard scheme, is designed to cover the region where the concentration field exhibits discontinuities, specifically the areas where diffusion occurs between nodes with different phase boundaries. The collocation scheme is applied to discretize the portion of the domain denoted as $\Omega^+$. In this scheme, the calculations are performed using monomial basis functions up to the second-order, as described in (3.23). In 3D, this choice corresponds to having 10 monomials and 123 collocation nodes. The peridynamic neighborhood in the multi-adaptive scheme, obtained using the meshfree WLS collocation approach, is shown in Fig. 3.36. A significant advantage of this approach over the (uniform, fine) scheme is evident, as the peridynamic neighborhoods within the fine grid consist of 7153 nodes, while in the multi-adaptive scheme, peridynamic neighborhoods within the coarse grid include only 123 collocation nodes. The time integration is performed using the explicit forward Euler algorithm, as described in Section 3.1.1. The simulation duration is 14 days with a time step $\Delta t$ of 90 seconds.

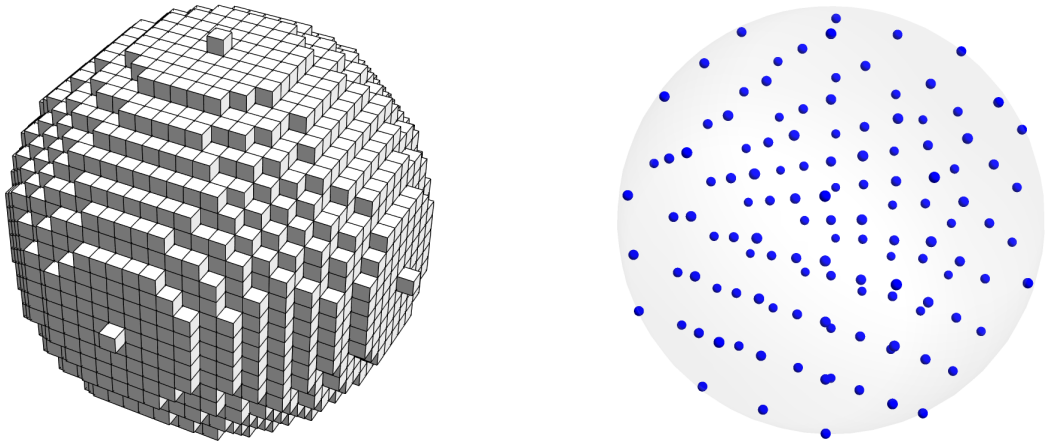

fine, standard coarse, collocation

Figure 3.36: The peridynamic neighborhood is depicted using the discretization schemes utilized in the 3D peridynamic corrosion example. In the standard scheme depicted on the left, the calculation involves 7153 nodes for the neighborhoods within the fine grid. On the right, in the multi-adaptive approach, the calculation is performed using only 123 collocation nodes for the neighborhoods within the coarse grid. Reproduced and adjusted from [100].

The concentration profiles of the solid metal and dissolved material within the liquid phase obtained from the peridynamic corrosion simulation of the Mg-10Gd implant screw immersed in a liquid electrolyte for 14 days are presented in Fig. 3.38. Results obtained from both the (*adaptive, hybrid*) scheme and the (*uniform, fine*) approach are depicted at two different time points. The results indicate a high level of agreement between the two models, with the corrosion patterns in the solid phase and the diffusion of dissolved material in the liquid phase closely matching each other. This confirms the effectiveness of the proposed multi-adaptive scheme in accurately modeling corrosion processes in geometrically complex, large-scale systems in 3D.

The relative volume loss of the solid phase over time is presented in Fig. 3.37 to further validate the multi-adaptive approach. Due to computational constraints, the results of the (*adaptive, hybrid*) scheme are compared to those of the (*uniform, fine*) approach for the first 2 days of corrosion. The multi-adaptive approach closely aligns with the relative volume loss of the reference solution during the computational period. However, the simulation of the (*adaptive, hybrid*) scheme is continued for the full 14-day corrosion period. The results indicate that over 40% of the solid phase dissolves after 14 days of simulated immersion.

The significant computational efficiency of the (*adaptive, hybrid*) scheme is evident from the comparison of run times and speedups with the (*uniform, fine*) approach. Tab. 3.9 provides detailed information on the number of active nodes, average run times per 100 time steps, and average speedups per 100 time steps for the two models. These results, obtained using parallelism on 48 cores, clearly indicate the superiority of the multi-adaptive scheme, as it achieves a remarkable speedup of 11.76 times compared to the (*uniform, fine*) approach. The substantial reduction in computational time, while maintaining a high level of accuracy, makes the multi-adaptive scheme an attractive choice for simulating corrosion processes in large-scale, geometrically complex problems in 3D. The results, combined with the validation of the solution presented in Fig. 3.38 and Fig. 3.37, underscore the effectiveness and practicality of the multi-adaptive approach in achieving efficient and accurate peridynamic corrosion simulations.

Table 3.9: The computational run times for the multi-adaptive implementation of peridynamic corrosion, with grid spacings set as $2\Delta x^- = \Delta x^+ = 0.075$ mm. Data available in [100].

| | **Uniform, Fine** | **Adaptive, Hybrid** | |
|---|---|---|---|
| | | $\Omega^+$ | $\Omega^-$ |
| No. of active nodes | 17155295 | 2032496 | 2816295 |
| Avg. run time per 100 time steps (48 cores) | 13406.3s | 1140.15s | |
| Avg. speed up per 100 time steps (48 cores; over uniform, fine) | – | 11.76 | |

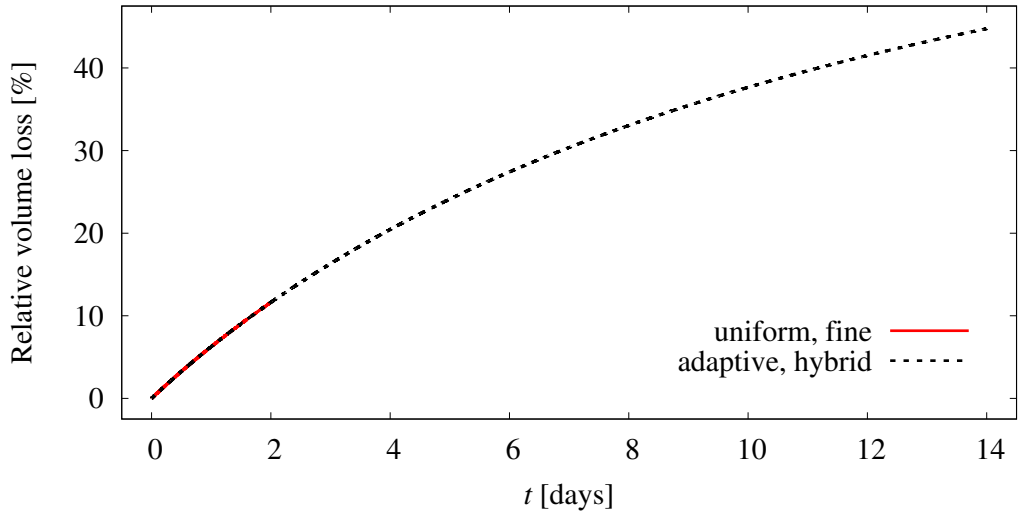


Figure 3.37: Illustration of the relative volume loss of the solid phase over time for the two approaches: (*uniform, fine*) and (*adaptive, hybrid*) in the multi-adaptive implementation of 3D peridynamic corrosion. Reproduced and adjusted from [100].

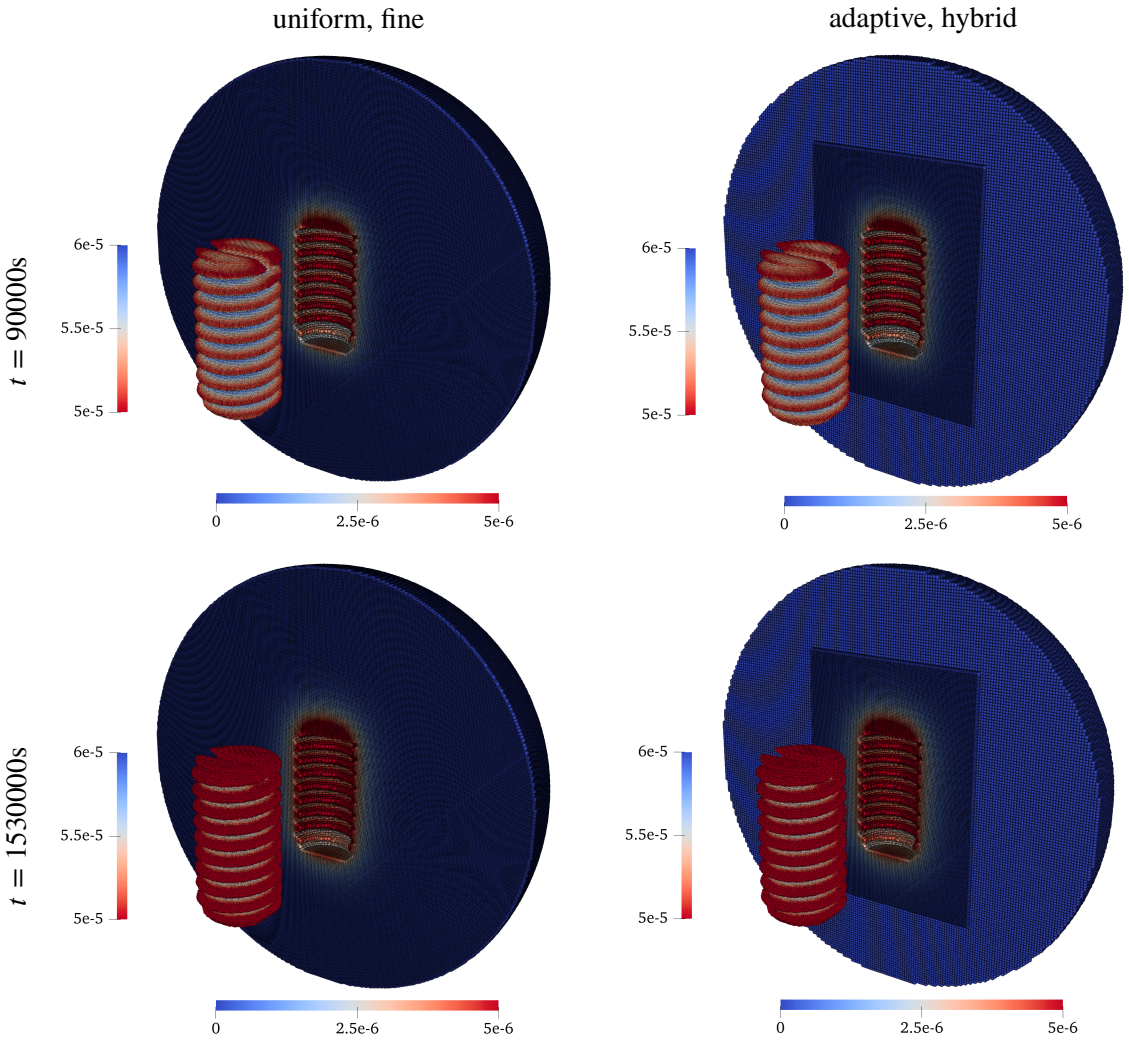


Figure 3.38: contour plots of the concentration field at two different time instants obtained by the two approaches, (*uniform, fine*) and (*adaptive, hybrid*), in the multi-adaptive implementation of the 3D peridynamic corrosion example. The concentration values are measured in [mol/mm$^3$]. The lighter color of the $\Omega^+$ solution domain in the (*adaptive, hybrid*) scheme compared to the same region in the (*uniform, fine*) solution is simply a visual effect resulting from the coarser grid spacing used to discretize that part of the domain. Reproduced and adjusted from [100]. Reproduced and adjusted from [100].

# Chapter 4

# Numerical Solution Strategies for Unbounded Domain Problems

In this chapter, we detail solution strategies for peridynamic models on unbounded domains, specifically for diffusion-type, scalar wave, and linear elasticity problems. In each case, the domain is truncated by a separating boundary (or boundary layer in nonlocal models), called the *absorbing boundary*, along which appropriate ABCs have to be imposed. Thus, the domain is separated into a near-field and far-field solution, where in the latter infinity or radiation conditions have to hold for the governing equation. The proposed ABCs in this chapter are constructed on the basis of semi-analytical solutions from EBFs which are collocated along the absorbing boundary layer. Next, an extrapolation step is applied in order to approximate the far-field solution at the next time step, thus establishing explicit Dirichlet-type ABCs formulated entirely in the time domain. We discuss the applicability and performance of the proposed ABCs for nonlocal peridynamic models as well as for CCM models solved via the FEM for diffusion and scalar wave models. The applicability towards classical linear elasticity solved via FEM is omitted here as this was already studied in the respective literature [95]. Various numerical examples in 2D and up to 3D problems in the case of diffusion-type problems are presented. The findings of this chapter have been published in various academic papers and thus the following chapter is mostly based on the discussions presented in peer-reviewed articles, particularly Section 4.1 is based on [123], Section 4.2 on [59], and Section 4.3 on [124].

## 4.1 Diffusion-Type Problems on Unbounded Domains

To derive the ABCs for diffusion-type problems, we start with the classical diffusion equation in a two-dimensional unbounded domain $\Omega_\infty \subset \mathbb{R}^2$, as depicted in Fig. 4.1 and alluded to in (2.44). The domain consists of an isotropic medium that surrounds various physical objects, including baffles and sources. The governing diffusion equation, based on the classical local theory, describes the behavior of the concentration field $C(\mathbf{x}, t)$ of the diffusing material at any point $\mathbf{x}$ in the unbounded domain and at time $t$. The equation is given by

$$\dot{C}(\mathbf{x}, t) = D\nabla^2 C(\mathbf{x}, t) + s(\mathbf{x}, t), \quad \mathbf{x} \in \Omega_\infty, \quad t > 0, \tag{4.1}$$

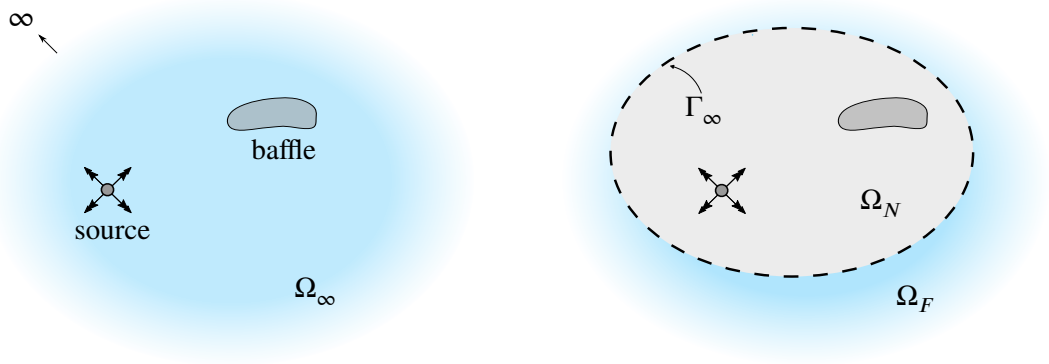


Figure 4.1: (Left) a generic unbounded-domain problem, (right) truncation of the exterior domain and specification of the computational domain. Reproduced from [123].

where $D > 0$ represents the diffusion coefficient, $s(\mathbf{x}, t)$ is a given source function, and $\nabla^2$ is the Laplacian operator. The initial condition for the concentration field is defined as

$$C(\mathbf{x}, 0) = C_0(\mathbf{x}), \tag{4.2}$$

where $C_0$ is a given function. Considering the unbounded nature of the medium, we impose the condition

$$\lim_{\|\mathbf{x}\| \to \infty} C(\mathbf{x}, t) = 0, \quad t > 0, \tag{4.3}$$

indicating that the concentration approaches zero at infinity.

Solving the governing equation (4.1) poses a challenge due to the unbounded nature of the medium. One approach to applying numerical methods, such as FEM, is to discretize a large portion of the infinite domain $\Omega_\infty$. However, this approach is computationally expensive and inefficient. To address this issue, the domain can be bounded, and computations can be limited to the region of interest. This is achieved by introducing an artificial boundary $\Gamma_\infty$, known as an *absorbing boundary*, as depicted in Fig. 4.1. The domain $\Omega_\infty$ is divided into a bounded domain $\Omega_N$ (*near-field* or computational domain) and an exterior domain $\Omega_F = \Omega_\infty / \Omega_N$ (*far-field*). The region $\Omega_N$ includes all the physical objects, and $\Gamma_\infty$ is positioned such that the support of the sources in (4.1) is contained within $\Omega_N$. Consequently, the homogeneous counterpart of (4.1) for the exterior domain is given by

$$\dot{C}(\mathbf{x}, t) = D\nabla^2 C(\mathbf{x}, t), \quad \mathbf{x} \in \Omega_F, \quad t > 0, \tag{4.4}$$

where the medium is initially at rest. Similarly, for the far-field in the peridynamic diffusion problem, the governing equation is

$$\dot{C}(\mathbf{x}, t) = \int_{\mathcal{H}_\mathbf{x}} J\left(C(\mathbf{x}', t) - C(\mathbf{x}, t), \mathbf{x}' - \mathbf{x}\right) \mathrm{d}V_{\mathbf{x}'}, \quad \mathbf{x} \in \Omega_F, \quad t > 0, \tag{4.5}$$

where $J$ is the kernel of the integral operator or the concentration flow density, which takes the form given in (2.42), and $\mathcal{H}_\mathbf{x}$ is the neighborhood of point $\mathbf{x}$. To ensure a well-posed problem in $\Omega_N$, ABCs need to be imposed on $\Gamma_\infty$. These ABCs are designed to capture the effects of the far-field and ensure that the bounded domain reproduces the solution of the original problem. Specifically, the concentration in $\Omega_N$ should be perfectly absorbed on $\Gamma_\infty$ and have a flux directed towards the

exterior domain, preventing any unphysical flux back to the near-field. According to (4.3), the flux should approach zero at infinity, indicating a vanishing concentration state. In this regard, a method for constructing time-dependent ABCs is introduced in the following sections. This method utilizes fundamental solutions (modes) that satisfy the governing equation of the exterior domain, as given in (4.4), to construct Dirichlet-type ABCs. The construction of these modes, for both classical and peridynamic diffusion, is outlined in the next section section.

### 4.1.1 Fundamental Solutions for Peridynamic Diffusion

In the following, we derive fundamental solutions, known as *modes*, for the governing equations in the far-field using real-valued EBFs. These modes, denoted by $\psi(\mathbf{x}, t)$, must satisfy the governing equations of either the classical local or the peridynamic diffusion equation (*cf.* (4.1) and (4.5)), respectively. The general form of $\psi$ in 2D is given by

$$\psi(\mathbf{x}, t) = \exp(\boldsymbol{\alpha} \cdot \mathbf{x} + \bar{\omega} t), \quad \boldsymbol{\alpha} = \left(\alpha_x, \alpha_y\right)^{\mathrm{T}}, \tag{4.6}$$

where $\alpha_x, \alpha_y, \bar{\omega} \in \mathbb{R}$ are given real-valued coefficients. To control the flux direction, we make the assumption

$$(\alpha_x, \alpha_y)^{\mathrm{T}} = k\,(\cos\phi, \sin\phi)^{\mathrm{T}}, \quad k \in \mathbb{R}, \quad 0 \leq \phi < \pi. \tag{4.7}$$

where $k$ affects the flux magnitude and $\phi$ determines the flux direction. By substituting $\psi$ into the governing far-field equation (4.4) for classical local diffusion, we obtain

$$\left[\bar{\omega} - D\left(k^2\left(\cos^2\phi + \sin^2\phi\right)\right)\right] \exp(\boldsymbol{\alpha} \cdot \mathbf{x} + \bar{\omega} t) = 0. \tag{4.8}$$

In order to obtain a non-trivial solution, we set the expression in the brackets to zero, leading to

$$\bar{\omega} = Dk^2, \tag{4.9}$$

which is referred to as the *characteristic equation* or *dispersion relation*. Substituting the upper equation into (4.6), we obtain modes that can be used to construct semi-analytical solutions for local diffusion. The modes take the form of

$$\psi(\mathbf{x}, t) = \exp\left(\boldsymbol{\alpha} \cdot \mathbf{x} + Dk^2 t\right). \tag{4.10}$$

To derive fundamental solutions for the governing far-field peridynamic diffusion equation, we consider once more a generic mode in the form of (4.6). By assuming $q = 1$ in (*cf.* (2.42)) and considering a constant influence function $\omega_0$ (*cf.* (2.12)), we substitute $\psi$ into the governing equation of the far-field (*cf.* (4.5)), resulting in

$$\dot{\psi}(\mathbf{x}, t) = \int_{\mathcal{H}\mathbf{x}} \kappa_0 \frac{\psi(\mathbf{x}', t) - \psi(\mathbf{x}, t)}{\|\mathbf{x}' - \mathbf{x}\|} \mathrm{d}V_{\mathbf{x}'}, \tag{4.11}$$

where $\kappa_0$ corresponds to the constant micro-diffusivity of the constant influence function $\omega_0$. By introducing the change of variables $\boldsymbol{\xi} = \mathbf{x}' - \mathbf{x}$ and using (4.6), equation (4.11) can be rewritten as

$$\left(\bar{\omega} - \kappa_0 \int_{\mathcal{H}} \frac{\exp(\boldsymbol{\alpha} \cdot \boldsymbol{\xi}) - 1}{\|\boldsymbol{\xi}\|} \mathrm{d}V_{\boldsymbol{\xi}}\right) \exp(\boldsymbol{\alpha} \cdot \mathbf{x} + \bar{\omega} t) = 0, \tag{4.12}$$

where $\mathcal{H}$ denotes the neighborhood around the origin. In order to obtain a non-trivial solution, we equate the expression inside the parentheses in (4.13) to zero, resulting in the characteristic equation for the far-field peridynamic diffusion in polar coordinates given by

$$\omega = \kappa_0 \int_0^{2\pi} \int_0^{\delta} \left[\exp(r\eta) - 1\right] \mathrm{d}r\mathrm{d}\theta, \tag{4.13}$$

where $\eta := \boldsymbol{\alpha} \cdot (\cos\theta, \sin\theta)$. However, finding an analytical solution for (4.13) is generally challenging. To simplify the expression and establish a connection with the local modes, we expand the integrand using a Taylor series expansion around zero with respect to $r\eta$, resulting in

$$\bar{\omega} = \kappa_0 \int_0^{2\pi} \int_0^{\delta} \left( \frac{r\eta}{1!} + \frac{r^2\eta^2}{2!} + \frac{r^3\eta^3}{3!} + \frac{r^4\eta^4}{4!} + \dots \right) \mathrm{d}r\mathrm{d}\theta. \tag{4.14}$$

which concludes in

$$\bar{\omega} = \kappa_0 \pi \left( \frac{k^2\delta^3}{6} + \frac{k^4\delta^5}{160} + \frac{k^6\delta^7}{8064} + \dots \right). \tag{4.15}$$

Thus, the nonlocal peridynamic mode can be written as

$$\psi(\mathbf{x}, t) = \exp\left( \boldsymbol{\alpha} \cdot \mathbf{x} + \kappa_0 \pi \left( \frac{k^2\delta^3}{6} + \frac{k^4\delta^5}{160} + \dots \right) t \right). \tag{4.16}$$

A comparison between the derived modes in (4.10) and (4.16) reveals that the main difference lies in the temporal components. By substituting $\kappa_0 = \frac{6D}{\pi\delta^3}$ into (4.15), we obtain

$$\bar{\omega} = Dk^2 \left( 1 + \frac{3}{80}(k\delta)^2 + \frac{1}{1344}(k\delta)^4 + \dots \right). \tag{4.17}$$

In the limit as $k\delta \to 0$, equation (4.9) is obtained, which shows that the nonlocal mode converges to the local mode when the micro-diffusivity is appropriately defined in terms of the diffusion coefficient $D$ and the horizon $\delta$. Tab. 4.1 presents the expressions for the micro-diffusivity constants, which are related to the diffusion coefficient of the local diffusion and the horizon, for different kernels in 1D, 2D, and 3D. Note that, the expression in (4.16) suggests that including higher-order terms from the Taylor expansion in (4.14) leads to a more accurate approximation of the nonlocal solution. However, when implementing the ABCs based on modes given by (4.16), it is important to consider that the absorbing boundary is located away from the regions where nonlocal effects, such as crack tips, are significant. As a result, even if only a few terms from the Taylor expansion are utilized, such as employing the local modes, it can still yield a satisfactory approximation of the far-field.

Table 4.1: The constants $\kappa_0$ for a constant influence function (*cf.* (2.12)) and $\kappa_1$ for a linear influence function (*cf.* (2.13)) in terms of the diffusion coefficient $D$ and the horizon $\delta$. These expressions are given for various integer kernel exponents $q$ in the kernel function $J_q$ (*cf.* (2.42)), where the index corresponds to value of $q$, in 1D, 2D, and 3D. Data available in [123].

| | 1D | | 2D | | | 3D | |
|---|---|---|---|---|---|---|---|
| | $J_0$ | $J_1$ | $J_0$ | $J_1$ | $J_2$ | $J_1$ | $J_2$ |
| $\kappa_0$ | $\frac{3D}{\delta^3}$ | $\frac{2D}{\delta^2}$ | $\frac{8D}{\pi\delta^4}$ | $\frac{6D}{\pi\delta^3}$ | $\frac{4D}{\pi\delta^2}$ | $\frac{6D}{\pi\delta^4}$ | $\frac{9D}{2\pi\delta^3}$ |
| $\kappa_1$ | $\frac{12D}{\delta^3}$ | $\frac{6D}{\delta^2}$ | $\frac{40D}{\pi\delta^4}$ | $\frac{24D}{\pi\delta^3}$ | $\frac{12D}{\pi\delta^2}$ | $\frac{30D}{\pi\delta^4}$ | $\frac{18D}{\pi\delta^3}$ |

### Infinity Condition for Diffusion-Type Problems

Fig. 4.2(a) depicts a circular region called the *cloud* centered at a point **x** and surrounded by an unbounded domain. Using a local coordinate system $(\bar{x}, \bar{y})$ at **x**, the far-field solution is approximated through a series of modes, characterized by temporal and spatial components. Considering a local mode, i.e., the leading term of the Taylor series expansion in (4.17), expressed in polar coordinates yields

$$\begin{aligned}\psi(r,\theta,t) &= \exp\left[kr\left(\cos\theta\cos\phi+\sin\theta\sin\phi\right)\right]\exp\left(Dk^2t\right)\\ &= \exp\left[kr\cos(\theta-\phi)\right]\exp\left(Dk^2t\right).\end{aligned} \tag{4.18}$$

To satisfy the infinity (or radiation) condition in the direction $\theta^*$, we substitute $\psi$ for $C$ in (4.3) and set $\theta = \theta^*$, which yields

$$\lim_{r\to\infty}\psi(r,\theta^*,t) = \lim_{r\to\infty}\exp\left[kr\cos(\theta^*-\phi)\right]\exp\left(Dk^2t\right) = 0. \tag{4.19}$$

To satisfy the infinity condition, under the assumption that $Dk^2t$ is finite, the following inequality

$$k\cos(\theta^*-\phi) < 0, \tag{4.20}$$

must hold at a given time $t > 0$. Depending on the sign of $k$ and the value of $\theta^*$, the condition (4.20) can be simplified by considering two different cases. In the case of the first quadrant of the local coordinate system, i.e., $\theta^* \in [0, \pi/2)$, the mode should satisfy the conditions given as

$$\begin{aligned}k>0:&\quad \frac{\pi}{2}+\theta^* < \phi < \frac{3\pi}{2}+\theta^*,\\ k<0:&\quad \frac{3\pi}{2}+\theta^* < \phi < 2\pi+\theta^* \quad\cup\quad \theta^* \le \phi < \frac{\pi}{2}+\theta^*,\end{aligned} \tag{4.21}$$

in order to fulfill the condition (4.20) at the angle $\theta^*$. The two cases described in (4.21) represent two halves of the unit circle, as depicted in Fig. 4.2(b). These semicircular regions illustrate the allowable range of flux direction $\phi$ (determined by the sign of $k$) that satisfies the infinity condition at $\theta^*$. The interface between the two semicircles is perpendicular to the $\theta^*$ direction and rotates accordingly as $\theta^*$ changes, as shown in Fig. 4.2(c).

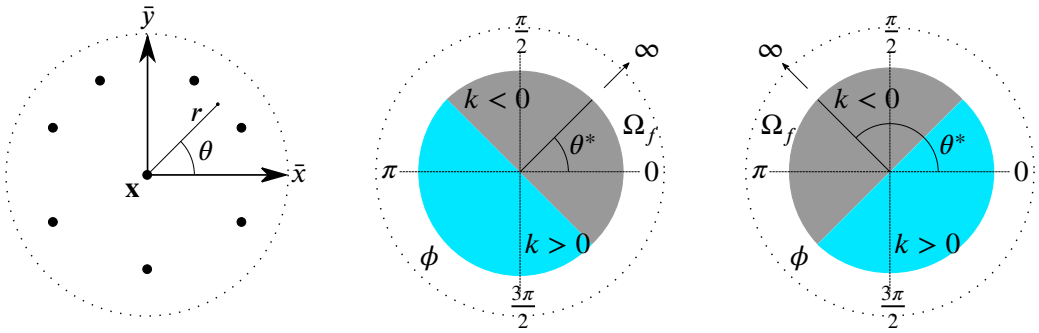


Figure 4.2: (a) A circular cloud surrounded by an unbounded domain. (b) The regions in the unit circle where the flux direction $\phi$ satisfies the infinity condition at angle $\theta^*$ within the first quadrant of the local coordinate system. (c) The valid regions of $\phi$ in (b) rotate accordingly as $\theta^*$ changes. Reproduced from [123].

Assuming that the infinity condition always occurs in the first quadrant of the local coordinate system ($\theta \in [0, \pi/2)$), we can define two valid regions, $\mathfrak{R}_1$ and $\mathfrak{R}_2$, on the unit circle corresponding to $\theta^* = 0$ and $\theta^* = \pi/2$, respectively. To satisfy the condition at any angle within the first quadrant, $\phi$ must be chosen from the intersection of these regions, which can be expressed as:

$$\mathfrak{R}_1 \cap \mathfrak{R}_2 = \begin{cases} \pi \leq \phi \leq 3\pi/2, & \text{for } k > 0, \\ 0 \leq \phi \leq \pi/2, & \text{for } k < 0. \end{cases} \tag{4.22}$$

In the subsequent sections, the solution strategies employed for addressing both the near-field and far-field problems are discussed, as well as the approach for patching the far-field with the near-field solution in a discretized peridynamic or FEM model.

### 4.1.2 Solution Strategy for Unbounded Domain Diffusion

The solution strategy involves two parts: approximating the near-field using either PD or FEM and advancing in time, and approximating the far-field and constructing the absorbing boundary conditions. The domain discretization for both the peridynamic grid and FEM mesh is illustrated in Fig. 4.3. In the peridynamic case, absorbing nodes are distributed near the absorbing boundary $\Gamma_\infty$, while in the FEM case only absorbing nodes along the boundary are needed. The domain is represented by a set of nodes $\mathbf{x}_i$ with their Cartesian coordinates. The time is discretized into instants, and an explicit forward Euler time integration scheme is used throughout the following examples. The time integration scheme utilizes the critical time step $\Delta t_{\text{crit}}$ determined by the CFL condition, given by

$$\Delta t_{\text{crit}} = \sigma_{\text{CFL}} \frac{\Delta x_{\text{min}}^2}{D}, \tag{4.23}$$

where $\Delta x_{\text{min}}$ represents the minimum peridynamic grid spacing or the minimum element size in FEM for spatial discretization. The parameter $\sigma_{\text{CFL}}$ corresponds to the CFL condition, with values of $\frac{1}{2}$, $\frac{1}{4}$, and $\frac{1}{8}$ for 1D, 2D, and 3D uniform discretizations, respectively.

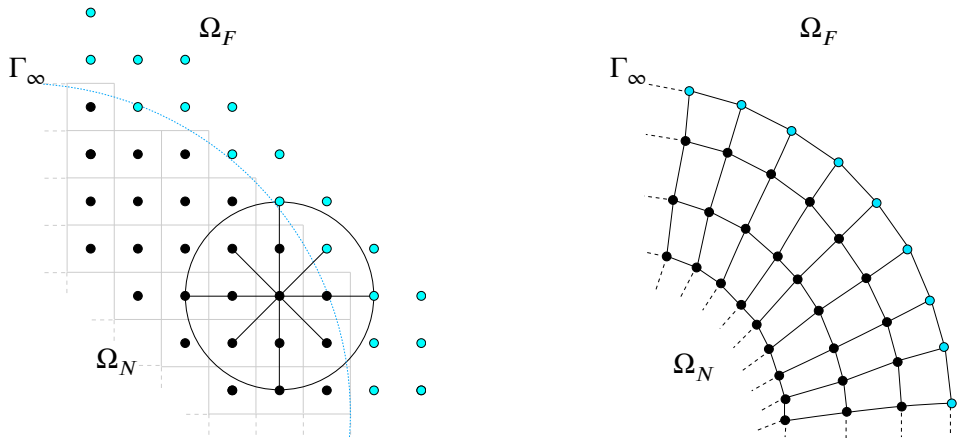


Figure 4.3: A subsection of a typical solution domain in the vicinity of the absorbing boundary is depicted in (a) for a peridynamic model utilizing a standard discretization scheme, and in (b) for a FEM model employing quadrilateral elements. Reproduced from [123].

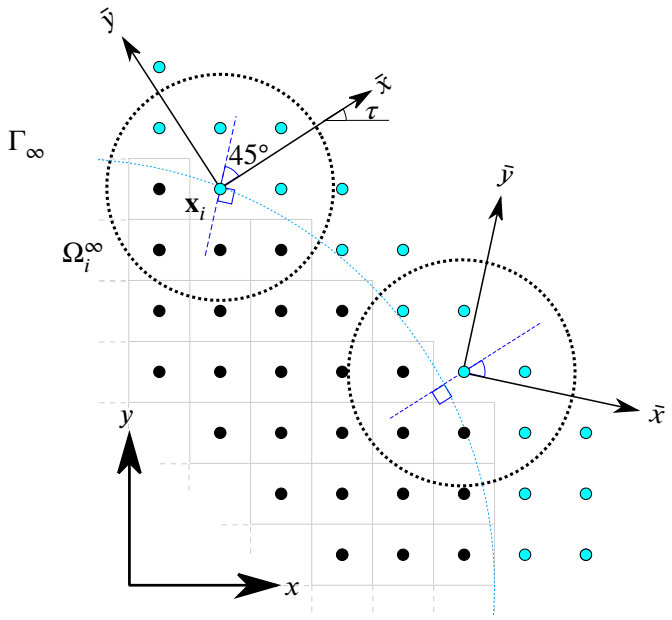


Figure 4.4: Two generic clouds with rotated local coordinate systems for the far-field approximation. Reproduced from [123].

An efficient way for updating the absorbing boundary nodes, as originally proposed by [125], is employed to approximate the far-field solution. At each time step, the far-field solution within the associated cloud of each absorbing node is approximated using the modes introduced in Section 4.1.1. This approximation provides the value of the absorbing node for the next time step, which is imposed as a Dirichlet boundary condition. Fig. 4.4 illustrates two generic clouds with differently oriented local coordinate systems. Consider a node $\mathbf{x}_i$ on the absorbing boundary (or boundary layer in the PD case) along with its associated cloud $\Omega_i^\infty$, as shown in Fig. 4.4. The local Cartesian coordinate system $(\bar{x}, \bar{y})$ is associated with each cloud, as shown in Fig. 4.4 for the 2D case. It is rotated by an angle $\tau$ to align the first quadrant with the exterior domain and ensure that the bisection line of the axes is perpendicular to the absorbing boundary. To transform a representative position vector $\mathbf{x}$ to the local coordinate system, a 2D rotation matrix $\mathbf{R}$ is used, resulting in the local coordinates $\bar{\mathbf{x}}$ given by

$$\bar{\mathbf{x}} = \mathbf{R}(\tau)(\mathbf{x} - \mathbf{x}_i), \quad \mathbf{R}(\tau) = \begin{bmatrix} \cos\tau & \sin\tau \\ -\sin\tau & \cos\tau \end{bmatrix}. \tag{4.24}$$

Note that, in 3D problems, the absorbing boundary $\Gamma_\infty$ is a truncating sphere, and the local coordinate system is rotated to ensure that the first octant aligns with the exterior domain. To simplify the analysis, we focus on the 2D case. The far-field solution variable $C_\infty(\bar{\mathbf{x}}, t)$ within the cloud $\Omega_i^\infty$ is approximated by expressing it as a linear combination of modes as

$$C_\infty(\bar{\mathbf{x}}, t) = \sum_{l=1}^{n_\phi} \sum_{m=1}^{n_k} a_{l,m} \exp\left[k_m \left(\bar{x}\cos\phi_l + \bar{y}\sin\phi_l\right) + Dk_m^2 t\right], \tag{4.25}$$

where $a_{l,m}$ are unknown coefficients of the approximation and $n_\phi$ and $n_k$ specify the number of modes. The angles $\phi_l$ are chosen from a set of equally spaced angles within the interval $\phi_l \in$

$[0, \pi/2]$, and $k_m$ are selected from a set of equally spaced negative values within the interval $k_m \in \Delta k[-1, 0)$, where $\Delta k > 0$. The selection of $\Delta k$ is crucial for ensuring the numerical stability and accuracy of the absorbing boundary conditions. In Section 4.1.3, we will discuss a method to carefully limit the value of $\Delta k$.

To determine the unknown coefficients in the approximation given by (4.25), we rely on the nodal values within the cloud. At the beginning of each time step, we consider the validity of the approximation within the time interval $[t^n, t^{n+1}]$, which can be expressed using a local time variable $\bar{t}$ in the interval $\bar{t} \in [0, \Delta t]$. While this interval as proposed in [125] is suitable for many cases, the use of a symmetric interval $[-\Delta t, \Delta t]$ has proven to enhance numerical stability in peridynamic scalar waves and elasticity problems. In diffusion problems, the choice of the interval shape has a negligible impact. Utilizing (4.25), we express this approximation as

$$C_\infty^n(\bar{\mathbf{x}}, \bar{t}) = \sum_{b=1}^{n_b} p_b^n \psi_b(\bar{\mathbf{x}}, \bar{t}) = \boldsymbol{\psi}(\bar{\mathbf{x}}, \bar{t})\mathbf{p}^n, \tag{4.26}$$

where the superscript $n$ indicates the validity of the approximation within local time interval. The series runs over $n_b$ modes and $q_b$ represents the corresponding unknown coefficients and the vectors $\boldsymbol{\psi}$ and $\mathbf{p}^n$ are given by

$$\begin{aligned} \boldsymbol{\psi}(\bar{\mathbf{x}}, \bar{t}) &:= \left(\psi_1(\bar{\mathbf{x}}, \bar{t}), \quad \psi_2(\bar{\mathbf{x}}, \bar{t}), \quad \cdots, \quad \psi_{n_b}(\bar{\mathbf{x}}, \bar{t})\right), \\ \mathbf{p}^n &:= \left(p_1^n, \quad p_2^n, \quad \cdots, \quad p_{n_b}^n\right)^{\mathrm{T}}. \end{aligned} \tag{4.27}$$

At the start of the $n$th time step, the nodal values within the cloud $\Omega_i^\infty$, associated with node $\mathbf{x}_i$ in Fig. 4.4, can be organized into a vector. Using (4.26) and taking into account that $\bar{t} = 0$ at the start of each step, this vector can be represented as

$$\mathbf{G}^n = \begin{pmatrix} C_{i,\infty}^n \\ \vdots \\ C_{j,\infty}^n \\ \vdots \end{pmatrix} = \begin{pmatrix} C_\infty^n(\bar{\mathbf{x}}_i, 0) \\ \vdots \\ C_\infty^n(\bar{\mathbf{x}}_j, 0) \\ \vdots \end{pmatrix} = \begin{bmatrix} \boldsymbol{\psi}(\bar{\mathbf{x}}_i, 0) \\ \vdots \\ \boldsymbol{\psi}(\bar{\mathbf{x}}_j, 0) \\ \vdots \end{bmatrix} \mathbf{p}^n = \mathbf{M}_G \mathbf{p}^n, \quad \mathbf{x}_j \in \Omega_i^\infty, \tag{4.28}$$

where $\mathbf{M}_G$ stands for the moment matrix of the local collocation procedure. When the number of nodes in the cloud is smaller than the number of modes $n_b$, the unknown coefficients $\mathbf{p}^n$ can be determined in terms of the nodal values of the cloud $\mathbf{G}^n$ using a least-squares collocation method. This can be expressed as

$$\mathbf{p}^n = \mathbf{M}_G^+ \mathbf{G}^n \tag{4.29}$$

where the superscript "+" denotes the Moore-Penrose generalized inverse. By substituting the expression for $\mathbf{p}^n$ from (4.29) into (4.26), we obtain an approximation for the solution within the cloud as

$$C_\infty^n(\bar{\mathbf{x}}, \bar{t}) = \boldsymbol{\psi}(\bar{\mathbf{x}}, \bar{t})\mathbf{M}_G^+ \mathbf{G}^n. \tag{4.30}$$

The upper equation provides an explicit time approximation of the solution within the cloud. To update the nodal value of the absorbing node at the $n$th time step, we can use the updating procedure given by

$$C_i^{n+1} \approx C_\infty^n(\bar{\mathbf{x}}_i, \Delta t) = \boldsymbol{\psi}(\mathbf{0}, \Delta t)\mathbf{M}_G^+ \mathbf{G}^n = \mathbf{V}_G \mathbf{G}^n, \tag{4.31}$$

where $\mathbf{V}_G$ represents the updating vector of the absorbing node. The right-hand side of (4.31) is known since the solver uses an explicit time marching algorithm. Thus, (4.31) provides Dirichlet-type ABCs for the absorbing node $\mathbf{x}_i$ based on the nodal values of its cloud at the time instant $t^n$. The simulation uses a constant time step $\Delta t$ and resets the local time at each step, allowing the updating vectors $\mathbf{V_G}$ of the absorbing nodes to be pre-computed since they remain constant. This significantly reduces the computational cost.

The absorbing layer in the peridynamic diffusion model is carefully chosen to ensure a complete circular (or spherical) shape for the near-field neighborhoods. This mitigates the *surface-effect* commonly found in peridynamic models with a narrower absorbing layer. The accuracy of the near-field solution, which is the main concern, can be affected by this error. The numerical examples in Section 4.1.4 provide a detailed illustration of this effect.

### 4.1.3 Implementation of Unbounded Domain Diffusion

The solution strategy for diffusion problems on unbounded domains preserves the near-field discretization scheme and is implemented in a straightforward manner. It involves discretizing the domain, identifying absorbing nodes, constructing neighborhoods (for peridynamic diffusion) and clouds for absorbing nodes, formulating equations, calculating updating vectors, and performing explicit time marching. The final system of equations, applicable to both peridynamic and FEM cases, is given by

$$\widetilde{\mathbf{M}}\dot{\mathbf{C}}_T + \widetilde{\mathbf{K}}\mathbf{C}_T = \widetilde{\mathbf{F}}, \tag{4.32}$$

where $\widetilde{\mathbf{M}}$ and $\widetilde{\mathbf{K}}$ represent mass and conductance matrices, $\mathbf{C}_T$ and $\dot{\mathbf{C}}_T$ contain the nodal values and their first time derivatives, and $\widetilde{\mathbf{F}}$ is the right-hand side. Note that the system remains the same for bounded and unbounded domains, with an additional procedure required for updating nodal values in the unbounded case.

Furthermore, an important consideration is the selection of modes, which is based on the specified intervals for $\phi$ and $k$ as mentioned in Section 4.1.1. The parameter $\Delta k$ plays a crucial role in the stability of the numerical solution as it directly affects the temporal part of the modes. In order to ensure boundedness and minimize numerical errors, the temporal component of the modes should be constrained. This can be achieved by selecting $\Delta k$ such that

$$0 < D\Delta k^2 \Delta t < 1, \tag{4.33}$$

where $\Delta t$ represents the time increment. Given (4.33), the following range for $\Delta k$ is obtained as

$$0 < \Delta k < \frac{1}{\sqrt{\sigma_{\text{CFL}}}\Delta x_{\min}}. \tag{4.34}$$

To ensure an accurate approximation of the far-field solution, it is necessary to include a sufficient number of neighboring nodes in the collocation process within each cloud. Our experience suggests that in 1D, 2D, and 3D cases, the radius $d_\infty$ should be chosen to encompass at least 3, 5, and 7 neighboring nodes, respectively. It is important to note that $d_\infty$ only determines the region of the least-squares approximation and does not represent the range of nonlocal interaction, which is represented by the peridynamic horizon $\delta$.

The numerical examples were implemented using the `C++` programming language. To enhance performance, we employed parallelization techniques with OpenMP directives. The efficient library `libkdtree` was used to construct neighborhoods and clouds, with more details available in [96]. To compute the Moore-Penrose generalized inverse in (4.29), we relied on the widely-used LAPACK library [5].

### 4.1.4 Classical and Peridynamic Diffusion on Unbounded Domains in 1D

In the first numerical example, we demonstrate the solution strategy for 1D unbounded domain problems using classical (local) and peridynamic diffusion. The diffusion parameter is $D = 1$, and the computational domain is $\Omega_N = (-30, 30)$. We validate the results against an extended domain within $\Omega_N$ from $(-150, 150)$. The initial concentration is given by $C_0(x) = \exp(-4x^2)$. Both the FEM model and the peridynamic model have the same spatial discretization and temporal resolution. The spatial discretization uses a grid size of $\Delta x = 0.125$, resulting in $2,401$ and $481$ nodes for the extended and truncated domain, respectively. The time duration of interest is $t_f = 250$, with a time increment of $\Delta t = 0.001$, corresponding to $250,000$ time steps. In the FEM model, two clouds are placed at $x = -30$ and $x = 30$, with local coordinate systems oriented towards the left and right directions, respectively. The far-field solution is constructed using $n_b = 20$ modes.

Fig. 4.6 presents the concentration field obtained at different time instants using the FEM solver for both the truncated domain and the extended domain. Only the portion of the reference solution corresponding to the truncated domain is shown for better comparison. The results indicate that the solution obtained on the truncated domain with ABCs closely resembles the reference solution. Additionally, the solution for the truncated domain is extended beyond the initial time duration up to $t_f = 4,000$, where the concentration eventually reaches zero as expected.

Fig. 4.7 provides further insights into the performance of the method by presenting the energy variation over time for both the truncated domain with ABCs and the extended domain. The energy is computed within the near-field and normalized with respect to its value at the initial time step. Additionally, the normalized energy difference between the two solutions is defined as

$$\Delta\Pi/\Pi_0(t) = \frac{|\Pi(t) - \Pi_{\text{ref}}(t)|}{\Pi_{\text{ref}}(0)}, \tag{4.35}$$

where $\Pi_{\text{ref}}(t)$ is the energy of the reference solution at time $t$. The results of the normalized energy difference for both the truncated domain with ABCs and the truncated domain with homogeneous Neumann boundary conditions are shown in Fig. 4.5.

The energy analysis presented in Fig. 4.7 confirms the good match between the energy dissipation in the near-field of the truncated domain with ABCs and the reference solution. In contrast, using homogeneous Neumann boundary conditions leads to a significant difference between the solutions, as shown in Fig. 4.5. These findings highlight the effectiveness of the ABCs in preventing spurious flux reflections and maintaining stability over long-term calculations. The stability of the approach is confirmed by the successful energy calculation up to $t_f = 4,000$, which corresponds to $4 \times 10^6$ time steps. Overall, the results validate the performance and reliability of the method in handling classical diffusion problems on unbounded 1D domains.

In the second part of this example, the peridynamic diffusion equation is employed with an absorbing layer thickness of $\delta = 4\Delta x$ and a cloud size of $d_\infty = \delta/2$ for the absorbing nodes. The absorbing layer thickness is set to $\delta$ to ensure that each neighborhood in the near-field has a complete integration domain. The concentration field is computed for both the truncated and extended domains, and the results are shown in Fig. 4.8. The energy variation over time is also analyzed, and the results are depicted in Fig. 4.9. It is evident that the truncated domain with ABCs yields accurate and consistent results, with a close agreement between the truncated and the extended domain solutions, even at the energy level.

Additional simulations were conducted using the peridynamic solver to investigate the influence of the absorbing layer thickness $\delta_L$ on the accuracy of the truncated domain solution. Varying values of $\delta_L$, including $3\Delta x$, $2\Delta x$, and $\Delta x$, were considered. The concentration field at $t = 250$ for

different $\delta_L$ values is depicted in Fig. 4.10. The results reveal that a smaller $\delta_L$ and thus a larger surface effect lead to reduced accuracy, particularly near the boundaries. Fig. 4.11 presents the normalized energy difference between the solutions of the truncated domain with different absorbing layer sizes and the reference solution. The findings demonstrate that satisfactory accuracy is achieved when $\delta_L$ is chosen to be at least $3\Delta x$.

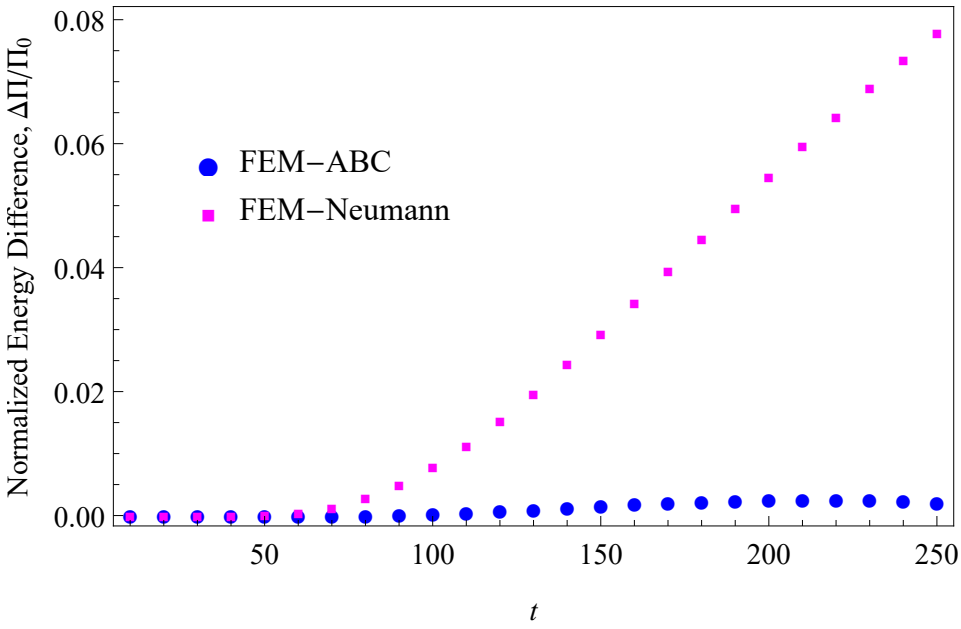


Figure 4.5: The normalized energy difference $\Delta\Pi/\Pi_0$ in 1D for the numerical examples in Section 4.1.4, using the FEM solver with and without ABCs. Reproduced from [123].

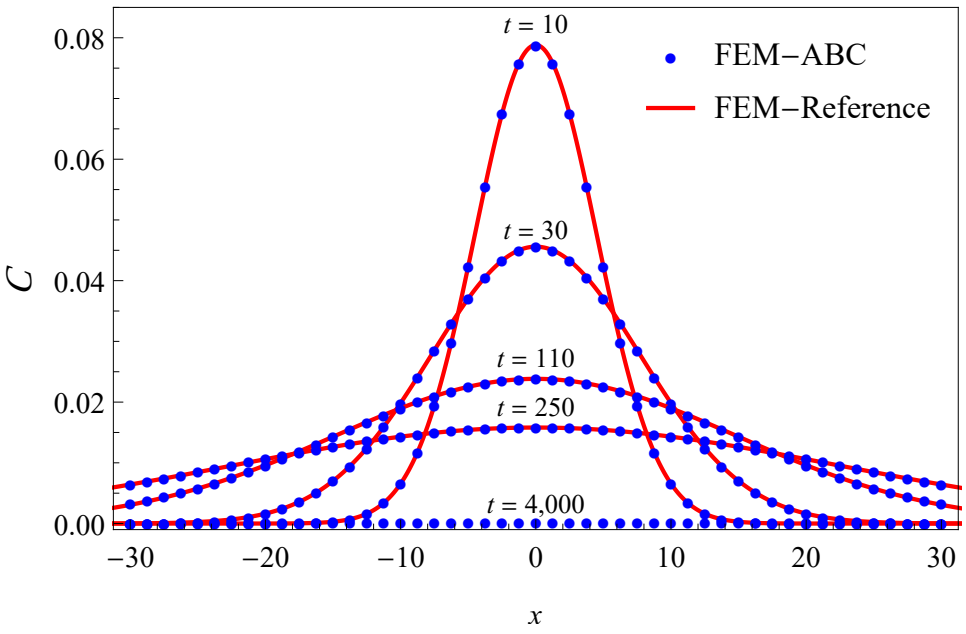


Figure 4.6: The concentration field obtained for the truncated domain and the extended domain in 1D for the numerical examples in Section 4.1.4, using the FEM solver. Reproduced from [123].

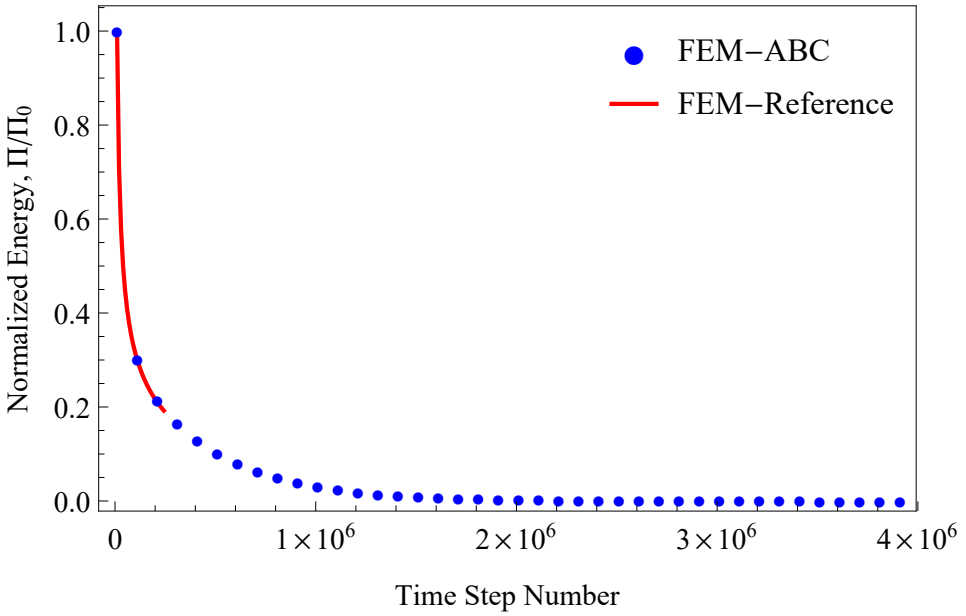


Figure 4.7: The variation of energy obtained for the truncated domain and the extended domain in 1D for the numerical examples in Section 4.1.4, using the FEM solver. Reproduced from [123].

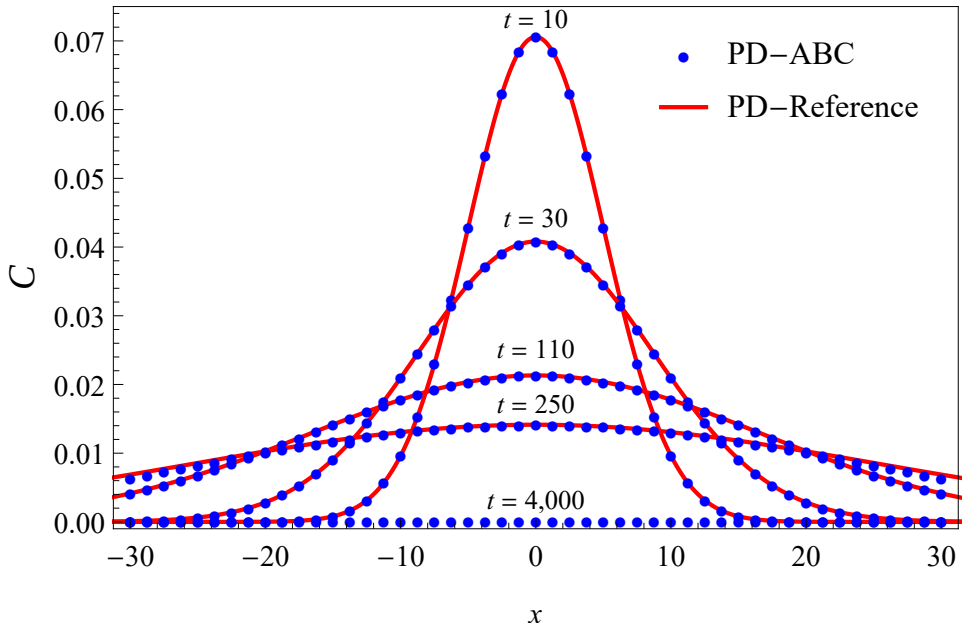


Figure 4.8: The concentration field obtained for the truncated domain and the extended domain in 1D for the numerical examples in Section 4.1.4, using the peridynamic solver. Reproduced from [123].

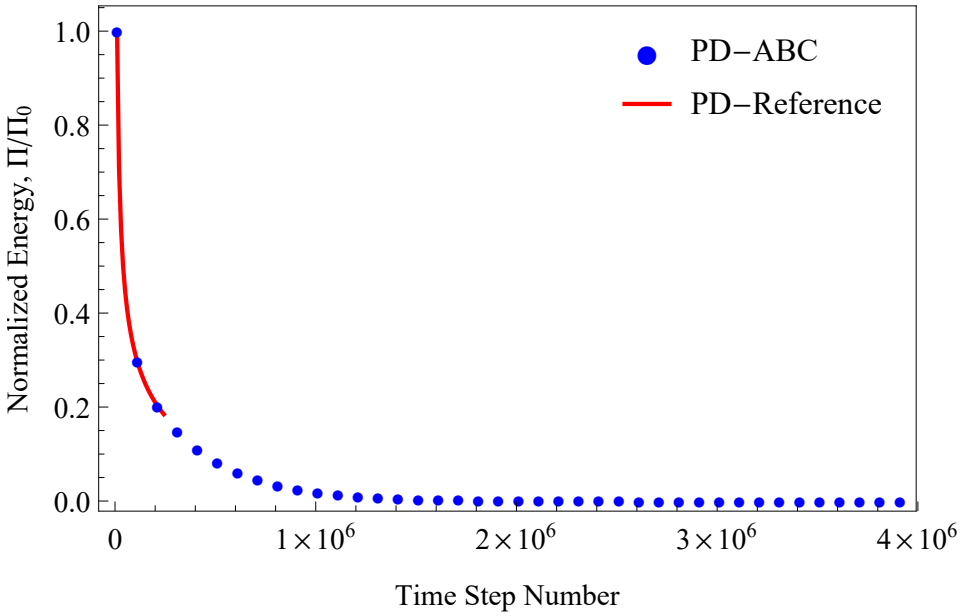


Figure 4.9: The variation of energy obtained for the truncated domain and the extended domain in 1D for the numerical examples in Section 4.1.4, using the peridynamic solver. Reproduced from [123].

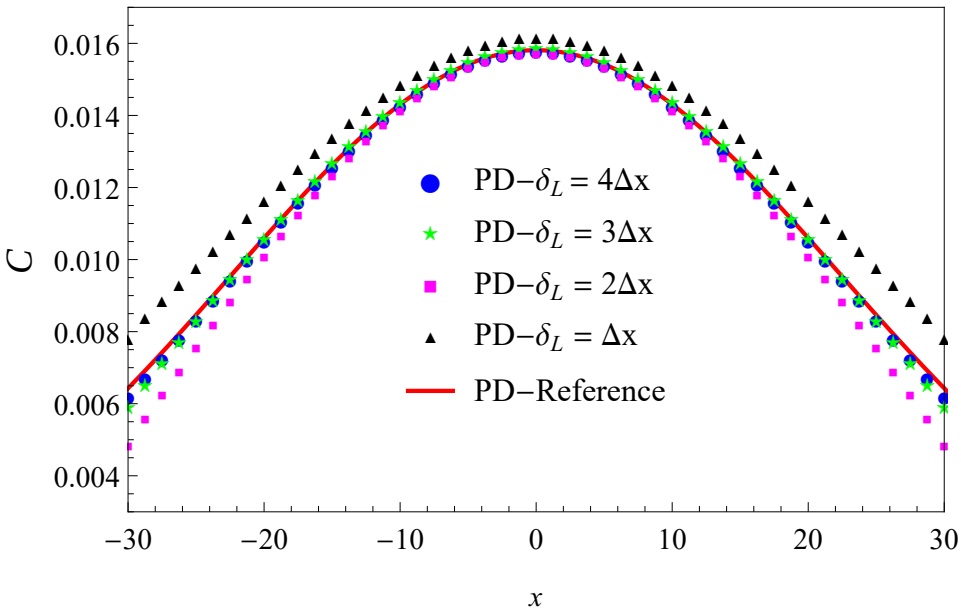


Figure 4.10: The concentration field in 1D obtained for the truncated domain and the extended domain at $t = 250$ for the numerical examples in Section 4.1.4, using the peridynamic solver with different sizes of the absorbing layer. Reproduced from [123].

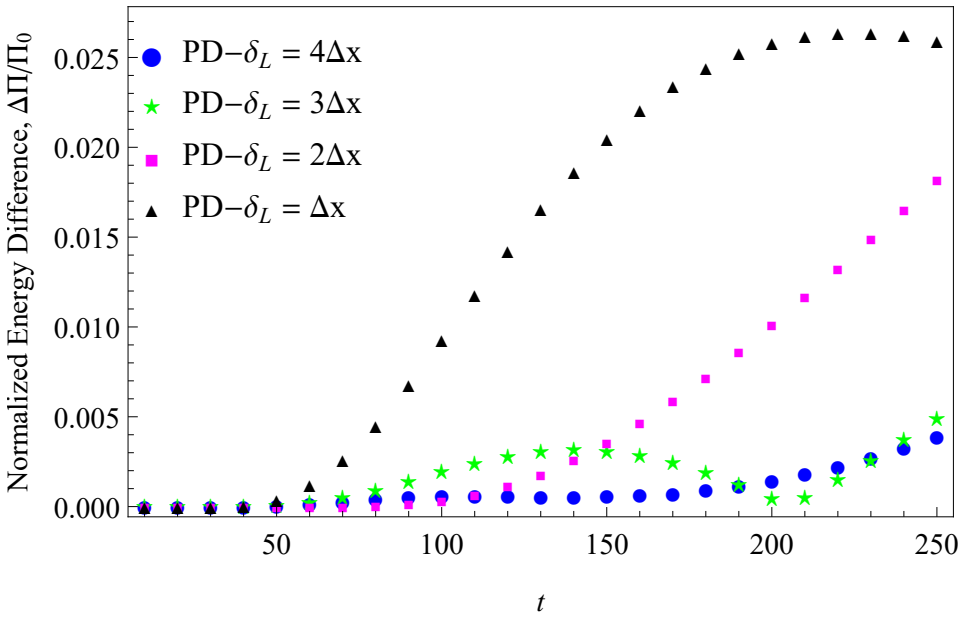


Figure 4.11: The normalized energy difference $\Delta\Pi/\Pi_0$ in 1d for the numerical examples in Section 4.1.4, using the peridynamic solver and taking different sizes of the absorbing layer. Reproduced from [123].

### 4.1.5 Peridynamic Corrosion on Unbounded Domains in 2D and 3D

This section presents two numerical simulations for evaluating the proposed ABCs in solving the standard peridynamic bi-material corrosion model for unbounded domains. These simulations are conducted in 2D and 3D, respectively. The 2D example compares the performance of the model equipped with the proposed ABCs to a model with homogeneous nonlocal Neumann boundary conditions. The comparison reveals that the numerical error of the model with Neumann boundary conditions grows over time, highlighting the superior accuracy and stability achieved by employing the proposed ABCs for unbounded domain corrosion problems. The numerical stability is further demonstrated by monitoring the total energy within the near-field over time. The 3D example involves a spherical specimen corroding within a larger spherical liquid domain. Due to the significant computational effort required for a reference solution on a much larger domain, the numerical performance of the ABCs is assessed qualitatively based on the concentration field, the outward-pointing concentration flux, and the monotonically decreasing near-field energy levels. These observations again demonstrate the stability of the model with ABCs and its ability to effectively transmit the concentration flux towards the far-field.

#### 2D Example with Reference Solution

In this 2D example, we investigate the effectiveness of the ABCs for a peridynamic corrosion problem on an unbounded domain. The problem involves the corrosion of a metallic specimen surrounded by an unbounded electrolyte, where the solid material dissolves into the liquid medium. The initial state consists of an intact metal represented by the HZG[1] letters with an initial concentration value of $C_0 = 2$, while the surrounding electrolyte has an initial concentration value of $C_0 = 0$. As the corrosion process occurs, the solid phase reduces, leading to the diffusion of dissolved material into the electrolyte.

In the peridynamic bi-material corrosion model, two micro-diffusivity parameters, $\kappa_{\text{liq}}$ and $\kappa_{\text{int}}$, are used to represent diffusion in the liquid and interfacial bonds, respectively. It is assumed that there is no flux between two points in the solid phase. The dissolution process is governed by a threshold concentration $C_{\text{sat}}$, below which a solid point is considered as a liquid point. This leads to the autonomous propagation of the dissolution front. In this example, the parameters $\delta = 0.04$, $C_{\text{sat}} = 0.8$, $\kappa_{\text{liq}} = 7,957.70$, and $\kappa_{\text{int}} = 795.77$ are used. As depicted in Fig. 4.12, the truncated domain is a circular region with a radius of 2, surrounded by an absorbing layer with a thickness equal to the peridynamic horizon $\delta$. Each absorbing node is associated with a cloud of radius $d_\infty = \delta/2$. The far-field is approximated using $n_b = 55$ modes in each cloud. To validate the results, the solution of an extended circular domain with a radius of 10 is used as the reference solution, with homogeneous Neumann boundary conditions imposed on the boundary. Both the truncated and extended domains are discretized with a grid spacing of $\Delta x = 0.02$, resulting in $31,417$ nodes for the truncated domain (including $2,500$ absorbing nodes) and $785,349$ nodes for the extended domain. The time stepping is performed using an incremental time step of $\Delta t = 3.3 \times 10^{-7}$ in both models.

The concentration levels of the metal within the truncated domain, using the ABCs, and the extended domain are compared at different time instants in Fig. 4.13. Regions with concentrations higher than 0.8 represent the solid phase. The results show that the solution of the truncated domain closely resembles that of the extended domain. The metal concentration gradually diffuses

[1]The acronym HZG stands for Helmholtz-Zentrum Geesthacht, which was the name for the Helmholtz-Zentrum Hereon between 2010 and 2021.

outwards and crosses the truncation boundary, following a similar pattern as the reference solution. By $t = 0.085$, the concentration within the near-field reaches almost zero, indicating that the ABCs are functioning effectively.

The effectiveness of the applied ABCs can be further assessed by examining the gradient field of concentration. Contour plots of the gradient field at different time instants are shown in Fig. 4.14. The arrows represent the direction of the gradient vectors, while the contours indicate their magnitude. Near the truncation boundary, all the arrows point towards the exterior domain, indicating that the boundary conditions are functioning appropriately over time. The accuracy of the solution is evaluated by comparing the truncated domain solution with the extended domain solution. The difference between these solutions is plotted in Fig. 4.15, using the normalized energy difference defined in (4.35). It is observed that the difference is relatively small when the absorbing layer is applied, while the solution of the truncated domain diverges from the reference solution when the absorbing layer is removed. The stability of the solution is demonstrated in Fig. 4.16, where the energy variation is shown for both the truncated and extended domains. The energy dissipates monotonically from the computational domain (near fiel), and the absorbing boundary layer exhibits stable behavior over $7 \times 10^6$ time steps, in good agreement with the reference solution.

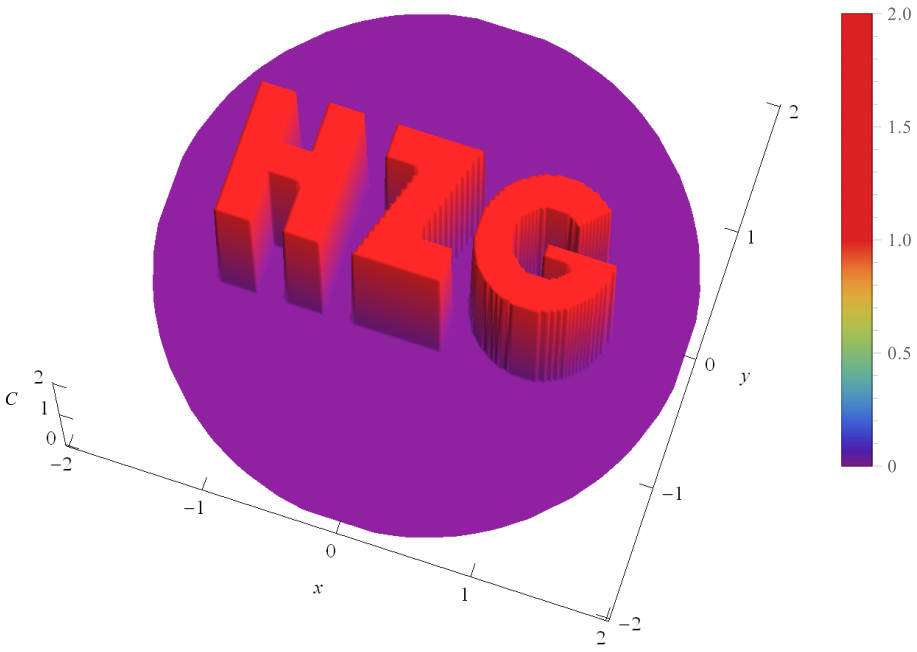


Figure 4.12: The initial metal concentration distribution in the 2D unbounded peridynamic bimaterial corrosion example in Section 4.1.5. Reproduced from [123].

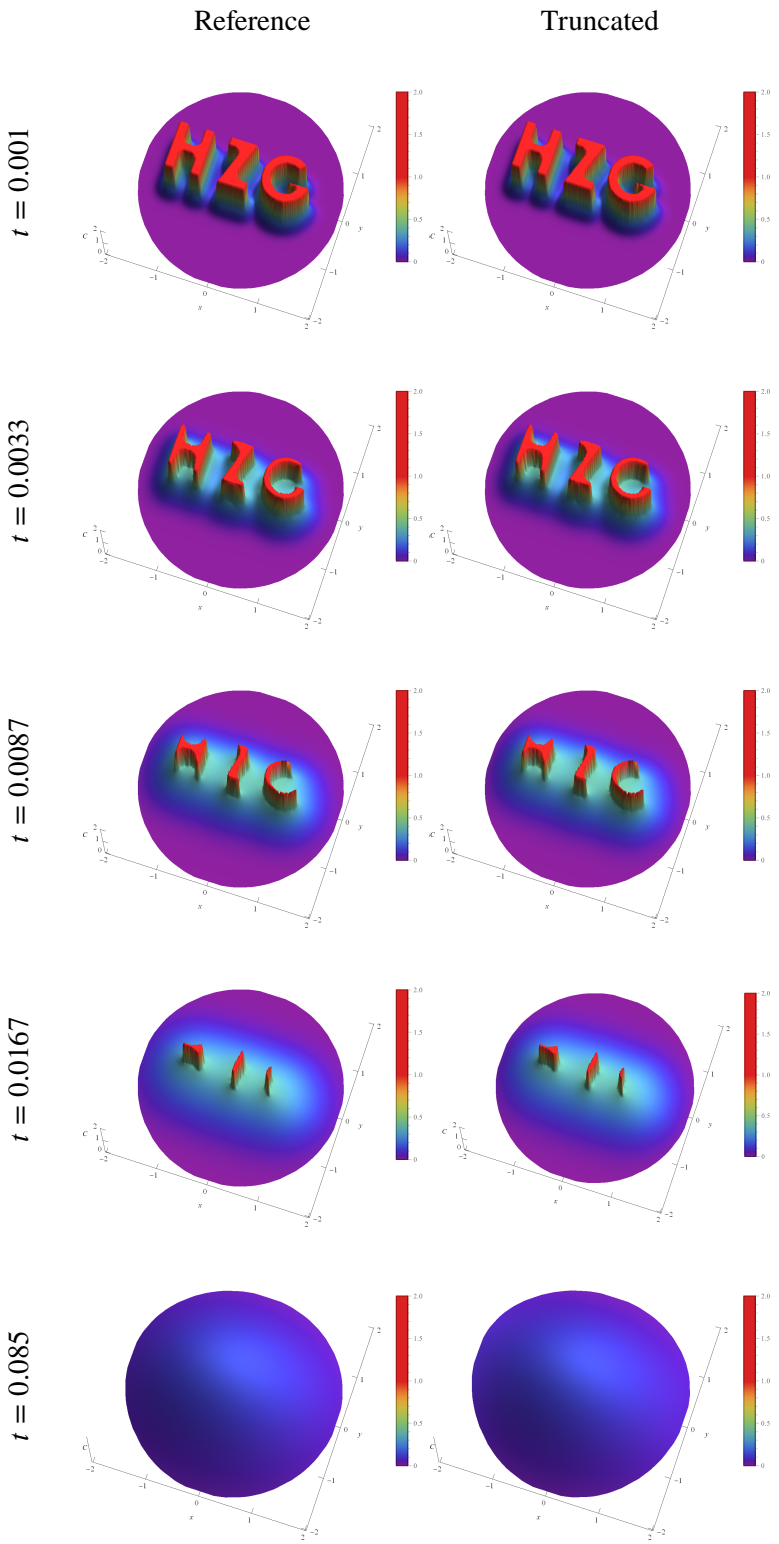


Figure 4.13: The concentration field at different time instants in the 2D unbounded peridynamic bi-material corrosion example in Section 4.1.5 for the reference solution (left column) and the solution of the truncated domain (right column). Reproduced from [123].

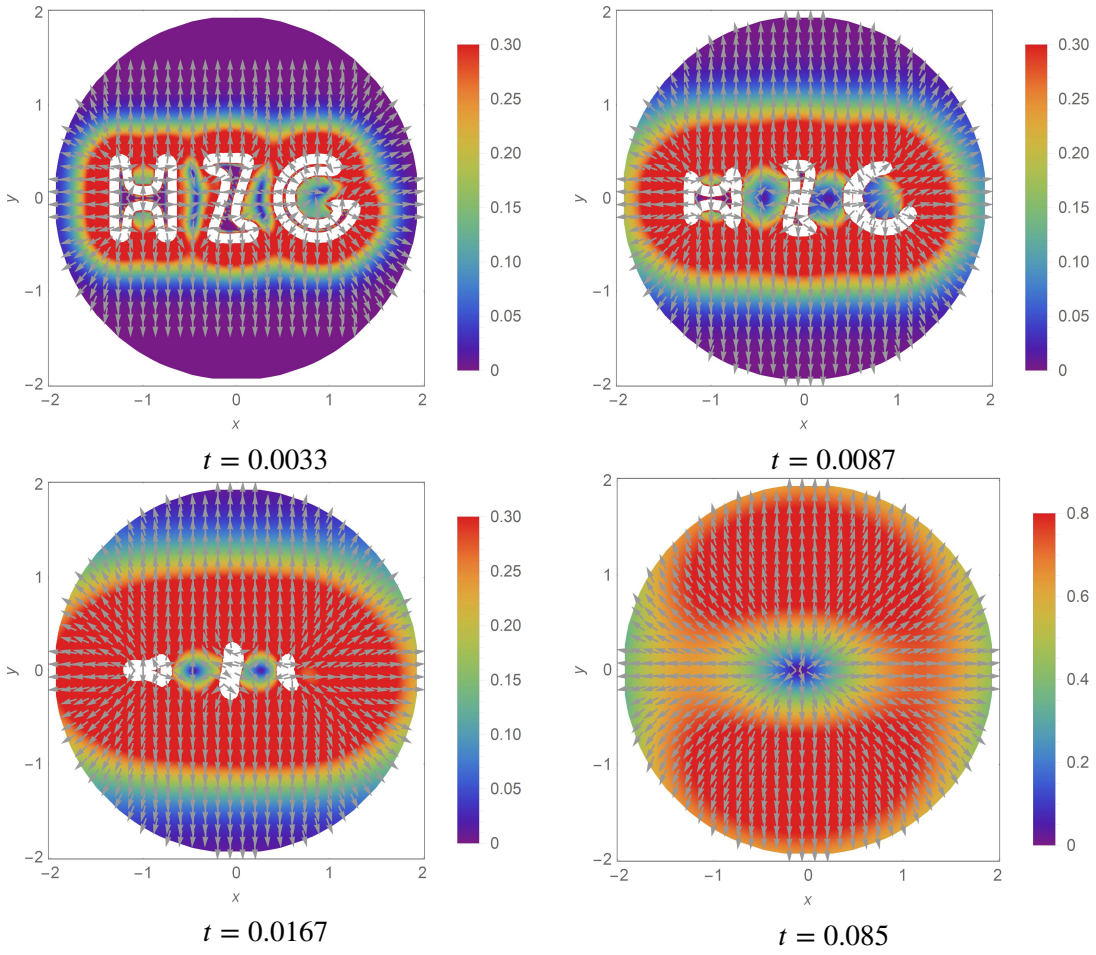


Figure 4.14: The concentration gradient field at various time instants in the 2D unbounded peridynamic bi-material corrosion example in Section 4.1.5. Reproduced from [123].

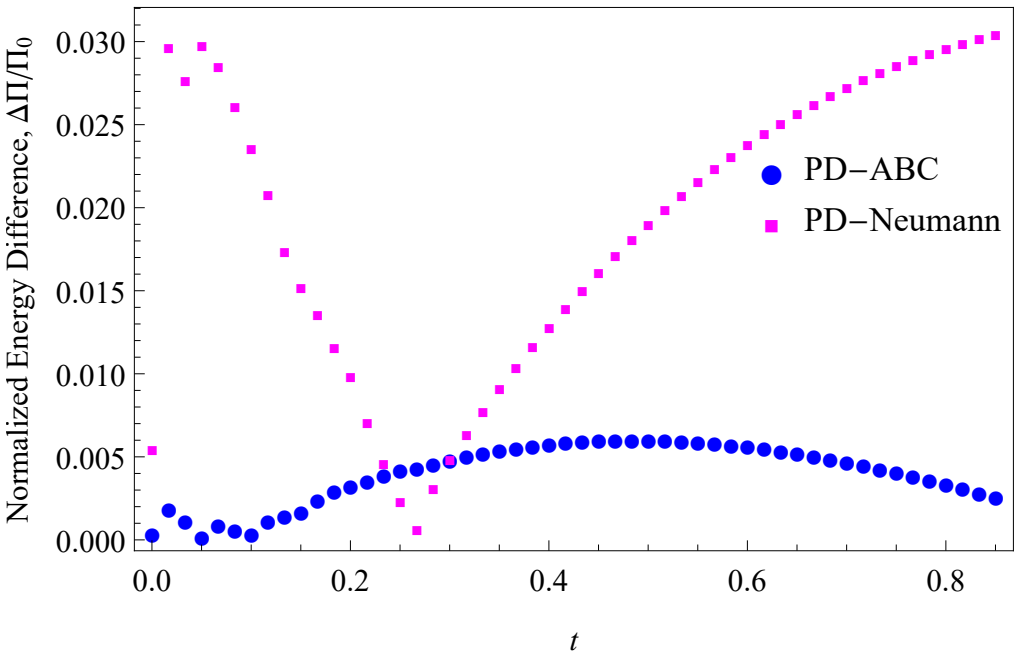


Figure 4.15: The normalized energy difference $\Delta\Pi/\Pi_0$ in the 2D unbounded peridynamic bi-material corrosion example in Section 4.1.5 for the truncated domain with and without ABCs. Reproduced from [123].

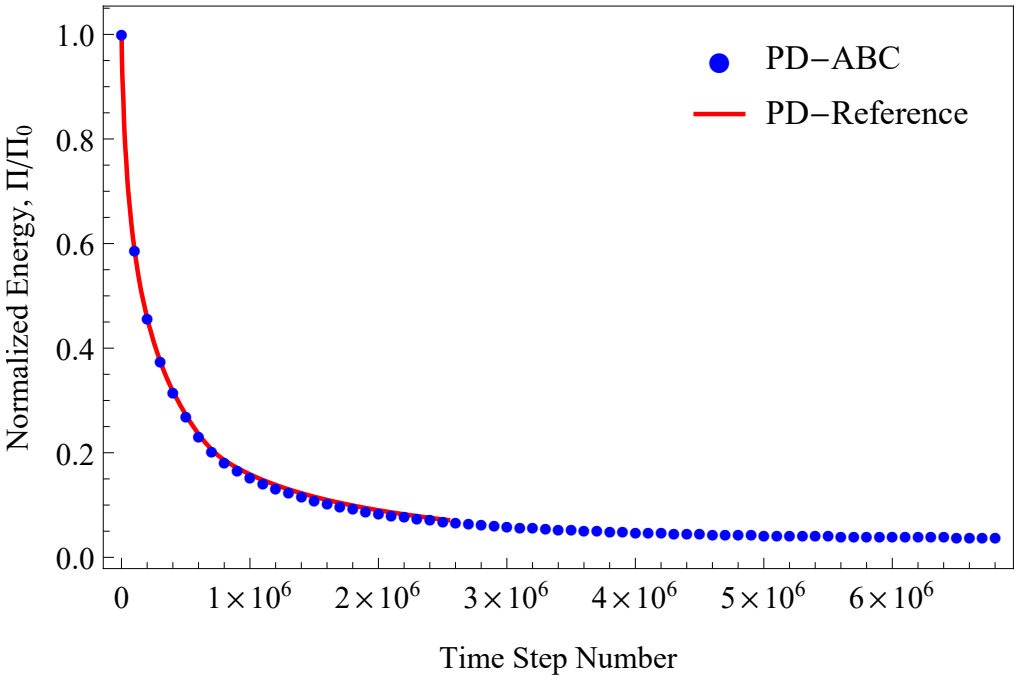


Figure 4.16: The variation of energy in the 2D unbounded peridynamic bi-material corrosion example in Section 4.1.5. Reproduced from [123].

### 3D Example of a Spherical Metallic Specimen

In this example, we extend the solution strategy for peridynamic bi-material corrosion problems to 3D unbounded domains. The dissolution process of a spherical metallic specimen, surrounded by an electrolyte, is simulated. The initial solid phase has a radius of 3.33 and the domain is truncated by a spherical boundary with a radius of 5. The peridynamic corrosion model parameters are set as $\delta = 0.2$, $C_{\text{sat}} = 0.8$, $\kappa_{\text{int}} = 795.77$, and $\kappa_{\text{liq}} = 7,957.7$. The absorbing layer has a thickness of $\delta$ and each absorbing node is associated with a cloud of radius $d_\infty = \delta/2$. The far-field solution in each cloud is approximated using $n_b = 605$ modes. The domain is discretized with a grid spacing of $\Delta x = \delta/2$, resulting in $523,155$ nodes for the computational domain (including $60,374$ absorbing nodes). A time step of $\Delta t = 3.33 \times 10^{-8}$ is used for time marching. Due to computational limitations, a quantitative validation of the solution against a reference solution obtained on a larger domain, as done in the previous 2D example, is not feasible. Therefore, only a qualitative comparison is performed in this 3D example.

Fig. 4.18 shows the metal concentration level and gradient field at different time instants for a corrosion problem on a spherical domain. Only a portion of the solution domain in the first octant is shown due to symmetry. The concentration plots indicate that the solid phase gradually decreases over time, with the corrosion front moving towards the center of the sphere. The gradient field results demonstrate that the solid concentration diffuses outwards from the domain with a flux perpendicular to the truncation surface, indicating the proper performance of the absorbing layer. The energy variation over time is presented in Fig. 4.19, showing a monotonic dissipation of energy without any instability observed. The calculations were performed for over $2 \times 10^6$ time steps.

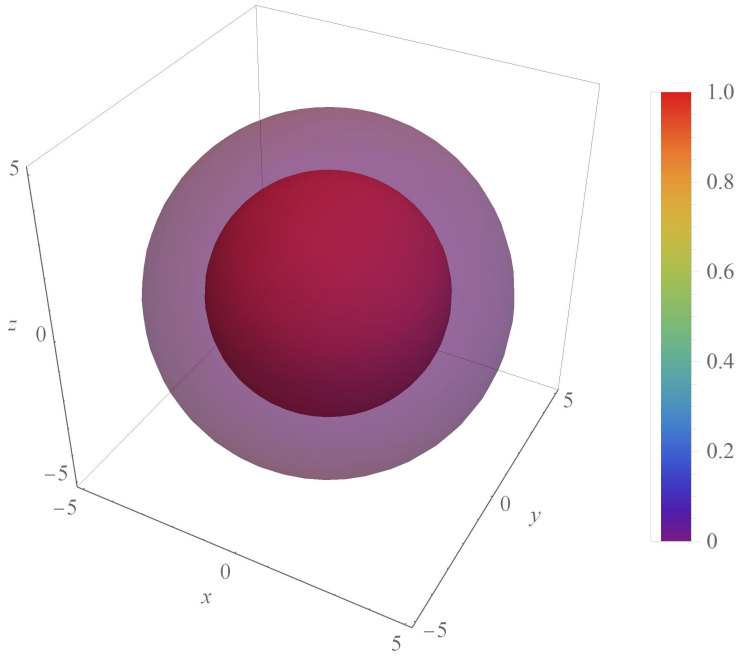


Figure 4.17: The initial concentration field in the 3D unbounded peridynamic bi-material corrosion example in Section 4.1.5. Reproduced from [123].

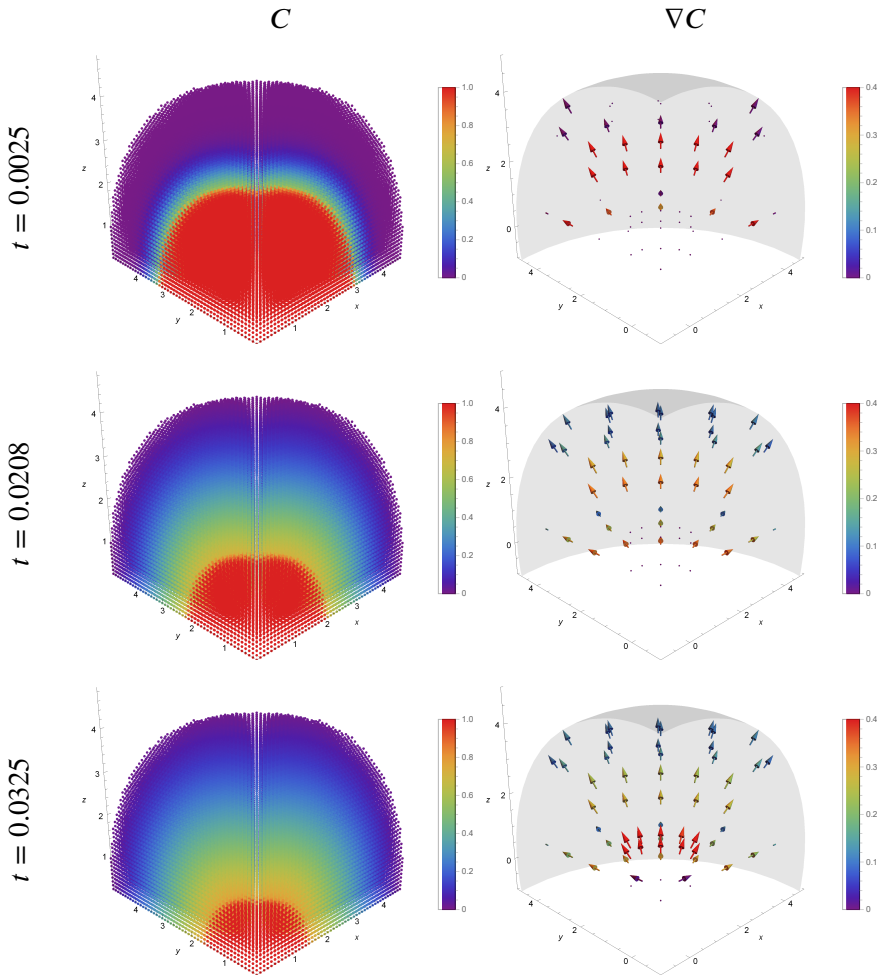


Figure 4.18: The concentration field (left column) and the gradient field (right column) within the first octant of the global coordinate system in the 3D unbounded peridynamic bi-material corrosion example in Section 4.1.5. Reproduced from [123].

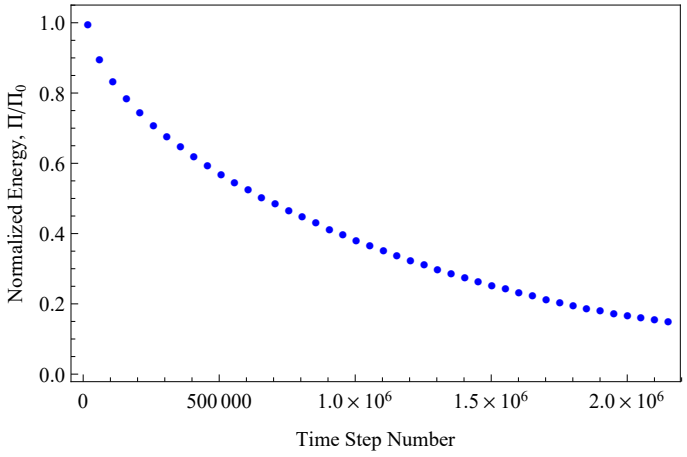


Figure 4.19: The variation of energy in the 3D unbounded peridynamic bi-material corrosion example in Section 4.1.5. Reproduced from [123].

## 4.2 Peridynamic Scalar Waves on Unbounded Domains

In the subsequent section, we expand the methodology discussed in Section 4.1, which addressed classical (local) and peridynamic diffusion-type unbounded domain problems, to tackle the viscous scalar wave equation in 2D for both CCM and PD. Similar to the approach in Section 4.1.1, we derive fundamental solutions for the peridynamic scalar wave equations using both constant and linear influence functions from (2.12) and (2.13). We construct a basis of feasible modes oriented to effectively transmit incident waves towards the far-field, aligning closely with the outward-pointing boundary normal. For peridynamic scalar wave problems, it is crucial to match the dispersion relations of these modes with the numerical discretization scheme used in the near-field, particularly under conditions of increased nonlocality (i.e., a large $\delta$ horizon relative to the grid spacing), to ensure numerical accuracy and stability. This condition is more critical for wave-type problems compared to peridynamic diffusion-type issues, which maintain high accuracy even when employing CCM model dispersion relations. We also explore the influence of the collocation procedure and the selection of feasible collocation points to ensure numerical stability, a common challenge in collocation schemes and similar numerical techniques. In Section 4.2.6, the applicability of the proposed ABCs is demonstrated for 2D CCM models solved via the FEM and compared to conventional first-order ABCs, showing enhanced accuracy and better handling of numerical issues arising from domain corners, typically a source of instabilities in conventional ABCs. Furthermore, as detailed in Section 4.2.7, the proposed ABCs adeptly manage complex wave patterns with various incident angles at the absorbing boundary layer, caused by scatterers within the near-field domain. This numerical study has been published and is further elaborated in [59].

### 4.2.1 Fundamental Solutions for Peridynamic Scalar Waves

In this section, we derive the fundamental solutions (or modes) for the wave propagation problem in the far-field using complex-valued EBFs. The methodology follows the approach outlined in Section 4.1.1 for diffusion-type problems. Although demonstrated in 2D, the same principles can be applied in 3D. We begin by considering a generic harmonic mode given by

$$\psi(\mathbf{x}, t) := \exp(\imath \boldsymbol{\alpha} \cdot \mathbf{x} + \imath \bar{\omega} t), \quad \boldsymbol{\alpha} = (\alpha_x, \alpha_y)^{\mathrm{T}}, \tag{4.36}$$

where $\alpha_x, \alpha_y, \bar{\omega} \in \mathbb{R}$. Here, $\imath$ is the imaginary unit defined by $\imath^2 = -1$. The components of $\boldsymbol{\alpha}$ are defined analogously to (4.7) as $\alpha_x = k \cos\phi$ and $\alpha_y = k \sin\phi$, where $k$ controls the spatial fluctuation of the wave and $\phi$ determines its direction. By substituting the general mode from equation (4.36) into the homogeneous far-field classical scalar wave equation (2.37) (with a zero right-hand side), we derive the expression

$$\left[-\bar{\omega}^2 + \chi^2 k^2 (\cos^2\phi + \sin^2\phi) + 2d\imath\bar{\omega}\right] \exp(\imath \boldsymbol{\alpha} \cdot \mathbf{x} + \imath \bar{\omega} t) = 0. \tag{4.37}$$

To obtain the solution, the expression within the square brackets must equal zero, yielding

$$\bar{\omega}^2 - 2d\imath\bar{\omega} - \chi^2 k^2 = 0. \tag{4.38}$$

The quadratic equation yields the local characteristic dispersion relation, given by

$$\bar{\omega} = \imath d \pm \sqrt{-d^2 + k^2 \chi^2}. \tag{4.39}$$

Substituting this result into (4.36), we obtain the modes for the classical scalar wave equation as

$$\psi(\mathbf{x},t) = \exp(-dt)\exp\left(\imath\boldsymbol{\alpha}\cdot\mathbf{x} \pm \imath\sqrt{-d^2+k^2\chi^2}t\right). \tag{4.40}$$

Similarly, inserting the generic mode (4.36) into the homogeneous far-field peridynamic scalar wave equation in (2.40), yields

$$\ddot{\psi}(\mathbf{x},t) - \int_{\mathcal{H}_\mathbf{x}} c_s\omega(\|\mathbf{x}'-\mathbf{x}\|)\frac{\psi(\mathbf{x}',t)-\psi(\mathbf{x},t)}{\|\mathbf{x}'-\mathbf{x}\|^p}\mathrm{d}V_{\mathbf{x}'} + 2d\dot{\psi}(\mathbf{x},t) = 0. \tag{4.41}$$

By shifting the integration region to the neighborhood $\mathcal{H}$ around the origin with horizon $\delta$, we can express (4.41) as

$$\left[-\bar{\omega}^2 - \int_{\mathcal{H}} c_s\omega(\|\boldsymbol{\xi}\|)\frac{\exp(\imath\boldsymbol{\alpha}\cdot\boldsymbol{\xi})-1}{\|\boldsymbol{\xi}\|^p}\mathrm{d}V_{\boldsymbol{\xi}} + 2d\imath\bar{\omega}\right]\exp(\imath\boldsymbol{\alpha}\cdot\mathbf{x}+\imath\bar{\omega}t) = 0. \tag{4.42}$$

A solution is obtained when the expression within the square brackets vanishes, thus

$$\bar{\omega}^2 - 2d\imath\bar{\omega} + \int_{\mathcal{H}} c_s\omega(\|\boldsymbol{\xi}\|)\frac{\exp(\imath\boldsymbol{\alpha}\cdot\boldsymbol{\xi})-1}{\|\boldsymbol{\xi}\|^p}\mathrm{d}V_{\boldsymbol{\xi}} = 0. \tag{4.43}$$

To evaluate the integral term, we employ the polar coordinate system, expressing the bond vector as $\boldsymbol{\xi} = r(\cos\theta,\sin\theta)$, and perform a Taylor expansion of the integrand. This yields

$$\begin{aligned}\int_{\mathcal{H}} c_s\omega(\|\boldsymbol{\xi}\|)\frac{\exp(\imath\boldsymbol{\alpha}\cdot\boldsymbol{\xi})-1}{\|\boldsymbol{\xi}\|^p}\mathrm{d}V_{\boldsymbol{\xi}} &= \int_0^\delta\int_0^{2\pi} c_s\omega(r)\frac{\exp(\imath r\eta)-1}{r^p}r\mathrm{d}\theta\mathrm{d}r \\ &= \int_0^\delta\int_0^{2\pi} c_s\omega(r)\frac{\left(\imath\eta r^2 - \frac{1}{2}\eta^2r^3 - \frac{1}{6}\imath\eta^3r^4 + \dots\right)}{r^p}\mathrm{d}\theta\mathrm{d}r,\end{aligned} \tag{4.44}$$

where $\eta := \boldsymbol{\alpha}\cdot(\cos\theta,\sin\theta) = k\cos(\phi-\theta)$. Considering a constant influence function $\omega$ (as given in (2.12)) and assuming $p = 2$ in the denominator, the integral term in (4.43) can be expanded using polar coordinates, yielding

$$\bar{\omega}^2 - 2d\imath\bar{\omega} + \left[-\frac{1}{4}\pi c_s(k\delta)^2 + \frac{1}{128}\pi c_s(k\delta)^4 - \frac{1}{6912}\pi c_s(k\delta)^6 + \dots\right] = 0. \tag{4.45}$$

It is worth noting that while $p = 2$ is a common choice in certain physical applications [13], the value of $p$ is not restricted to a specific value in general. The quadratic equation for $\bar{\omega}$ yields the nonlocal characteristic dispersion relation of the far-field governing equation as

$$\bar{\omega} = \imath d \pm \sqrt{-d^2 + \frac{1}{4}\pi c_s(k\delta)^2 - \frac{1}{128}\pi c_s(k\delta)^4 + \frac{1}{6912}\pi c_s(k\delta)^6 + \dots.}. \tag{4.46}$$

For the specific choice of the micromodulus $c_s = \frac{4\chi^2}{\pi\delta^2}$, we can express (4.46) as

$$\bar{\omega} = \imath d \pm \sqrt{-d^2 + k^2\chi^2\left(1 - \frac{1}{32}(k\delta)^2 + \frac{1}{1728}(k\delta)^4 + \dots\right)}, \tag{4.47}$$

which, in the limit as $k\delta \to 0$, recovers the local characteristic dispersion relation given by (4.39). Inserting (4.47) into (4.36), we obtain the mode of the peridynamic scalar wave equation for $p = 2$ with a constant influence function (*cf.* (2.12)) as

$$\psi(\mathbf{x}, t) = \exp(-dt) \exp\left( \imath \boldsymbol{\alpha} \cdot \mathbf{x} \pm \imath \sqrt{-d^2 + k^2\chi^2 \left(1 - \frac{1}{32}(k\delta)^2 + \frac{1}{1728}(k\delta)^4 + \dots\right)} t \right). \tag{4.48}$$

For a linear influence function with $p = 2$, following the same procedure as before, we obtain the relation

$$\bar{\omega}^2 - 2d\imath\bar{\omega} + \left[ -\frac{1}{12}\pi c_s (k\delta)^2 + \frac{1}{640}\pi c_s (k\delta)^4 - \frac{1}{48384}\pi c_s (k\delta)^6 + \dots \right]. \tag{4.49}$$

Solving for $\bar{\omega}$ in (4.49), we obtain the dispersion relation given by

$$\bar{\omega} = \imath d \pm \sqrt{-d^2 + \frac{1}{12}\pi c_s (k\delta)^2 - \frac{1}{640}\pi c_s (k\delta)^4 + \frac{1}{48384}\pi c_s (k\delta)^6 + \dots.} \tag{4.50}$$

Choosing the micromodulus constant as $c_s = \frac{12\chi^2}{\pi\delta^2}$, the above equation can be written as

$$\bar{\omega} = \imath d \pm \sqrt{-d^2 + k^2\chi^2 \left( 1 - \frac{3}{160}(k\delta)^2 + \frac{1}{4032}(k\delta)^4 + \dots \right)}, \tag{4.51}$$

which in the limit as $k\delta \to 0$ also recovers the local characteristic dispersion relation (4.39). Insertion of (4.51) into (4.36) yields the mode of the peridynamic scalar wave equation for $p = 2$ given a linear influence function (*cf.* (2.13)) as

$$\psi(\mathbf{x}, t) = \exp(-dt) \exp\left( \imath \boldsymbol{\alpha} \cdot \mathbf{x} \pm \imath \sqrt{-d^2 + k^2\chi^2 \left( 1 - \frac{3}{160}(k\delta)^2 + \frac{1}{4032}(k\delta)^4 + \dots \right)} t \right). \tag{4.52}$$

Therefore, by selecting a specific influence function and value for $p$, we can construct modes that satisfy the governing equation in the far-field for the peridynamic scalar wave problem. However, to ensure that the modes satisfy the radiation condition at infinity, further considerations are required, which are addressed in the following section.

### Infinity Condition for Scalar Wave Equations

We start by focusing on a node $\mathbf{x}_i$ located on the absorbing boundary (or boundary layer in the peridynamic case) and its corresponding cloud $\Omega_i^\infty$, as depicted in Fig. 4.20. Each cloud has its own local Cartesian coordinate system $(\bar{x}, \bar{y})$, where the positive $\bar{x}$-axis is oriented towards the far-field. It is important to note that while the local cloud coordinate system in Fig. 4.4 for unbounded diffusion problems was oriented such that the bisection line of the axes is perpendicular to the absorbing boundary, in the case of wave problems, the orientation is chosen to be consistent with the conventions used in existing literature on ABCs. In such literature, it is often assumed that incident waves are absorbed along a local coordinate axis, and therefore, the orientation is kept consistent with that convention. We consider the local position vector $\bar{\mathbf{x}}$, which can be obtained through the coordinate transformation in (4.24) of a representative vector $\mathbf{x}$ with respect to the local coordinate system centered at $\mathbf{x}_i$.

Within the cloud $\Omega_i^\infty$, the field variable is denoted as $u_\infty(\bar{\mathbf{x}}, t)$ and approximated through a linear combination of modes as

$$\begin{aligned} u_\infty(\bar{\mathbf{x}}, t) = \sum_{l=1}^{n_\phi} \sum_{m=1}^{n_k} a_{l,m} \exp(-dt) \exp\left(\imath k_m \left(\cos\phi_l \bar{x} + \sin\phi_l \bar{y}\right) - \imath\tilde{\omega}(k_m)t\right) \\ + b_{l,m} \exp(-dt) \exp\left(\imath k_m \left(\cos\phi_l \bar{x} + \sin\phi_l \bar{y}\right) + \imath\tilde{\omega}(k_m)t\right), \end{aligned} \tag{4.53}$$

where $a_{l,m}$ and $b_{l,m}$ represent unknown coefficients, while $n_\phi$ and $n_k$ determine the number of modes, where the former indicates the number of wave directions, and the latter specifies the number of spatial wave fluctuations. The value $\tilde{\omega}(k_m)$ is determined by the characteristic dispersion relation of the governing equation corresponding to the problem. For example, for the dispersion relation of the classical wave in (4.39), it follows that

$$\tilde{\omega}(k_m) = \sqrt{-d^2 + k_m^2 \chi^2} \tag{4.54}$$

It is important to note that the damping coefficient $d$ should not be chosen arbitrarily high to ensure physical feasibility, and is limited by the characteristic dispersion relation. For instance, in (4.39), we have the constraint

$$d^2 \leqslant k_m^2 \chi^2, \quad \forall k_m. \tag{4.55}$$

Following the approach described in Section 4.2.1 for unbounded diffusion problems and considering the chosen orientation for the local coordinate system of the cloud in the unbounded wave propagation problem, we select the values of $\phi_l$ and $k_m$ from two symmetric intervals as

$$\begin{aligned} \phi_l &\in [-\Delta\phi, \Delta\phi], \qquad \Delta\phi \geq 0, \\ k_m &\in [-\Delta k, \Delta k], \qquad \Delta k > 0, \end{aligned} \tag{4.56}$$

where $\Delta\phi$ and $\Delta k$ are pre-determined values that control the selection of wave directions and fluctuations in space, respectively. In Section 4.1.3, an inequality condition (4.34) was derived to limit $\Delta k$ for diffusion problems, ensuring the stability of the numerical method based on the CFL condition and thus the spatial resolution of the computational domain. Similarly, for the wave propagation problem, we will apply a similar procedure based on the sampling theorem to provide boundaries for $\Delta k$, as proposed in [125, 95]. The choice of these parameters is crucial as it can impact the numerical stability and accuracy of the solution. Therefore, the selection of appropriate values for $\Delta\phi$ and $\Delta k$ should be made with care, taking into consideration the specific characteristics of the problem and the desired level of accuracy. In Section 4.2.3, we address this issue in more detail in the context of the numerical implementation of the proposed ABCs for the wave propagation problem. The different orientations described by $\Delta\phi$ in (4.56) define half-spaces centered at the cloud's central node $\Omega_i^\infty$ corresponding to the incident wave angles, and are depicted in Figure 4.21.

It is worth noting that when $\Delta\phi = 0$, the incident angle of the respective mode aligns parallel to the positive $\bar{x}$-axis. Analyzing a small region around $\Delta\phi = 0$, we observe that the first term in (4.53) corresponds to outgoing waves, while the second term represents incoming waves. To effectively absorb the incoming waves from the near-field at the truncating boundary, it is necessary to set the coefficients $b_{l,m}$ in (4.53) to zero. Consequently, the expression for $u_\infty(\bar{\mathbf{x}}, t)$ reads as

$$u_\infty(\bar{\mathbf{x}}, t) = \sum_{l=1}^{n_\phi} \sum_{m=1}^{n_k} a_{l,m} \exp(-dt) \exp\left(\imath k_m \left(\cos\phi_l \bar{x} + \sin\phi_l \bar{y}\right) - \imath\tilde{\omega}(k_m)t\right). \tag{4.57}$$

By expressing the field variable $u_\infty$ in polar coordinates $(\bar{x}, \bar{y}) = r(\cos\theta, \sin\theta)$, where $-\pi \leq \theta \leq \pi$, we arrive at the representation

$$\begin{aligned} u_\infty(r,\theta,t) &= \sum_{l=1}^{n_\phi}\sum_{m=1}^{n_k} a_{l,m}\exp(-dt)\exp\left(\imath k_m\left(r\cos\theta\cos\phi_l + r\sin\theta\sin\phi_l\right) - \imath\tilde{\omega}(k_m)t\right) \\ &= \sum_{l=1}^{n_\phi}\sum_{m=1}^{n_k} a_{l,m}\exp(-dt)\exp\left(\imath k_m r\cos\left(\theta-\phi_l\right) - \imath\tilde{\omega}(k_m)t\right). \end{aligned} \tag{4.58}$$

This expression describes the outgoing waves from the near-field. To ensure that only outgoing waves are present, the following condition

$$\cos\left(\theta - \phi_l\right) > 0, \quad \forall l, \tag{4.59}$$

must be satisfied. It can further be simplified to

$$-\frac{\pi}{2} + \phi_l < \theta < \frac{\pi}{2} + \phi_l. \tag{4.60}$$

The condition in (4.60) defines a half-space centered at $\mathbf{x}_i$ with an angle $\phi_l$ relative to the local $\bar{x}$-axis, representing the outward boundary normal. By adjusting $\phi_l$, we can accommodate incoming waves with different incident angles. In the following, we adopt a symmetric interval for $\phi_l$ as specified in (4.56) and address the selection of $\Delta\phi$ in Section 4.2.3.

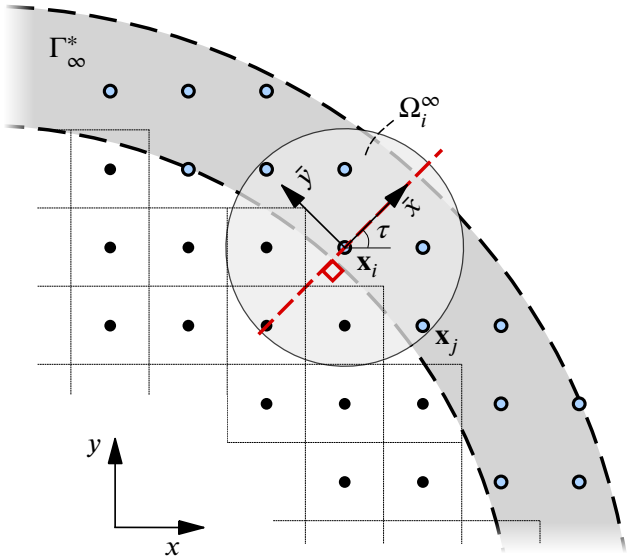


Figure 4.20: Illustration of a portion of the solution domain for the peridynamic scalar wave equation, focusing on the vicinity of the absorbing boundary layer, denoted as $\Gamma^*_\infty$, and a cloud region, $\Omega_i^\infty$, centered at a node $\mathbf{x}_i$ on the absorbing boundary. The cloud region is associated with a local coordinate system, $(\bar{x}, \bar{y})$, which is rotated by an angle $\tau$ to facilitate the far-field approximation. Notably, the orientation of the local coordinate system in this illustration is different from the choice provided in Fig. 4.4 for unbounded diffusion problems, such that the $\bar{x}$-axis aligns with the boundary normal. Reproduced from [59].

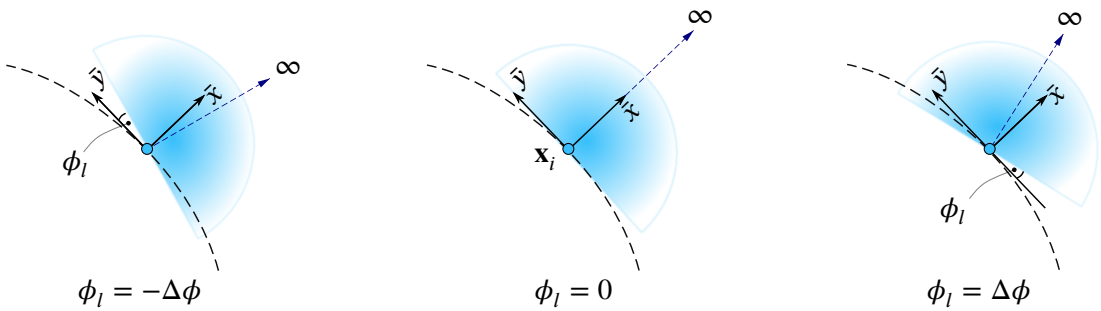


Figure 4.21: The propagation region of outgoing waves from a generic absorbing node towards the far-field, showcasing different values of the angle $\phi_l$, where $\phi_l$ falls within the interval $\Delta\phi[-1, 1]$. Reproduced from [59].

### 4.2.2 Solution Strategy for Unbounded Domain Scalar Waves

This section outlines the numerical solution approach for unbounded scalar wave problems, both classical and peridynamic. The near-field solution is discretized in time and space to approximate the solution at specific time instances $t^n$ and at nodes $\mathbf{x}_i$, using a fixed time step $\Delta t$. In the numerical examples provided below, we adopt the explicit velocity-Verlet scheme, as shown in (3.9), for time integration. This scheme is employed for both the classical scalar wave equation and the peridynamic wave equation. For the classical scalar wave equation described by (2.37), we utilize the FEM for spatial discretization, which transforms the weak form into a linear system of equations. On the other hand, for the peridynamic scalar wave equation in (2.40), we employ the standard discretization scheme as given in (3.3) to approximate its strong form. For the peridynamic case, the computational domain is discretized into a regular grid with a grid spacing of $\Delta x$ across the entire computational domain. Each grid cell's center represents a computational node, associated with a volume of $\Delta V_i = (\Delta x)^3$ in 3D or an area of $(\Delta x)^2$ in 2D. To handle the integration term in (2.40), we sum over the grid points within the peridynamic horizon $\delta$. Similar to the algebraic system represented in (eqref) for diffusion problems, in both cases (PD and FEM), the final system of equations is formulated as

$$\widetilde{\mathbf{M}}\ddot{\mathbf{U}}^n + \widetilde{\mathbf{D}}\dot{\mathbf{U}}^n + \widetilde{\mathbf{K}}\mathbf{U}^n = \widetilde{\mathbf{F}}^n, \tag{4.61}$$

where $\widetilde{\mathbf{M}}$ represents the mass matrix, the damping matrix is defined as $\widetilde{\mathbf{D}} := 2d\widetilde{\mathbf{M}}$, and $\widetilde{\mathbf{K}}$ is the stiffness matrix. At each time step $t^n$, we have the force vector $\widetilde{\mathbf{F}}^n$ on the right-hand side. The nodal acceleration, velocity, and displacement vectors at time $t^n$ are denoted as $\ddot{\mathbf{U}}^n$, $\dot{\mathbf{U}}^n$, and $\mathbf{U}^n$, respectively. To perform time integration, the velocity-Verlet scheme for both the nodal vector $\mathbf{U}^{n+1}$ and the first time derivative $\dot{\mathbf{U}}^{n+1}$ at the time $t^{n+1}$, are given by

$$\begin{aligned}
\mathbf{U}^{n+1} &= \mathbf{U}^n + \Delta t\dot{\mathbf{U}}^n + \frac{\Delta t^2}{2}\widetilde{\mathbf{M}}^{-1}\left(\widetilde{\mathbf{F}}^n - \widetilde{\mathbf{K}}\mathbf{U}^n - 2d\widetilde{\mathbf{M}}\dot{\mathbf{U}}^n\right), \\
\dot{\mathbf{U}}^{n+1} &= \frac{1}{1+\Delta td}\left(\dot{\mathbf{U}}^n + \frac{\Delta t}{2}\widetilde{\mathbf{M}}^{-1}\left(\widetilde{\mathbf{F}}^n - \widetilde{\mathbf{K}}\mathbf{U}^n - 2d\widetilde{\mathbf{M}}\dot{\mathbf{U}}^n\right) + \frac{\Delta t}{2}\widetilde{\mathbf{M}}^{-1}\left(\widetilde{\mathbf{F}}^{n+1} - \widetilde{\mathbf{K}}\mathbf{U}^{n+1}\right)\right).
\end{aligned} \tag{4.62}$$

### Conventional Absorbing Boundary Conditions

In this section, we provide the derivation of the conventional ABCs up to the first-order of approximation to effectively compare the results of the proposed scheme with the standard approaches in CCM for hyperbolic-type equations, specifically the scalar wave equation. The derivation of the conventional first-order ABCs for the classical (local) scalar wave equation in viscous media largely follows [97]. We assume that the local coordinate system at each point of the absorbing boundary $\Gamma_\infty$ is oriented so that the exterior domain lies in the half-space $x \geqslant 0$, where the $x$-axis is normal to the boundary and points towards the exterior domain. To this end, the governing equation of the far-field reads as follows:

$$\ddot{u} - \chi^2 \left(u_{xx} + u_{yy}\right) + 2d\dot{u} = 0, \quad x \geqslant 0, \quad y \in \mathbb{R}, \quad t > 0, \tag{4.63}$$

where $u_{xx}$ and $u_{yy}$ denote second partial derivatives with respect to the spatial coordinates in the $x$- and $y$-directions, respectively. The exterior domain is initially at rest:

$$\begin{aligned} u(\mathbf{x}, 0) &= 0, \quad x \geqslant 0, \quad y \in \mathbb{R}, \\ \dot{u}(\mathbf{x}, 0) &= 0, \quad x \geqslant 0, \quad y \in \mathbb{R}. \end{aligned} \tag{4.64}$$

In order to apply the Fourier transform to the field variable $u$ in time, we have to extend it to negative times by setting the corresponding values for $t < 0$ to zero. We denote the prolonged field variable for negative and positive times as $\tilde{u}$. As the initial conditions are zero according to (4.64) for $x \geqslant 0$, the following homogeneous wave equation is obtained for $\tilde{u}$:

$$\ddot{\tilde{u}} - \chi^2 \left(\tilde{u}_{xx} + \tilde{u}_{yy}\right) + 2d\dot{\tilde{u}} = 0, \quad x \geqslant 0, \quad y \in \mathbb{R}, \quad t \in \mathbb{R}. \tag{4.65}$$

Then, we apply the Fourier transform in the time $t$ and $y$-direction to obtain the ordinary differential equation in the dual coordinates $(k, \bar{\omega})$ as follows:

$$-\bar{\omega}^2 \hat{\tilde{u}} - \chi^2 \hat{\tilde{u}}_{xx} + \chi^2 k^2 \hat{\tilde{u}} + \imath\bar{\omega} 2d \hat{\tilde{u}} = 0, \tag{4.66}$$

where $\hat{\tilde{u}}$ denotes the Fourier transform of the prolonged field variable $\tilde{u}$. For a fixed tuple $(k, \bar{\omega})$ in the Fourier space, a general solution for (4.66) is given in the following form:

$$\hat{\tilde{u}}(x, k, \bar{\omega}) = \sum_{j=1}^{2} \alpha_j(k, \bar{\omega}) \exp\left(\lambda_j(k, \bar{\omega}) x\right), \tag{4.67}$$

where $\alpha_j(k, \bar{\omega})$ and $\lambda_j(k, \bar{\omega})$ denote unknown coefficients that generally depend on the dual coordinates $k$ and $\bar{\omega}$. By inserting the exponential ansatz function from (4.67) in (4.66), the following relation is obtained for a representative pair of coefficients $\lambda$ and $k$:

$$\lambda^2 = k^2 - \frac{\bar{\omega}^2}{\chi^2} + \imath\bar{\omega}\frac{2d}{\chi^2}. \tag{4.68}$$

Defining the auxiliary variable $z := \dfrac{\chi k}{\bar{\omega}}$, the two solutions of the quadratic equation (4.68) can be expressed as

$$\lambda_{1/2} = \pm\imath\frac{\bar{\omega}}{\chi}\sqrt{1 - z^2 - \imath z\frac{2d}{\chi k}}. \tag{4.69}$$

For the derivation of the first-order ABCs, we perform a first-order Taylor series expansion in (4.69) for $z$ around $z = 0$. In doing so, we obtain the following approximation:

$$\lambda_{1/2} \approx \pm \left( \imath \frac{\bar{\omega}}{\chi} + \frac{d}{\chi} \right). \tag{4.70}$$

Note that higher-order Taylor series expansions would likewise be conceivable; however, the subsequent equations turn out to be increasingly complex. Inserting the two approximate solutions from (4.70) in (4.67) and using the inverse Fourier transform, a general solution for $\tilde{u}$ reads as follows:

$$\begin{aligned} \tilde{u} = &\int_{-\infty}^{\infty} \int_{-\infty}^{\infty} \alpha_+(k, \bar{\omega}) \exp\left( \left( \imath \frac{\bar{\omega}}{\chi} + \frac{d}{\chi} \right) x + \imath k y + \imath \bar{\omega} t \right) \mathrm{d}k \mathrm{d}\bar{\omega} \\ &+ \int_{-\infty}^{\infty} \int_{-\infty}^{\infty} \alpha_-(k, \bar{\omega}) \exp\left( \left( -\imath \frac{\bar{\omega}}{\chi} - \frac{d}{\chi} \right) x + \imath k y + \imath \bar{\omega} t \right) \mathrm{d}k \mathrm{d}\bar{\omega}, \end{aligned} \tag{4.71}$$

where we distinguish the positive and negative solutions of (4.70) in terms of the corresponding coefficients $\alpha_+$ and $\alpha_-$, respectively. Since the term $\frac{d}{\chi}$ is nonnegative and the solution $\tilde{u}$ is bounded, the corresponding coefficient must be zero, i.e., $\alpha_+ \equiv 0$. Therefore, we can simplify (4.71) and express it as follows:

$$\tilde{u} = \int_{-\infty}^{\infty} \int_{-\infty}^{\infty} \alpha_-(k, \bar{\omega}) \exp\left( \left( -\imath \frac{\bar{\omega}}{\chi} - \frac{d}{\chi} \right) x + \imath k y + \imath \bar{\omega} t \right) \mathrm{d}k \mathrm{d}\bar{\omega}. \tag{4.72}$$

By evaluating (4.72) at $x = 0$, we recognize that $\alpha_-(k, \bar{\omega}) = \hat{\tilde{u}}(0, k, \bar{\omega})$. Subsequent differentiation of (4.72) with respect to $x$ and subtracting the right-hand side yields for $x = 0$:

$$\tilde{u}_x(0, y, t) - \int_{-\infty}^{\infty} \int_{-\infty}^{\infty} \hat{\tilde{u}}(0, k, \bar{\omega}) \left( -\imath \frac{\bar{\omega}}{\chi} - \frac{d}{\chi} \right) \exp(\imath k y + \imath \bar{\omega} t) \mathrm{d}k \mathrm{d}\bar{\omega} = 0, \tag{4.73}$$

where we emphasized the explicit variable dependencies of the prolonged field variable $\tilde{u}_x$ and its Fourier transform $\hat{\tilde{u}}$ in the notation. In Fourier space, (4.73) reads as follows:

$$\hat{\tilde{u}}_x(0, k, \bar{\omega}) + \imath \frac{\bar{\omega}}{\chi} \hat{\tilde{u}}(0, k, \bar{\omega}) + \frac{d}{\chi} \hat{\tilde{u}}(0, k, \bar{\omega}) = 0. \tag{4.74}$$

Multiplying (4.74) by $\chi$ and applying the inverse Fourier transform finally yields the first-order approximation to the exact ABCs as

$$\dot{u}(0, y, t) + \chi u_x(0, y, t) + d u(0, y, t) = 0, \tag{4.75}$$

which is a partial differential equation that has to be enforced on the absorbing boundary $\Gamma_\infty$ (at $x = 0$). In the form of a partial differential equation, it does not necessitate the previous superscript notation of the prolonged solution $\tilde{u}$ as we only consider the solution for $t \geq 0$. Note that, for a vanishing damping coefficient $d = 0$, the relation in (4.75) corresponds to the conventional zeroth-order ABCs provided in [97].

### Proposed Nonlocal Absorbing Boundary Conditions

The far-field approximation procedure closely follows the methodology outlined in Section 4.1.2 for unbounded diffusion problems, with the emphasis on the necessary adaptations required to address wave propagation problems. The ABCs are constructed using a linear combination of semi-analytical far-field solutions given in (4.58), with their unknown coefficients determined through a collocation procedure. Both the classical and peridynamic scalar wave equations follow the same process for constructing the ABCs, and no distinction is made between the two at this stage. Consequently, we obtain Dirichlet-type ABCs that are applicable to the nodes at each discrete time step through constant updating vectors. It is worth noting that while the classical scalar wave equation involves a boundary surface (depicted as $\Gamma_\infty$ in Fig. 4.1 for unbounded diffusion-type problems), the peridynamic scalar wave equation utilizes a boundary layer (represented as $\Gamma^*_\infty$ in Fig. 4.21).

We approximate the field variable and its first time derivative at the nodes within the cloud, $\bar{\mathbf{x}} \in \Omega_i^\infty$. Instead of using the time interval $[t^n, t^n + \Delta t]$ as utilized in Section 4.1.2 for unbounded diffusion-type problems and proposed in the original work [125], we now assume a symmetric interval $[t^n - \Delta t, t^n + \Delta t]$ where the approximation is considered valid. This choice has been found particularly effective in stabilizing the numerical simulation, especially for unbounded peridynamic scalar wave problems. Further details on the stability analysis are provided in the next section. By defining the approximation in the local time coordinate $\bar{t} \in [-\Delta t, \Delta t]$, we express the approximation around the time instant $t^n$ as

$$\begin{aligned} u^n_\infty(\bar{\mathbf{x}}, \bar{t}) &= \sum_{m=1}^{n_b} p^n_m \psi_m(\bar{\mathbf{x}}, \bar{t}) = \boldsymbol{\psi}(\bar{\mathbf{x}}, \bar{t})\mathbf{p}^n, \\ v^n_\infty(\bar{\mathbf{x}}, \bar{t}) &= \sum_{m=1}^{n_b} q^n_m \dot{\psi}_m(\bar{\mathbf{x}}, \bar{t}) = \dot{\boldsymbol{\psi}}(\bar{\mathbf{x}}, \bar{t})\mathbf{q}^n, \end{aligned} \tag{4.76}$$

where $u^n_\infty(\bar{\mathbf{x}}, \bar{t})$ and $v^n_\infty(\bar{\mathbf{x}}, \bar{t})$ represent the field variable and its first time derivative, respectively, at node $\bar{\mathbf{x}}$ and time $\bar{t}$ (in the local time). Here, $\psi_m$ and $\dot{\psi}_m$ denote the $m$th mode and its first time derivative, respectively, and $n_b$ is the number of modes. The constant unknown coefficients $p^n_m$ and $q^n_m$ correspond to the presumed *local* time interval around $t^n$. It is important to note that we assume two separate sets of coefficient vectors $\mathbf{p}^n$ and $\mathbf{q}^n$, allowing the approximation of $u^n_\infty$ and $v^n_\infty$ independently of each other. This approach is possible due to the construction of ABCs involving a WLS approximation of the coefficient vectors, which is generally not unique. Moreover, approximating the field variable and its first time derivative separately has been found to enhance numerical stability. In the rightmost expressions in (4.76), we adopt vector notation for simplicity, where

$$\begin{aligned} \boldsymbol{\psi}(\bar{\mathbf{x}}, \bar{t}) &:= \left(\psi_1(\bar{\mathbf{x}}, \bar{t}), \quad \psi_2(\bar{\mathbf{x}}, \bar{t}), \quad \cdots, \quad \psi_{n_b}(\bar{\mathbf{x}}, \bar{t})\right), \\ \dot{\boldsymbol{\psi}}(\bar{\mathbf{x}}, \bar{t}) &:= \left(\dot{\psi}_1(\bar{\mathbf{x}}, \bar{t}), \quad \dot{\psi}_2(\bar{\mathbf{x}}, \bar{t}), \quad \cdots, \quad \dot{\psi}_{n_b}(\bar{\mathbf{x}}, \bar{t})\right), \\ \mathbf{p}^n &:= \left(p^n_1, \quad p^n_2, \quad \cdots, \quad p^n_{n_b}\right)^{\mathrm{T}}, \\ \mathbf{q}^n &:= \left(q^n_1, \quad q^n_2, \quad \cdots, \quad q^n_{n_b}\right)^{\mathrm{T}}. \end{aligned} \tag{4.77}$$

Let us now introduce the vectors

$$\begin{aligned}\mathbf{g}^n(\bar{\mathbf{x}}) &:= \begin{pmatrix} u^n_\infty(\bar{\mathbf{x}},0) \\ u^n_\infty(\bar{\mathbf{x}},-\Delta t)\end{pmatrix} = \begin{bmatrix} \boldsymbol{\psi}(\bar{\mathbf{x}},0) \\ \boldsymbol{\psi}(\bar{\mathbf{x}},-\Delta t)\end{bmatrix}\mathbf{p}^n, \\ \mathbf{h}^n(\bar{\mathbf{x}}) &:= \begin{pmatrix} v^n_\infty(\bar{\mathbf{x}},0) \\ v^n_\infty(\bar{\mathbf{x}},-\Delta t)\end{pmatrix} = \begin{bmatrix} \dot{\boldsymbol{\psi}}(\bar{\mathbf{x}},0) \\ \dot{\boldsymbol{\psi}}(\bar{\mathbf{x}},-\Delta t)\end{bmatrix}\mathbf{q}^n,\end{aligned} \tag{4.78}$$

where the vectors $\mathbf{g}^n(\bar{\mathbf{x}})$ and $\mathbf{h}^n(\bar{\mathbf{x}})$ represents the field variable and its first time derivative at the local time steps $\bar{t}=0$ and $\bar{t}=-\Delta t$, respectively. To determine the unknown coefficient vectors $\mathbf{p}^n$ and $\mathbf{q}^n$, we organize, the nodal values within the cloud into vectors $\mathbf{G}^n$ and $\mathbf{H}^n$ as

$$\mathbf{G}^n = \begin{pmatrix} \mathbf{g}^n(\bar{\mathbf{x}}_i) \\ \vdots \\ \mathbf{g}^n(\bar{\mathbf{x}}_j) \\ \vdots \end{pmatrix} = \begin{pmatrix} u^n_{i,\infty} \\ u^{n-1}_{i,\infty} \\ \vdots \\ u^n_{j,\infty} \\ u^{n-1}_{j,\infty} \\ \vdots \end{pmatrix} = \mathbf{M}_G\mathbf{p}^n, \quad \mathbf{H}^n = \begin{pmatrix} \mathbf{h}^n(\bar{\mathbf{x}}_i) \\ \vdots \\ \mathbf{h}^n(\bar{\mathbf{x}}_j) \\ \vdots \end{pmatrix} = \begin{pmatrix} v^n_{i,\infty} \\ v^{n-1}_{i,\infty} \\ \vdots \\ v^n_{j,\infty} \\ v^{n-1}_{j,\infty} \\ \vdots \end{pmatrix} = \mathbf{M}_H\mathbf{q}^n, \quad \mathbf{x}_j \in \Omega^\infty_i, \tag{4.79}$$

where $u^n_{i,\infty} := u^n_\infty(\bar{\mathbf{x}}_i,0)$, $u^n_{j,\infty} := u^n_\infty(\bar{\mathbf{x}}_j,0)$, $u^{n-1}_{i,\infty} := u^n_\infty(\bar{\mathbf{x}}_i,-\Delta t)$, $u^{n-1}_{j,\infty} := u^n_\infty(\bar{\mathbf{x}}_j,-\Delta t)$, $v^n_{i,\infty} := v^n_\infty(\bar{\mathbf{x}}_i,0)$, $v^n_{j,\infty} := v^n_\infty(\bar{\mathbf{x}}_j,0)$, $v^{n-1}_{i,\infty} := v^n_\infty(\bar{\mathbf{x}}_i,-\Delta t)$, $v^{n-1}_{j,\infty} := v^n_\infty(\bar{\mathbf{x}}_j,-\Delta t)$, and $\mathbf{M}_G$ and $\mathbf{M}_H$ represent the moment matrices of the collocation procedure. If the number of nodes in the cloud is less than the number of modes, $n_b$, the coefficient vectors $\mathbf{p}^n$ and $\mathbf{q}^n$ can be obtained through

$$\begin{aligned}\mathbf{p}^n &= \mathbf{M}^+_G\mathbf{G}^n, \\ \mathbf{q}^n &= \mathbf{M}^+_H\mathbf{H}^n,\end{aligned} \tag{4.80}$$

where the Moore-Penrose generalized inverses of the respective moment matrices are denoted as $\mathbf{M}^+_G$ and $\mathbf{M}^+_H$. Using these generalized inverses and substituting the expressions from (4.80) for the coefficient vectors into (4.76), we obtain the expressions

$$\begin{aligned}u^n_\infty(\bar{\mathbf{x}},\bar{t}) &= \boldsymbol{\psi}(\bar{\mathbf{x}},\bar{t})\mathbf{M}^+_G\mathbf{G}^n, \\ v^n_\infty(\bar{\mathbf{x}},\bar{t}) &= \dot{\boldsymbol{\psi}}(\bar{\mathbf{x}},\bar{t})\mathbf{M}^+_H\mathbf{H}^n.\end{aligned} \tag{4.81}$$

To calculate the values of the field variable $u^{n+1}_i$ and its first time derivative $v^{n+1}_i$ at the central node of the cloud $\mathbf{x}_i$, we evaluate (4.81) at this node and for the local time $\bar{t}=\Delta t$ yielding

$$\begin{aligned}u^{n+1}_i &\approx u^n_\infty(\bar{\mathbf{x}}_i,\Delta t) = \boldsymbol{\psi}(\mathbf{0},\Delta t)\mathbf{M}^+_G\mathbf{G}^n = \mathbf{V}_G\mathbf{G}^n, \\ v^{n+1}_i &\approx v^n_\infty(\bar{\mathbf{x}}_i,\Delta t) = \dot{\boldsymbol{\psi}}(\mathbf{0},\Delta t)\mathbf{M}^+_H\mathbf{H}^n = \mathbf{V}_H\mathbf{H}^n,\end{aligned} \tag{4.82}$$

where the constant updating vectors $\mathbf{V}_G$ and $\mathbf{V}_H$ are associated with node $\mathbf{x}_i$ and can be computed prior to the simulation. Since the nodal values forming $\mathbf{G}^n$ and $\mathbf{H}^n$ on the right-hand sides of (4.82) are already known at the time instant $t^n$, we can conveniently apply Dirichlet-type ABCs to the absorbing boundary nodes during each time step. This results in an efficient extrapolation in time procedure, where only the nodal values are required when implementing the ABCs. As a consequence, the computational overhead is minimized, making the numerical approach computationally practical and efficient.

### 4.2.3 Implementation of Unbounded Domain Scalar Waves

This section delves into crucial considerations related to implementing ABCs for scalar wave propagation in numerical simulations, focusing on compatibility with the chosen near-field solution method and ensuring numerical stability. The numerical examples in this section, like those for diffusion problems in Section 4.1.5, were implemented in `C++` programming language. We used OpenMP directives for parallelization, the `libkdtree` library to construct neighborhoods and clouds, and the LAPACK library [5] for computing the Moore-Penrose generalized inverses in (4.80). While the proposed approach to tackle unbounded domain problems has shown robustness and accuracy for both classical and peridynamic diffusion problems, ensuring accurate and stable simulations for unbounded scalar wave propagation problems demands additional attention.

In both classical and peridynamic scalar wave problems in viscous media, similar to the discussion in Section 4.1.3 for diffusion problems, a crucial aspect involves the meticulous choice of the parameters $\Delta\phi$ and $\Delta k$, along with their corresponding ranges as specified in (4.56). For $\Delta\phi$, a range of $[-1, 1]$ with at least 10 subdivisions is proposed, and $\Delta\phi = \pi/4$ has been found to yield satisfactory results. To maintain stable numerical simulations and prevent unwanted wave reflections, it is essential to avoid excessively high $\Delta\phi$ values, while not restricting the range of incident waves that can be effectively absorbed too much. According to the Nyquist-Shannon sampling theorem, the second parameter, $\Delta k$, influencing the spatial mode fluctuations, should satisfy

$$0 < \Delta k \leqslant \frac{\pi}{\Delta x}, \tag{4.83}$$

where $\Delta x$ is the grid spacing. For the parameter $k$, we suggest using at least 10 evenly spaced subdivisions within the interval $[-\Delta k, \Delta k]$, similar to the choice made for the interval of $\phi$. Note that, the extrapolation procedure employed for the ABCs resembles a fixed-point iteration scheme over extended time periods. It is known that fixed-point iterations contract only when they are Lipschitz continuous. To ensure numerical stability in practice, we find that the norm of the updating vectors $\mathbf{V}_G$ and $\mathbf{V}_H$ should not exceed the value of 2, as two time steps are used for extrapolation in (4.82) over multiple time steps. The maximum norm $\|\mathbf{V}\|_{\max} := \max_{i=1,\dots,N} |V_i|$ for a vector $\mathbf{V} \in \mathbb{R}^N$ is preferred over the Euclidean norm in practice. For the following numerical examples, we select and report $\Delta k$ to satisfy this condition.

#### Matching Near-Field and Far-Field Dispersion Relations

For accurately transmitting outgoing waves to the far-field in numerical simulations, especially in the peridynamic case, we need to reevaluate the nonlocal characteristic dispersion relations presented in (4.47), and (4.51). These equations were derived at the continuum level and may not precisely capture the dynamics of discrete systems, which exhibit discrete dispersion relations. To address this, we utilize the standard meshfree modified one-point Gaussian quadrature of PD for discretizing the spatial integral in (4.43), instead of relying on the Taylor expansion as given in (4.44), yielding

$$\bar{\omega}^2 - 2d\imath\bar{\omega} + \sum_{j\in\mathcal{F}_0} c_s\omega(\|\mathbf{x}_j\|)\frac{\exp\left(\imath k(x_j\cos\phi + y_j\sin\phi)\right) - 1}{\|\mathbf{x}_j\|^p}\beta(\mathbf{x}_j)\Delta V_j \approx 0, \tag{4.84}$$

where $\mathcal{F}_0$ represents the set of family nodes around the origin. The solution that satisfies the quadratic expression on the left-hand side of (4.84) yields the *nonlocal numerical dispersion rela-*

*tion*, given by

$$\bar{\omega} = \imath d \pm \sqrt{-d^2 - \sum_{j \in \mathcal{F}_0} c_s \omega(\|\mathbf{x}_j\|) \frac{\exp\left(\imath k \left(x_j \cos\phi + y_j \sin\phi\right)\right) - 1}{\|\mathbf{x}_j\|^p} \beta(\mathbf{x}_j) \Delta V_j}, \tag{4.85}$$

which is consistent with the standard discretization scheme of PD and ensures accurate representation of the nonlocal dynamics in the discrete system. It is important to note that this procedure can also be applied to other discretization schemes used for the near-field solution in a similar manner. Unlike previous works [125, 95], which primarily focused on local equations, the current approach involves selecting modes that align with the dispersion relation of the discrete nonlocal system. This alignment is crucial for ensuring numerical stability and accuracy when dealing with nonlocal wave problems.

Fig. 4.22 presents a comparison of the nonlocal numerical dispersion relation (4.85) for a selected value of $\delta = 2$, considering negligible damping ($d = 0$) and a constant influence function $\bar{\omega}$ as given in (2.12). The figure shows this nonlocal numerical dispersion relation in contrast with the corresponding nonlocal characteristic dispersion relation derived from a Taylor expansion (4.47) and the local characteristic dispersion relation (4.39). We analyze two cases for the nonlocal characteristic dispersion relation: one with a lower-order (4th-order) and one with a higher-order (26th-order) Taylor expansion. Similarly, we investigate the nonlocal numerical dispersion relation for two scenarios: a coarser ($\Delta x = \delta/2$) and a finer discretization ($\Delta x = \delta/8$). As $k\delta \to 0$, both the continuum and discrete dispersion relations approach the linear, local dispersion relation, but they deviate significantly for larger values of $k\delta$. To accurately compute the nonlocal characteristic dispersion relation, employing a high-order Taylor expansion or fine discretization is essential, yielding comparable results. Fig. 4.22 illustrates the differences between the discrete and continuum-level dispersion relations, emphasizing the need to match the dispersion relations of the far-field modes with the discrete near-field dynamics. To ensure compatible and accurate ABCs, the neighboring points, mesh size, and horizon used to evaluate the nonlocal numerical dispersion relation (4.85) must align with the parameters of the near-field, ensuring the correspondence between the dispersion relations used in the far-field and those of the (discrete) near-field.

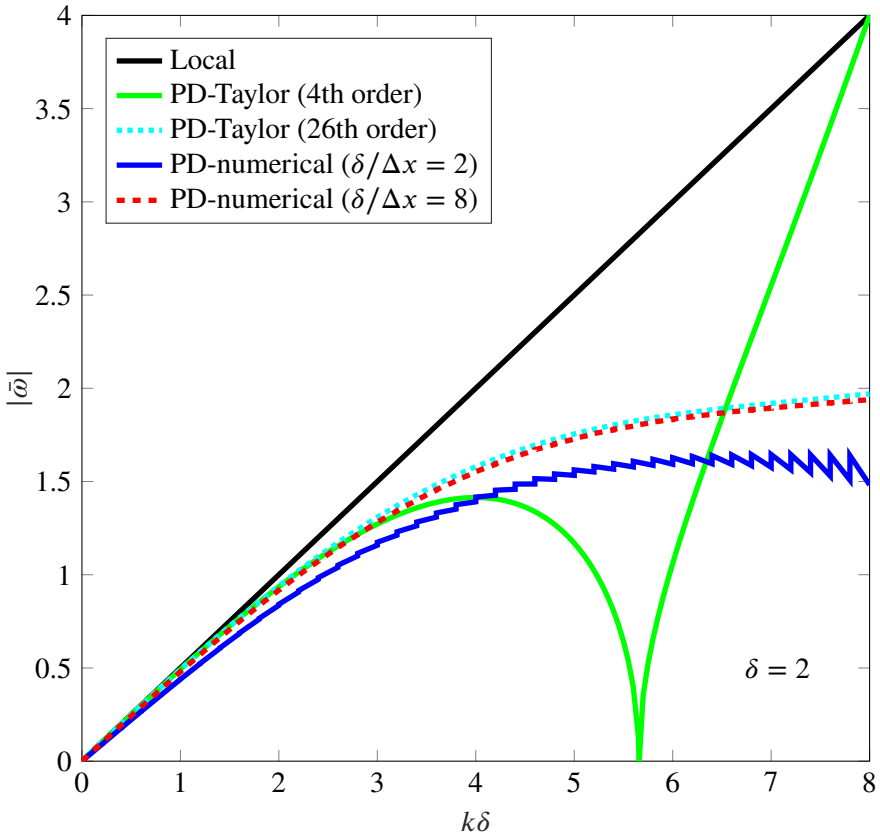


Figure 4.22: Comparison between the nonlocal numerical dispersion relation (*PD-numerical*) and the nonlocal characteristic dispersion relation based on Taylor expansions (*PD-Taylor*), as well as the linear, local characteristic dispersion relation (*Local*) in a non-viscous medium ($d = 0$). The figure depicts the PD-Taylor for two different Taylor expansion orders (4th and 26th orders) and PD-numerical for two distinct discretizations ($\delta/\Delta x = 2, 8$). To avoid negative ranges, the graphs are plotted over the absolute value of $\bar{\omega}$. Reproduced and adjusted from [59].

### Greedy Sparse Method Approach for Improved Conditioning

The issue of numerical stability in scalar wave propagation problems is closely related to the selection of collocation nodes in (4.79) and the solution procedure involving the Moore-Penrose inverse matrices in (4.80). In practice, it has been found that using all family nodes within the cloud, $\Omega_i^\infty$, as shown in the top-left part of Fig. 4.23, can lead to numerically unstable simulations due to poorly conditioned moment matrices in (4.79). The observed instability may be attributed to the fact that the extrapolation on the central node $\mathbf{x}_i$ incorporates information from nodes that are spatially ahead of it. In the context of the peridynamic scalar wave equation, this implies that the temporal prediction of the outgoing wavefront on the central node $\mathbf{x}_i$ includes information from nodes to which the wavefront has not yet arrived. To address this stability issue, we introduce an extrapolation region $\mathcal{E}_i^\infty(\Delta\phi) \subset \Omega_i^\infty$ for the absorbing node $\mathbf{x}_i$. This region is a conic subset of the cloud and is defined as

$$\mathcal{E}_i^\infty(\Delta\phi) = \left\{ \bar{\mathbf{x}} \in \Omega_i^\infty \,:\, \frac{\pi}{2} + \Delta\phi < \arg(\bar{\mathbf{x}}) < \frac{3\pi}{2} - \Delta\phi \right\}. \tag{4.86}$$

The illustration of this region can be found in the top-right part of Fig. 4.23. To enhance numerical stability in our simulations, we consider nodes only within the extrapolation region, which can be achieved by limiting the spread of a cone around the central node $\mathbf{x}_i$. This extrapolation region, denoted as $\mathcal{E}_i^\infty(\Delta\phi)$, is defined by the angle $\Delta\phi$, and for our purposes, we set it to $\pi/4$, a value that accommodates the maximum angle of incident waves and yields satisfactory results in practice.

An equally important consideration is the selection and number of collocation nodes employed within the extrapolation region, especially for scenarios involving high resolutions or large horizons. Efficient meshfree methods aim to strike a balance between minimizing computational costs and achieving the smallest possible error [111]. It is beneficial to use a minimum number of nodes with adequate distances from each other to improve the conditioning of the moment matrices in (4.80) and ensure the numerical stability of the simulation. Previous research has explored various techniques for identifying an optimal set of collocation nodes, often referred to as *greedy sparse methods* [111, 43]. However, these methods can be iterative and computationally expensive. In contrast, we propose a straightforward and efficient approach based on the meshfree WLS collocation scheme, which was introduced and utilized in Section 3.2 to develop efficient numerical solution techniques for peridynamic models. First, we introduce a fixed set of *auxiliary nodes* within the cloud, represented by blue markers in the bottom-left illustration of Fig. 4.23. We then restrict the collocation process to the nearest nodes to these auxiliary nodes within the extrapolation region $\mathcal{E}_i^\infty(\Delta\phi)$, as depicted in the bottom-right illustration of Fig. 4.23. This reduction in the number of nodes involved in collocation leads to improved computational performance and better conditioning of the moment matrices. It's important to note that the arrangement of collocation nodes should ideally be symmetric to avoid potential instabilities [111].

It is important to highlight that this approach, which utilizes EBFs, differs from other meshfree approaches like the FPM. In the FPM, increasing the number of nodes in the cloud improves the solution accuracy due to fewer basis functions available. However, with EBFs, we require a higher number of modes, leading to a higher ratio of modes to collocation nodes. This increase in modes is necessary to efficiently absorb incoming waves with various wave numbers and orientations. Increasing the number and density of nodes in the cloud may adversely affect the conditioning of moment matrix and lead to instability. To further enhance the numerical stability of the collocation procedure, we suggest an iterative approach to reduce the node density. This involves decreasing the number of nodes along the cloud coordinate axes by a factor of 2, as conceptually depicted in the

lower right corner of Fig. 4.23. Although this approach may not yield the most optimal collocation nodes, as described in [111, 43], it has been observed to effectively enhance the conditioning of the moment matrices in (4.79). To ensure numerical stability prior to simulation, we recommend monitoring the condition numbers of the moment matrices. Based on our numerical investigations, condition numbers within the range of approximately $10^{11}$ to $10^{12}$ typically guarantee numerical stability. Therefore, we suggest to iteratively reduce the node density by a factor of 2 until the condition numbers fall within this specified range. This approach offers a user-friendly and practical means of ensuring numerical stability, especially for clouds with a large number of nodes that may lead to poor condition numbers. While it may not be the optimal choice of collocation nodes, it has proven effective in practice.

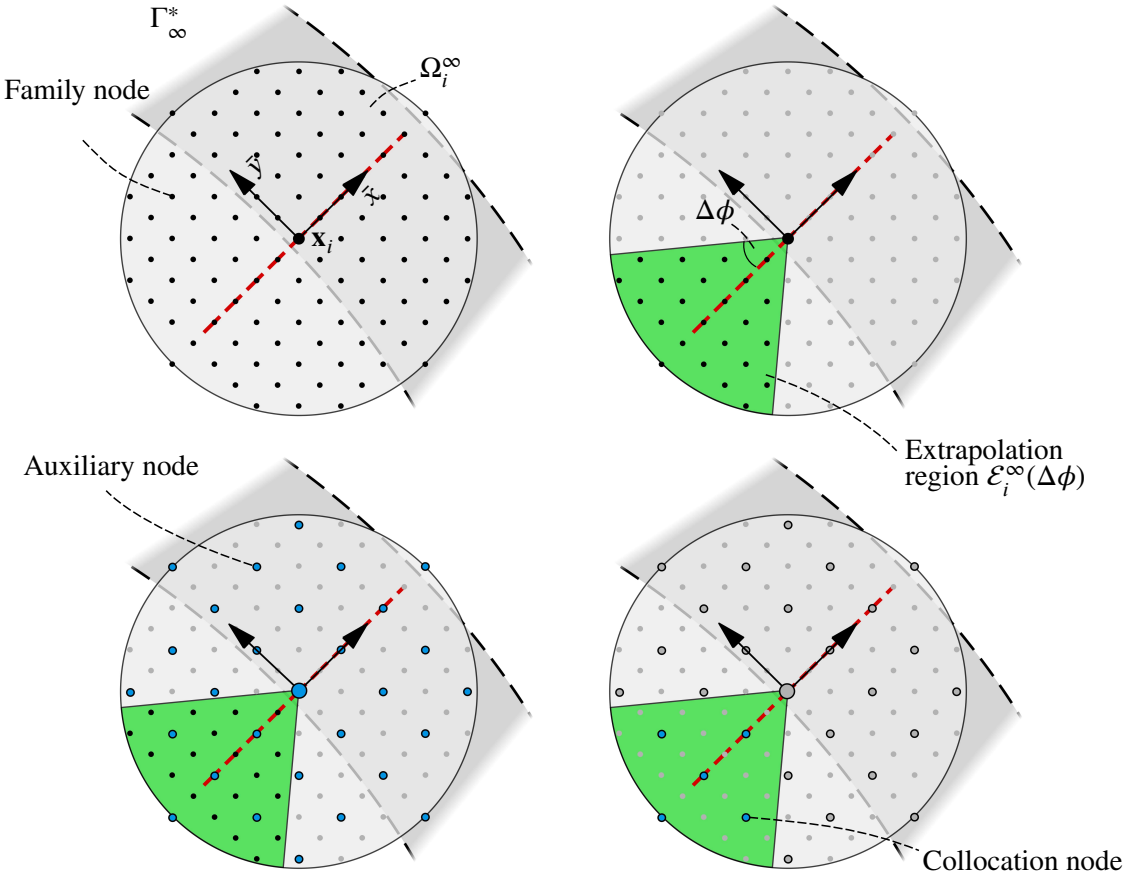


Figure 4.23: The procedure to select the collocation nodes: (top left) the neighborhood $\Omega_i^\infty$ of node $\mathbf{x}_i$ in the boundary layer $\Gamma_\infty^*$, including its whole family nodes, (top right) selection of the extrapolation region, (bottom left) setting the auxiliary grid centered at $\mathbf{x}_i$, and (bottom right) selection of the collocation nodes with respect to the auxiliary grid. Reproduced and adjusted from [59].

### 4.2.4 1D Peridynamic Wave Propagation

In this example, we investigate the numerical performance of the ABCs for peridynamic scalar wave propagation on a 1D unbounded viscous domain. We first compare the continuous and discrete dispersion relations to construct modes for the ABCs, ensuring matching dispersion relations between the near-field and the far-field. Next, we analyze the impact of the number of modes on the numerical solution accuracy. Finally, we test the constructed ABCs on a 1D highly dispersive peridynamic wave propagation system. Due to the presence of high-frequency components in the waves, fine spatial and temporal resolutions are required for computational feasibility, leading us to conduct the following investigations in 1D. Assuming the kernel exponent $p$ in (2.40) as 0, the homogeneous 1D peridynamic wave equation is given by

$$\ddot{u}(x,t) - \int_{-\delta}^{+\delta} c_s \omega(|\xi|)\,(u(x+\xi,t) - u(x,t))\,\mathrm{d}\xi + 2d\dot{u}(x,t) = 0. \tag{4.87}$$

To obtain the dispersion relation of the continuous system, we substitute the generic mode, given by $\psi(x,t) = \exp(\imath\alpha x + \imath\bar{\omega}t)$, for $u$ in (4.87) and obtain

$$\left(-\bar{\omega}^2 - \int_{-\delta}^{+\delta} c_s(\exp(\imath\alpha\xi) - 1)\mathrm{d}\xi + 2d\imath\bar{\omega}\right)\exp(\imath\alpha x + \imath\bar{\omega}t) = 0. \tag{4.88}$$

Following a procedure similar to (4.141), we arrive at the dispersion relation given by

$$\bar{\omega}^2 - 2d\imath\bar{\omega} = \int_{-\delta}^{+\delta} c_s(1 - \cos(\alpha\xi))\,\mathrm{d}\xi. \tag{4.89}$$

Assuming $c_s = \frac{3\chi^2}{\delta^3}$ where $\chi^2$ represents the propagation wave speed, the expression for $\bar{\omega}^2$ in (4.89) can be expressed in closed-form as

$$\bar{\omega}^2 - 2d\imath\bar{\omega} = \frac{6\chi^2(\alpha\delta - \sin(\alpha\delta))}{\alpha\delta^3}. \tag{4.90}$$

Notably, by employing a Taylor series expansion of $\sin(\alpha\delta)$ around the origin and assuming that $\alpha\delta \ll 1$, we obtain the expression

$$\bar{\omega}^2 - 2d\imath\bar{\omega} = \frac{6\chi^2(\alpha\delta - (\alpha\delta - \frac{(\alpha\delta)^3}{3!} + \ldots))}{\alpha\delta^3} \approx \chi^2\alpha^2, \tag{4.91}$$

which leads to the continuous dispersion relation of the classical (local) wave equation, given by

$$\bar{\omega} = \imath d \pm \sqrt{-d^2 + \chi^2\alpha^2}. \tag{4.92}$$

Let us consider a uniform spatial discretization of the system in question with $N+1$ points, denoted by $X = \{x_0, x_1, \ldots, x_N\}$, where the grid size is $\Delta x = \delta/m$ with $m \in \mathbb{N}$. This implies that $x_i = i\Delta x$ for $i = 0, 1, \ldots, N$. The governing equation of motion on the discrete spatial domain at time $t \geq 0$ can be expressed as

$$\ddot{u}_i - \sum_{\substack{j=i-m \\ j\neq i}}^{i+m} c_s \omega(|(j-i)\Delta x|)\left(u_j - u_i\right)\beta\left((j-i)\Delta x\right)\Delta x + 2d\dot{u}_i = 0, \tag{4.93}$$

where $u_i := u(x_i, t)$, $\dot{u}_i := \dot{u}(x_i, t)$ and $\ddot{u}_i = \ddot{u}(x_i, t)$. We consider the influence function according to (eqref) as $\bar{\omega}(|(j-i)\Delta x|) \equiv 1$ and once again choose $c_s = 3\chi^2/\delta^3$. To construct the ABCs using (4.82), we need modes that match the numerical dispersion relation given in (4.93). For this purpose, we insert the spatially discrete mode $\psi_i = \exp(\imath\alpha(i\Delta x) + \imath\bar{\omega}t)$ for $u_i$ into (4.93), resulting in

$$\left(-\bar{\omega}^2 - \sum_{\substack{j=i-m \\ j\neq i}}^{i+m} c_s \left(\exp(\imath\alpha(j-i)\Delta x) - 1\right)\beta((j-i)\Delta x)\Delta x + 2d\imath\bar{\omega}\right)\exp(\imath\alpha(i\Delta x) + \imath\bar{\omega}t) = 0. \tag{4.94}$$

Similar to the procedure in (4.85), we can replace the difference in spatial indices $(j-i)$ with a running index $l$ to obtain the numerical dispersion relation for the 1D system as

$$\bar{\omega} = \imath d \pm \sqrt{-d^2 - \sum_{\substack{l=-m \\ l\neq 0}}^{m} c_s \left(\exp(\imath\alpha l\Delta x) - 1\right)\beta(l\Delta x)\Delta x}. \tag{4.95}$$

Figure 4.24 compares the dispersion relations in (4.90), (4.92), and (4.95) for a case study with parameters $\chi^2 = 1$, $d = 0$, and $\delta = 10$. The numerical dispersion relation in (4.95) is plotted for three different grid spacings $\Delta x$, ranging from coarse to fine. As observed in the 2D investigation (see Fig. 4.22), as $\alpha\delta \to 0$, both the analytical and numerical peridynamic dispersion relations approach the local dispersion relation. However, significant deviations between the local and peridynamic dispersion relations appear for large values of $\alpha\delta$. This discrepancy indicates that the ABCs developed for classical models may not directly apply to peridynamic models. To obtain accurate ABCs, it becomes crucial to construct the modes used for the far-field solution with a numerical dispersion relation that closely emulates the discrete near-field dynamics. Interestingly, when $\delta/\Delta x \approx 10$, the numerical dispersion relation closely aligns with the analytical one. This finding suggests that employing the analytical dispersion relation would lead to computationally expensive calculations to achieve accurate ABCs, even in 1D. Thus, adopting the numerical dispersion relation proves to be a viable and computationally efficient strategy, particularly when $\delta/\Delta x$ is not excessively large.

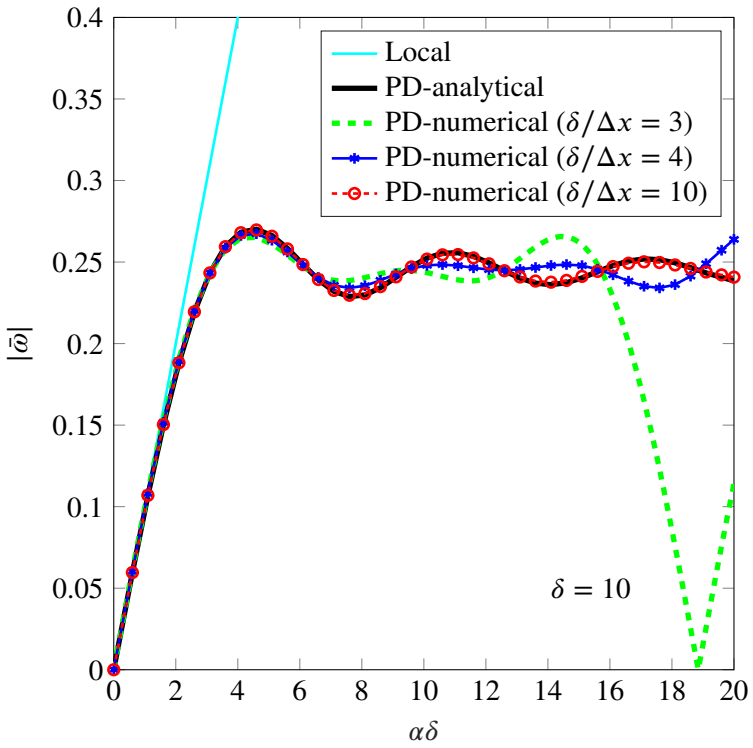


Figure 4.24: Comparison of the peridynamic dispersion relations in 1D at both the discrete and continuum levels for the case study in 4.2.4. The graphs are plotted for the absolute values of $\bar{\omega}$ to avoid negative ranges. Reproduced from [124].

### Effect of Mode Quantity on Numerical Solution Accuracy

In this section, we demonstrate the significance of using an appropriate number of modes for the construction ABCs to achieve accurate solutions. For this purpose, we investigate a wave propagation problem in a 1D non-viscous ($d = 0$) unbounded domain $(-\infty, \infty)$ governed by the equation in (4.87). The propagation wave speed is chosen as $\chi^2 = 1$, and the peridynamic horizon is set to $\delta = 0.6$. Our computational domain is confined to the region $(-10, 10)$, while for validation, we take the solution from an extended domain $(-50, 50)$ as the reference solution. The initial displacement condition that serves as the excitation source is given by

$$u^0(x) = \exp(-x^2). \tag{4.96}$$

We discretize the spatial domain using a grid spacing of $\Delta x = 0.2$, resulting in 501 nodes for the extended domain and 101 nodes for the truncated (computational) domain. This setup includes three absorbing nodes on each side of the computational domain. The simulation spans a time duration of 25 units, ensuring that $u$ near the boundaries of the extended domain remains nearly zero. The simulation employs the velocity-Verlet algorithm for time integration with a time step of $\Delta t = 0.001$, resulting in a total of 25,000 time steps. For the evaluation, we set $\Delta\alpha = \pi/2$, and to assess the accuracy of the method, we examine different numbers of modes separately ranging from 1 to 5.

Fig. 4.25 compares the accuracy of the ABCs using different numbers of modes ($n_b$). The plot shows the energy difference between the solutions of the truncated domain with varying modes and the reference solution over time. Increasing the number of modes in the ABCs leads to higher accuracy until it reaches a certain level, constrained by the discretization. After surpassing a specific number of modes (four in this case), further additions do not significantly improve the accuracy, indicating convergence. Fig. 4.26 presents the displacement field results obtained by the proposed method using five modes, showing close agreement with the reference solution at four different time instants.

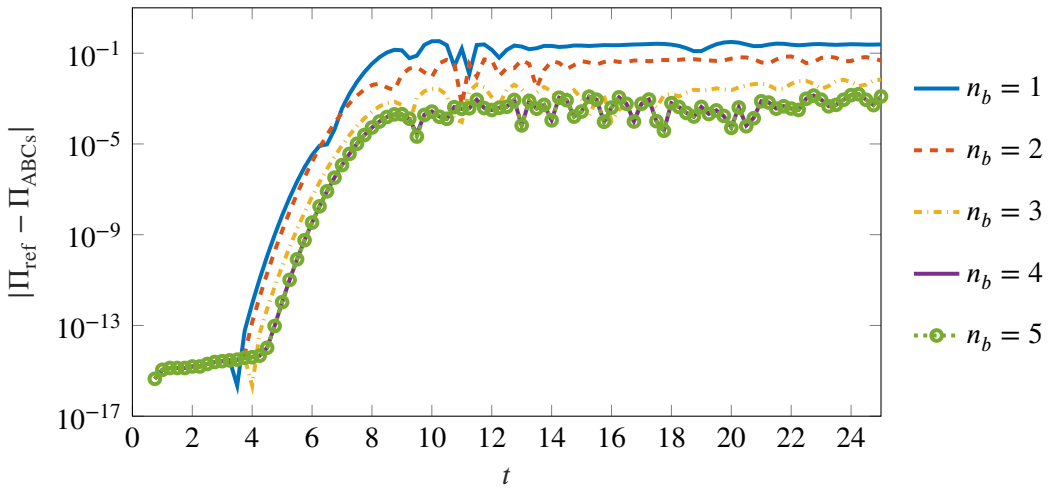


Figure 4.25: The accuracy of the ABCs on a 1D non-viscous unbounded domain is compared in terms of total energy, using different numbers of modes $n_b$. Reproduced from [124].

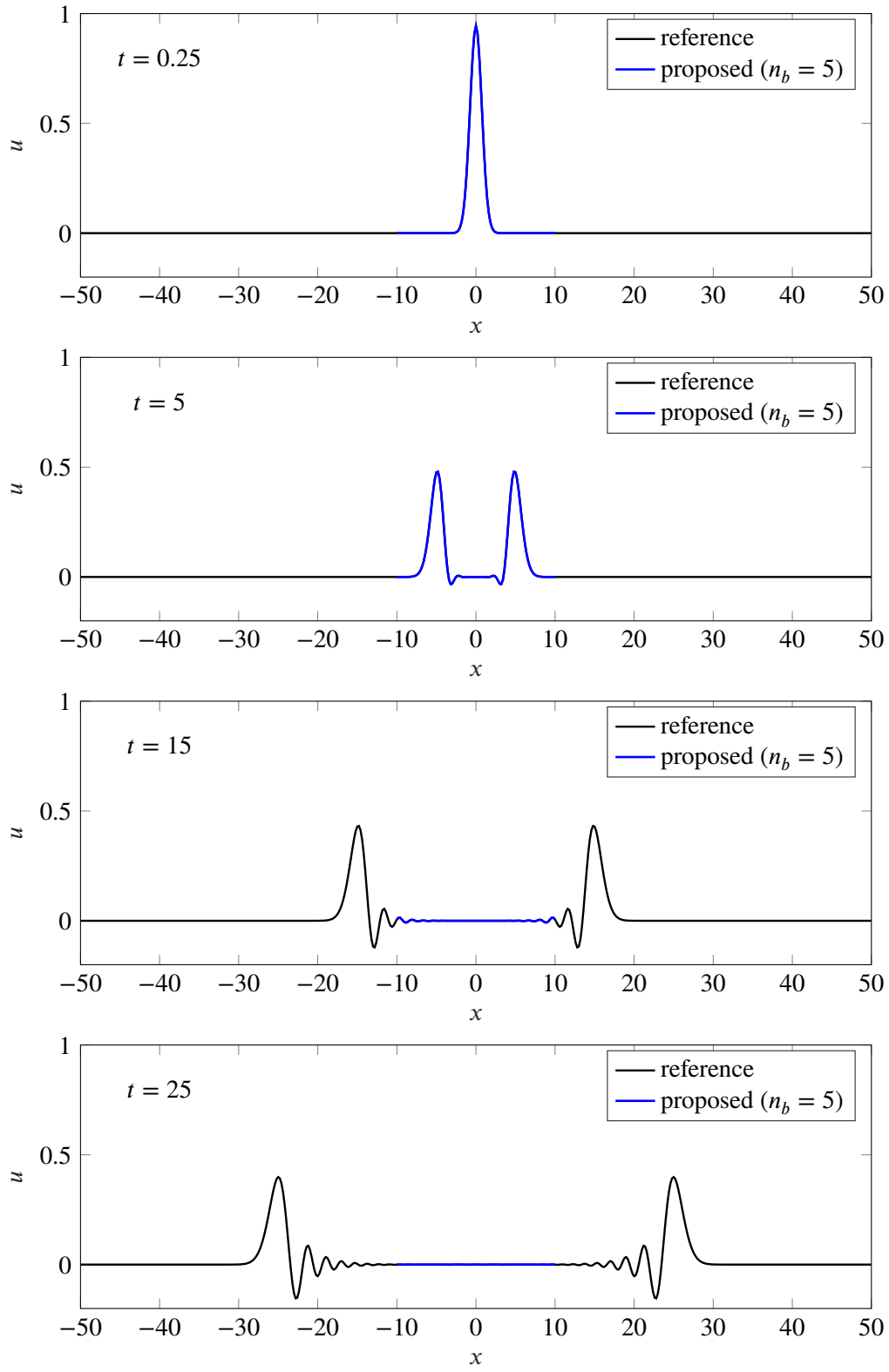


Figure 4.26: The displacement field at four different time instants of the 1D non-viscous wave propagation problem in Section 4.2.4. Reproduced and adjusted from [124].

**Assessing the Numerical Performance on Highly Dispersive Waves**

In this section, we assess the numerical performance of the ABCs on a 1D viscous unbounded domain containing waves with high-frequency components. The computational domain is defined as $(-10, 10)$, and the system parameters are set to $\chi^2 = 10$ and $d = 5 \times 10^{-4}$. For the space discretization, we choose $\Delta x = 0.01$, leading to 2001 nodal points inside the domain and 25 absorbing nodes at each boundary. The horizon size is fixed at $\delta = m\Delta x = 0.25$ with $m = 25$, and the time step is set to $\Delta t = 1 \times 10^{-4}$. The simulation runs over a total of $150,000$ time steps. To obtain a reference solution, we use a larger computational domain of $(-60, 60)$ with the same system parameters, resulting in a total of 12001 nodal points. To introduce high-frequency components in the wave, we initialize the field variable with a steep pulse represented by

$$u_i^0 = \exp\left(-20 \log\left(2\right) x_i^2\right). \tag{4.97}$$

This initial condition generates a propagating wave exhibiting highly dispersive behavior, as depicted in Fig. 4.27. To construct the modes required for the far-field approximation, we select them from a symmetric interval given by

$$\alpha_l \in [-\Delta\alpha, \Delta\alpha], \quad \Delta\alpha > 0, \quad l = (0, 1, \dots, n_b), \tag{4.98}$$

where we choose $\Delta\alpha = 1$ and divide the interval into $n_b = 20$ evenly spaced subdivisions. To guarantee numerical stability before the simulation, we follow the stabilization steps described in Section 4.2.3. By excluding nodes ahead of the absorbing boundary node within the clouds, and monitoring the condition numbers of moment matrices and the norms of updating vectors, we ensure stability. In this example, no further node reduction is required for the absorbing boundary clouds, as illustrated in Fig. 4.23, but it may become necessary for different system parameters. Therefore, we recommend monitoring the condition numbers and updating vector norms to ensure numerical stability prior to the simulation, if needed, reducing the number of cloud nodes until the condition numbers and updating vector norms fall within the specified ranges, as provided in Section 4.2.3.

Fig. 4.27 displays the results of the reference solution and the truncated domain equipped with ABCs. Notably, the waves exhibit high frequency tails due to the chosen horizon size of $\delta = 0.25$ and the initial condition (see e.g., [117]). The truncated domain exhibits a remarkable resemblance to the reference solution, confirming the method's effectiveness in handling highly dispersive waves with significant high-frequency components and large $m$ values. Throughout the simulation period, the method maintains numerical stability.

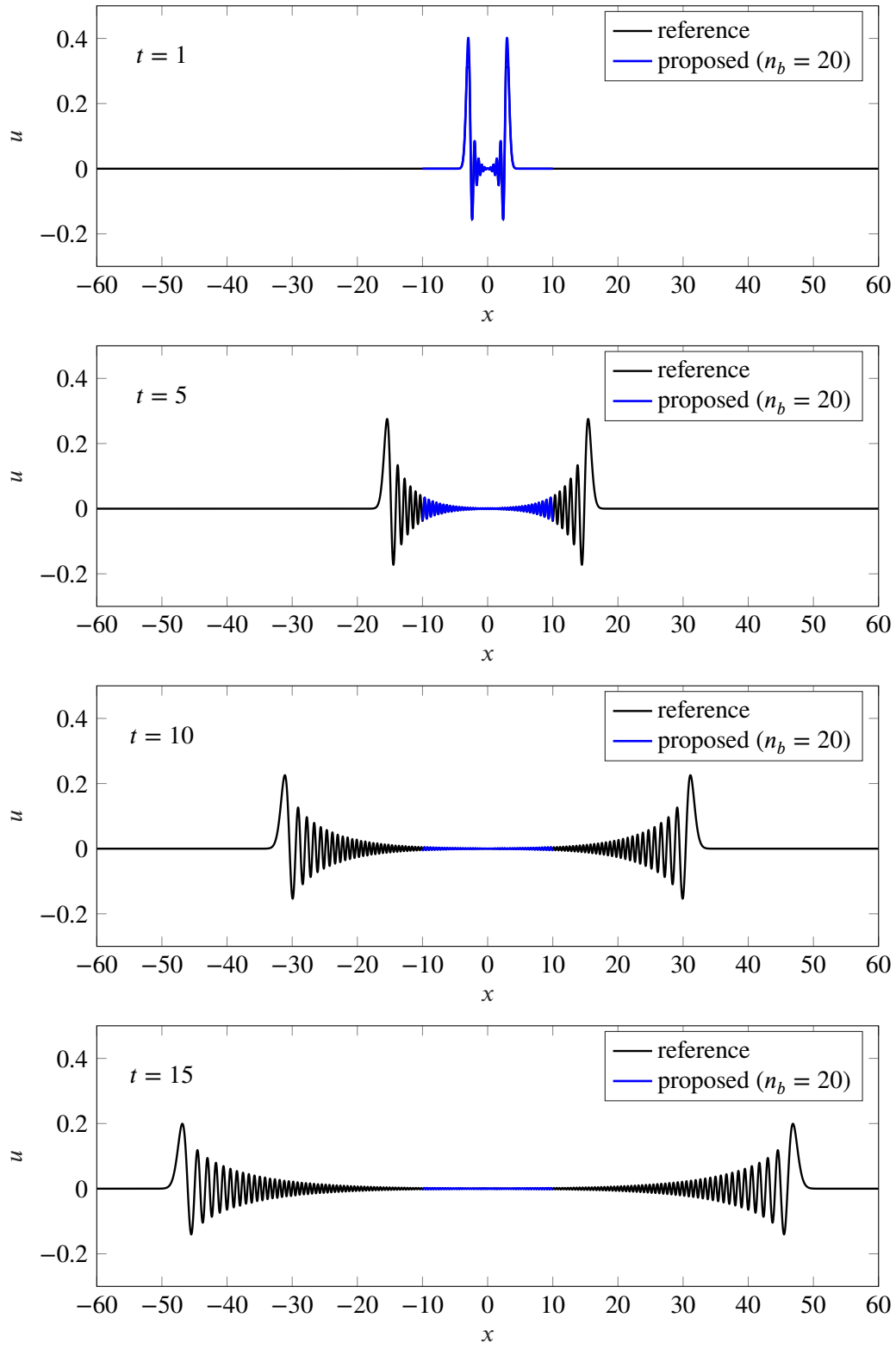


Figure 4.27: Propagation of peridynamic waves in a 1D viscous domain at four different time instants. Given the system parameters, the waves develop high-frequency tails as they propagate towards both ends of the computational domain. Reproduced from adjusted from [59].

### 4.2.5 2D Classical Scalar Waves on Unbounded Domains

In this example, we examine the classical (local) scalar wave equation in a 2D viscous medium as described by (2.37). The near-field solution is obtained using FEM with linear shape functions. Fig. 4.28 presents the results at different times. The near-field region is a square domain, $(-26, 26)\times(-26, 26)$, discretized with square elements of edge length $\Delta x = 0.5$. We show three sets of results: the reference solution on a larger domain, $(-126, 126) \times (-126, 126)$, with homogeneous Dirichlet boundary conditions (left column), the near-field solutions using the proposed ABCs (middle column), and the near-field solutions using conventional first-order ABCs (right column). These are referred to as *reference*, *proposed*, and *conventional*, respectively. The conventional first-order ABCs derivation for the classical wave equation in viscous media is provided in Section 4.2.2. The proposed ABCs are implemented only on the outermost boundary nodes.

The truncated models consist of a total of $11,025$ nodes and $10,816$ elements, while the reference model utilizes $251,001$ nodes and $250,000$ elements. For time integration, each model applies the explicit velocity-Verlet scheme with a time step of $\Delta t = 5 \times 10^{-4}$. The wave propagation speed is set to $\chi^2 = 1$, and the medium damping coefficient is $d = 0.0125$. For ensuring stable numerical simulations in 2D and achieving reasonable norms of the updating vectors in (4.82), along with appropriate condition numbers of the moment matrices in (4.80), we empirically set the parameter $\Delta k$ from (4.56) to 1. This choice of $\Delta k$ has been found to yield satisfactory results and supports the stability of the simulation. The initial conditions according to (2.39), with $u_0(\mathbf{x}) = \exp\left(-\frac{\log 2}{9}(\|\mathbf{x}\|)\right)$ and $\dot{u}_0(\mathbf{x}) = 0$, represent a pulse-like excitation.

Fig. 4.28 compares the near-field solutions between the truncated domain models and the reference solution at selected time instances. The proposed model effectively transmits the wave outward without significant reflections, even when the wave reaches the near-field boundary. On the other hand, the conventional first-order ABCs result in noticeable reflections, especially at $t = 40$ and $t = 50$, as evident from the absolute value of the solution differences $|u(\mathbf{x}, t) - u_{\text{ref}}(\mathbf{x}, t)|$ for the final time step $t = 50$, as shown in Fig. 4.29. The left column of Fig. 4.29 depicts the solution difference for the model equipped with the proposed ABCs, while the right column shows the difference for the conventional model. Notably, in the conventional model, reflections primarily originate from the near-field corners, consistent with the known susceptibility of corners to cause numerical instabilities [108].

To assess the numerical stability of the proposed ABCs model, we present the normalized energy evolution within the near-field in Fig. 4.30 (right). The plot shows the course of the normalized energy, with respect to the initial energy of the system $E_0$, over a total of $5 \times 10^6$ time steps, and it is compared to the energy evolution of the reference solution. The energy at time $t \geq 0$ is defined as

$$E(t) = \frac{1}{2} \int_{\Omega_N} \left( \dot{u}^2(\mathbf{x}, t) + \chi^2 \left[ \left( \frac{\partial u(\mathbf{x}, t)}{\partial x} \right)^2 + \left( \frac{\partial u(\mathbf{x}, t)}{\partial y} \right)^2 \right] \right) \mathrm{d}V_{\mathbf{x}}, \tag{4.99}$$

where $\Omega_N$ represents the integration region. During the entire simulation duration, no signs of unstable behavior are observed, confirming the numerical stability of the proposed ABCs method. Furthermore, the comparison of accuracy between the proposed and conventional models is illustrated in Fig. 4.30 (top). The time evolution of the near-field solution at a selected node is plotted for all three models employed. As shown in Fig. 4.28 and Fig. 4.29, it is evident that the solution of the proposed model agrees well with the reference solution, while the conventional model exhibits significant reflections.

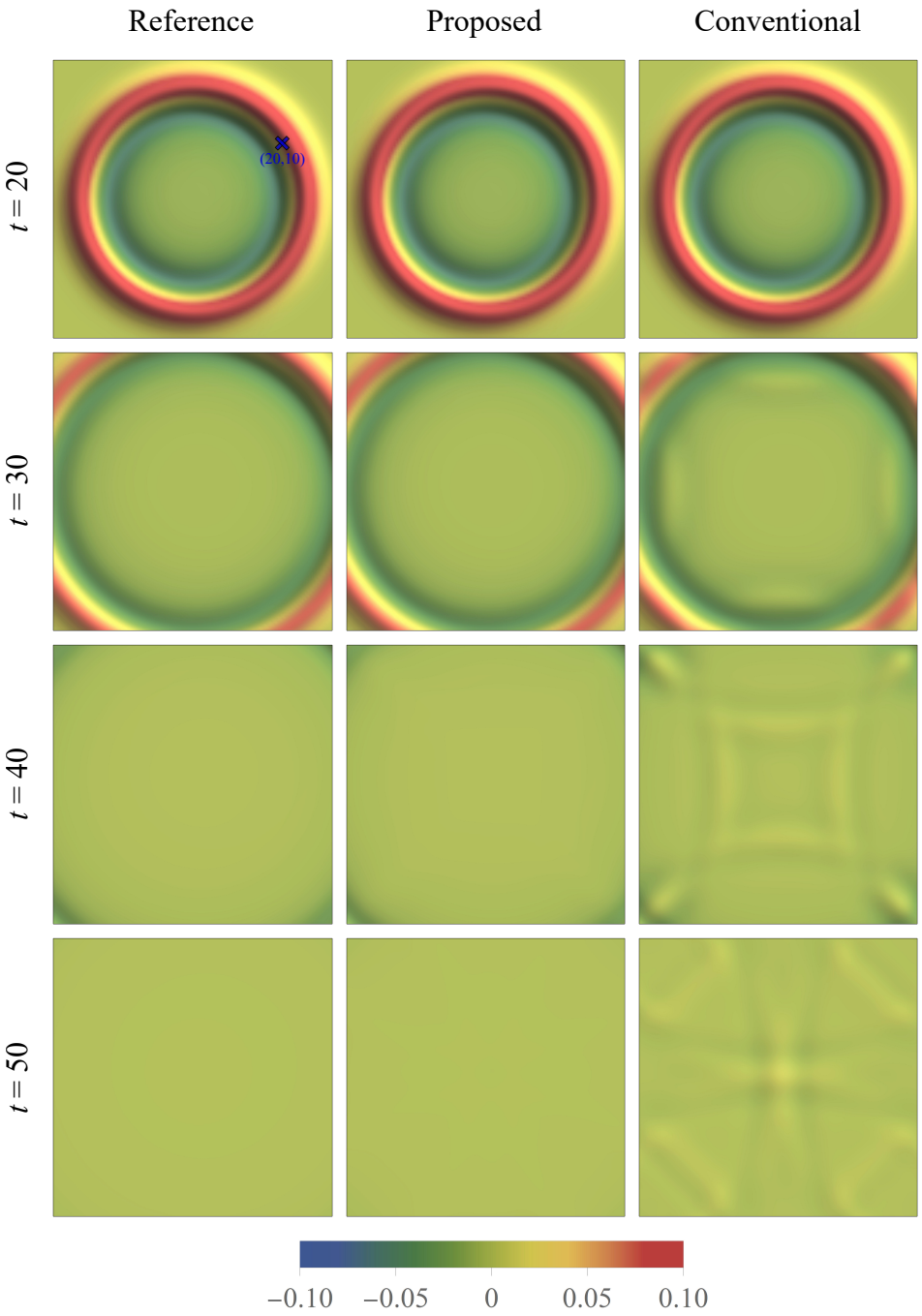


Figure 4.28: Near-field solutions at various time instances for the classical scalar wave equation in 2D viscous media. The left column shows the reference model, the middle column corresponds to the model equipped with the proposed ABCs, and the right column represents the model with conventional first-order ABCs. Reproduced from [59].

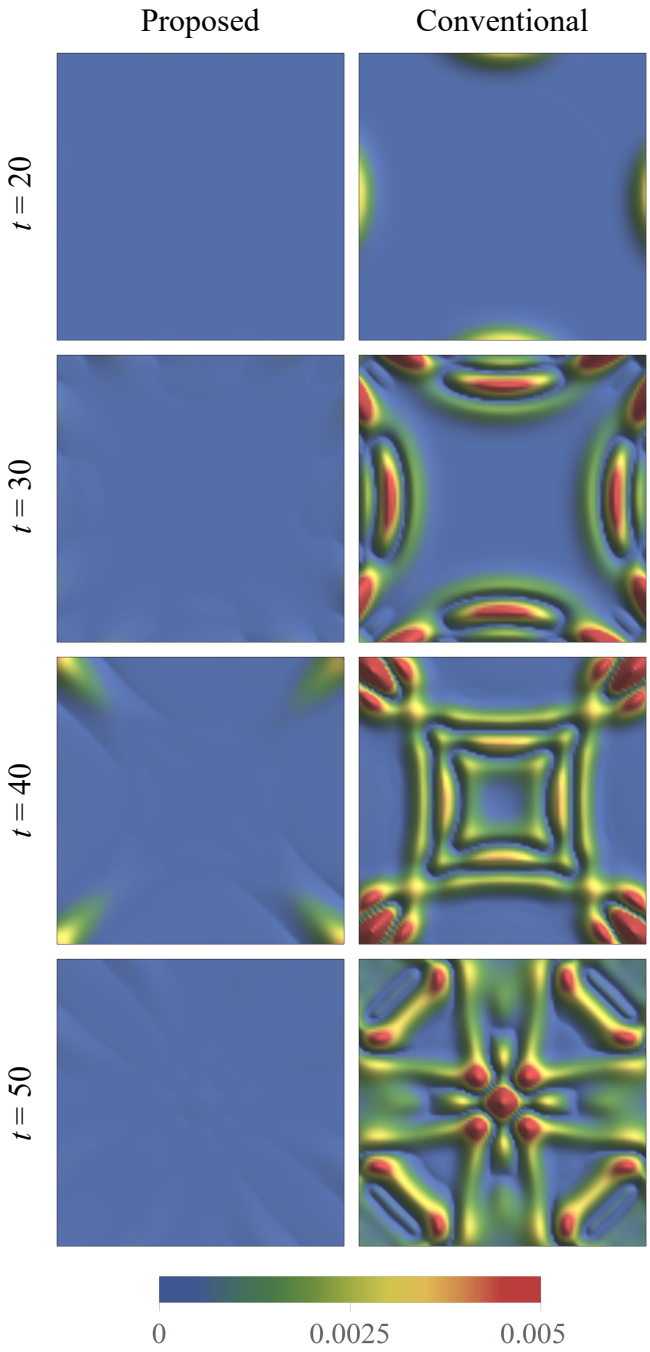


Figure 4.29: Absolute difference between the solutions of the proposed and the reference model (left), as well as the absolute difference between the conventional and the reference model (right) at different time instances in 2D. Reproduced from [59].

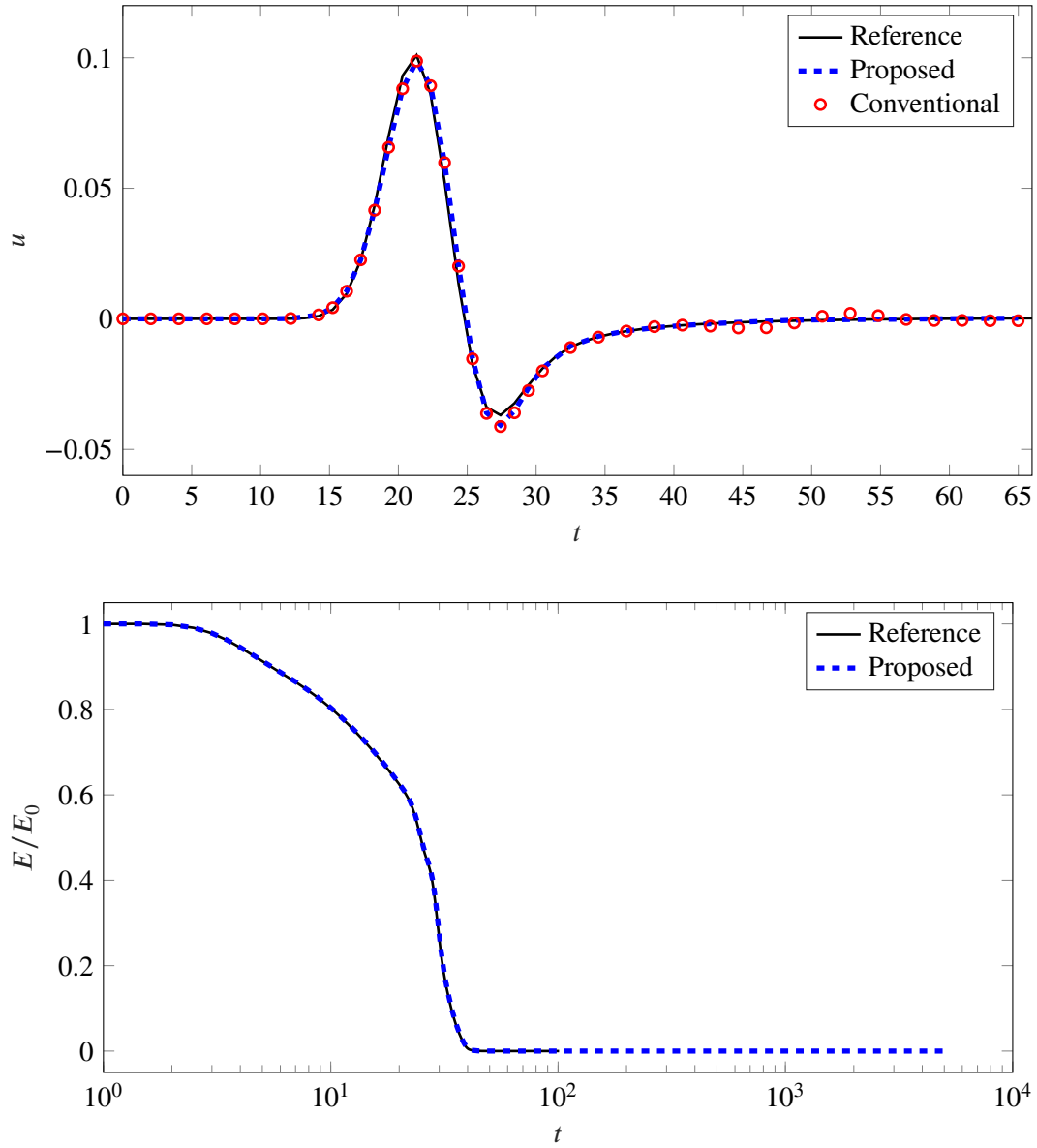


Figure 4.30: Top: The time evolution of the solution at the point $\mathbf{x} = (20, 10)$ (see Figure 4.28) for the various models employed. Bottom: Comparison of the normalized energy evolution over time between the proposed and the reference model. Reproduced from [59].

### 4.2.6 2D Peridynamic Scalar Waves on Unbounded Domains

In this example, we apply the proposed ABCs to the peridynamic scalar wave equation (2.40) with a constant influence function given by (2.12) and $p = 2$. The governing equation in the near-field is discretized using the standard discretization scheme of PD, and is represented by a circular domain with a radius of $R = 26$, as shown in Fig. 4.31. The computational domain is discretized using regular square cells with a grid size of $\Delta x = 0.25$, and the horizon is set to $\delta = 1.5$.

We compare three models at different time instants: the left column in Fig. 4.31 presents the reference solution obtained on a much larger domain ($R = 126$) with homogeneous Dirichlet boundary conditions, and the middle and right columns depict two versions of the proposed model using different dispersion relations. The model in the middle column, referred to as *Proposed-A*, employs the discrete peridynamic dispersion relation from (4.85). On the other hand, the model in the right column, denoted as *Proposed-B*, uses the local characteristic dispersion relation (4.39) derived for the classical wave equation (2.37). In both Proposed-A and Proposed-B models, the ABCs are applied to a layer with a width equal to the horizon $\delta$. Additionally, we reduce the number of collocation nodes based on Figure 4.23 to improve overall conditioning and computational efficiency.

The proposed models Proposed-A and Proposed-B utilize a discretization resulting in a total of $33,949$ nodes, while the reference model employs $797,889$ nodes. Time integration is performed using the explicit velocity-Verlet scheme from (3.9) with a time step of $\Delta t = 1 \times 10^{-4}$. The wave propagation speed is assumed as $\chi^2 = 1$, and the medium damping coefficient is set to $d = 0.0125$. Similarly to the previous example in Section 4.2.5, we choose the parameter $\Delta k$ from (4.56) as $\Delta k = 1$. The initial conditions consist of a pulse given by $u_0(\mathbf{x}) = \exp(-\log 2(\|\mathbf{x}\|))$ and $\dot{u}_0(\mathbf{x}) = 0$.

Fig. 4.31 presents a comparison of the near-field solutions between the two proposed models at four selected time instances. Both Proposed-A and Proposed-B models effectively absorb the incident waves. However, the Proposed-A model shows fewer reflections compared to Proposed-B, particularly at times $t = 40$ and $t = 50$ after the wave departs the near-field. To further illustrate this, Fig. 4.32 displays the absolute value of the difference between the solution of each proposed model and the reference solution. The left column represents the results for the Proposed-A model, while the right column depicts the results for Proposed-B model. The observed differences in reflection behavior can be attributed to the choices of dispersion relations in each model. Proposed-A utilizes a discrete peridynamic dispersion relation that matches the numerical method employed in the near-field, resulting in reduced reflections. On the other hand, Proposed-B employs the local characteristic dispersion relation that significantly differs from the discrete peridynamic dispersion relation, leading to more prominent reflections.

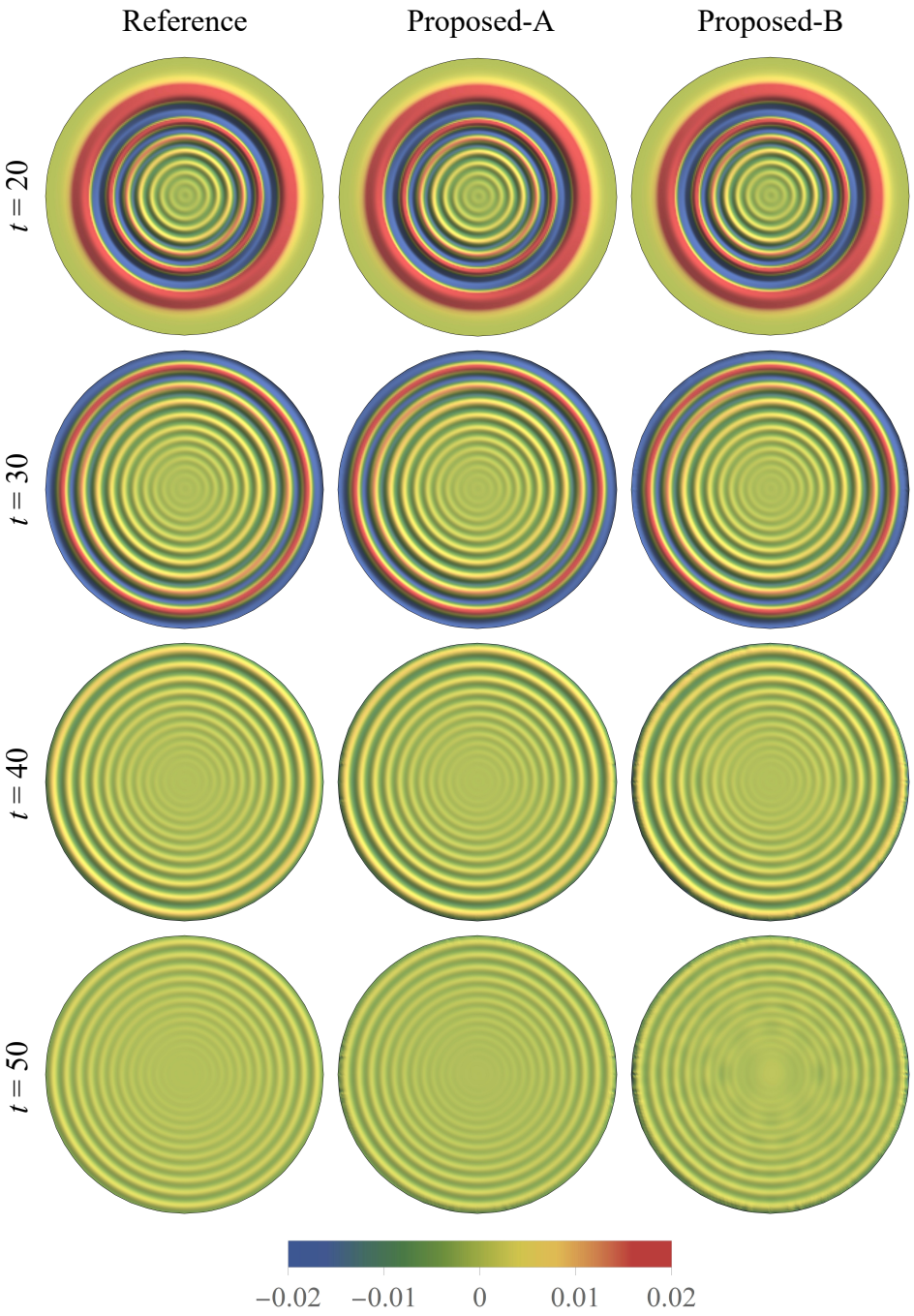


Figure 4.31: Near-field solutions at different time instances for the peridynamic scalar wave equation in 2D. The left column displays the results obtained from the reference model. In the middle and right columns, the solutions from the proposed models are depicted. The middle column corresponds to the model equipped with ABCs based on modes using the discrete peridynamic dispersion relation (Proposed-A), while the right column corresponds to the ABCs based on modes with the local characteristic dispersion relation (Proposed-B). Reproduced from [59].

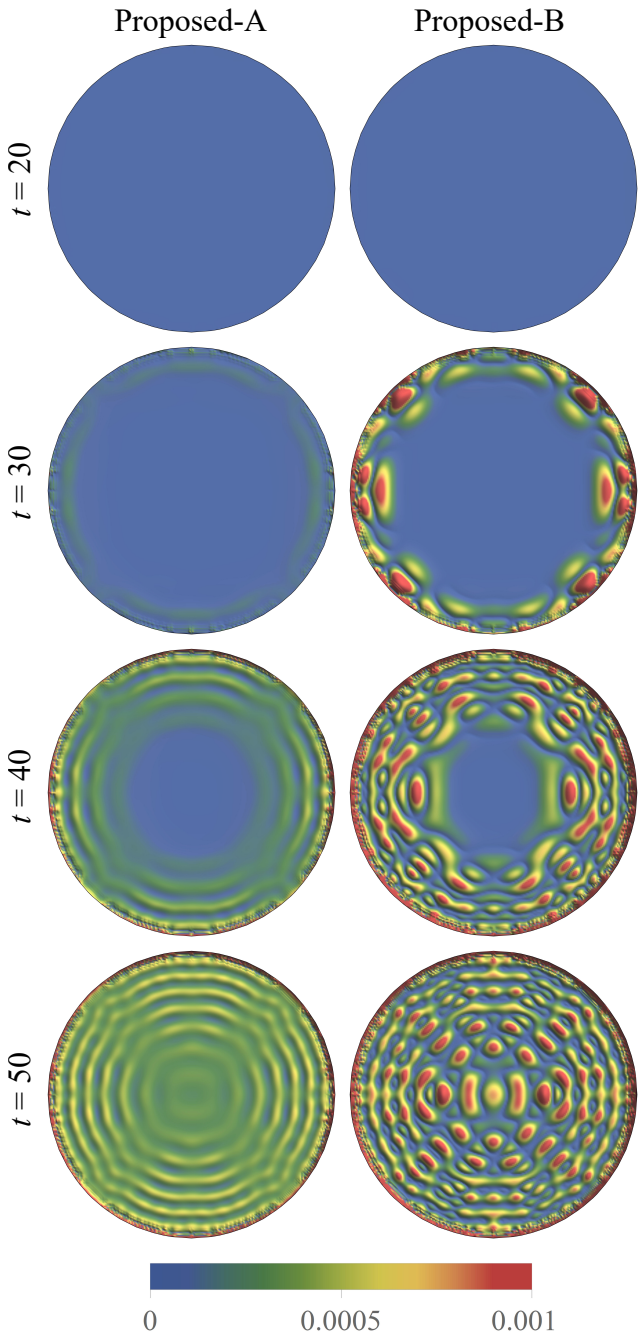


Figure 4.32: The absolute difference between the solutions of the proposed models and the reference model at various time instances. The left plot shows the comparison between the proposed model (Proposed-A) equipped with ABCs based on modes using the discrete peridynamic dispersion relation and the reference model. The right plot demonstrates the comparison between the proposed model (Proposed-B) with the local characteristic dispersion relation and the reference model. Reproduced from [59].

### 4.2.7 2D Peridynamic Scalar Waves on Discontinuous Unbounded Domains

In this section, we further demonstrate the effectiveness of the proposed ABCs in a more challenging scenario, involving two notches in the near-field, as shown in Fig. 4.33. The notches are created by breaking all the bonds that intersect the corresponding line segments. Apart from the horizon size, set to $\delta = 0.75$ in this example, the model parameters remain the same as in the previous example, while the initial conditions are consistent with the setup provided in Section 4.2.6. For this case, we focus solely on comparing the solution of the Proposed-A model (see Fig. 4.31) with the reference solution, omitting the comparison with the Proposed-B model. The presence of notches leads to reflections within the near-field, resulting in a complex wave state with multiple waves impinging on the near-field boundary at various angles. Nevertheless, as shown in Fig. 4.33, the ABCs effectively absorb the incident waves, providing a solution that closely matches the reference solution despite the complexity of the problem.

To further assess the solution of the Proposed-A model, we analyze the time evolution of the field variable at a specific point and compare it with the reference solution in Fig. 4.34. Initially, the solutions show excellent agreement for the chosen near-field with domain radius $R = 26$. However, as time progresses, slight deviations from the reference solution become noticeable in the Proposed-A model. These discrepancies can be attributed to the complex wave state and the relatively large angles of incidence on the absorbing boundary. Improving solution accuracy in relation to the reference solution can be achieved by reducing the angles of incident waves relative to the boundary normal vectors. This can be accomplished by increasing the radius of the near-field, which effectively enlarges the distance between the absorbing boundary and the notches. As demonstrated in Fig. 4.34, the solution accuracy of the Proposed-A model considerably improves relative to the reference solution when using a larger near-field with domain radius $R = 42$. However, it is essential to note that there is always a trade-off between numerical accuracy and computational efficiency when determining the domain size of the near-field.

In this numerical example, we encounter a challenging scenario with two notches in the near-field, leading to wave reflections from multiple incident angles at the absorbing boundary. To enhance numerical accuracy in such cases, one approach is to enlarge the numerical domain, as illustrated in Fig. 4.34, although this can significantly increase computational costs. Another parameter that can potentially impact result accuracy is $\Delta\phi$ from (4.56), which governs the range of angles for the modes used to construct the ABCs. However, simply increasing $\Delta\phi$ may not always yield better outcomes and could even lead to numerical instability due to reflections from the absorbing boundary back to the near-field (see e.g. [125]). Hence, striking a careful balance between numerical accuracy and computational efficiency becomes essential, especially for complex problems like the one described here.

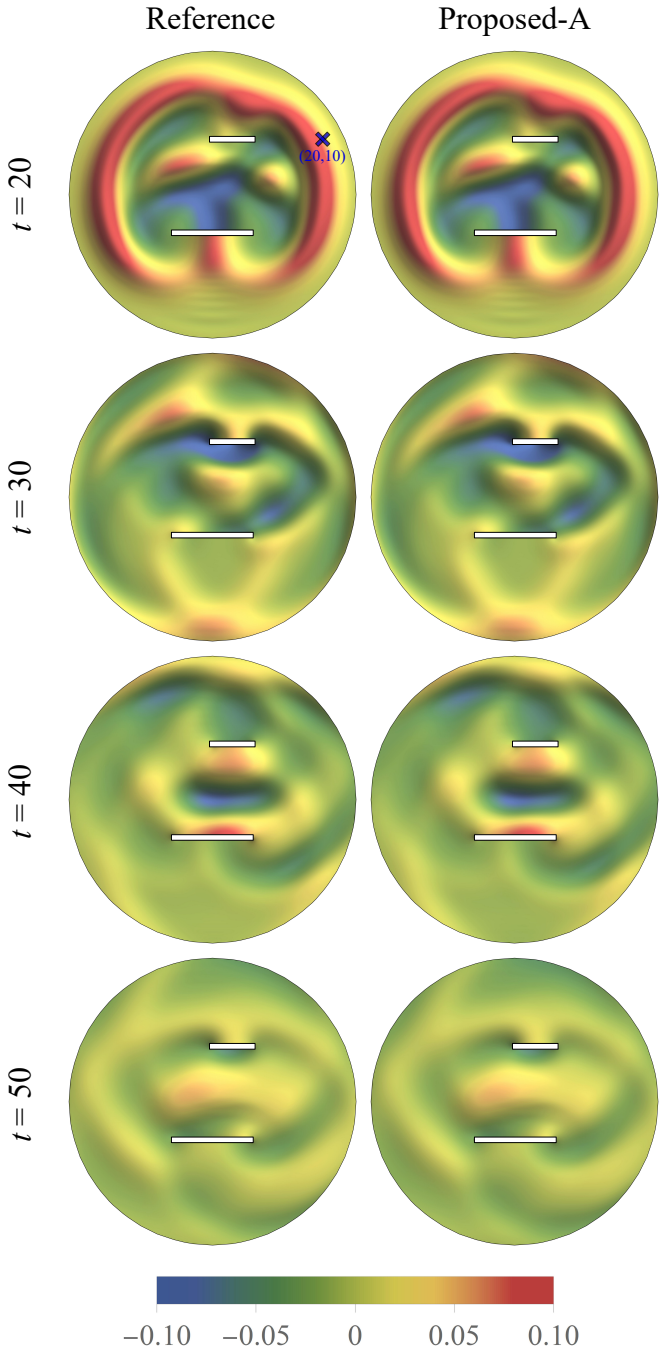


Figure 4.33: Near-field solutions at various time instances for the PD scalar wave equation. In the left column, we have the reference model, and the right column showcases the proposed model equipped with ABCs using modes based on the discrete PD dispersion relation (Proposed-A model). Reproduced from [59].

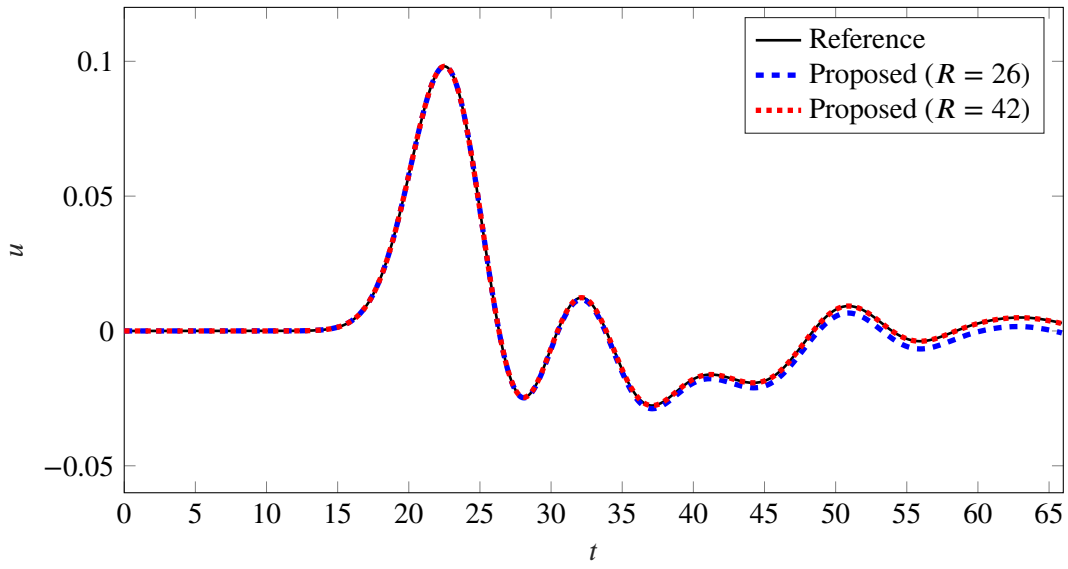


Figure 4.34: Time evolution of the solution at $\mathbf{x} = (20, 10)$ (see Figure 4.33) for both the reference model and the proposed model with the discrete peridynamic dispersion relation (Proposed-A model). The results are presented for two near-fields, one with a domain radius of $R = 26$ and the other with a domain radius of $R = 42$. Reproduced from [59].

## 4.3 Bond-Based Peridynamics on Unbounded Domains

In the concluding section of this chapter, we explore how the proposed ABCs are applied to vectorial waves governed by the linear bond-based PD equation in 2D. This method extends the approaches previously employed for peridynamic diffusion and scalar waves equations, as outlined in Sections 4.1 and 4.2. We examine the propagation of 2D elastic waves within a generic, unbounded, homogeneous, and isotropic domain $\Omega_\infty$, potentially containing scatterers and source terms. The domain is truncated by an absorbing boundary $\Gamma_\infty$, which divides $\Omega_\infty$ into the bounded near-field $\Omega_N$ and the far-field $\Omega_F = \Omega_\infty / \Omega_N$. The governing equation at a point $\mathbf{x} \in \Omega_\infty$ at time $t \geq 0$ is

$$\rho \ddot{\mathbf{u}}(\mathbf{x}, t) = \int_{\mathcal{H}_\mathbf{x}} c \frac{\boldsymbol{\xi} \otimes \boldsymbol{\xi}}{\|\boldsymbol{\xi}\|^3} \boldsymbol{\eta} \, \mathrm{d}V_{\mathbf{x}'} + \mathbf{b}(\mathbf{x}, t), \quad \mathbf{x} \in \Omega_N. \tag{4.100}$$

Here, $\rho$ represents mass density, $\mathbf{u}$ the displacement vector along $x$- and $y$-axes in the global coordinate system, $\ddot{\mathbf{u}}$ indicates the acceleration and the second time derivative of $\mathbf{u}$, and $\mathbf{b}$ is a known body force density. The initial conditions are specified as

$$\mathbf{u}(\mathbf{x}, 0) = \mathbf{u}^0(\mathbf{x}), \quad \dot{\mathbf{u}}(\mathbf{x}, 0) = \mathbf{v}^0(\mathbf{x}), \quad \mathbf{x} \in \Omega_\infty, \tag{4.101}$$

where $\mathbf{u}^0(\mathbf{x})$ and $\mathbf{v}^0(\mathbf{x})$ are predefined functions. The near-field encompasses the entire support of the sources in (4.100) and the initial conditions from (4.101). In the far-field $\Omega_F$, which behaves as a linear elastic medium with a constant influence function, the force-free equation of motion at $\mathbf{x}$ for $t \geq 0$ is expressed as

$$\rho \ddot{\mathbf{u}}(\mathbf{x}, t) = \int_{\mathcal{H}_\mathbf{x}} c \frac{\boldsymbol{\xi} \otimes \boldsymbol{\xi}}{\|\boldsymbol{\xi}\|^3} \boldsymbol{\eta} \, \mathrm{d}V_{\mathbf{x}'}, \quad \mathbf{x} \in \Omega_F. \tag{4.102}$$

The far-field $\Omega_F$ is modeled as a linear elastic medium that is initially at rest with a constant influence function. To simulate the unbounded domain solution, it is crucial to transmit elastic waves across $\Gamma_\infty$ into the near-field without reflections. To achieve this, ABCs are applied to the truncating boundary, derived from far-field solutions in the time domain. This approach builds on the techniques used in [95] for addressing the unbounded classical linear elasticity problem in 2D. Further, in [93], a coupled PD-CCM method was employed for crack propagation in 2D unbounded domains. Here, the near-field was approximated using standard meshfree discretization of PD and integrated with a FEM approach along the boundary assuming the validity of CCM equation in this region. This coupling scheme assumes that displacement behaviors may be accurately obtained via the CCM sufficiently distant from the crack tip, allowing boundary conditions within the CCM domain to be effectively implemented using local methods like conventional ABCs [40]. However, it is important to recognize that PD-CCM coupling can sometimes generate spurious wave reflections at the coupling zone in dynamic scenarios, which is a consequence of the different dispersion relations between PD and CCM [144]. To address unbounded domain problems in 2D linear bond-based PD, we initially formulate the semi-analytical solutions for the far-field, utilizing harmonic plane wave solutions, or modes, that satisfy the governing equation presented in (4.102). These modes form the basis for the proposed ABCs, based on a collocation and extrapolation scheme analogous to methods described for the peridynamic diffusion and scalar wave equation. The first step involves deriving the analytical dispersion relations from classical linear elasticity, extending these to bond-based peridynamic through a power series expansion that can be approximated to any desired accuracy. Following this, we develop the discrete linear bond-based peridynamic modes and establish the ABCs within a solution scheme for the far-field domain.

### 4.3.1 Dispersion Relations in Classical Elasticity and Bond-Based Peridynamics

In this section, we detail the derivation of analytical dispersion relations for CCM and bond-based PD. More detailed studies on peridynamic elastic wave dispersion relations are given in the respective literature [128, 116, 23]. We consider the vector-valued plane wave mode $\boldsymbol{\psi}(\mathbf{x}, t)$ that satisfies the governing equation from (4.102), represented as

$$\boldsymbol{\psi}(\mathbf{x}, t) = \boldsymbol{\gamma} \exp(\imath \boldsymbol{\alpha} \cdot \mathbf{x} + \imath \bar{\omega} t), \quad \boldsymbol{\alpha} = (\alpha_x, \alpha_y)^{\mathrm{T}}, \quad \boldsymbol{\gamma}(\boldsymbol{\alpha}, \bar{\omega}) = \begin{pmatrix} \gamma_x(\boldsymbol{\alpha}, \bar{\omega}) \\ \gamma_y(\boldsymbol{\alpha}, \bar{\omega}) \end{pmatrix}, \tag{4.103}$$

where $\imath^2 = -1$ denotes the imaginary unit, and the constants $(\alpha_x, \alpha_y, \bar{\omega}) \in \mathbb{R}^3$ determine the wave's properties. Here, $\bar{\omega}$ modulates the frequency, $\alpha_x$ and $\alpha_y$ dictate spatial oscillations and wave direction, and $\boldsymbol{\gamma}$ serves as an eigenvector with a prescribed norm of $\|\boldsymbol{\gamma}\| = 2$ for the purpose of numerical stability. Drawing parallels to the methods in Section 4.2.1, we perform a coordinate transformation into to polar coordinates as

$$\boldsymbol{\alpha} = k(\cos\phi, \sin\phi)^{\mathrm{T}}, \quad k \in \mathbb{R}, \quad -\pi < \phi \leq \pi, \tag{4.104}$$

where $k$ influences the amplitude of oscillations and $\phi$ specifies the wave direction. In the case of classical linear elasticity, the governing equation of motion is given by

$$\rho \ddot{\mathbf{u}}(\mathbf{x}, t) = \mathbf{S}^{\mathrm{T}} \mathbf{D} \mathbf{S} \mathbf{u}(\mathbf{x}, t), \quad \mathbf{S}^{\mathrm{T}} = \begin{bmatrix} \frac{\partial}{\partial x} & 0 & \frac{\partial}{\partial y} \\ 0 & \frac{\partial}{\partial y} & \frac{\partial}{\partial x} \end{bmatrix}, \quad \mathbf{D} = \begin{bmatrix} D_1 & D_2 & 0 \\ D_2 & D_1 & 0 \\ 0 & 0 & D_3 \end{bmatrix}, \tag{4.105}$$

where $\mathbf{S}$ is the strain operator in 2D linear elasticity, and $\mathbf{D}$ is the matrix of material constants, which in the case of plane stress condition is given by

$$D_1 = \frac{E}{1-\nu^2}, \quad D_2 = \frac{E\nu}{1-\nu^2}, \quad D_3 = \frac{E}{2(1+\nu)}, \tag{4.106}$$

where $E$ denotes the Young's modulus and $\nu$ is Poisson's ratio. We employ the plane-wave mode described in (4.103) and substitute this mode for $\mathbf{u}$ in (4.105), which results in the vector-valued eigenvalue problem

$$(\mathbf{M}^{\mathrm{CE}} - \rho\bar{\omega}^2 \mathbf{I}) \boldsymbol{\gamma} \exp(\imath \boldsymbol{\alpha} \cdot \mathbf{x} + \imath \bar{\omega} t) = \mathbf{0}, \tag{4.107}$$

where $\mathbf{I}$ is the identity matrix and $\mathbf{M}^{\mathrm{CE}}(k, \phi) \in \mathbb{R}^{2\times 2}$ is characterized by

$$\mathbf{M}^{\mathrm{CE}}(k, \phi) = k^2 \begin{bmatrix} D_1 N_1^2 + D_3 N_2^2 & (D_2 + D_3) N_1 N_2 \\ (D_2 + D_3) N_1 N_2 & D_3 N_1^2 + D_1 N_2^2 \end{bmatrix}, \quad \mathbf{N} = \begin{pmatrix} N_1 \\ N_2 \end{pmatrix} := \begin{pmatrix} \cos\phi \\ \sin\phi \end{pmatrix}. \tag{4.108}$$

Next, we assume a Poisson's ratio of $\nu = \frac{1}{3}$, which corresponds to the plane stress condition, and aligns with the constraints inherent in bond-based PD models. Thus, the solution of the eigenvalue problem in (4.107) is given by

$$\mathbf{M}^{\mathrm{CE}}(k, \phi) = \frac{9E}{8} k^2 \begin{bmatrix} N_1^2 + \frac{1}{3} N_2^2 & \frac{2}{3} N_1 N_2 \\ \frac{2}{3} N_1 N_2 & \frac{1}{3} N_1^2 + N_2^2 \end{bmatrix}, \tag{4.109}$$

Solving (4.107) for $\bar{\omega}$ determines the angular frequencies and corresponding eigenvectors under plane stress conditions, which are expressed as

$$\bar{\omega}_P = \pm \sqrt{\frac{E}{\rho(1-\nu^2)}} k, \quad \boldsymbol{\gamma}_P = \begin{pmatrix} N_1 \\ N_2 \end{pmatrix}, \qquad \bar{\omega}_S = \pm \sqrt{\frac{E}{2\rho(1+\nu)}} k, \quad \boldsymbol{\gamma}_S = \begin{pmatrix} -N_2 \\ N_1 \end{pmatrix}, \tag{4.110}$$

where solutions represent pressure and shear waves, respectively. When the linear bond-based PD equation, free of body force density fields, serves as the governing equation instead of (4.105), the components of the generalized mass matrix, in the following denoted as $\mathbf{M}^{\mathrm{PD}}$, within the eigenvalue problem (4.107) are modified accordingly and given by

$$M_{ij}^{\mathrm{PD}}(k,\phi) = \int_{\mathcal{H}} \frac{c}{\|\boldsymbol{\xi}\|^3} \xi_i \xi_j (1 - \cos(k\mathbf{N}\cdot\boldsymbol{\xi}))\, \mathrm{d}V_{\boldsymbol{\xi}}, \quad i,j = 1,2. \tag{4.111}$$

When transformed into polar coordinates, with $\xi_1 = r\cos\theta$ and $\xi_2 = r\sin\theta$, the components may be expressed as

$$M_{11}^{\mathrm{PD}}(k,\phi) = c\int_0^{\delta}\int_0^{2\pi} \cos^2\theta \left[1 - \cos(kr(N_1\cos\theta + N_2\sin\theta))\right] \mathrm{d}\theta\mathrm{d}r, \tag{4.112}$$

$$M_{12}^{\mathrm{PD}}(k,\phi) = c\int_0^{\delta}\int_0^{2\pi} \cos\theta\sin\theta \left[1 - \cos(kr(N_1\cos\theta + N_2\sin\theta))\right] \mathrm{d}\theta\mathrm{d}r, \tag{4.113}$$

$$M_{22}^{\mathrm{PD}}(k,\phi) = c\int_0^{\delta}\int_0^{2\pi} \sin^2\theta \left[1 - \cos(kr(N_1\cos\theta + N_2\sin\theta))\right] \mathrm{d}\theta\mathrm{d}r, \tag{4.114}$$

$$M_{21}^{\mathrm{PD}}(k,\phi) = M_{12}^{\mathrm{PD}}(k,\phi). \tag{4.115}$$

The double integrals may be expressed in form of an infinite power series expansion by employing the Taylor series expansion for $\cos(\theta)$ given by

$$\cos(\theta) = \sum_{n=0}^{\infty} (-1)^n \frac{\theta^{2n}}{(2n)!} = 1 + \sum_{n=1}^{\infty} (-1)^n \frac{\theta^{2n}}{(2n)!}. \tag{4.116}$$

Thus, we consider the following integral

$$\begin{aligned}
&\int_0^{\delta}\int_0^{2\pi} \cos^m\theta \sin^{2-m}\theta \left[1 - \cos(kr(N_1\cos\theta + N_2\sin\theta)\right] \mathrm{d}\theta\mathrm{d}r \\
&= -\int_0^{\delta}\int_0^{2\pi} \cos^m\theta\sin^{2-m}\theta \sum_{n=1}^{\infty} (-1)^n \frac{(kr(N_1\cos\theta + N_2\sin\theta))^{2n}}{(2n)!} \mathrm{d}\theta\mathrm{d}r \\
&= \sum_{n=1}^{\infty} \frac{(-1)^{n+1}k^{2n}}{(2n)!} \int_0^{\delta} r^{2n} \int_0^{2\pi} \cos^m\theta\sin^{2-m}\theta (N_1\cos\theta + N_2\sin\theta)^{2n} \mathrm{d}\theta\mathrm{d}r \\
&= \sum_{n=1}^{\infty} \frac{(-1)^{n+1}k^{2n}}{(2n)!} \frac{\delta^{2n+1}}{2n+1} \int_0^{2\pi} \cos^m\theta\sin^{2-m}\theta (N_1\cos\theta + N_2\sin\theta)^{2n} \mathrm{d}\theta \\
&= k^2\delta^3 \sum_{n=1}^{\infty} \frac{(-1)^{n+1}(k\delta)^{2(n-1)}}{(2n+1)!} \mathrm{I}[m,n] \\
&= k^2\delta^3 \left(\frac{1}{3!}\mathrm{I}[m,1] - \frac{(k\delta)^2}{5!}\mathrm{I}[m,2] + \frac{(k\delta)^4}{7!}\mathrm{I}[m,3] + \ldots\right), \quad m = 0,1,2
\end{aligned} \tag{4.117}$$

where the function $\mathrm{I}[m,n]$ is defined as

$$\mathrm{I}[m,n] := \int_0^{2\pi} \cos^m\theta\sin^{2-m}\theta (N_1\cos\theta + N_2\sin\theta)^{2n} \mathrm{d}\theta. \tag{4.118}$$

Assuming the micromodulus is $c = \frac{9E}{\pi\delta^3}$, the generalized mass matrix from (4.112) for the eigenvalue problem in the linear bond-based PD framework can be detailed as

$$M_{11}^{\mathrm{PD}}(k,\phi) = \frac{9E}{\pi}k^2 \sum_{n=1}^{\infty} \frac{(-1)^{n+1}(k\delta)^{2(n-1)}}{(2n+1)!}\mathrm{I}[2,n]$$
$$= \frac{9E}{\pi}k^2 \left( \frac{1}{3!}\mathrm{I}[2,1] - \frac{(k\delta)^2}{5!}\mathrm{I}[2,2] + \frac{(k\delta)^4}{7!}\mathrm{I}[2,3] + \ldots \right), \tag{4.119}$$

$$M_{12}^{\mathrm{PD}}(k,\phi) = \frac{9E}{\pi}k^2 \sum_{n=1}^{\infty} \frac{(-1)^{n+1}(k\delta)^{2(n-1)}}{(2n+1)!}\mathrm{I}[1,n]$$
$$= \frac{9E}{\pi}k^2 \left( \frac{1}{3!}\mathrm{I}[1,1] - \frac{(k\delta)^2}{5!}\mathrm{I}[1,2] + \frac{(k\delta)^4}{7!}\mathrm{I}[1,3] + \ldots \right), \tag{4.120}$$

$$M_{22}^{\mathrm{PD}}(k,\phi) = \frac{9E}{\pi}k^2 \sum_{n=1}^{\infty} \frac{(-1)^{n+1}(k\delta)^{2(n-1)}}{(2n+1)!}\mathrm{I}[0,n]$$
$$= \frac{9E}{\pi}k^2 \left( \frac{1}{3!}\mathrm{I}[0,1] - \frac{(k\delta)^2}{5!}\mathrm{I}[0,2] + \frac{(k\delta)^4}{7!}\mathrm{I}[0,3] + \ldots \right), \tag{4.121}$$

$$M_{21}^{\mathrm{PD}}(k,\phi) = M_{12}^{\mathrm{PD}}(k,\phi). \tag{4.122}$$

Given the relation $N_1^2 + N_2^2 = 1$, we compute the values of I[m, n] for $m = 0, 1, 2$ and $n = 1, 2, 3$, resulting in

$$\mathrm{I}[0,1] = \frac{1}{4}(N_1^2 + 3N_2^2)\pi = \frac{1}{4}(1 + 2N_2^2)\pi, \tag{4.123}$$

$$\mathrm{I}[0,2] = \frac{1}{8}(N_1^2 + N_2^2)(N_1^2 + 5N_2^2)\pi = \frac{1}{8}(1 + 4N_2^2)\pi, \tag{4.124}$$

$$\mathrm{I}[0,3] = \frac{5}{64}(N_1^2 + N_2^2)^2(N_1^2 + 7N_2^2)\pi = \frac{5}{64}(1 + 6N_2^2)\pi, \tag{4.125}$$

$$\mathrm{I}[1,1] = \frac{1}{2}N_1N_2\pi, \tag{4.126}$$

$$\mathrm{I}[1,2] = \frac{1}{2}N_1N_2(N_1^2 + N_2^2)\pi = \frac{1}{2}N_1N_2\pi, \tag{4.127}$$

$$\mathrm{I}[1,3] = \frac{15}{32}N_1N_2(N_1^2 + N_2^2)^2\pi = \frac{15}{32}N_1N_2\pi, \tag{4.128}$$

$$\mathrm{I}[2,1] = \frac{1}{4}(3N_1^2 + N_2^2)\pi = \frac{1}{4}(1 + 2N_1^2)\pi, \tag{4.129}$$

$$\mathrm{I}[2,2] = \frac{1}{8}(N_1^2 + N_2^2)(5N_1^2 + N_2^2)\pi = \frac{1}{8}(1 + 4N_1^2)\pi, \tag{4.130}$$

$$\mathrm{I}[2,3] = \frac{5}{64}(N_1^2 + N_2^2)^2(7N_1^2 + N_2^2)\pi = \frac{5}{64}(1 + 6N_1^2)\pi, \tag{4.131}$$

which can be used to derive the components of the generalized mass matrix $\mathbf{M}^{\mathrm{PD}}$, resulting in the following expressions

$$M_{11}^{\mathrm{PD}}(k,\phi) = \frac{9E}{8}k^2\left(\frac{1}{3}(1+2N_1^2) - (1+4N_1^2)\frac{(k\delta)^2}{5!} + \frac{5}{8}(1+6N_1^2)\frac{(k\delta)^4}{7!} + \dots\right), \tag{4.132}$$

$$M_{12}^{\mathrm{PD}}(k,\phi) = \frac{9E}{8}k^2\left(\frac{2}{3}N_1N_2 - 4N_1N_2\frac{(k\delta)^2}{5!} + \frac{15}{4}N_1N_2\frac{(k\delta)^4}{7!} + \dots\right), \tag{4.133}$$

$$M_{22}^{\mathrm{PD}}(k,\phi) = \frac{9E}{8}k^2\left(\frac{1}{3}(1+2N_2^2) - (1+4N_2^2)\frac{(k\delta)^2}{5!} + \frac{5}{8}(1+6N_2^2)\frac{(k\delta)^4}{7!} + \dots\right) \tag{4.134}$$

$$M_{21}^{\mathrm{PD}}(k,\phi) = M_{12}^{\mathrm{PD}}(k,\phi). \tag{4.135}$$

Note that, the leading terms of $\mathbf{M}^{\mathrm{PD}}$ align with those of $\mathbf{M}^{\mathrm{CE}}$ as shown in (4.109). In the limit of $k\delta \to 0$, these matrices converge and become equal. By approximating $\mathbf{M}^{\mathrm{PD}}$ up to a specified order $N$, we obtain the following expressions

$$M_{11}^{\mathrm{PD}}(k,\phi) \approx \frac{9E}{\pi}k^2\sum_{n=1}^{N}\frac{(-1)^{n+1}(k\delta)^{2(n-1)}}{(2n+1)!}\mathrm{I}[2,n], \tag{4.136}$$

$$M_{12}^{\mathrm{PD}}(k,\phi) \approx \frac{9E}{\pi}k^2\sum_{n=1}^{N}\frac{(-1)^{n+1}(k\delta)^{2(n-1)}}{(2n+1)!}\mathrm{I}[1,n], \tag{4.137}$$

$$M_{22}^{\mathrm{PD}}(k,\phi) \approx \frac{9E}{\pi}k^2\sum_{n=1}^{N}\frac{(-1)^{n+1}(k\delta)^{2(n-1)}}{(2n+1)!}\mathrm{I}[0,n], \tag{4.138}$$

$$M_{21}^{\mathrm{PD}}(k,\phi) = M_{12}^{\mathrm{PD}}(k,\phi). \tag{4.139}$$

With these approximations in place, solutions to the eigenvalue problem as described in (4.143) for various orders $N$, can then be derived. The results are summarized in Table 4.2 for $N = 1, 2, 3$.

Table 4.2: Approximations for $\bar{\omega}_P$ and $\bar{\omega}_S$ and their corresponding eigenvectors. Data available in [124].

| $N$ | $\bar{\omega}_P$ | $\boldsymbol{\gamma}_P$ | $\bar{\omega}_S$ | $\boldsymbol{\gamma}_S$ |
|---|---|---|---|---|
| 1 | $\pm\sqrt{\frac{9E}{8\rho}}k$ | $\begin{pmatrix}N_1\\N_2\end{pmatrix}$ | $\pm\sqrt{\frac{3E}{8\rho}}k$ | $\begin{pmatrix}-N_2\\N_1\end{pmatrix}$ |
| 2 | $\pm\sqrt{\frac{9E}{8\rho}}k\sqrt{1-\frac{1}{24}(k\delta)^2}$ | $\begin{pmatrix}N_1\\N_2\end{pmatrix}$ | $\pm\sqrt{\frac{3E}{8\rho}}k\sqrt{1-\frac{1}{40}(k\delta)^2}$ | $\begin{pmatrix}-N_2\\N_1\end{pmatrix}$ |
| 3 | $\pm\sqrt{\frac{9E}{8\rho}}k\sqrt{1-\frac{1}{24}(k\delta)^2+\frac{1}{1152}(k\delta)^4}$ | $\begin{pmatrix}N_1\\N_2\end{pmatrix}$ | $\pm\sqrt{\frac{3E}{8\rho}}k\sqrt{1-\frac{1}{40}(k\delta)^2+\frac{1}{2688}(k\delta)^4}$ | $\begin{pmatrix}-N_2\\N_1\end{pmatrix}$ |

### 4.3.2 Fundamental Solutions for Discretized Bond-Based Peridynamics

To derive fundamental solutions for the discretized linear bond-based PD system and construct ABCs based on semi-analytical solutions, we start by assuming that the wave direction of the modes is oriented towards any angle on the unit circle, though this will eventually be restricted to only describe outgoing waves from the near-field. First, we substitute a general mode $\boldsymbol{\psi}$ from (4.103) for $\mathbf{u}$ in the continuous linear bond-based PD equation in (4.102), yielding

$$\rho\ddot{\boldsymbol{\psi}}(\mathbf{x},t) = \int_{\mathcal{H}_\mathbf{x}} c\frac{\boldsymbol{\xi}\otimes\boldsymbol{\xi}}{\|\boldsymbol{\xi}\|^3}(\boldsymbol{\psi}(\mathbf{x}+\boldsymbol{\xi},t)-\boldsymbol{\psi}(\mathbf{x},t))\,\mathrm{d}V_{\mathbf{x}'}. \tag{4.140}$$

With the bond vector $\boldsymbol{\xi} := \mathbf{x}' - \mathbf{x}$ defined, we focus the range of integration towards the neighborhood $\mathcal{H} := \left\{\boldsymbol{\xi}\in\mathbb{R}^2 : \|\boldsymbol{\xi}\le\delta\|\right\}$ around the origin and perform minor algebraic manipulations, resulting in

$$-\rho\omega^2\boldsymbol{\gamma}\exp(\imath\boldsymbol{\alpha}\cdot\mathbf{x}+\imath\omega t) = \left(\int_{\mathcal{H}} c\frac{\boldsymbol{\xi}\otimes\boldsymbol{\xi}}{\|\boldsymbol{\xi}\|^3}(\exp(\imath\boldsymbol{\alpha}\cdot\boldsymbol{\xi})-1)\,\mathrm{d}V_{\boldsymbol{\xi}}\right)\boldsymbol{\gamma}\exp(\imath\boldsymbol{\alpha}\cdot\mathbf{x}+\imath\omega t). \tag{4.141}$$

The integral in (4.141) is rephrased as

$$\begin{aligned}
\int_{\mathcal{H}} c\frac{\boldsymbol{\xi}\otimes\boldsymbol{\xi}}{\|\boldsymbol{\xi}\|^3}(\exp(\imath\boldsymbol{\alpha}\cdot\boldsymbol{\xi})-1)\,\mathrm{d}V_{\boldsymbol{\xi}} &= -\int_{\mathcal{H}} c\frac{\boldsymbol{\xi}\otimes\boldsymbol{\xi}}{\|\boldsymbol{\xi}\|^3}(1-\exp(\imath\boldsymbol{\alpha}\cdot\boldsymbol{\xi}))\,\mathrm{d}V_{\boldsymbol{\xi}}\\
&= -\frac{1}{2}\int_{\mathcal{H}} c\frac{\boldsymbol{\xi}\otimes\boldsymbol{\xi}}{\|\boldsymbol{\xi}\|^3}(1-\exp(\imath\boldsymbol{\alpha}\cdot\boldsymbol{\xi}))\,\mathrm{d}V_{\boldsymbol{\xi}}\\
&\quad -\frac{1}{2}\int_{\mathcal{H}} c\frac{\boldsymbol{\xi}\otimes\boldsymbol{\xi}}{\|\boldsymbol{\xi}\|^3}(1-\exp(-\imath\boldsymbol{\alpha}\cdot\boldsymbol{\xi}))\,\mathrm{d}V_{\boldsymbol{\xi}}\\
&= -\int_{\mathcal{H}} c\frac{\boldsymbol{\xi}\otimes\boldsymbol{\xi}}{\|\boldsymbol{\xi}\|^3}\left(1-\frac{\exp(\imath\boldsymbol{\alpha}\cdot\boldsymbol{\xi})+\exp(-\imath\boldsymbol{\alpha}\cdot\boldsymbol{\xi})}{2}\right)\mathrm{d}V_{\boldsymbol{\xi}}\\
&= -\int_{\mathcal{H}} c\frac{\boldsymbol{\xi}\otimes\boldsymbol{\xi}}{\|\boldsymbol{\xi}\|^3}(1-\cos(\boldsymbol{\alpha}\cdot\boldsymbol{\xi}))\,\mathrm{d}V_{\boldsymbol{\xi}},
\end{aligned} \tag{4.142}$$

where the second line involves a change of variable $\boldsymbol{\xi}\to-\boldsymbol{\xi}$. This formulation results in a generalized vector-valued eigenvalue problem, previously provided in (4.107), and restated here for convenience, yielding

$$(\mathbf{M}^{\mathrm{PD}} - \rho\bar{\omega}^2\mathbf{I})\boldsymbol{\gamma}\exp(\imath\boldsymbol{\alpha}\cdot\mathbf{x}+\imath\bar{\omega}t) = \mathbf{0}. \tag{4.143}$$

Calculating $\mathbf{M}^{\mathrm{PD}}$ in (4.143) accurately is essential for the stability and accuracy of constructing ABCs using a basis of harmonic modes. Although the analytical calculation of $\mathbf{M}^{\mathrm{PD}}$'s integral components at the continuum level is shown in Section 4.3.1, even at higher order approximations, the obtained characteristic dispersion relations may not precisely represent the dynamics of the discrete (or discretized) system. This discrepancy, which may lead to inconsistencies between the far-field and near-field solutions, thus rendering the ABCs scheme inaccurate and unstable, was demonstrated in Section 4.2.3 for the peridynamic scalar wave equation and illustrated in Fig. 4.22. The issue exacerbates with increasing nonlocality of the model when $\delta$ becomes larger relative to the grid spacing, resulting in highly dispersive waves. Consequently, the integrals in (4.111) must be approximated using the same integration scheme as the near-field. Using the standard meshfree discretization scheme detailed in Section 3.1, we approximate

$$M_{11}^{\mathrm{PD}} \approx \sum_{\mathbf{x}_j \in \mathcal{F}_i} \frac{c}{\|\mathbf{x}_j - \mathbf{x}_i\|^3}(x_j - x_i)^2 \left(1 - \cos(\boldsymbol{\alpha} \cdot (\mathbf{x}_j - \mathbf{x}_i))\right) \beta(\mathbf{x}_j - \mathbf{x}_i)\Delta V_j, \tag{4.144}$$

$$M_{12}^{\mathrm{PD}} \approx \sum_{\mathbf{x}_j \in \mathcal{F}_i} \frac{c}{\|\mathbf{x}_j - \mathbf{x}_i\|^3}(x_j - x_i)(y_j - y_i) \left(1 - \cos(\boldsymbol{\alpha} \cdot (\mathbf{x}_j - \mathbf{x}_i))\right) \beta(\mathbf{x}_j - \mathbf{x}_i)\Delta V_j, \tag{4.145}$$

$$M_{22}^{\mathrm{PD}} \approx \sum_{\mathbf{x}_j \in \mathcal{F}_i} \frac{c}{\|\mathbf{x}_j - \mathbf{x}_i\|^3}(y_j - y_i)^2 \left(1 - \cos(\boldsymbol{\alpha} \cdot (\mathbf{x}_j - \mathbf{x}_i))\right) \beta(\mathbf{x}_j - \mathbf{x}_i)\Delta V_j, \tag{4.146}$$

$$M_{21}^{\mathrm{PD}} = M_{12}^{\mathrm{PD}}. \tag{4.147}$$

This adaptation enables the recovery of nonlocal numerical dispersion relations of the discrete system. Analogous to the approach described in Section 4.2 for the peridynamic scalar wave equation, this strategy facilitates constructing a far-field solution consistent with the discretization employed in the near-field. It is important to highlight that the discretization of the integrals from (4.111) is executed based on a square lattice as depicted in Fig. 3.1, and thus, numerical dispersion relations are utilized to construct ABCs with a set of consistent modes. To determine the solutions $\bar{\omega}$ to the eigenvalue problem in (4.143), eigenvalues are obtained by solving $\det(\mathbf{Q}) = 0$ with the corresponding eigenvectors $\boldsymbol{\gamma} \in \ker(\mathbf{Q})$, leading to the dispersion relations of the bond-based PD system in 2D. The solution results in four roots for $\bar{\omega}$

$$\bar{\omega} = \pm\bar{\omega}_P, \quad \boldsymbol{\gamma} = \boldsymbol{\gamma}_P \tag{4.148}$$

$$\bar{\omega} = \pm\bar{\omega}_S, \quad \boldsymbol{\gamma} = \boldsymbol{\gamma}_S, \tag{4.149}$$

where the indices are indicative of pressure and shear waves, respectively, with their components as

$$\begin{aligned} \bar{\omega}_P(k,\phi) &= \frac{\sqrt{\sqrt{(M_{11} - M_{22})^2 + 4M_{12}M_{21}} + M_{11} + M_{22}}}{\sqrt{2\rho}}, \\ \bar{\omega}_S(k,\phi) &= \frac{\sqrt{-\sqrt{(M_{11} - M_{22})^2 + 4M_{12}M_{21}} + M_{11} + M_{22}}}{\sqrt{2\rho}}, \end{aligned} \tag{4.150}$$

and the corresponding eigenvectors

$$\begin{aligned} \boldsymbol{\gamma}_P(k,\phi) &= \begin{pmatrix} \sqrt{(M_{11} - M_{22})^2 + 4M_{12}M_{21}} + M_{11} - M_{22} \\ 2M_{21} \end{pmatrix}, \\ \boldsymbol{\gamma}_S(k,\phi) &= \begin{pmatrix} -\sqrt{(M_{11} - M_{22})^2 + 4M_{12}M_{21}} - M_{11} + M_{22} \\ 2M_{21} \end{pmatrix}. \end{aligned} \tag{4.151}$$

As a result, we identify two types of modes within the framework of bond-based PD: pressure modes, also known as dilation plane-waves, and shear modes, referred to as distortional plane-waves. Notably, the frequency for pressure modes, $\bar{\omega}_P$, is higher than that for shear modes, $\bar{\omega}_S$, a relationship consistent with observations in CCM models. These modes can be mathematically expressed as

$$\begin{aligned} \boldsymbol{\psi}_P(\mathbf{x},t) &= \boldsymbol{\gamma}_P(k,\phi)\exp(\imath k(x\cos\phi + y\sin\phi) \pm \imath\bar{\omega}_P t), \\ \boldsymbol{\psi}_S(\mathbf{x},t) &= \boldsymbol{\gamma}_S(k,\phi)\exp(\imath k(x\cos\phi + y\sin\phi) \pm \imath\bar{\omega}_S t). \end{aligned} \tag{4.152}$$

These formulations will be utilized to construct an approximation of the far-field solution. This approach enables the modeling of wave propagation dynamics more accurately by capturing the distinct behaviors of dilation and distortional movements within the medium.

### Infinity Condition for Bond-Based Peridynamics

To derive the infinity condition for bond-based PD, consider a specific section of a solution domain adjacent to the absorbing boundary as depicted in Fig. 4.20 for the scalar peridynamic wave equation. Near the boundary, the domain is extended by an absorbing boundary layer with a thickness of $\delta$. Following the methodologies discussed in Section 4.1.2 and Section 4.2.2, for each absorbing node $\mathbf{x}_i$ within this layer, we construct a circular cloud neighborhood $\Omega_i^\infty$ centered at $\mathbf{x}_i$. Each cloud around the absorbing nodes represents a finite region where the modes are collocated and the ABCs are applied. Although the radius of the cloud is set equal to $\delta$ for simplicity, it is important to note that this radius is independent of the horizon, which is a material parameter and length scale of the model. Within each of these absorbing boundary clouds, the far-field solution is then approximated using the peridynamic elastic modes as the basis functions.

Within the local Cartesian coordinates of cloud $(\bar{x}, \bar{y})$, aligned such that the $\bar{x}$-axis points normal to $\Gamma_\infty$ with its positive direction towards the far-field, the coordinates of a node $\mathbf{x}$ relative to the local coordinate system, originating at $\mathbf{x}_i$, are obtained through a rotation matrix $\mathbf{R}(\tau)$ with the rotation angle depicted in Fig. 4.20 as $\tau$, given by $\bar{\mathbf{x}} = \mathbf{R}(\tau)(\mathbf{x} - \mathbf{x}_i)$ as described in (4.24). The far-field solution of the displacement vector at cloud $\Omega_i^\infty$ is then approximated using a series of basis functions from (4.152), yielding

$$\begin{aligned}\mathbf{u}_\infty(\bar{\mathbf{x}}, t) = \sum_{l=1}^{n_\phi}\sum_{m=1}^{n_k}\Big(&a_{l,m}\boldsymbol{\gamma}_P(k_m,\phi_l)\exp(\imath k_m\eta_l - \imath\bar{\omega}_P(k_m,\phi_l)t)\\ &+ b_{l,m}\boldsymbol{\gamma}_S(k_m,\phi_l)\exp(\imath k_m\eta_l - \imath\bar{\omega}_S(k_m,\phi_l)t)\\ &+ c_{l,m}\boldsymbol{\gamma}_P(k_m,\phi_l)\exp(\imath k_m\eta_l + \imath\bar{\omega}_P(k_m,\phi_l)t)\\ &+ d_{l,m}\boldsymbol{\gamma}_S(k_m,\phi_l)\exp(\imath k_m\eta_l + \imath\bar{\omega}_S(k_m,\phi_l)t)\Big),\end{aligned} \tag{4.153}$$

where $(\bar{x}, \bar{y}) = (x - x_i, y - y_i)$, $\eta_l = (\bar{x}\cos\phi_l + \bar{y}\sin\phi_l)$, $a_{l,m}$, $b_{l,m}$, $c_{l,m}$, and $d_{l,m}$ are unknown coefficients, with $n_\phi$ and $n_k$ specifying the number of modes at different directions and magnitudes of spatial oscillations. The bar notation is used to indicate the representation in local Cartesian coordinates of the cloud. As discussed in prior studies on CCM elasticity models [95, 125] and similar to the approaches outlined in the previous sections, the values of $\phi_l$ and $k_m$ are chosen from the intervals

$$\begin{aligned}\phi_l &\in [-\Delta\phi, \Delta\phi], \qquad \Delta\phi \geq 0,\\ k_m &\in (0, \Delta k], \qquad\quad \Delta k > 0,\end{aligned} \tag{4.154}$$

where $\Delta\phi$ and $\Delta k$ are constant parameters. From the general form of all potential modes and their directions in (4.152), we select those propagating towards the exterior domain to effectively transmit the near-field energy into the far-field. Evaluating $\eta_k$ in (4.153) at $\phi = 0$, we consider plane waves propagating parallel to the $\bar{x}$-axis. Considering the orientation of the local coordinate system and the positive values of $\omega_P$, $\omega_S$, and $k$, we infer that for $\phi = 0$ and angles close to it (where $\eta > 0$), the first two terms in (4.153) represent outgoing waves from the near-field, while the remaining terms denote incoming waves. Consequently, for constructing the ABCs, we disregard incoming waves, setting $c_{l,m} = d_{l,m} = 0$. This simplification reduces the far-field solution in (4.153) to

$$\begin{aligned}\mathbf{u}_\infty(\bar{\mathbf{x}}, t) = \sum_{l=1}^{n_\phi}\sum_{m=1}^{n_k}\Big(&a_{l,m}\boldsymbol{\gamma}_P(k_m,\phi_l)\exp(\imath k_m\eta_l - \imath\bar{\omega}_P(k_m,\phi_l)t)\\ &+ b_{l,m}\boldsymbol{\gamma}_S(k_m,\phi_l)\exp(\imath k_m\eta_l - \imath\bar{\omega}_S(k_m,\phi_l)t)\Big),\end{aligned} \tag{4.155}$$

where, transforming into the polar coordinate system $(\bar{x}, \bar{y}) = r(\cos\theta, \sin\theta)$ with $-\pi \leq \theta \leq \pi$, it can be expressed as

$$\begin{aligned}\mathbf{u}_\infty(\bar{\mathbf{x}}, t) = \sum_{l=1}^{n_\phi}\sum_{m=1}^{n_k}\Big(&a_{l,m}\boldsymbol{\gamma}_P(k_m,\phi_l)\exp\left(\imath k_m r(\cos\theta\cos\phi_l + \sin\theta\sin\phi_l) - \imath\bar{\omega}_P(k_m,\phi_l)t\right)\\ &+ b_{l,m}\boldsymbol{\gamma}_S(k_m,\phi_l)\exp\left(\imath k_m r(\cos\theta\cos\phi_l + \sin\theta\sin\phi_l) - \imath\bar{\omega}_S(k_m,\phi_l)t\right)\Big)\\ = \sum_{l=1}^{n_\phi}\sum_{m=1}^{n_k}\Bigg(&a_{l,m}\boldsymbol{\gamma}_P(k_m,\phi_l)\exp\left(\imath k_m r\cos(\theta-\phi_l) - \imath\bar{\omega}_P(k_m,\phi_l)t\right)\\ &+ b_{l,m}\boldsymbol{\gamma}_S(k_m,\phi_l)\exp\left(\imath k_m r\cos(\theta-\phi_l) - \imath\bar{\omega}_S(k_m,\phi_l)t\right)\Bigg).\end{aligned} \tag{4.156}$$

Given that $k$, $\bar{\omega}_P$, $\bar{\omega}_S$, and $r$ are positive and non-zero, the above equation exclusively represents outgoing plane waves and characterizes the far-field solution under the condition

$$\cos(\phi_l - \theta) > 0, \tag{4.157}$$

thus yielding

$$-\frac{\pi}{2} + \phi_l < \theta < \frac{\pi}{2} + \phi_l. \tag{4.158}$$

Note that, the condition in (4.158) defines a half-space centered at the cloud's central node $\Omega_i^\infty$, corresponding to the incident angle $\phi$ relative to the local $\bar{x}$-axis (the outward boundary normal), as discussed in Section 4.2.1 for the peridynamic scalar wave equation and depicted in Fig. 4.21. Similar to the approach employed for the peridynamic scalar wave equation, the vectorial modes employed here determined by specific $\phi$ values direct waves crossing $\Gamma^\infty$ from the near-field to propagate parallel to the bisector of the relevant half-space, extending into the exterior domain. Fig. 4.21 illustrates how adjusting $\phi$ rotates the half-space around $\mathbf{x}_i$. To manage incoming waves from the near-field at various angles, symmetric ranges of $\phi$, as in (4.154), are chosen for transmission or absorption. Notably, $\Delta\phi$ must not exceed certain limits to prevent plane waves from redirecting incoming waves back to the near-field, thereby avoiding spurious reflections from the absorbing layer.

### 4.3.3 Solution Strategy for Unbounded Domain Bond-Based Peridynamics

To derive the proposed ABCs for the bond-based peridynamic elasticity equation, we have to determine the unknown coefficients in terms of the displacement and velocity values at the nodes within the absorbing clouds. Similar to the method described in Section 4.2.2 for developing ABCs for the peridynamic scalar wave equation, we utilize a collocation method based on the WLS approach, akin to the FPM. First, we consider both the displacements and velocities of the cloud nodes $\mathbf{x}_j \in \Omega_i^\infty$, aiming to approximate these using a feasible basis of modes. We assume the approximation holds for a symmetric time interval $[t^n - \Delta t, t^n + \Delta t]$ centered at time $t^n$, and convert time into the local coordinate $\bar{t} := t - t^n$, where $\bar{t} \in [-\Delta t, \Delta t]$ is defined within a symmetric time

interval. Consequently, we approximate the displacements and the velocities at time $t^n$ as

$$\begin{aligned}\mathbf{u}_{\infty}^{n}(\mathbf{x},\bar{t}) &= \begin{pmatrix} u_{1,\infty}^{n}(\mathbf{x},\bar{t}) \\ u_{2,\infty}^{n}(\mathbf{x},\bar{t}) \end{pmatrix} = \mathbf{R}^{\mathrm{T}}(\tau)\sum_{k=1}^{n_b} p_k^n \boldsymbol{\psi}_k(\bar{\mathbf{x}},\bar{t}), \quad \mathbf{x}\in\Omega_i^{\infty}, \quad -\Delta t \le \bar{t} \le \Delta t, \\ \mathbf{v}_{\infty}^{n}(\mathbf{x},\bar{t}) &= \begin{pmatrix} v_{1,\infty}^{n}(\mathbf{x},\bar{t}) \\ v_{2,\infty}^{n}(\mathbf{x},\bar{t}) \end{pmatrix} = \mathbf{R}^{\mathrm{T}}(\tau)\sum_{k=1}^{n_b} q_k^n \dot{\boldsymbol{\psi}}_k(\bar{\mathbf{x}},\bar{t}), \quad \mathbf{x}\in\Omega_i^{\infty}, \quad -\Delta t \le \bar{t} \le \Delta t,\end{aligned} \tag{4.159}$$

where $n_b = n_\phi \times n_k$ denotes the number of modes, $\boldsymbol{\psi}_k$ is the $k$th mode with its corresponding unknown coefficient $p_k^n$ for the specified local time interval, and $\dot{\boldsymbol{\psi}}_k$ is the time derivative of the $k$th mode, with each mode's derivative associated with its own unknown coefficient $q_k^n$. It is important to note that, akin to the approach employed for the peridynamic scalar wave equation, the approximations for $\mathbf{u}_{\infty}^n$ and $\mathbf{v}_{\infty}^n$ are performed independently, hence $p_k^n$ and $q_k^n$ may differ. The equations in (4.159) can be represented in matrix form as

$$\begin{aligned}\mathbf{u}_{\infty}^{n}(\mathbf{x},\bar{t}) &= \mathbf{R}^{\mathrm{T}}(\tau)\boldsymbol{\Psi}(\bar{\mathbf{x}},\bar{t})\mathbf{p}^n, \\ \mathbf{v}_{\infty}^{n}(\mathbf{x},\bar{t}) &= \mathbf{R}^{\mathrm{T}}(\tau)\dot{\boldsymbol{\Psi}}(\bar{\mathbf{x}},\bar{t})\mathbf{q}^n,\end{aligned} \tag{4.160}$$

where $\boldsymbol{\Psi}, \dot{\boldsymbol{\Psi}} \in \mathbb{R}^{2\times n_b}$ represent the modal basis and its time derivatives, respectively. The vectors $\mathbf{p}^n$ and $\mathbf{q}^n$, each of size $n_b$, contain the unknown constant coefficients

$$\begin{aligned}\boldsymbol{\Psi}(\bar{\mathbf{x}},\bar{t}) &= \left[\boldsymbol{\gamma}_1 \exp(\imath\boldsymbol{\alpha}_1\cdot\bar{\mathbf{x}} + \imath\bar{\omega}_1\bar{t}), \quad \boldsymbol{\gamma}_2 \exp(\imath\boldsymbol{\alpha}_2\cdot\bar{\mathbf{x}} + \imath\bar{\omega}_2\bar{t}), \quad \cdots, \quad \boldsymbol{\gamma}_{n_b} \exp(\imath\boldsymbol{\alpha}_{n_b}\cdot\bar{\mathbf{x}} + \imath\bar{\omega}_{n_b}\bar{t})\right], \\ \dot{\boldsymbol{\Psi}}(\bar{\mathbf{x}},\bar{t}) &= \left[\boldsymbol{\gamma}_1\imath\bar{\omega}_1 \exp(\imath\boldsymbol{\alpha}_1\cdot\bar{\mathbf{x}} + \imath\bar{\omega}_1\bar{t}), \quad \boldsymbol{\gamma}_2\imath\bar{\omega}_2 \exp(\imath\boldsymbol{\alpha}_2\cdot\bar{\mathbf{x}} + \imath\bar{\omega}_2\bar{t}), \quad \cdots, \quad \boldsymbol{\gamma}_{n_b}\imath\bar{\omega}_{n_b} \exp(\imath\boldsymbol{\alpha}_{n_b}\cdot\bar{\mathbf{x}} + \imath\bar{\omega}_{n_b}\bar{t})\right], \\ \mathbf{p}^n &= \left(p_1^n, \quad p_2^n, \quad \cdots, \quad p_{n_b}^n\right)^{\mathrm{T}}, \\ \mathbf{q}^n &= \left(q_1^n, \quad q_2^n, \quad \cdots, \quad q_{n_b}^n\right)^{\mathrm{T}}.\end{aligned} \tag{4.161}$$

The known displacements and velocities of the absorbing cloud nodes, $\bar{\mathbf{x}}_j \in \Omega_i^{\infty}$, at the known time instances $t^n$ and $t^{n-1}$ are compiled into vectors $\bar{\mathbf{G}}^n$ and $\bar{\mathbf{H}}^n$ as

$$\bar{\mathbf{G}}^n = \begin{pmatrix} \mathbf{u}_{i,\infty}^n \\ \mathbf{u}_{i,\infty}^{n-1} \\ \vdots \\ \mathbf{u}_{j,\infty}^n \\ \mathbf{u}_{j,\infty}^{n-1} \\ \vdots \end{pmatrix} = \mathbf{M}_G\mathbf{p}^n, \quad \bar{\mathbf{H}}^n = \begin{pmatrix} \mathbf{v}_{i,\infty}^n \\ \mathbf{v}_{i,\infty}^{n-1} \\ \vdots \\ \mathbf{v}_{j,\infty}^n \\ \mathbf{v}_{j,\infty}^{n-1} \\ \vdots \end{pmatrix} = \mathbf{M}_H\mathbf{q}^n, \tag{4.162}$$

where $\mathbf{u}_{i,\infty}^n := \mathbf{u}_{\infty}^n(\mathbf{x}_i,0)$, $\mathbf{u}_{j,\infty}^n := \mathbf{u}_{\infty}^n(\mathbf{x}_j,0)$, $\mathbf{u}_{i,\infty}^{n-1} := \mathbf{u}_{\infty}^n(\mathbf{x}_i,-\Delta t)$, $\mathbf{u}_{j,\infty}^{n-1} := \mathbf{u}_{\infty}^n(\mathbf{x}_j,-\Delta t)$, $\mathbf{v}_{i,\infty}^n := \mathbf{v}_{\infty}^n(\mathbf{x}_i,0)$, $\mathbf{v}_{j,\infty}^n := \mathbf{v}_{\infty}^n(\mathbf{x}_j,0)$, $\mathbf{v}_{i,\infty}^{n-1} := \mathbf{v}_{\infty}^n(\mathbf{x}_i,-\Delta t)$, $\mathbf{v}_{j,\infty}^{n-1} := \mathbf{v}_{\infty}^n(\mathbf{x}_j,-\Delta t)$, and $\mathbf{M}_G$ and $\mathbf{M}_H$ are the moment matrices from the collocation procedure, given by

$$\mathbf{M}_G = \begin{bmatrix} \mathbf{R}^{\mathrm{T}}(\tau)\boldsymbol{\Psi}(\mathbf{0},0) \\ \mathbf{R}^{\mathrm{T}}(\tau)\boldsymbol{\Psi}(\mathbf{0},-\Delta t) \\ \vdots \\ \mathbf{R}^{\mathrm{T}}(\tau)\boldsymbol{\Psi}(\bar{\mathbf{x}}_j,0) \\ \mathbf{R}^{\mathrm{T}}(\tau)\boldsymbol{\Psi}(\bar{\mathbf{x}}_j,-\Delta t) \\ \vdots \end{bmatrix}, \quad \mathbf{M}_H = \begin{bmatrix} \mathbf{R}^{\mathrm{T}}(\tau)\dot{\boldsymbol{\Psi}}(\mathbf{0},0) \\ \mathbf{R}^{\mathrm{T}}(\tau)\dot{\boldsymbol{\Psi}}(\mathbf{0},-\Delta t) \\ \vdots \\ \mathbf{R}^{\mathrm{T}}(\tau)\dot{\boldsymbol{\Psi}}(\bar{\mathbf{x}}_j,0) \\ \mathbf{R}^{\mathrm{T}}(\tau)\dot{\boldsymbol{\Psi}}(\bar{\mathbf{x}}_j,-\Delta t) \\ \vdots \end{bmatrix}. \tag{4.163}$$

Given that the system in (4.163) is overdetermined, i.e., the number of cloud nodes is fewer than the number of modes, the unknown coefficients in (4.160) can be obtained through the Moore-Penrose generalized inverse operator, denoted by the superscript '+', as

$$\begin{aligned} \mathbf{p}^n &= \mathbf{M}_G^+ \bar{\mathbf{G}}^n, \\ \mathbf{q}^n &= \mathbf{M}_H^+ \bar{\mathbf{H}}^n. \end{aligned} \tag{4.164}$$

By inserting the coefficient vectors into (4.160), we obtain the approximated far-field solution for displacements and velocities as within the cloud region $\mathbf{x} \in \Omega_i^\infty$ and for the time period, given by $t^n \leq t \leq t^{n+1}$, as

$$\begin{aligned} \mathbf{u}_\infty^n(\mathbf{x}, \bar{t}) &= \mathbf{R}^{\mathrm{T}}(\tau) \boldsymbol{\Psi}(\bar{\mathbf{x}}, \bar{t}) \mathbf{M}_G^+ \bar{\mathbf{G}}^n, \\ \mathbf{v}_\infty^n(\mathbf{x}, \bar{t}) &= \mathbf{R}^{\mathrm{T}}(\tau) \dot{\boldsymbol{\Psi}}(\bar{\mathbf{x}}, \bar{t}) \mathbf{M}_H^+ \bar{\mathbf{H}}^n. \end{aligned} \tag{4.165}$$

To compute the displacements and velocities of the central cloud node $\mathbf{x}_i$ at $t^{n+1}$, we evaluate the equations in (4.165) at $\bar{\mathbf{x}}_i \equiv \mathbf{0}$ and $\bar{t} = \Delta t$, yielding

$$\begin{aligned} \mathbf{u}_i^{n+1} &\approx \mathbf{u}_\infty^n(\mathbf{x}_i, \Delta t) = \mathbf{R}^{\mathrm{T}}(\tau) \boldsymbol{\Psi}(\mathbf{0}, \Delta t) \mathbf{M}_G^+ \bar{\mathbf{G}}^n = \bar{\mathbf{V}}_G \bar{\mathbf{G}}^n, \\ \mathbf{v}_i^{n+1} &\approx \mathbf{v}_\infty^n(\mathbf{x}_i, \Delta t) = \mathbf{R}^{\mathrm{T}}(\tau) \dot{\boldsymbol{\Psi}}(\mathbf{0}, \Delta t) \mathbf{M}_H^+ \bar{\mathbf{H}}^n = \bar{\mathbf{V}}_H \bar{\mathbf{H}}^n, \end{aligned} \tag{4.166}$$

where $\bar{\mathbf{V}}_G$ and $\bar{\mathbf{V}}_H$ are constant vectors used to update the nodal values at each explicit time step. Note that, the modes approximating the far-field solution are constructed assuming fully circular neighborhood regions, as indicated by the integration domain in (4.144), thus surface effects on the boundary layer are avoided. Moreover, each absorbing node is treated individually, negating the need to distribute boundary values across nodes within the boundary layer, thus simplifying the implementation of standard Dirichlet- and Neumann-type boundary conditions.

### 4.3.4 Implementation of Unbounded Domain Bond-Based Peridynamics

In this section, we outline the computer implementation of the proposed ABCs for the bond-based peridynamic elasticity equation. To establish a benchmark, each numerical example compares against a reference solution derived from a considerably larger bounded-domain problem. This reference is equipped with homogeneous nonlocal Neumann boundary conditions and involves up to 12 million nodes within the computational domain. For efficient computation, we utilize an extensively parallelized in-house code developed in `C++`, drawing from an existing PD research code as detailed in [93, 96]. The implementation leverages OpenMP directives to enable shared memory multiprocessing parallelism across 48 cores. Simulations are conducted on a computational node within the in-house HPC cluster at the Helmholtz Zentrum Hereon. This node features two 24-core 2.1 GHz Intel Xeon Scalable Platinum 8160 processors.

For the neighborhood search, we adopt the method described in [96], utilizing a space partitioning strategy based on the k-d tree algorithm, which efficiently handles computational complexity of $\mathcal{O}(N \log N)$. We utilize the `libkdtree++` library, which offers efficient implementations and user-friendly interfaces for handling such computations.

Prior to the time-marching process, we calculate the updating vectors for the absorbing nodes using the Moore-Penrose generalized inverse. This step is particularly computationally intensive when the number of modes is large or the nonlocality of the model increases, as indicated by an increasing PD horizon $\delta$ relative to the grid spacing. To address this, we solve the associated minimization problem using Householder transformations through the DGELSD function from

the LAPACK library [5]. The resulting updating vectors $\bar{\mathbf{V}}_G$ and $\bar{\mathbf{V}}_H$ in (4.166) are computed and stored once before the simulation begins. This addition to a standard bond-based peridynamic solver involves merely a single extra step in the time-marching sequence, specifically, performing a matrix-vector multiplication between the updating vectors and the nodal values of each absorbing node's neighboring points.

Additionally, as explored in Sections 4.1.2 and 4.2.2 for peridynamic diffusion-type and scalar wave equations, respectively, the values of $\Delta\phi$ and $\Delta k$ are chosen from symmetric intervals in (4.154) at equidistant subdivisions, resulting in $n_\phi$ and $n_k$ values for $\phi$ and $k$. A sufficient number of $n_b = n_\phi \times n_k$ modes, as shown in Section 4.2.4 for a 1D peridynamic wave equation, is required for an accurate approximation of the far-field solution at the absorbing boundary layer. It is also crucial that the range selections in (4.154) are judicious and remain within feasible bounds. For instance, as suggested in [95], setting $\Delta\phi \leq \pi/8$ ensures that waves near the normal to the absorbing boundary are effectively absorbed. Alternatively, exploring different restrictions as proposed in Section 4.1.3 and Section 4.2.3 may also prove feasible in practical applications. Moreover, the choice of $\Delta k$ should be such that the appropriate norms of the updating vectors $\mathbf{V}_G$ and $\mathbf{V}_H$ do not exceed 1, maintaining Lipschitz continuity and ensuring stable simulations over extended periods. In addition, as discussed in Section 4.2.3, the Nyquist-Shannon sampling theorem places an upper limit on $\Delta k$ as

$$0 < \Delta k \leq \frac{\pi}{\Delta x}. \tag{4.167}$$

It should be pointed out that selection of a suitable value for $\Delta\kappa$, satisfying the condition in (4.167), can quickly be done through a trial test on a sample cloud prior to the simulation. This is due to the fact that the updating vectors are pre-calculated and remain constant throughout the numerical simulation.

### 4.3.5 2D Elastic Wave Motion on Unbounded Domains

In this numerical example, we evaluate the accuracy and stability of the proposed ABCs on an unbounded-domain problem governed by the linear bond-based peridynamic elasticity equation in 2D. The layout of the reference and computational domain are illustrated in Fig. 4.35. The reference domain is spatially discretized into 12,566,345 nodes, whereas the computational domain comprises 196,321 nodes, including 6,268 absorbing nodes. The excitation source is an initial displacement field defined by (4.101), represented as a bounded Gaussian pulse centered at the origin of the global coordinate system as

$$\begin{aligned} \mathbf{u}^0(r,\theta) &= \begin{cases} \exp(-\frac{1}{100}r^2)(\cos\theta, \sin\theta)^{\mathrm{T}} & 0 < r \leq 40, \quad 0 \leq \theta < 2\pi, \\ \mathbf{0} & \text{elsewhere,} \end{cases} \\ \mathbf{v}^0(r,\theta) &= \mathbf{0}. \end{aligned} \tag{4.168}$$

This setup is used to examine scenarios involving non-diffracted and highly-diffracted wave motions, which are detailed in the subsequent sections.

**Non-Diffracted Peridynamic Wave Motion**

The initial condition for the example in Section 4.3.5 is shown in Fig. 4.36. Furthermore, Fig. 4.37 presents the displacement field's magnitude at four different times for the bounded, proposed, and reference solutions. The highly dispersive wave begins crossing the boundary by approximately $t = 0.021$ ms. In the bounded solution, the wave reflects back, while in the proposed solution (equipped with the proposed ABCs), it progresses into the exterior domain with minimal reflection, aligning closely with the reference solution. By $t = 0.21$ ms, much of the wave has left the computational domain in the reference scenario, and the remaining wave in the proposed solution closely matches the reference, demonstrating the accuracy of the ABCs on the absorbing boundary layer over time. To further evaluate the numerical performance of the proposed approach, we compute the total energy, i.e., the sum of kinetic and potential energy, within the computational domain for all three approaches over time. The total energy of the discrete system, $Pi^n$, at time step $t^n$ is defined in (4.169) as the sum of kinetic and potential energy contributions across all nodes as

$$\begin{aligned}\Pi^n &:= \frac{1}{2}\sum_{i=1}^{N_p}\rho\|\mathbf{v}_i^n\|^2 V_i + \frac{1}{2}\sum_{i=1}^{N}\sum_{j\in\mathcal{F}_i} w(\mathbf{u}_j^n - \mathbf{u}_i^n, \mathbf{x}_j - \mathbf{x}_i)\beta(\mathbf{x}_j - \mathbf{x}_i)V_j V_i \\ &\equiv \Pi_{\mathrm{k}}^n + \Pi_{\mathrm{p}}^n,\end{aligned} \tag{4.169}$$

where $\Pi_{\mathrm{k}}$ and $\Pi_{\mathrm{p}}$ represent the kinetic and potential energy, respectively, and $N_p$ is the total number of nodal points in the computational domain. Fig. 4.38 depicts the energy variation over time for the three scenarios. Initially, all solutions align well until the wave front reaches the computational boundary. Once the wave crosses the boundary, the bounded solution exhibits oscillatory behavior in both kinetic and potential energy, which fluctuates around a constant mean value. In contrast, the energy in the proposed solution remains consistent with the reference solution, demonstrating the effectiveness of the proposed ABCs in avoiding wave reflections. The total energy in the proposed solution decreases monotonically once the wave contacts the boundary, mirroring the reference solution's trend, thus confirming the absence of significant wave reflections back to the near-field. Stability tests over 100,000 time steps indicate no emerging numerical instabilities from the absorbing boundary layer.

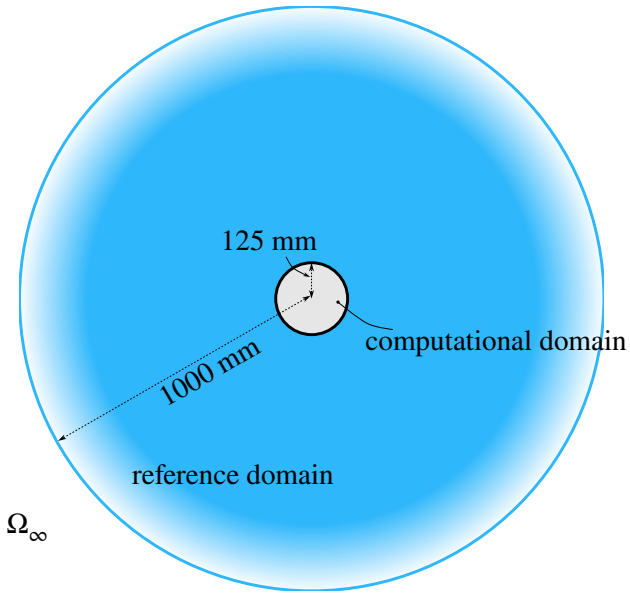


Figure 4.35: Illustration of the reference and computational domain for the numerical example in Section 4.3.5. Reproduced from [124].

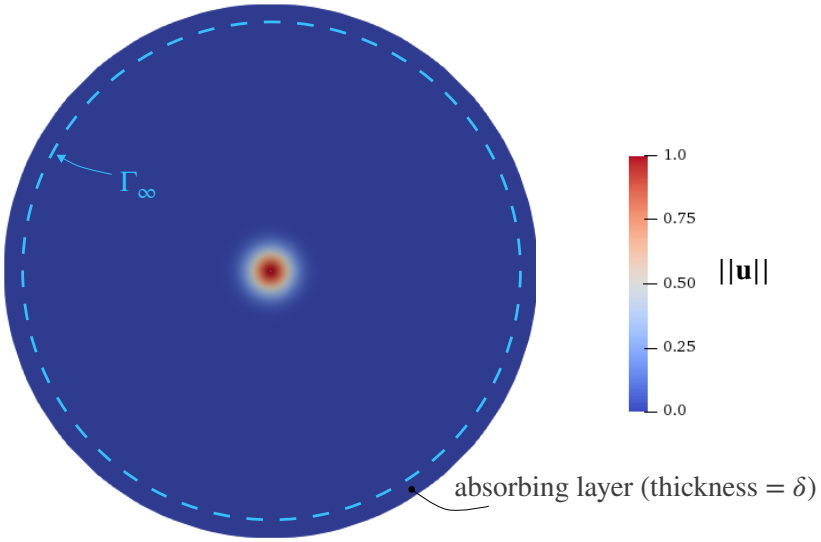


Figure 4.36: The initial displacement condition for the numerical example in Section 4.3.5 is shown with the absorbing boundary layer exaggerated in width for improved visualization. Reproduced from [124].

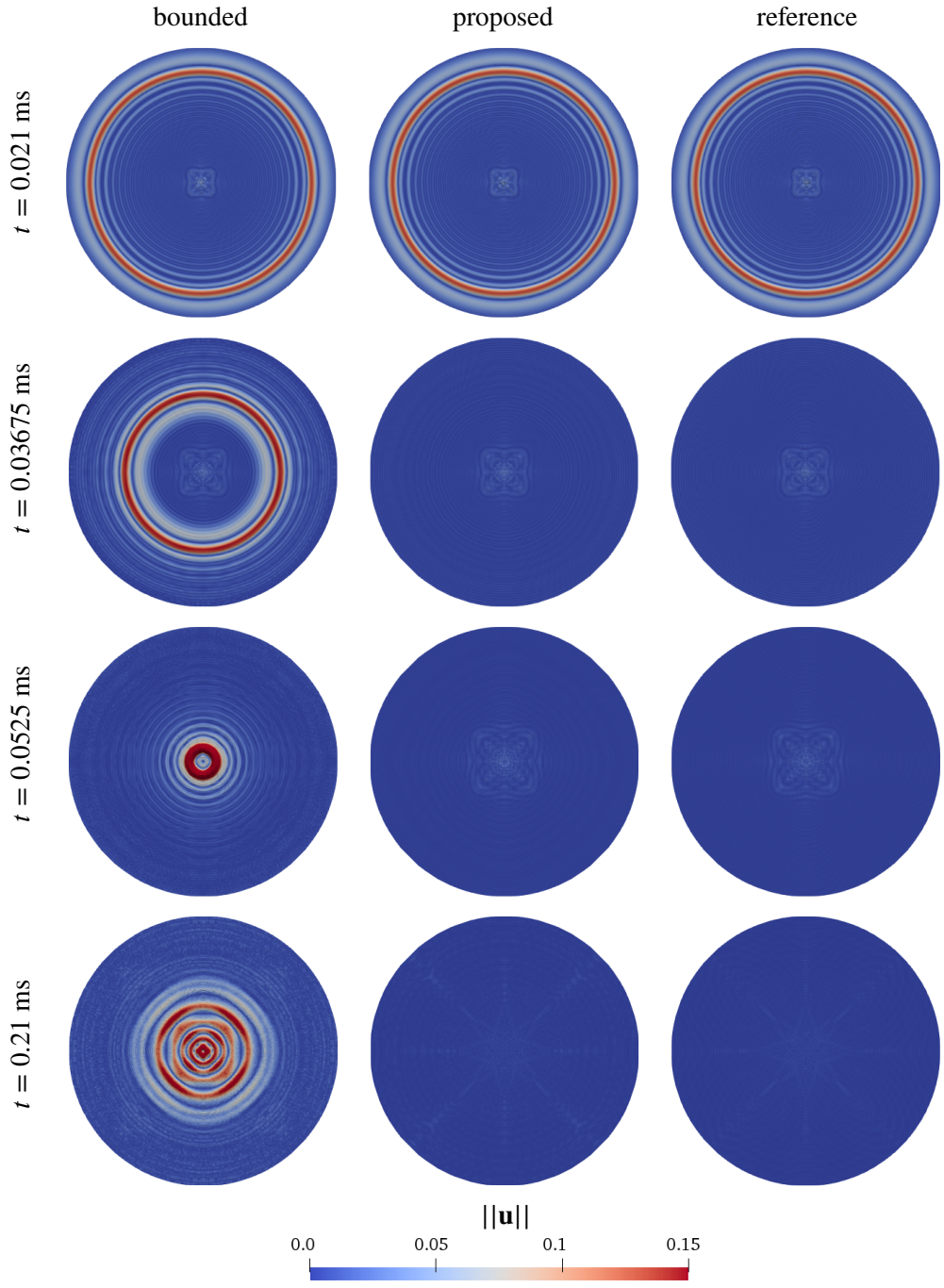


Figure 4.37: Contour plots illustrating displacement magnitude during the wave pulse propagation at different time intervals within the computational domain, as employed in the numerical example of Section 4.3.5. Reproduced from [124].

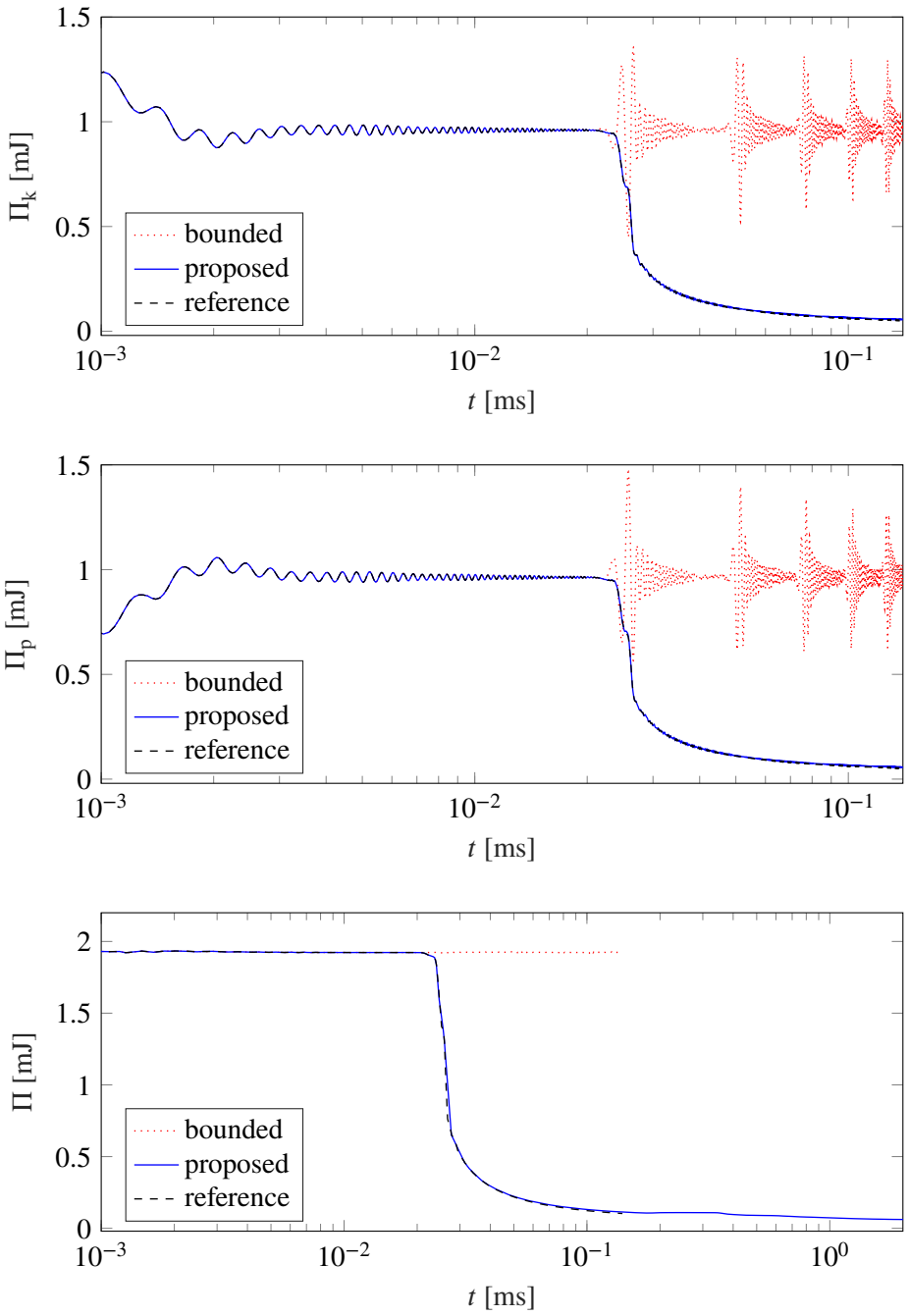


Figure 4.38: Plots of the evolution of kinetic (top), potential (middle), and total energy (bottom) within the computational domain in the numerical example of Section 4.3.5. Reproduced and adjusted from [124].

### Highly-Diffracted Peridynamic Wave Motion

In the subsequent numerical example, we evaluate the performance of the proposed ABCs in scenarios characterized by highly-diffracted peridynamic elastic waves. To facilitate this, we modify the earlier problem setup by introducing obstacles in the form of randomly distributed defects within the computational domain, as shown in Fig. 4.39. These defects act as barriers where no peridynamic bond connections are formed between material points across the defects.

Fig. 4.40 illustrates the contours of the displacement field magnitude at four distinct time points within the computational domain. Due to the defects, the wave pulse becomes highly diffracted, leading to waves propagating at various incidence angles toward the far-field. As observed in Fig. 4.40, the truncated domain solution equipped with the proposed ABCs closely aligns with the reference solution. Additionally, Fig. 4.41 shows that the energy dissipation pattern in the proposed solution closely matches that of the reference solution, with the energy decreasing monotonically once the wave reaches the boundary. Like in the non-diffracted case, the solver exhibits stable behavior over 100,000 time steps without encountering any instabilities.

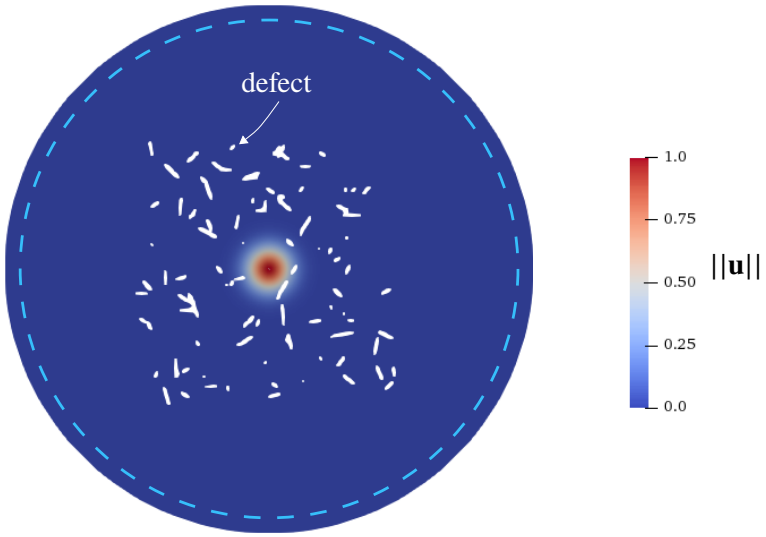


Figure 4.39: Initial condition in the computational domain for the numerical example detailed in Section 4.3.5, including an illustration of the absorbing boundary layer. Reproduced from [124].

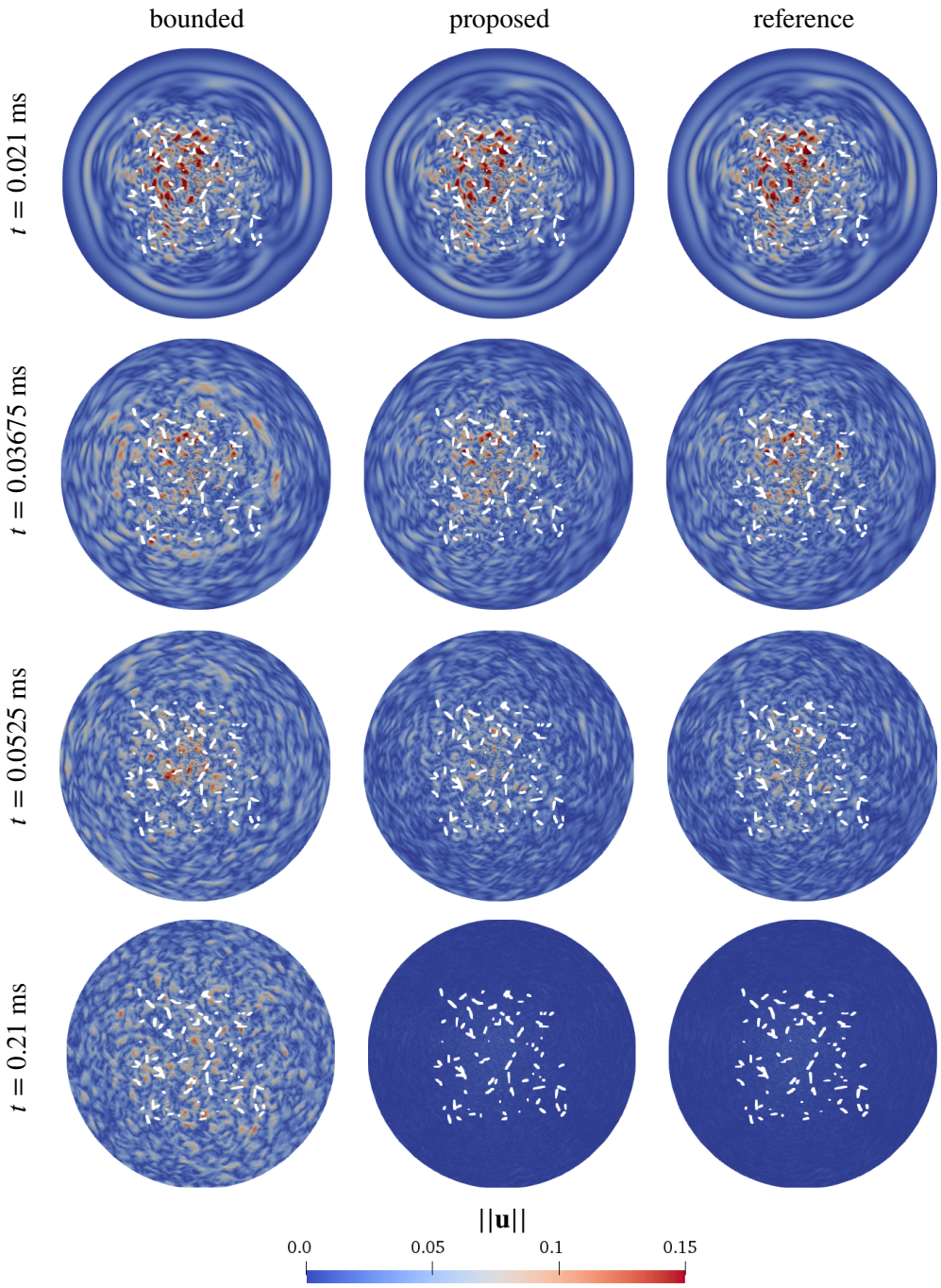


Figure 4.40: Contour plots of the magnitude of displacement during the wave pulse propagation at various time points within the computational domain for the numerical example outlined in Section 4.3.5. Reproduced from [124].

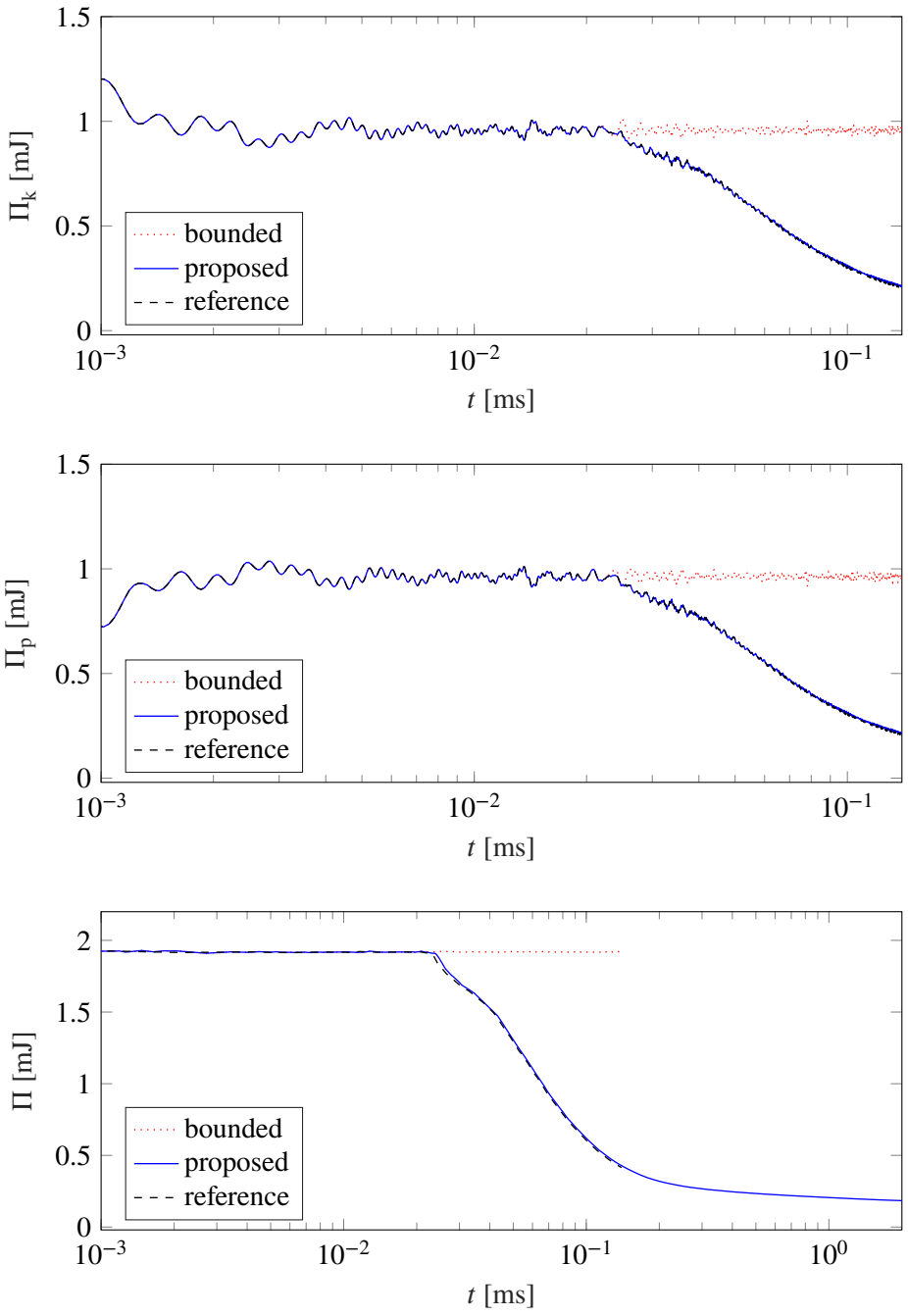


Figure 4.41: The evolution of kinetic (top), potential (middle), and total energy (bottom) within the computational domain in the numerical example of Section 4.3.5. Reproduced and adjusted from [124].

### 4.3.6 Brittle Fracture and Dynamic Crack Propagation in a 2D Half-Space

In the final example, we apply the proposed ABCs to a crack-propagation problem within a semi-unbounded half-space domain in 2D, a scenario commonly explored in geophysical applications and soil-structure interactions (see e.g. [57]). The reference and computational domains are depicted in Fig. 4.42, with further details of the computational setup shown in Fig. 4.43, highlighting two vertical notches of identical lengths. The upper surface adheres to a homogeneous nonlocal Neumann boundary condition, while the region between the notches is subjected to the impact of a rigid projectile, implementing a Dirichlet condition on the velocity at $16.5 \times 10^3$ mm/s as shown in Fig. 4.43.

The spatial discretization results in 6,929,209 nodes for the reference domain and 98,411 nodes for the computational domain, including 3138 absorbing nodes, with the simulation spanning a total 0.21 ms. Fig. 4.44 presents contour plots of damage, displacement magnitude, and $y$-component of velocity at the final time instant for all three scenarios. Despite the highly dispersive wave field caused by the impact and crack nucleation at the tips, the results confirm that the proposed ABCs effectively reproduce the reference solution. Conversely, the bounded solution shows wave reflections from the truncated boundary back to the near-field, causing stress intensities around the notches to increase. This results in longer cracks that diverge from those observed in the reference solution, highlighting the impact of boundary effects on the accuracy of the simulation outcomes.

To further evaluate the accuracy of the proposed solution compared to the reference solution, Fig. 4.45 displays the crack paths emanating from the right notch at the last recorded time instant. The comparison reveals that the crack path generated by the proposed solution not only closely matches the reference solution in terms of length but also accurately follows the same direction at a similar angle. These results underscore the effectiveness of the proposed ABCs in accurately replicating the dynamic behavior and outcomes of the computational reference model in scenarios involving dynamic crack propagation.

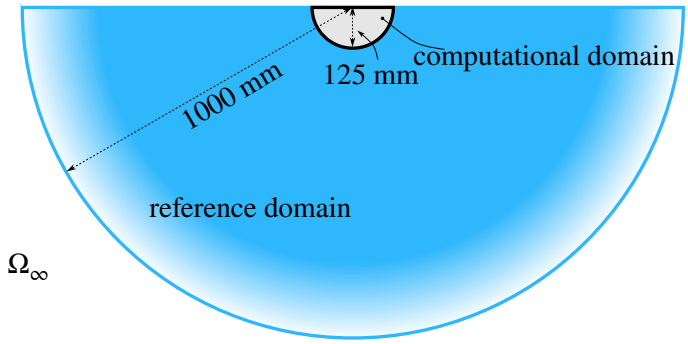


Figure 4.42: Schematic representation of the reference and computational domains in the numerical example of Section 4.3.6. Reproduced from [124].

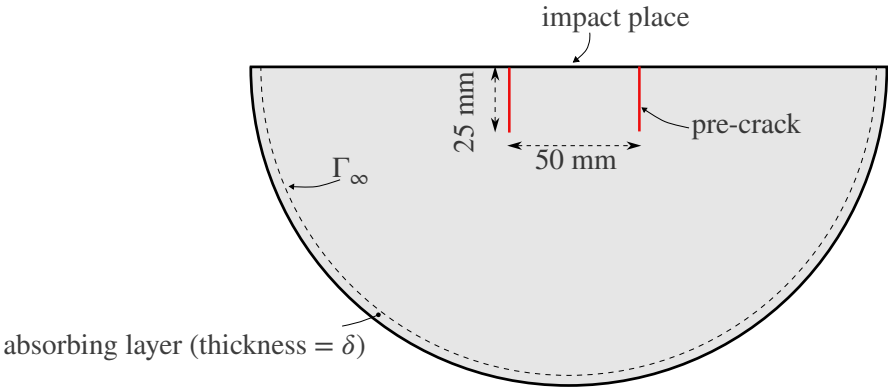


Figure 4.43: Schematic representation of the computational domain with two notches in the numerical example of Section 4.3.6. Reproduced from [124].

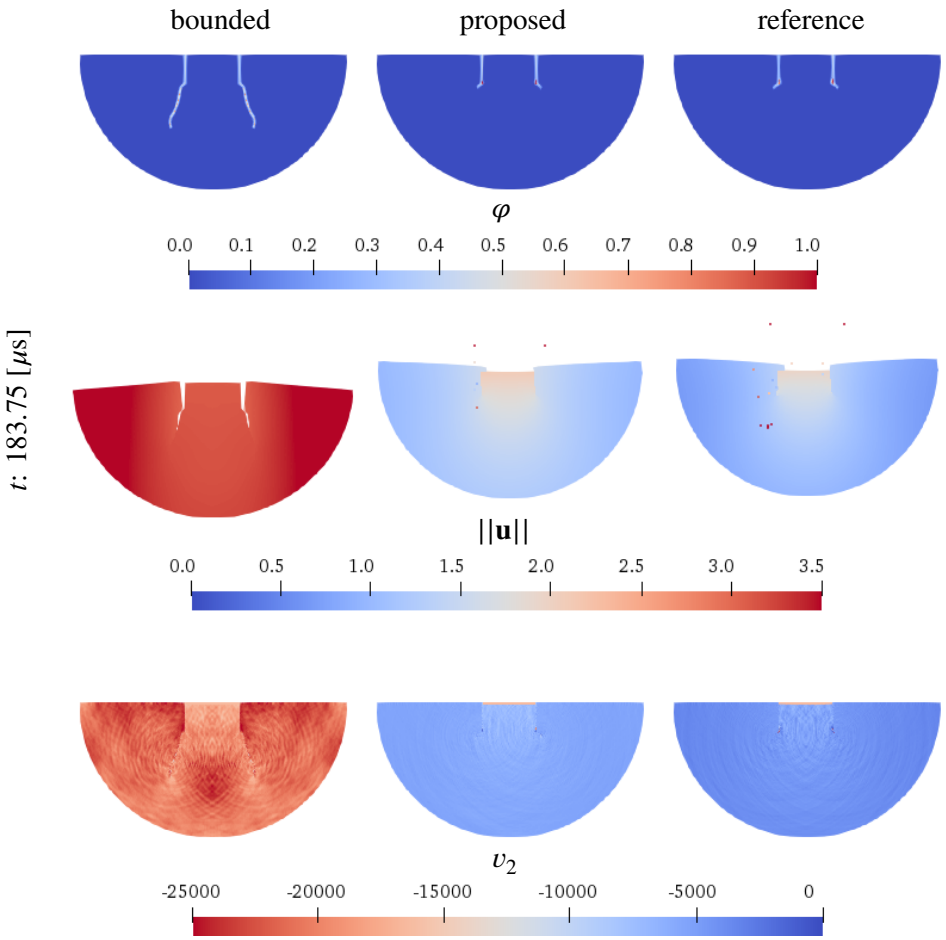


Figure 4.44: Contour plots of the damage field (top) in the undeformed configuration, magnitude of displacement field (middle) in the deformed configuration, and $y$-component of velocity field (bottom) in the undeformed configuration of the computational domain at the final time step of the numerical example presented in Section 4.3.6. Reproduced from [124].

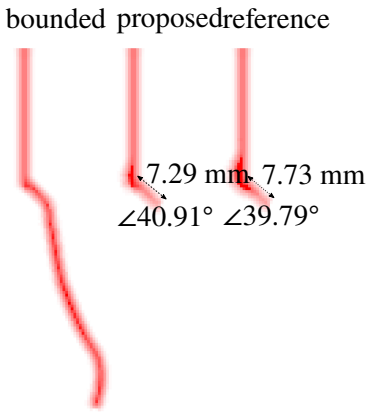


Figure 4.45: Comparison of final crack paths of the numerical example in Section 4.3.6. Reproduced from [124].

# Chapter 5

# Multi-Physics Simulation of Bio-Degradable Magnesium-Based Bone Implants

In this chapter, we examine the use of peridynamic models, specifically the peridynamic bi-material and NNPP corrosion systems, for modeling the bio-degradation of magnesium-based bone implant screws, focusing on the alloys Mg-5Gd and Mg-10Gd. These alloys are chosen for their favorable properties and compatibility, as highlighted in experimental studies. We begin by reviewing data collection from an experimental *in vitro* bio-corrosion setup in simulated physiological conditions, noting that the fluid is regularly changed to avoid saturation, allowing us to model the dissolution process as an unbounded diffusion problem. This setup ensures that the peridynamic model accurately reflects the simulated physiological conditions. We detail how the peridynamic bi-material corrosion model is parameterized using volume loss data via Particle Swarm Optimization (PSO), achieving high accuracy in simulating macroscopic volume loss over several weeks. While this model captures the general corrosion behavior, it only implicitly represents layer deposition and precipitation effects at the corrosion surface. To include additional ionic components found in the liquid electrolyte, we employ the NNPP system, which enhances the model's ability to depict the distribution of ions in SBF. Additionally, we discuss employing surrogate modeling to bridge *in vitro* and *in vivo* results, thereby enhancing the applicability of our findings. We conclude by linking peridynamic bio-corrosion simulation to mechanical analysis techniques typically based on classical local methods and FEM strategies. While peridynamic models for constitutive damage and correspondence are well documented, detailed examinations of Mg-5Gd and Mg-10Gd post-corrosion are scarce. Thus, we employ a traditional FEM-based damage plasticity approach to assess the residual mechanical strength of the corroded screws after extended immersion, projecting their durability over their intended lifetime within a digital life-cycle simulation framework. The results and findings summarized in this chapter were published in various academic papers. Specifically, Section 5.1, Section 5.2, and Section 5.4 are heavily based on [60], while the results of Section 5.2.4 are available in [58], and Section 5.3 contains material from [2].

## 5.1 Experimental Data and Mechanics of Magnesium-Based Implants

In this section, we provide a comprehensive discussion on the experimental data acquisition and material data parameters that underpin both the peridynamic corrosion and FEM damage plasticity simulations for Mg-5Gd and Mg-10Gd alloys. Starting with an overview of the bio-corrosion experiments, including a detailed description of the electrolyte media and materials used, we then delve into the micro-structural and mechanical characterizations of these alloys. The mechanical parameters used in the residual mechanical analysis are also introduced.

To approximate the degradation profiles of Mg-5Gd and Mg-10Gd *in vivo*, *in vitro* degradation tests are performed in media mimicking body fluids, where samples are submerged under controlled conditions, such as in a well plate. During these quasi-static immersion tests, the electrolyte is regularly replaced to prevent ion depletion or salt saturation, effectively simulating the hydrodynamic conditions found in biological tissue environments and helping control salt and deposit formations during the bio-degradation process based on the ion composition of the medium [48]. Influenced by local chemical conditions like pH values and temperature, chemical compounds precipitate within the bulk medium and on the implant surface, forming a thin degradation layer, which acts as a partially protective film whose thickness and composition significantly affect the degradation dynamics. In the absence of galvanic corrosion from metal impurities, the degradation primarily hinges on ion diffusion through the nanoporous layer [154]. Precipitation leads to ion depletion, altering the chemical reaction equilibrium, influencing degradation rates, and affecting the interaction of ions with the metal on a unit area. Despite these factors, macroscopic implant degradation is measurable through methods like hydrogen evolution, weight loss, or volume loss. Specifically, volume loss is gauged using micro-computed tomography ($\mu$CT), a non-destructive, high-resolution 3D imaging technique, by comparing pre and post-degradation sample images [152, 151].

The experimental procedures, detailed in [75] and illustrated in Fig. 5.1, involve M2 $\times$ 4 mm threaded bone implant screws measuring 2 mm in diameter and 4 mm in length with a $0.5 \times 0.5$ mm slotted head were crafted from Mg-5Gd and Mg-10Gd. For the *in vitro* testing, the screws were immersed in a complex cell culture medium (either $\alpha$-Minimum Essential Medium or Dulbecco's Modified Eagle's Medium, supplemented with 10% Fetal Bovine Serum and 1% Penicillin / Streptomycin) for periods of {1, 2, 3, 4, 8} weeks under cell culture conditions (37°C, 5% $CO_2$, 20% $O_2$, and 95% relative humidity). After immersion in a cell-culture-like medium for up to 8 weeks, the screws are cleaned, the degradation layer removed, and re-imaged to assess degradation. The conditions under which these experiments are conducted, including the regular refreshing of the immersion medium, are consistent with standard cell culture environments. The post-test tomographic data is processed to calculate the macroscopic material volume loss, illustrated in Fig. 5.1, and defined as

$$V_L(t) = \frac{V_0 - V(t)}{V_0}, \tag{5.1}$$

where $V_0$ and $V(t)$ represent the volume of the metallic material before and after the test at time $t$, respectively. Continuing, the microstructural and mechanical properties of these alloys are extensively documented in [56]. In our FEM-based damage plasticity analysis, a Young's modulus of 43 GPa and a Poisson's ratio of 0.3 are assigned. The alloys exhibit isotropic hardening modeled using exponential Voce-type stress-strain functions. As shown in Fig. 5.2, Mg-10Gd, with its higher Gd content, exhibits greater yield stress and tensile strength than Mg-5Gd. These stress-strain functions are inputted for the damage plasticity computations, as further discussed in Section 5.4. Our analyses account for finite deformations by employing logarithmic Hencky strain measures.

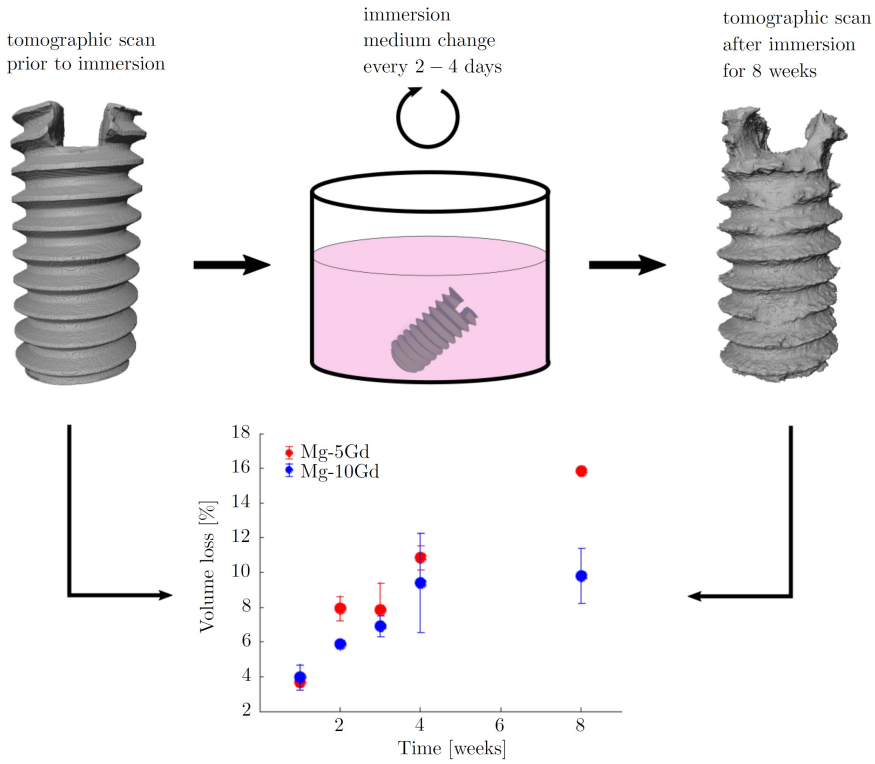


Figure 5.1: Schematic of the bio-corrosion experiment: Initial screw volume was determined using $\mu$CT images. After immersion in the degradation medium and removal of the degradation layer with chromic acid, the screw was reimaged. Volume loss was calculated from these images. Data sourced from [75] and image reproduced from [60].

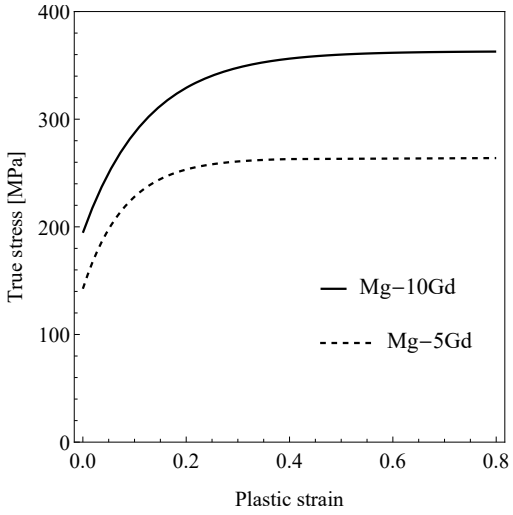


Figure 5.2: Extrapolated stress-strain curves for Mg-5Gd and Mg-10Gd. Reproduced from [60].

## 5.2 Peridynamic Bio-Corrosion Simulation of Bone Implant Screws

In the next sections, the results of the numerical *in vitro* peridynamic bio-corrosion simulations and the calibration of model parameters are discussed. First, we derive a peridynamic constitutive corrosion model that effectively correlates the macroscopically observable volume loss over time with the diffusivity of peridynamic interface bonds. Following this, we illustrate a method for optimizing peridynamic corrosion models using low fidelity models with reduced spatial resolution through the PSO algorithm. We then demonstrate how these estimated parameters are transferred to a high-resolution, i.e., the high fidelity, peridynamic bi-material and NNPP corrosion models.

For robust 3D corrosion simulations, we developed a highly parallelized code using the `C++11` programming language. These simulations are run on a dual-socket computational node at the Helmholtz Zentrum Hereon's in-house HPC cluster, equipped with 24-core 2.1 GHz Intel Xeon Scalable Platinum 8160 processors, supporting shared memory multiprocessing on 48 cores via OpenMP directives. We utilize the `libkdtree++` library for its efficient implementation of the *k-d tree* algorithm to construct peridynamic neighborhoods. Mathematical operations, particularly those involving linear algebra, leverage the LAPACK software library [5]. The linear systems of equations were iteratively solved using the Generalized Minimal Residual Method (GMRES). The PSO algorithm employs a hybrid parallelism combining shared memory programming on each computational node with distributed memory parallelization across nodes using the Message Passing Interface (MPI) standard. This optimization involves a network of 10 computational nodes, each utilizing 5 cores.

### 5.2.1 Semi-Empricial Volume Loss Corrosion Kinetics Model

In this section, we examine the constitutive assumptions associated with the kinetics of electrochemical corrosion of binary Mg-Gd implant materials at the metal-electrolyte interface. Specifically, these assumptions relate to the peridynamic micro-diffusivity of solid-liquid interface bonds and the definition of electric overpotential $\eta$ used in our modeling approach. Here, $\eta$ denotes a relative positive shift in the corrosion potential of the bare immersed Mg-Gd system. Assuming a Tafel-like behavior at the material interface allows a precise mathematical description of the change in Mg dissolution current. It is presumed that an increase in $\eta$ is linked to precipitation and deposit formation, which captures the effect of a decrease in anodic dissolution current due to precipitation. Thus, increased micro-diffusivity for the corrosion interface bonds may lead to a precipitation layer on the corrosion surface since the concentration of the liquid electrolyte cannot exceed the saturation limit $C_{\text{sat}}$. We adopt the approach from [63], which proposes an implicit mechanism to account for deposit and precipitation layer formation in peridynamic corrosion models. When a solid node near the solid-liquid interface has a liquid node with a concentration at or above $C_{\text{sat}}$, the micro-diffusivity of all active bonds in this neighborhood is temporarily set to zero, suppressing diffusion as long as this condition is met. This approach captures the potential drop due to electrical resistance from deposits without explicitly measuring their thickness, constitution, or composition.

It is important to note, that temporarily inhibiting the diffusion of Mg ions is an overestimation since the formation of a precipitation layer reduces but does not entirely stop the interface flux. For instance, as shown by [22] for the ZE10 alloy, the interface flux decreases to between 0.15 and 0.25. However, due to the uncertainty in the exact reduction of diffusion flux, it is practical to interrupt the diffusion flux altogether. By calibrating the micro-diffusivity (or Fickian diffusion coefficient), an average diffusion flux can be achieved over time, approximating the permeability properties of the electrolytic environment on the corrosion rate. This approach ensures close alignment between

simulation results and experimental volume loss data, eliminating an additional calibration parameter. The results of the calibrated peridynamic corrosion model are presented in Section 5.2.3. Using the peridynamic bi-material bio-corrosion model with the standard discretization in PD, the quadrature summation in (3.4), along with an implicit time discretization, yields

$$\dot{C}_i^{n+1} - \sum_{j \in \mathcal{F}_i} \kappa_{ij}^{n+1} \left( \frac{C_j^{n+1} - C_i^{n+1}}{\|\mathbf{x}_j - \mathbf{x}_i\|^{n_d+2q}} \right) \Delta V_j = 0, \tag{5.2}$$

where $\kappa_{ij}^{n+1}$ denotes the micro-diffusivity for the bond $\boldsymbol{\xi} = \mathbf{x}_j - \mathbf{x}_i$ and time instance $t^{n+1}$. The equation in (5.2) can be expressed in a global matrix-vector form, collecting all the concentration values and their time derivatives at the nodal points into global vectors, as

$$\dot{\mathbf{C}}_T^{n+1} - \widetilde{\mathbf{K}}^{n+1} \mathbf{C}_T^{n+1} = \mathbf{0}, \tag{5.3}$$

where $\widetilde{\mathbf{K}}^{n+1} \in \mathbb{R}^{N_p \times N_p}$, with $N_p$ denoting the number of nodal points in the domain, is a symmetric and time-dependent global conductance matrix with entries given by

$$\widetilde{K}_{ii} = - \sum_{j \in \mathcal{F}_i} \frac{\kappa_{ij}^{n+1}}{\|\mathbf{x}_j - \mathbf{x}_i\|^{n_d+2q}} \Delta V_j, \tag{5.4}$$

$$\widetilde{K}_{ij} = \frac{\kappa_{ij}^{n+1}}{\|\mathbf{x}_j - \mathbf{x}_i\|^{n_d+2q}} \Delta V_j, \tag{5.5}$$

and the global vector of nodal concentrations $\mathbf{C}_T^{n+1} \in \mathbb{R}^{N_p}$ is defined as

$$\mathbf{C}_T^{n+1} = \begin{bmatrix} \vdots \\ C_i^{n+1} \\ \vdots \\ C_j^{n+1} \\ \vdots \end{bmatrix}. \tag{5.6}$$

The micro-diffusivities, and thus the entries of the conductance matrix $\widetilde{\mathbf{K}}^{n+1}$, are updated at time step $t^{n+1}$ as summarized in Algorithm 1. As proposed by the mechanism in [63], this update accounts for the effect of precipitation layer formation without the need to compute its composition or thickness. The peridynamic micro-diffusivity parameter determines the corrosion progression as it dictates the speed and characteristics of the anodic dissolution process. Given the definition of the overpotential $\eta_j^{n+1}$, evaluated at $\mathbf{x}_j$ and $t^{n+1}$, the micro-diffusivity $\kappa_{ij,\text{int}}^{n+1}$ in the standard bi-material peridynamic corrosion model for interface bonds at $t^{n+1}$, assuming $\mathbf{x}_j$ is in the solid metal phase, can be expressed as

$$\kappa_{ij,\text{int}}^{n+1} = \frac{3(1-q)D_{\text{int}}}{\pi\delta^{2-2q}} 10^{\left(\frac{\eta_j^{n+1}}{\beta_a}\right)} = \frac{3(1-q)D_{\text{int}}}{\pi\delta^{2-2q}} 10^{\left(\frac{\phi_{\text{corr}} - I_j^{n+1} R_j^{n+1}}{\beta_a}\right)}, \tag{5.7}$$

where $D_{\text{int}}$ is the Fickian diffusion coefficient at the metal-electrolyte interface, $q$ is the kernel exponent, $\phi_{\text{corr}}$ is the effective corrosion potential, $\beta_a$ is the anodic Tafel slope (according to the modeling approach) and $I_j^{n+1} R_j^{n+1}$ is the potential drop, where $I_j^{n+1}$ refers to the total anodic current

and $R_j^{n+1}$ is the electrical resistance related to the deposit formation and the electrolyte conductivity both at time step $t^{n+1}$. Note that, for simplicity in implementation, the interface diffusivity, $\kappa_{ij,\text{int}}^{n+1}$, can be assigned to material points in the solid metal phase. Additionally, the diffusion between solid-solid diffusion bonds can be effectively excluded from the numerical computation, as diffusion in the solid bulk is typically slower by several orders of magnitude compared to the material dissolution into the surrounding liquid electrolyte. The electric current $I^{n+1}$ at time step $t^{n+1}$ can be estimated based on the relation:

$$I_j^{n+1} = zF\frac{C_j^{n+1} - C_j^n}{\Delta t}\Delta V_j, \tag{5.8}$$

where $z$ is the ion charge number, $F$ is Faraday's constant, $\Delta V_j$ is the cell volume associated with $\mathbf{x}_j$, and $\Delta t$ is the time increment. The electrical resistance $R_i^{n+1}$ can be influenced by factors like the ohmic drop due to the electrolyte or resistive films at the interface. The precipitation layer's impact on overpotential is included implicitly and thus excluded from this resistance. Algorithm 1 provides a schematic overview of implementing temporary diffusion inhibition between the solid material and the liquid electrolyte when the saturation constant $C_{\text{sat}}$ is exceeded. For a detailed overview, refer to [90].

**Algorithm 1** Mechanism for the description of implicit precipitation layer formation at $t^{n+1}$.

Initialize conductance matrix $\widetilde{\mathbf{K}} \leftarrow \mathbf{0}$
**for all** nodes $\mathbf{x}_i$ **do**
  **for all** nodes $\mathbf{x}_j$ in the neighborhood $\mathcal{F}_i$ **do**
    **if** $\mathbf{x}_i$ in metal phase **then**
      **if** $\mathbf{x}_j$ in electrolyte phase **and** $C_j^n \geq C_{\text{sat}}$ **then**
        $\widetilde{K}_{ij} \leftarrow 0 \quad \forall j$
        $\widetilde{K}_{ji} \leftarrow 0 \quad \forall j$
        **break**
      **else**
        Update $\widetilde{K}_{ij}$ according to (5.5)
        Update $\widetilde{K}_{ii}$ according to (5.4)
      **end if**
    **else if** $\mathbf{x}_i$ in liquid phase **then**
      **if** $\mathbf{x}_j$ in solid phase **and** $C_i^n \geq C_{\text{sat}}$ **then**
        $\widetilde{K}_{ij} \leftarrow 0$
      **else**
        Update $\widetilde{K}_{ij}$ according to (5.5)
        Update $\widetilde{K}_{ii}$ according to (5.4)
      **end if**
    **end if**
  **end for**
**end for**

Given the complexity, determining the exact functional relationship for electric resistance is generally impractical. Therefore, we propose a practical phenomenological approach to develop a constitutive peridynamic bio-corrosion model that effectively connects the experimentally observed macroscopic volume loss to the peridynamic micro-diffusivity parameter (or Fickian interface diffusion coefficient). In this approach, the time-dependent behavior of the overpotential is replaced by volume loss using a semi-empirical corrosion rate equation. Semi-empirical corrosion models are widely used since they offer accurate predictions on corrosion rates and depths for various systems with minimal parameter calibration [28, 47]. We adopt the model from [47] to binary Mg-Gd alloys, where the average corrosion depth, and hence volume loss, is given by

$$V_L(t) = l \log\left(1 + \frac{t}{\tau}\right), \tag{5.9}$$

where $l, \tau$ are model parameters related to the corrosion depth and speed of progression. Derivation with respect to time yields the volume loss rate, which in the case of homogeneous corrosion represents the corrosion rate

$$\frac{\partial}{\partial t} V_L(t) = \frac{l}{\tau + t}, \tag{5.10}$$

which be rewritten implicitly in terms of volume loss as

$$\dot{V}_L(t) = \frac{l}{\tau} 10^{\left(-\frac{V_L(t)}{l}\right)}. \tag{5.11}$$

Using Faraday's 2nd law of electrolysis, we can relate the anodic current density to the mass of dissolved material. By incorporating (5.11) into Faraday's 2nd law, we obtain

$$i_a(t) = \frac{lzF\rho}{\tau MA} 10^{\left(-\frac{V_L(t)}{l}\right)} = \tilde{i}_0 10^{\left(-\frac{V_L(t)}{l}\right)}, \tag{5.12}$$

where $\tilde{i}_0$ represents the anodic current density at $t = 0$, or at zero initial volume loss $V_L(0) = 0$. The relationship in (5.12) is similar to the Tafel equation in electrochemical kinetics but connects volume loss to anodic current density instead of overpotential. Since the peridynamic bi-material corrosion model assumes a linear relationship between the micro-diffusivity of solid (undissolved) interface bonds and the anodic current density $i_a$, we can derive a corresponding expression for micro-diffusivity as a function of volume loss as

$$\kappa_{ij,\text{int}}^{n+1} = \frac{3(1-q)D_{\text{int}}}{\pi\delta^{2-2q}} 10^{\left(-\frac{V_L^{n+1}}{l}\right)}. \tag{5.13}$$

The semi-empirical corrosion model replaces the time evolution of the overpotential with the experimentally observable volume loss of the metallic sample. By calibrating the model using experimental volume loss data, the corrosion process can be accurately described through peridynamic micro-diffusivity, which in turn, ensures the correct representation of the anodic dissolution process. Note that the constitutive relation derived in (5.13) for the standard peridynamic bi-material corrosion model can also be used in the generalized NNPP corrosion formalism to describe the anodic dissolution of the metallic sample, considering the presence of various ionic components in the systems. This constitutive assumption has been consistently applied in the numerical studies of this chapter for both bi-material and NNPP corrosion systems.

### 5.2.2 Parameter Calibration on Low Fidelity Peridynamic Bio-Corrosion Models

Calibrating the constitutive parameters of peridynamic corrosion models, typically depends on extensive experimental data, such as electrochemical polarization curves or saturation concentrations $C_{\text{sat}}$ for the specific corrosion system at hand. However, data availability is often limited or nonexistent. For example, proteins in the electrolyte can deposit on the measuring electrode's surface, complicating the acquisition of polarization curves. Additionally, certain model parameters, such as the exponent $q$ of the peridynamic kernel function in (2.49), cannot be directly measured experimentally. Given the numerous uncontrolled parameters and resulting uncertainties, a meta-heuristic evolutionary algorithm like PSO is a suitable choice. This optimization algorithm effectively estimates parameters, allowing exploration of the potentially vast parameter space.

Two separate parameter optimizations are conducted to calibrate the peridynamic corrosion models using Mg-5Gd and Mg-10Gd volume loss data sets. Experimental details, including a $\mu$CT analysis of microstructure and overall volume loss over an 8-week immersion period, are provided in [73, 60]. To explore the parameter space thoroughly, a large number of iterations is required, necessitating a highly efficient simulation. Therefore, the PSO procedure is performed on a low-resolution model, termed the low fidelity model, and the estimated parameters are then adjusted for a subsequent high-resolution, or high fidelity model. The parameter values are restricted within boundaries shown in Table (5.1), which denote the physically feasible subspace and provide beneficial starting conditions for the optimization algorithm. For Mg-5Gd, $C_{\text{Solid}}$ is $66082.4\,\text{mol}/\text{m}^3$, and for Mg-10Gd, it is $62575.3\,\text{mol}/\text{m}^3$. Note that the peridynamic kernel exponents $q$ were initially included in the parameter vector and optimization process. However, the optimizer tended to set these values to 0, the assumed parametric boundary. This behavior increased the norm in the kernel function and enhanced the model's nonlocality, thus fully utilizing its nonlocal capabilities. Due to this boundary convergence observed during the optimization, the kernel exponent $q$ is excluded from further discussion. The parameter $l$ must be adjusted when transferring it to the high fidelity model, due to deviations in total volume and corrosion surface caused by the coarser discretization of the low fidelity model. Assuming equal electric current densities between the low and high fidelity models, and neglecting initial volume loss in (5.12), the adjustment is given by

$$l_{\text{high}} = \frac{A_{\text{high}}}{A_{\text{low}}} l_{\text{low}}, \tag{5.14}$$

where $A_{\text{low}}$ and $A_{\text{high}}$ represent the corrosion surfaces of the low and high fidelity models, respectively, and $l_{\text{high}} \equiv l$ is the adjusted proportionality constant for the high fidelity model. For the models of the headless $\text{M2} \times 4\,\text{mm}$ bone implant screw geometry used in this study, the correction factor is $\frac{A_{\text{high}}}{A_{\text{low}}} = 1.1275$. Fig. 5.3 shows the computational domain and initial condition of the low fidelity peridynamic bi-material corrosion model, where the solid metal part of the implant bone screw is depicted in red, and the surrounding parts represent the liquid electrolyte, with a total of $34,153$ nodes used to discretize the geometry. The quadratic error between the experimentally observed volume loss data, shown in Fig. 5.1, and the simulation is employed as the objective function of the numerical parameter optimization procedure

$$\min_{\mathbf{p}} \mathcal{L}(\mathbf{p}) = \min_{\mathbf{p}} \sum_{i \in \mathcal{I}} \left( V^i_{\text{L,exp}} - V^i_{\text{L,sim}}(\mathbf{p}) \right)^2, \tag{5.15}$$

where $\mathbf{p}$ is the parameter vector, $V^i_{\text{L,exp}}$ is the experimentally observed volume loss, and $V^i_{\text{L,sim}}(\mathbf{p})$ is the simulated volume loss, both evaluated at the discrete time instances $\mathcal{I} = 1, 2, 3, 4, 8$ weeks.

The PSO algorithm undergoes 1000 iterations, were stagnation in minimizing the loss function, and thus a local minima, occurs after 957 iteration for Mg-10Gd and 611 iterations for Mg-5Gd. Despite the algorithm's inherent randomness potentially allowing further reduction in the loss function, a satisfactory agreement with the experimental data is achieved for less than 1000 iterations. The results of the parameter calibration for Mg-10Gd and Mg-5Gd on the fidelity model are summarized in Table 5.1. The next section demonstrates how these results are applied to the high fidelity corrosion model.

Table 5.1: peridynamic bi-material corrosion model parameters calibrated on the low fidelity model. Data available in [60].

| Parameter | Mg-5Gd | Mg-10Gd | Range | Unit |
|---|---|---|---|---|
| $D_{\text{int}}$ | $2.8779 \times 10^{-15}$ | $1.3956 \times 10^{-14}$ | $(\epsilon, 4.2 \times 10^{-8})$ | $[\text{m}^2\,\text{s}^{-1}]$ |
| $D_{\text{liq}}$ | $8.6822 \times 10^{-9}$ | $2.1051 \times 10^{-10}$ | $(\epsilon, 4.2 \times 10^{-6})$ | $[\text{m}^2\,\text{s}^{-1}]$ |
| $C_{\text{Sat}}$ | 0.6608 | 0.6257 | $(C_{\text{Solid}} \times 10^{-5}, C_{\text{Solid}} \times 0.33)$ | $[\text{mol}\,\text{m}^{-3}]$ |
| $l$ | 0.2355 | 0.064 | $(0.01, 1/\epsilon)$ | $[\text{m}^3]$ |

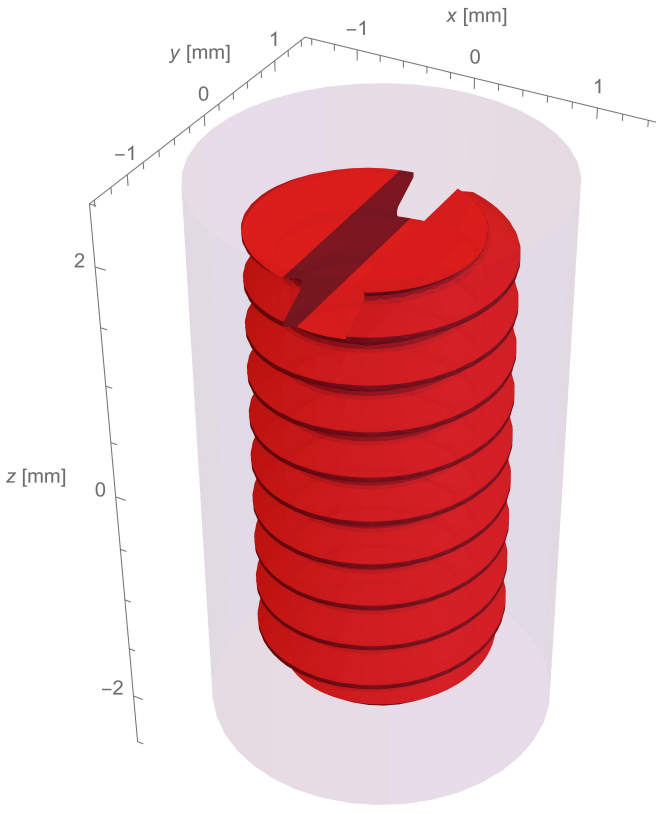


Figure 5.3: Computational domain of the low fidelity model used for parameter optimization of the headless M2 × 4 mm bone implant screw. Reproduced from [60].

### 5.2.3 Peridynamic Bi-Material Bio-Corrosion Simulation on High Fidelity Models

After calibration of peridynamic bi-material model parameters using experimental volume loss data on Mg-5Gd and Mg-10Gd, simulations were performed based on the initial condition shown in Fig. 5.4. Following the multi-grid approach for adaptive mesh refinement of peridynamic diffusion-type models, as outlined in Section 3.4, the computational domain is divided into $\Omega^-$ and $\Omega^+$, discretized with 50 µm and 100 µm respectively. This resolution suffices as the anodic dissolution rate of the systems at hand ensures numerical convergence. The region $\Omega^-$ encompasses the entire implant screw geometry and adjacent liquid domain parts, with nonlocal ABCs enforced on the $\Omega^+$ boundaries to numerically mimic the experimental *in vitro* electrolyte exchange every 2-4 days. The computational domain is discretized using $241,740$ nodes for $\Omega^+$ and $408,205$ nodes for $\Omega^-$, totaling $649,945$ nodes. Uniform discretization of $\Omega^-$ across the domain would increase the node count to $2,143,611$.

Fig. 5.5 shows the simulated volume loss progression over time. The experimental volume loss data is represented by blue and red data points for Mg-5Gd and Mg-10Gd, respectively. Simulation curves are plotted for a fully fine discretization of 50 µm (denoted as *Fine*) versus the multi-grid approach (denoted as *Multi-grid*). The simulation results show good qualitative agreement with experimental data for both materials. The developed peridynamic bi-material constitutive model, with numerical parameter optimization using experimental volume loss data, captures the macroscopic corrosion behavior well. Minor deviations between the multi-grid approach and full discretization are noticeable but remain relatively small. For Mg-10Gd, the multi-grid approach yields slightly more accurate results compared to the experimental data. However, this may be due to the specific parameters obtained from the calibration procedure and the multi-grid domain definition, and does not indicate general superiority. As reported in Table 5.2, employing the multi-grid approach significantly reduces the number of nodal points, leading to a substantial decrease in simulation time. For Mg-5Gd, the total simulation time is reduced by more than 12 times, and for Mg-10Gd, it is reduced by more than 6 times.

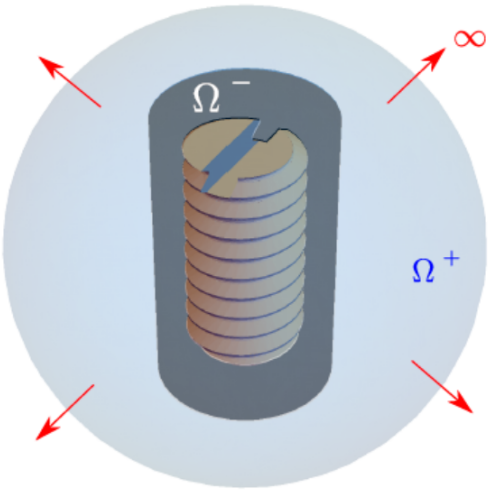


Figure 5.4: The problem domain containing the M2 × 4 mm headless bone implant screw with two distinct discretizations $\Omega^-$ and $\Omega^+$ as well as the ABCs as indicated by the red arrows on the domain boundary. Reproduced from [60].

Table 5.2: Run-times and node numbers for full discretization compared to the multi-grid approach.

| | Full | Multi-grid |
|---|---|---|
| No. of nodes | 2,143,611 | 649,945 |
| Run-time Mg-5Gd [s] | 75,741 | 6,125 |
| Run-time Mg-10Gd [s] | 20,677 | 3,129 |

Fig. 5.6 illustrates the peridynamic bi-material corrosion simulation over eight weeks of immersion for Mg-5Gd. The left columns show the solid metal phase of the implant screw geometry, while the right columns depict the surrounding liquid electrolyte (not to scale). The concentration of Mg ions is depicted in both columns. Corrosion progresses primarily on the outer surfaces of the implant screw, reducing concentration in these peripheral areas. The experimentally observed corrosion rate is higher initially and decreases over time, resulting in an initially higher concentration of Mg-ions in the electrolyte's adjacent areas. This relationship describes the initiation phase without the formation of precipitates and deposition layers and is correctly captured in the peridynamic bi-material corrosion simulation, as shown in Fig. 5.6 (right). The ABCs mimic an unbounded domain, allowing a continuous outflow of Mg ions, leading to a decreasing concentration in the electrolyte over time. The corrosion process for Mg-10Gd is quantitatively similar to that shown in Fig. 5.6, hence only one simulation sequence is shown for clarity.

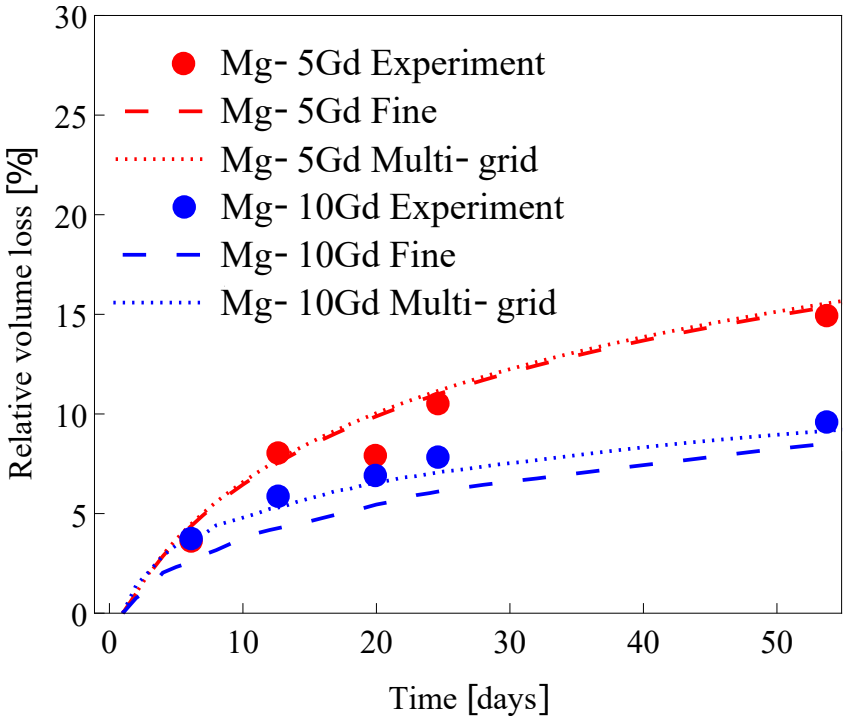


Figure 5.5: Experimental and simulation volume loss for Mg-5Gd and Mg-10Gd, respectively. Reproduced from [60].

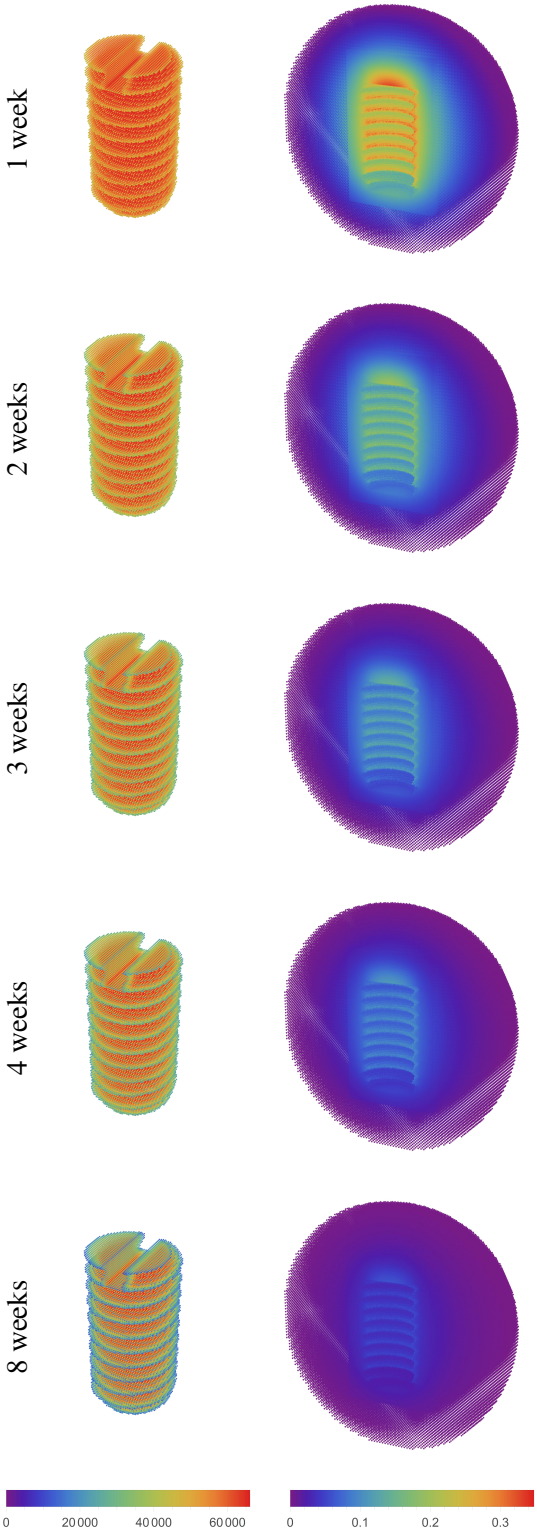


Figure 5.6: Peridynamic corrosion simulation for Mg-5Gd over 8 weeks of immersion. The left column depicts the concentration profile of the solid (undissolved) metal implant screw while the right one shows the concentration of Mg ions in the surrounding liquid phase. The colorbar is expressed in the unit $\mathrm{mol}/\mathrm{m}^3$. Reproduced and adjusted from [60].

### 5.2.4 Multi-Ionic Bio-Corrosion Simulation of Implants in Simulated Body Fluid

In this section, we build upon the results from Section 5.2.3, where close alignments between experimental volume loss data and the peridynamic bi-material bio-corrosion model were obtained. We utilize the complete 3D NNPP system to simulate and model the *in vitro* degradation of a M2 × 4 mm headless bone implant screw under physiological conditions. This approach allows us to obtain detailed information about the electromigration of different ionic components in the liquid solution, incorporate various electrochemical reactions, and consider the formation of deposits and precipitates around the bone implant screw. This study focuses on the Mg-10Gd binary magnesium alloy, though the same analysis can be applied to Mg-5Gd as well.

The bone implant samples are immersed in SBF, which simulates physiological conditions. The chemical composition and ionic concentrations of SBF, as detailed in [150], serve as the initial and boundary conditions for the numerical simulation, listed in Tab. 5.3. The immersion process is assumed to be quasi-static, with regular electrolyte refreshment to prevent ion depletion or salt saturation in the medium [73]. This configuration replicates tissue hydrodynamics without convective flow, controlling salt and deposit layer formation during the bio-corrosion based on the ion composition. Due to the absence of established and consistent ABCs for the full NNPP system, our analysis is limited to applying nonlocal Dirichlet boundary conditions over a layer with thickness $\delta$ across the boundary. However, assuming the electrostatic potential is small at the boundary layer and that quasi-static conditions with negligible chemical reaction rates are present, it might be justifiable to apply a set of peridynamic diffusion equations instead of the coupled NNPP system near the boundary, and impose nonlocal ABCs for diffusion-type problems as discussed in Section 4.1 of Chapter 4 of this dissertation.

In modeling the electrochemical degradation of Mg-10Gd bone implant screws in SBF, we assume gadolinium is ideally homogenized and do not model its effects separately. Adopting the description in [150], our system includes both chemical and electrochemical reactions. The dissolution of Mg ions into the liquid electrolyte and the concurrent formation of hydrogen gas are represented by

$$\mathrm{Mg(s)} \rightarrow \mathrm{Mg^{2+}(aq)} + 2\mathrm{e^-}, \tag{5.16}$$

$$2\mathrm{H^+(aq)} + 2\mathrm{e^-} \rightarrow \mathrm{H_2} \tag{5.17}$$

where (s) indicates a solid state and (aq) represents an aqueous phase. Furthermore, we include several precipitating components within the corrosion system, described by

$$\mathrm{Mg^{2+}(aq)} + 2\mathrm{OH^-(aq)} \rightarrow \mathrm{Mg(OH)_2(s)}, \tag{5.18}$$

$$\mathrm{Mg^{2+}(aq)} + \mathrm{HCO_3^-(aq)} \rightarrow \mathrm{Mg(CO)_3(s)} + \mathrm{H^+(aq)}, \tag{5.19}$$

$$\mathrm{Mg^{2+}(aq)} + \mathrm{HCO_3^-(aq)} + 3\mathrm{H_2O(aq)} \rightarrow \mathrm{Mg(HCO)_3OH \cdot 2H_2O(s)} + \mathrm{H^+(aq)}, \tag{5.20}$$

$$3\mathrm{Mg^{2+}(aq)} + 2\mathrm{HPO_4^{2-}(aq)} + 8\mathrm{H_2O(aq)} \rightarrow \mathrm{Mg_3(PO_4)_2 \cdot 8H_2O(s)} + 2\mathrm{H^+(aq)}, \tag{5.21}$$

$$\mathrm{Ca^{2+}(aq)} + 2\mathrm{OH^-(aq)} \rightarrow \mathrm{Ca(OH)_2(s)} \tag{5.22}$$

$$\mathrm{Ca^{2+}(aq)} + \mathrm{HCO_3^-(aq)} \rightarrow \mathrm{CaCO_3(s)} + \mathrm{H^+(aq)} \tag{5.23}$$

$$5\mathrm{Ca^{2+}(aq)} + 3\mathrm{HPO_4^{2-}(aq)} + \mathrm{H_2O(aq)} \rightarrow \mathrm{Ca_5OH(PO_4)_3(s)} + 4\mathrm{H^+(aq)}. \tag{5.24}$$

The latter system describes the precipitation of brucite (*cf.* (5.18)), magnesite (*cf.* (5.19)), nesquehonite (*cf.* (5.20)), bobierrite (*cf.* (5.21)), portlandite (*cf.* (5.22)), calcite (*cf.* (5.23)), and hydroxyapatite (*cf.* (5.24)). The corresponding dissolution equilibrium constants, expressed as logarithmic

pK values at 37 °C, are adopted and refined from [71, 150], and are listed in Tab. 5.4. Moreover, we take into account the dissociation of water, hydrogen carbonate, and hydrogen phosphate within the liquid electrolyte solution as

$$\mathrm{H_2O(aq)} \rightleftharpoons \mathrm{H^+(aq) + OH^-(aq)} \tag{5.25}$$

$$\mathrm{HCO_3^-(aq)} \rightleftharpoons \mathrm{CO_3^{2-}(aq) + H^+(aq)} \tag{5.26}$$

$$\mathrm{HPO_4^{2-}(aq)} \rightleftharpoons \mathrm{PO_4^{3-}(aq) + H^+(aq)}. \tag{5.27}$$

Local chemical conditions, such as pH level and temperature $T$, influence which compounds precipitate either on the implant's surface — forming a degradation layer — or within the bulk electrolyte. This layer acts as a partially protective film, significantly impacting the corrosion rate and extent. A numerical analysis from [150] determined which reactions from (5.18) to (5.24) need to be computed by assessing the fractions of precipitates forming in SBF at $T = 37\,°\mathrm{C}$, based on pH values, and confirming these findings with experimental results. Portlandite was found not to form in corrosion experiments of biodegradable materials and is therefore excluded from this study. The NNPP system consists of 11 unknown field variables, including the electrostatic potential $\phi$, derived from the nonlocal Poisson equation (2.64), and 10 concentration distributions

$$\begin{aligned} &C_1 = [\mathrm{Mg}^{z_1}], \quad C_2 = [\mathrm{H}^{z_2}], \quad C_3 = [\mathrm{OH}^{z_3}], \\ &C_4 = [\mathrm{HCO_3}^{z_4}], \quad C_5 = [\mathrm{CO_3}^{z_5}], \quad C_6 = [\mathrm{HPO_4}^{z_6}], \\ &C_7 = [\mathrm{PO_4}^{z_7}], \quad C_8 = [\mathrm{Ca}^{z_8}], \quad C_9 = [\mathrm{Na}^{z_9}], \quad C_{10} = [\mathrm{Cl}^{z_{10}}] \end{aligned} \tag{5.28}$$

where $C_1, C_2, \dots, C_{10}$ represent the molar concentrations of the ionic species, and $z_1, z_2, \dots, z_{10}$ are their respective charge numbers. The initial and boundary values used in the numerical simulation are summarized in Tab. 5.3. The chemical reaction terms are directly derived from (5.16) to (5.27) and are imposed on specific parts of the computational domain. Thus, the dissolution of Mg ions, as described by (5.16), and the associated hydrogen formation from (5.17), are calculated at point $\mathbf{x}_i$ within the DCL at time $t^{n+1}$. This is accounted for through an explicit time reaction term affecting the hydrogen ion concentration $C_2$, given by

$$R^{n+1}_{\mathrm{H_2},i} = \frac{J_{\mathrm{H_2}}}{z_2 F c_{\mathrm{solid}}} \exp\left(-\frac{\alpha_{\mathrm{H_2}} F}{RT}\eta_i^n\right), \qquad \exists \mathbf{x} \in \mathcal{F}_i \,:\, \varphi(\mathbf{x}_i, t^n) \neq \varphi(\mathbf{x}, t^n), \tag{5.29}$$

where $J_{\mathrm{H_2}}$ is the proportionality factor at zero overpotential, and $\alpha_{\mathrm{H_2}}$ is the charge transfer coefficient. Generally, a total of $r$ reactions within the system can be characterized by

$$\sum_{k=1}^{N} p_{k,i} C_k(\mathbf{x}, t) \rightleftharpoons \sum_{k=1}^{N} q_{k,i} C_k(\mathbf{x}, t), \qquad i = 1, 2, \dots, r, \tag{5.30}$$

where $N$ is the total number of species, and $p_{k,i}$ and $q_{k,i}$ are the stoichiometric coefficients for the $i$th chemical reaction. A general reaction term at a material point $\mathbf{x}$ and time $t$ can thus be expressed as

$$R_k(\mathbf{x}, t) = \sum_{i=1}^{r} k_{b,i} \left( K_{\mathrm{eq},i} - (q_{k,i} - p_{k,i}) \prod_{n=1}^{N} c_n^{q_{n,i}}(\mathbf{x}, t) \right), \qquad k = 1, 2, \dots, N, \tag{5.31}$$

where $k_{b,i}$ is the backward reaction rate for the $i$th chemical reaction, and $K_{\mathrm{eq},i}$ is the corresponding equilibrium constant. The reactions from (5.18) to (5.27) are applied to the entire liquid electrolyte

phase as well as within the solid and liquid subdomains of the DCL, as schematically shown in Fig. 2.6. In contrast, the dissociation reactions of water, hydrogen carbonate, and hydrogen phosphate are considered only in the liquid phase.

Table 5.3: Initial and Boundary Condition for 3D Bone Implant Screw Degradation. Data available in [58].

| Species | Initial Value in Solid | Initial Value in Liquid | Boundary Condition |
|---|---|---|---|
| $C_1$ | 1 | 0 | 0 |
| $C_2$ | 0 | $10^{-4}/66082.4$ | $10^{-4}/66082.4$ |
| $C_3$ | 0 | $10^{-4}/66082.4$ | $10^{-4}/66082.4$ |
| $C_4$ | 0 | $34.88/66082.4$ | $34.88/66082.4$ |
| $C_5$ | 0 | 0 | 0 |
| $C_6$ | 0 | $1.39/66082.4$ | $1.39/66082.4$ |
| $C_7$ | 0 | 0 | 0 |
| $C_8$ | 0 | $2.31/66082.4$ | $2.31/66082.4$ |
| $C_9$ | 0 | $142/66082.4$ | $142/66082.4$ |
| $C_{10}$ | 0 | $109.9/66082.4$ | $109.9/66082.4$ |
| $\phi$ | 0 | 0 | 0 |

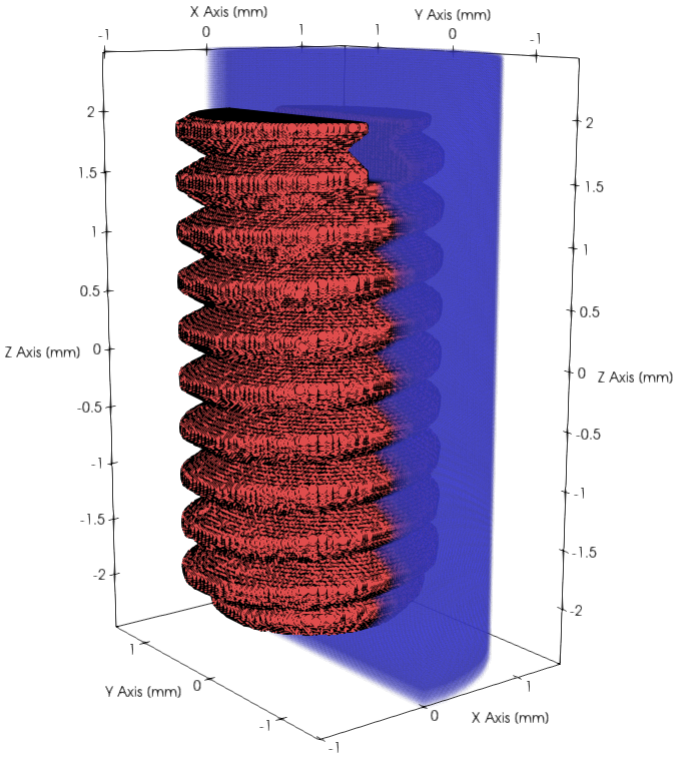


Figure 5.7: The initial solid metallic phase on a regular grid for the M2 × 4 mm headless bone implant screw, shown alongside a cross-sectional cut of the surrounding cylindrical liquid electrolyte phase of SBF. Reproduced from [58].

The constitutive peridynamic corrosion model, based on the semi-empirical corrosion rate equation detailed in Section 5.2.1, governs the dissolution of Mg ions into the solution and is applied to the full NNPP corrosion model in this example. Here, the diffusion coefficient $D_1(t)$ for the Mg ion concentration $C_1$ is defined as

$$D_1(t) = \begin{cases} D_{1,\text{liq}}, & \varphi(\mathbf{x}_j, t) = 0 \wedge \varphi(\mathbf{x}_i, t) = 0, \quad \text{(liquid-liquid bonds)} \\ D_{1,\text{int}} 10^{\left(-V_L(t)/l\right)}, & \varphi(\mathbf{x}_j, t) = 1 \oplus \varphi(\mathbf{x}_i, t) = 1, \quad \text{(interface bonds)} \\ D_{1,\text{sol}}, & \varphi(\mathbf{x}_j, t) = 1 \wedge \varphi(\mathbf{x}_i, t) = 1, \quad \text{(solid-solid bonds)} \end{cases}, \tag{5.32}$$

where $D_{1,\text{liq}}$ and $D_{1,\text{int}}$ are the constant diffusion coefficients for liquid-liquid and interface bonds, respectively. A small diffusion coefficient $D_{1,\text{sol}}$ is included for solid-solid bonds to account for the effects related to subsurface corrosion within the solid Mg material near the corrosion surface. Since we compute the formation of deposits through chemical reaction terms in (5.18) to (5.24), we do not use the implicit mechanism from Algorithm 1 for the temporary blockage of interface bonds due to deposit layer formations. For the remaining ionic species the constitutive model is defined as

$$D_k = \begin{cases} D_{k,\text{liq}}, & \varphi(\mathbf{x}_j, t) = 0 \wedge \varphi(\mathbf{x}_i, t) = 0, \quad \text{(liquid-liquid bonds)} \\ \varepsilon D_{k,\text{liq}}, & \varphi(\mathbf{x}_j, t) = 1 \oplus \varphi(\mathbf{x}_i, t) = 1, \quad \text{(interface bonds)} \\ 0, & \varphi(\mathbf{x}_j, t) = 1 \wedge \varphi(\mathbf{x}_i, t) = 1, \quad \text{(solid-solid bonds)} \end{cases}, \quad k = 2, 3, ..., N, \tag{5.33}$$

where $N = 10$ represents the total number of species in the system. The diffusion coefficient for interface bonds is denoted as $D_{k,\text{int}} := \varepsilon D_{k,\text{liq}}$, with $\varepsilon$ as the ratio of tortuosity to porosity across the DCL. Moreover, the electrical conductivity assumed in the nonlocal Poisson equation in (2.64) is considered constant for this analysis and the equation is solved exclusively in the liquid phase. The parameters used in the numerical study are detailed in Tab. 5.4.

The numerical simulation was conducted over a simulated immersion period of 56 days within a cylindrical computational domain with a radius of 3 mm and a height of 5 mm. A regular grid size of 20 µm was employed, resulting in a total of 4, 393, 605 computational nodes. The simulation used a time step size of $\Delta t = 3$ h and a peridynamic horizon of 60 µm. To manage the computational load of solving the full NNPP system of electromigration, which is more demanding than the reduced peridynamic bi-material corrosion model from Section 5.2.3, the liquid domain size was chosen to be slightly smaller. The initial configuration, depicting the solid metal phase ($\varphi = 1$) of the M2 × 4 mm headless bone implant screw, is shown in Fig. 5.7, with the surrounding liquid electrolyte phase of SBF ($\varphi = 0$). Detailed initial and boundary conditions for this simulation are provided in Tab. 5.3. Note that the concentration values are scaled by $C_{\text{solid}} = 66\,082.4\,\text{mol/m}^3$, the concentration of the intact solid Mg-10Gd material, which scales the maximum Mg ion concentration to a unitary value.

Fig. 5.8 shows the progression of corrosion through macroscopic volume loss over time for the bone implant screw. The results indicate good agreement between the simulated and experimental mean values for Mg-10Gd implant screws over an 8-week immersion period. Experimental data for species distribution in the context of *in vitro* bio-corrosion of Mg-based implants are often unavailable, so the presented results provide a qualitative analysis. Fig. 5.10 displays the normalized concentration distributions of Mg, hydrogen, hydrogen carbonate, and hydrogen phosphate ions within the computational domain after 8 weeks of simulated immersion. Concentration values are normalized against the intact material concentration of Mg-10Gd. Corrosion progresses

most rapidly along the screw threads, as shown by reduced Mg concentration values in Fig. 5.10a. This aligns with a homogeneous corrosion profile and uniform diffusion coefficients, preventing increased localization and irregular pitting corrosion. This is consistent with the literature [73] and the results obtained in Section 5.2.3 using the peridynamic bi-material corrosion model. The concentrations of other components stabilize quickly and are omitted for brevity. Fig. 5.10d shows hydrogen phosphate ion accumulation within the screw slot, indicating higher concentration in this confined region. This pattern is also partially observed for hydrogen carbonate in Fig. 5.10c.

To further assess the numerical findings, Fig. 5.9 illustrates the averaged pH value across the radius of the cylindrical screw from the phase transition corrosion interface. The observed increase in pH across the screw radius (Fig. 5.9) and the decrease in hydrogen ions (Fig. 5.10b) qualitatively agree with experimental results from [150]. However, the experimental pH values reported in [150] are slightly higher than those in our numerical study. This discrepancy may be partially due to their 28-day immersion experiments in SBF using pure Mg, compared to the Mg-10Gd alloy and 56-day (8 weeks) simulated immersion used in our study. Furthermore, the model parameters, as reported in Tab. 5.4, are primarily derived from literature suggestions and approximations and may require adjustments for the specific corrosion system at hand. Additionally, the choice of boundary conditions and the size of the computational domain significantly affect the numerical outcomes. A larger domain with more surrounding liquid electrolyte could potentially minimize discrepancies with experimental observations; however, this would significantly increase the overall computational effort.

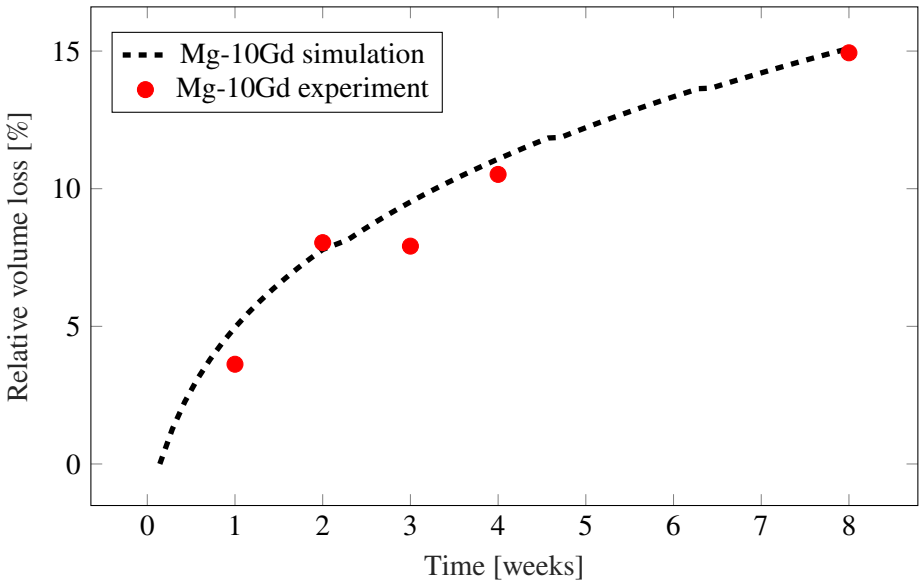


Figure 5.8: Volume loss over time as a weight percentage of the Mg-10Gd bone implant screw, with experimental data from [73, 60]. Reproduced from [58].

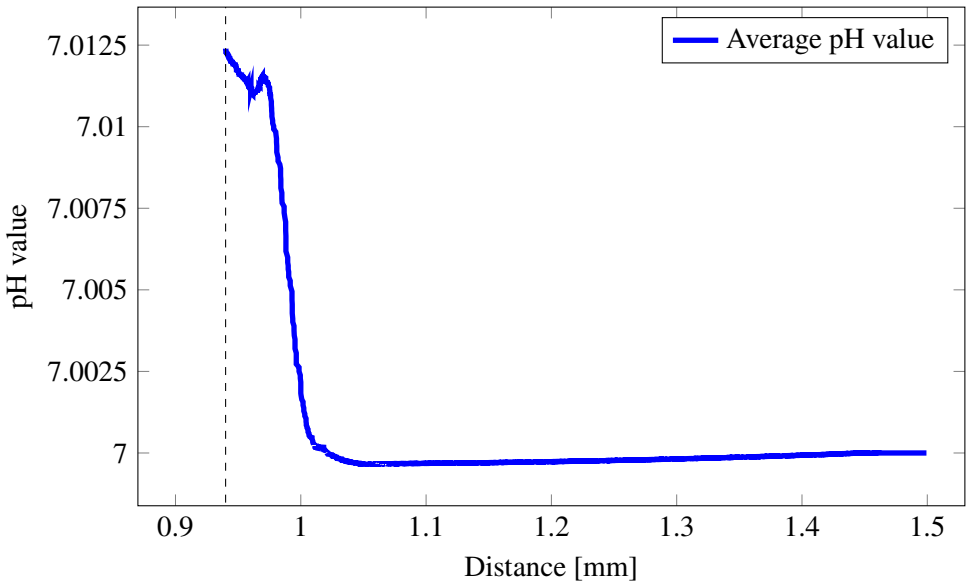


Figure 5.9: Average pH value across the bone implant screw radius at height $z = 0$ in the liquid phase, with the solid-liquid boundary marked by a dashed vertical line. Reproduced from [58].

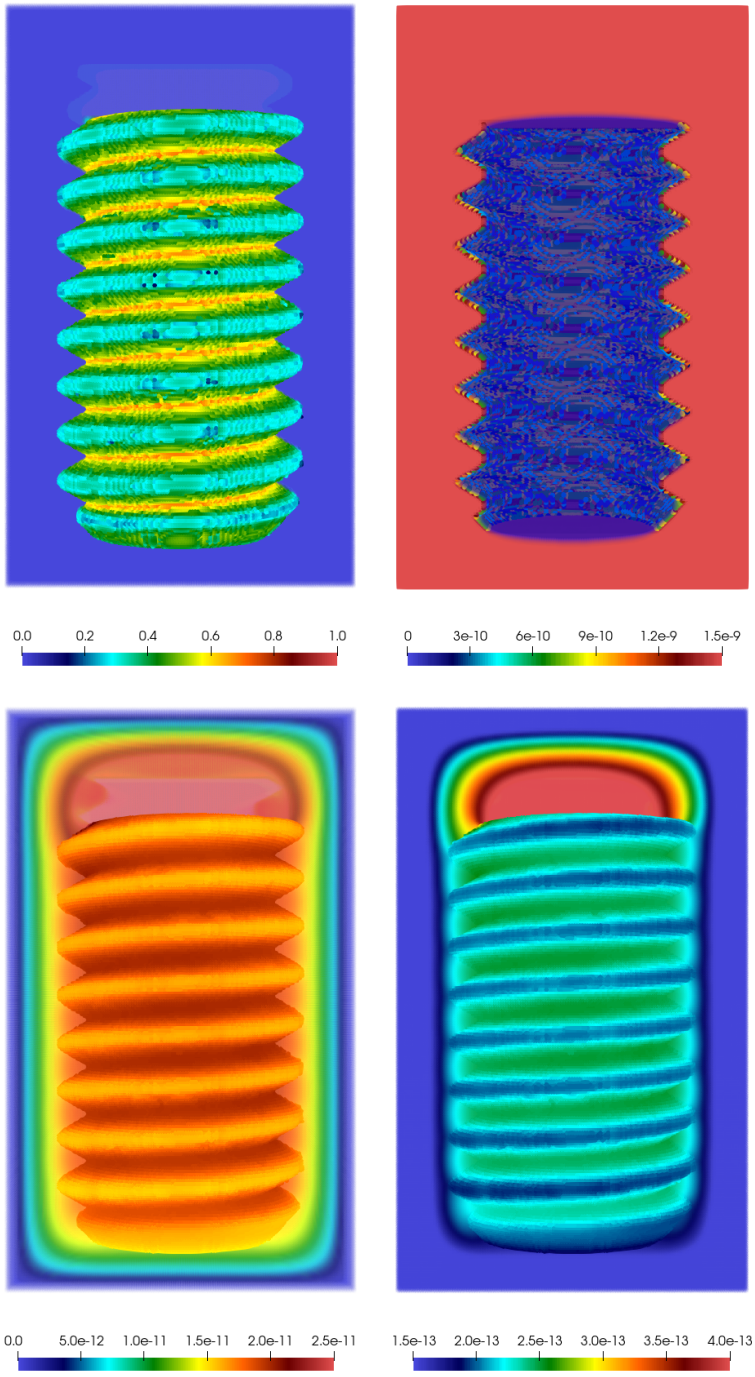


Figure 5.10: Normalized concentration distributions of various ionic species after 8 weeks of simulated immersion in SBF: (top, left) magnesium ($C_1$), (top, right) hydrogen ions ($C_2$), (bottom, left) hydrogen carbonate ($C_4$), (bottom, right) hydrogen phosphate ($C_6$). Reproduced from [58].

Table 5.4: Simulation and Model Parameters for 3D Bone Implant Screw Degradation. Data available in [58].

| Symbol | Value | Unit | Description |
|---|---|---|---|
| $T$ | 298.15 | K | Temperature |
| $G$ | 8.3145 | $\mathrm{J\,mol^{-1}\,K^{-1}}$ | Gas constant |
| $F$ | 96485 | $\mathrm{C\,mol^{-1}}$ | Faraday's constant |
| $\delta$ | 60 | µm | Peridynamic horizon |
| $z_1$ | 2 | - | Charge number for $C_1$ |
| $z_2$ | 1 | - | Charge number for $C_2$ |
| $z_3$ | $-1$ | - | Charge number for $C_3$ |
| $z_4$ | $-1$ | - | Charge number for $C_4$ |
| $z_5$ | $-2$ | - | Charge number for $C_5$ |
| $z_6$ | $-2$ | - | Charge number for $C_6$ |
| $z_7$ | $-3$ | - | Charge number for $C_7$ |
| $z_8$ | 2 | - | Charge number for $C_8$ |
| $z_9$ | 1 | - | Charge number for $C_9$ |
| $z_{10}$ | $-1$ | - | Charge number on species $c_{10}$ |
| $\varepsilon$ | $10^{-3}$ | - | Tortuosity to porosity ratio |
| $l$ | 11.0524 | $\mathrm{m}^3$ | Constitutive parameter (*cf.* (5.32)) |
| $C_{\mathrm{solid}}$ | 66082.4 | $\mathrm{mol/m^3}$ | Concentration of Mg-10Gd |
| $C_{\mathrm{sat}}$ | 2312.88 | $\mathrm{mol/m^3}$ | Saturation value of Mg-10Gd in SBF |
| $D_{1,\mathrm{liq}}$ | $7.1 \times 10^{-10}$ | $\mathrm{m^2/s}$ | Diffusivity of $C_1$ for liquid-liquid bonds |
| $D_{1,\mathrm{int}}$ | $1 \times 10^{-15}$ | $\mathrm{m^2/s}$ | Diffusivity of $C_1$ for interface bonds |
| $D_{1,\mathrm{sol}}$ | $2.125 \times 10^{-17}$ | $\mathrm{m^2/s}$ | Diffusivity of $C_1$ for solid-solid bonds |
| $D_{2,\mathrm{liq}}$ | $9.31 \times 10^{-9}$ | $\mathrm{m^2/s}$ | Diffusivity of $C_2$ for liquid-liquid bonds |
| $D_{2,\mathrm{int}}$ | $9.31 \times 10^{-13}$ | $\mathrm{m^2/s}$ | Diffusivity of $C_2$ for interface bonds |
| $D_{3,\mathrm{liq}}$ | $5.27 \times 10^{-9}$ | $\mathrm{m^2/s}$ | Diffusivity of $C_3$ for liquid-liquid bonds |
| $D_{3,\mathrm{int}}$ | $5.27 \times 10^{-12}$ | $\mathrm{m^2/s}$ | Diffusivity of $C_3$ for interface bonds |
| $D_{4,\mathrm{liq}}$ | $1.19 \times 10^{-9}$ | $\mathrm{m^2/s}$ | Diffusivity of $C_4$ for liquid-liquid bonds |
| $D_{4,\mathrm{int}}$ | $1.19 \times 10^{-12}$ | $\mathrm{m^2/s}$ | Diffusivity of $C_4$ for interface bonds |
| $D_{5,\mathrm{liq}}$ | $9.23 \times 10^{-10}$ | $\mathrm{m^2/s}$ | Diffusivity of $C_5$ for liquid-liquid bonds |
| $D_{5,\mathrm{int}}$ | $9.23 \times 10^{-13}$ | $\mathrm{m^2/s}$ | Diffusivity of $C_5$ for interface bonds |
| $D_{6,\mathrm{liq}}$ | $6.9 \times 10^{-10}$ | $\mathrm{m^2/s}$ | Diffusivity of $C_6$ for liquid-liquid bonds |
| $D_{6,\mathrm{int}}$ | $6.9 \times 10^{-13}$ | $\mathrm{m^2/s}$ | Diffusivity of $C_6$ for interface bonds |
| $D_{7,\mathrm{liq}}$ | $6.12 \times 10^{-10}$ | $\mathrm{m^2/s}$ | Diffusivity of $C_7$ for liquid-liquid bonds |
| $D_{7,\mathrm{int}}$ | $6.12 \times 10^{-13}$ | $\mathrm{m^2/s}$ | Diffusivity of $C_7$ for interface bonds |
| $D_{8,\mathrm{liq}}$ | $7.93 \times 10^{-10}$ | $\mathrm{m^2/s}$ | Diffusivity of $C_8$ for liquid-liquid bonds |
| $D_{8,\mathrm{int}}$ | $7.93 \times 10^{-13}$ | $\mathrm{m^2/s}$ | Diffusivity of $C_8$ for interface bonds |
| $D_{9,\mathrm{liq}}$ | $1.33 \times 10^{-9}$ | $\mathrm{m^2/s}$ | Diffusivity of $C_9$ for liquid-liquid bonds |
| $D_{9,\mathrm{int}}$ | $1.33 \times 10^{-12}$ | $\mathrm{m^2/s}$ | Diffusivity of $C_9$ for interface bonds |
| $D_{10,\mathrm{liq}}$ | $2.03 \times 10^{-9}$ | $\mathrm{m^2/s}$ | Diffusivity of $C_{10}$ for liquid-liquid bonds |
| $D_{10,\mathrm{int}}$ | $2.03 \times 10^{-12}$ | $\mathrm{m^2/s}$ | Diffusivity of $C_{10}$ for interface bonds |

Continued on next page

**Table 5.4 continued from previous page**

| Symbol | Value | Unit | Description |
|---|---|---|---|
| $\epsilon$ | $6.1 \times 10^6$ | $\mathrm{S\,m^{-1}}$ | Electrical conductivity in SBF |
| $\mathrm{pK}_{\mathrm{brucite}}$ | 15.97 | - | Equilibrium constant in (5.18) |
| $\mathrm{pK}_{\mathrm{magnesite}}$ | 4.73 | - | Equilibrium constant in (5.19) |
| $\mathrm{pK}_{\mathrm{nesquehonite}}$ | $-4.49$ | - | Equilibrium constant in (5.20) |
| $\mathrm{pK}_{\mathrm{bobierrite}}$ | $-2.98$ | - | Equilibrium constant in (5.21) |
| $\mathrm{pK}_{\mathrm{calcite}}$ | $-1.8$ | - | Equilibrium constant in (5.23) |
| $\mathrm{pK}_{\mathrm{hydroxyapatite}}$ | $-35.42$ | - | Equilibrium constant in (5.24) |
| $\mathrm{pK}_{\mathrm{water}}$ | 13.61 | - | Equilibrium constant in (5.25) |
| $\mathrm{pK}_{\mathrm{carbonate}}$ | 10.24 | - | Equilibrium constant in (5.26) |
| $\mathrm{pK}_{\mathrm{phosphate}}$ | 10.24 | - | Equilibrium constant in (5.27) |
| $J_{\mathrm{H_2}}$ | $-2 \times 10^{-3}$ | $\mathrm{A\,m\,mol^{-1}}$ | Pre-exponential coefficient in (5.29) |
| $k_{b,1}$ | $9.0245 \times 10^{-21}$ | $\mathrm{m^7/mol^2 s}$ | Backward reaction rate in (5.18) |
| $k_{b,2}$ | $7.0332 \times 10^{-9}$ | $\mathrm{m^7/mol^2 s}$ | Backward reaction rate in (5.19) |
| $k_{b,3}$ | $7.0023 \times 10^{-10}$ | $\mathrm{m^7/mol^2 s}$ | Backward reaction rate in (5.20) |
| $k_{b,4}$ | $1.0798 \times 10^{-2}$ | $\mathrm{m^7/mol^2 s}$ | Backward reaction rate in (5.21) |
| $k_{b,5}$ | $8.0037 \times 10^{-24}$ | $\mathrm{m^7/mol^2 s}$ | Backward reaction rate in (5.23) |
| $k_{b,6}$ | $9.001 \times 10^{-16}$ | $\mathrm{m^7/mol^2 s}$ | Backward reaction rate in (5.24) |
| $k_{b,7}$ | $1.4 \times 10^2$ | $\mathrm{m^3/mol/s}$ | Backward reaction rate in (5.25) |
| $k_{b,8}$ | $1.4 \times 10^2$ | $\mathrm{m^3/mol/s}$ | Backward reaction rate in (5.26) |
| $k_{b,9}$ | $1.4 \times 10^2$ | $\mathrm{m^3/mol/s}$ | Backward reaction rate in (5.27) |

## 5.3 Surrogate Modeling for *in vitro* and *in vivo* Bio-Corrosion

In the following section, we aim to demonstrate the applicability of peridynamic corrosion models to address the discrepancy between *in vitro* and *in vivo* bio-degradation results for Mg-based bone implants. We showcase the effectiveness of these models in predicting degradation behavior under physiological conditions and highlight how efficient surrogate modeling can be used to enhance their utility. By employing Kriging surrogate modeling, we optimized key parameters that describe the diffusion of Mg ions within the liquid electrolyte and the porous degradation layer of formed deposits on the corrosion surface. These surrogate models were calibrated using both *in vitro* and *in vivo* experimental data, allowing for a detailed comparison of degradation rates and macroscopic volume loss in both environments. Since this section primarily focuses on numerical efficiency and aims to demonstrate how peridynamic corrosion models can be valuable tools for efficient simulation, we use the peridynamic bi-material bio-corrosion model from Section 5.2.3 as the underlying model for the Kriging surrogate model. This choice is made over the full NNPP corrosion system due to its efficiency, although the NNPP system could also be employed if detailed distribution of various ionic components and precise chemical reaction descriptions of precipitation product formation near the corrosion surface are required, albeit at a substantially higher computational cost. Utilizing this approach, we aim to effectively bridge the gap between *in vitro* and *in vivo* results while significantly reducing computational effort compared to direct numerical simulations. This methodology offers a practical tool for large-scale studies and long-term corrosion simulations, facilitating implant material design and the evaluation of biodegradable Mg-based implants, as well as their clinical application.

Analogous to the numerical parameter calibration of the peridynamic bi-material corrosion model in Section 5.2.2, we use *in vitro* and *in vivo* experimentally obtained relative volume loss data for the Mg-5Gd and Mg-10Gd binary alloys on M2 $\times$ 4 mm headless bone implant screws. The *in vitro* setup, detailed in Section 5.1, involved immersing the screws in a specific medium that mimics physiological conditions over 8 weeks. For the *in vivo* tests, the screws were implanted into rat tibia with healing durations of 4, 8, and 12 weeks. Similar to the *in vitro* case, synchrotron radiation-based $\mu$CT imaging was used to study the morphology of the degraded screws. Experimental details can be found in [73, 155, 156, 157].

For a more comprehensive discussion of the numerical results, considering that the peridynamic corrosion model parameter calibration was based on experimental volume loss data, the analysis in corrosion science typically also includes the discussion of the Degradation Rate (DR). Analyzing the DR offers insights into the dynamics of corrosion, such as the rate of material degradation over time and the identification of critical periods of rapid degradation, which is more effective than simply examining volume loss alone. Given the definition of the relative volume loss in (5.1), the DR, expressed typically in mm year$^{-1}$, for $t > 0$ can be computed by means of the time-dependent volume loss as

$$DR(t) = \frac{V_0 - V(t)}{A_0 t}, \tag{5.34}$$

where $V_0$ is the initial intact material volume of the sample, $A_0$ is the initial intact material surface area, and $V(t)$ is the current sample volume at time $t$.

Kriging, or Gaussian process modeling, has been applied in this section to create a surrogate model for studying the bio-corrosion behavior of Mg-based implants, following the methodology in [150]. This approach treats the peridynamic bi-material bio-corrosion model as a black box model, using a data-driven method to develop the Kriging-based surrogate model. Training data are

sampled from the input distribution in the parameter space and evaluated using the computationally intensive black-box model. The resulting observations help construct the surrogate model across the input distribution domain. Latin Hypercube Sampling (LHS) is used to generate 30 sample sets for the input parameters ($D_{\text{int}}$ and $D_{\text{liq}}$), as shown in Fig. 5.11, ensuring the entire feasible domain of the peridynamic corrosion model is covered. This is crucial as the of input data distribution significantly impacts the surrogate model's prediction quality [46].

The training data, $\mathcal{X}, \mathcal{Y}$, involves evaluating the peridynamic model output $\mathcal{Y}$ for $N$ sample points of the input parameter vector $\mathcal{X}$. Here, $\mathcal{Y}$ represents the Quantity of Interest (QoI), specifically the volume loss of Mg-5Gd and Mg-10Gd headless bone implant screws. The general mathematical representation of the Kriging surrogate model is given by

$$\mathcal{M}(x) = \beta^T f(x) + \sigma^2 Z(x, \omega), \tag{5.35}$$

where $\mathcal{M}$ is the Kriging mapping function, which is a realization of the Gaussian process used to calculate the volume loss $\mathcal{Y}$ for any input parameter vector $\mathcal{X}$ over a finite period. The term $\beta^T f(x)$ represents the trend of the Kriging model, which is the mean value of the Gaussian process, and $\sigma^2 Z(x, \omega)$ is the realization of the stochastic process assumed to have zero mean and unit variance $Z(x, \omega)$. Here, $\sigma$ is the variance of the process, and $\omega$ represents the underlying probability space defined by the correlation function of the stochastic process [163]. The performance of the Kriging-based surrogate model, based on the training simulation data generated from the peridynamic model, is estimated by the leave-one-out error, $\varepsilon_{LOO}$, defined as

$$\varepsilon_{LOO} = \frac{1}{N_e}\left[\frac{\sum_{i=1}^{N_e}(\mathcal{M}(x_i) - \mathcal{M}_{(-i)}(x_i))^2}{\text{Var}\,(\mathcal{M}(\mathcal{X}))}\right], \tag{5.36}$$

where $N_e$ is the number of data points considered during Kriging, $\mathcal{M}_{(-i)}(x_i)$ denotes the Kriging surrogate model obtained using all points of the numerical Experimental Design (ED) except $x_i$, and $\mathcal{M}(\mathcal{X})$ is the corresponding surrogate model response of the initial numerical ED generated using the original model [163]. The Kriging-based surrogate model is calibrated using experimental data from both in vitro and in vivo degradation tests of binary Mg-Gd biodegradable implant alloy materials. The calibration process involves dividing the model domain into equal intervals and re-sampling each interval using LHS. Intervals with higher uncertainty are further subdivided and sampled. The goodness of calibration is measured by the Mean Absolute Error (MAE), calculated as

$$\text{MAE} = \frac{\sum_{j=1}^{N}|y_t - \hat{y}_j|}{N}, \tag{5.37}$$

where $N$ is the number of measurement points, $y_t$ is the mean experimental value at time $t$ for the volume loss at the $j$th point, and $\hat{y}_j$ is the Kriging surrogate model response at the $j$th point. The Kriging-based surrogate model is implemented using the Kriging module within the UQLAB framework [89], which is installed and integrated under the BSD 3-clause license in MATLAB 2021b.

The Kriging surrogate models are trained to predict volume loss of the bone implant screws over time based on computational ED data collected from 30 LHS-generated random samples of the target parameters. The input parameter ranges were set as $D_{\text{int}} \in [1\times10^{-17}, 1\times10^{-12}]\text{m}^2/\text{s}$ and $D_{\text{liq}} \in [1\times10^{-12}, 1\times10^{-7}]\text{m}^2/\text{s}$, similar to the ranges used during peridynamic bi-material corrosion model parameter optimization discussed in Section 5.2.2. These surrogate models accurately

capture the QoI for both Mg-5Gd and Mg-10Gd implant alloys for *in vitro* bio-corrosion and material degradation, as shown by their performance compared to the peridynamic model in Fig. 5.12. The *in vivo* peridynamic corrosion model response was assessed based on numerical findings, with test ranges confirmed by experimental data from [76]. The surrogate model errors, represented by $\varepsilon_{LOO}$, ranged from $2.1\times10^{-3}$ to $5.5\times10^{-3}$ for Mg-5Gd and $1.7\times10^{-3}$ to $3.1\times10^{-3}$ for Mg-10Gd. Additionally, the Kriging surrogate model significantly reduces the computational time required to simulate the entire domain over the simulated immersion duration, taking only 23.6 s compared to approximately 3 h for the corresponding 3D peridynamic bi-material bio-corrosion model.

Moreover, the key parameters of the peridynamic corrosion models, $D_{\text{int}}$ and $D_{\text{liq}}$, were calibrated and optimized using predictions from the Kriging surrogate model. The model outputs were validated against volume loss data obtained from $\mu$CT measurements for both *in vitro* bio-corrosion and material degradation [76] as well as *in vivo* experiments [74]. The optimized values for the Fickian diffusion coefficients $D_{\text{int}}$ and $D_{\text{liq}}$ for Mg-5Gd and Mg-10Gd in both *in vitro* and *in vivo* cases are provided in Table 5.5. Peridynamic corrosion model responses were obtained over 8 weeks (56 days) of simulated immersion, with the Kriging models initially trained and calibrated on this period. To capture time points from *in vivo* experiments, surrogate model responses were extrapolated to 100 days. The diffusivity of Mg ions was found to be an order of magnitude higher *in vivo* compared to *in vitro*, consistent with the reported bio-corrosion and material degradation behavior of bone implant screws [74, 76].

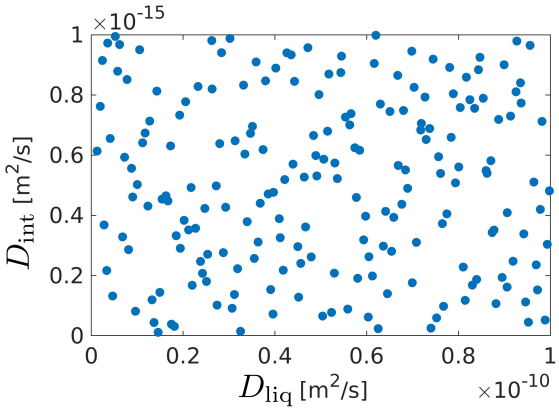


Figure 5.11: The LHS-generated sampling domain for $D_{\text{int}}$ and $D_{\text{liq}}$. Reproduced from [2].

Table 5.5: Optimized *in vitro* and *in vivo* diffusivity parameters measured via Kriging-based surrogate models and MAE compared to experimental data. Reproduced from [2].

| | ***in vitro*** | | ***in vivo*** | | |
|---|---|---|---|---|---|
| | **Mg-5Gd** | **Mg-10Gd** | **Mg-5Gd** | **Mg-10Gd** | **Units** |
| $D_{\text{int}}$ | $2.9 \times 10^{-15}$ | $1.78 \times 10^{-15}$ | $7.8 \times 10^{-14}$ | $9.6 \times 10^{-14}$ | $\text{m}^2\,\text{s}^{-1}$ |
| $D_{\text{liq}}$ | $8.7 \times 10^{-9}$ | $1.44 \times 10^{-9}$ | $5.4 \times 10^{-8}$ | $8.4 \times 10^{-8}$ | $\text{m}^2\,\text{s}^{-1}$ |
| MAE | 0.03 | 0.08 | 0.31 | 0.44 | - |

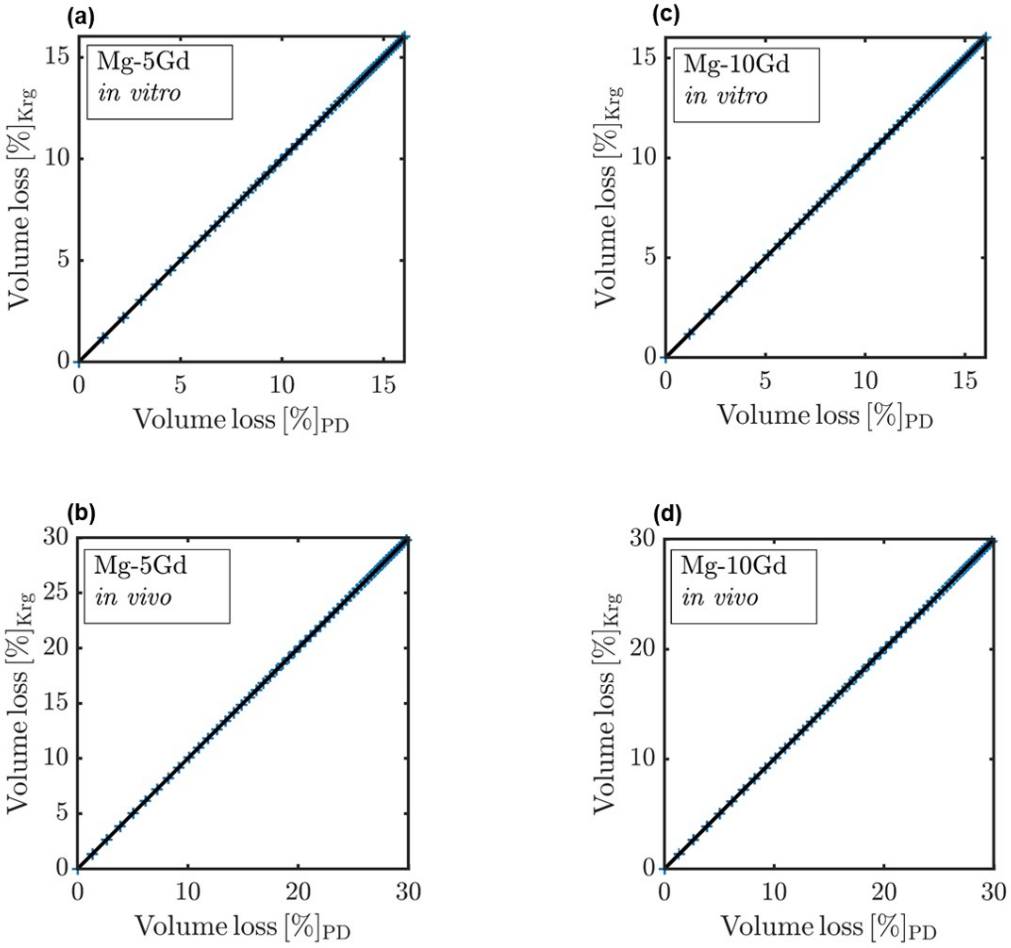


Figure 5.12: Comparison between the QoI, i.e., the macroscopic volume loss of the headless bone implant screws, computed by the 3D peridynamic bi-material bio-corrosion model and Kriging surrogate model predictions for (**a**) Mg-5Gd *in vitro*, (**b**) Mg-5Gd *in vivo*, (**c**) Mg-10Gd *in vitro*, and (**d**) Mg-10Gd *in vivo*. Reproduced from [2].

The comparison of surrogate model responses, calibrated to experimental data over 100 days of bio-corrosion and material degradation for Mg-5Gd and Mg-10Gd implants, in both *in vitro* and *in vivo* conditions, is shown in Fig. 5.13(a). For the *in vitro* case, the simulated volume loss aligns well with $\mu$CT measurements, as shown by the scatter plots in Fig. 5.13(a),(b) [76], with MAE values of 0.03 for Mg-5Gd and 0.08 for Mg-10Gd. Similarly, the *in vivo* simulated volume loss corresponds closely with $\mu$CT data [74], indicated by the scatter plots in Fig. 5.13(a),(b), with MAE values of 0.31 for Mg-5Gd and 0.44 for Mg-10Gd. However, the accuracy of the surrogate model parameter calibration is subject to uncertainties in the experimental data, particularly the high standard deviation visible in Fig. 5.13(a). Calibration was further constrained by the limited number of data points, with *in vitro* data spanning five time points between 1 and 8 weeks, and *in vivo* data covering three time points: 4, 8, and 12 weeks. The parameter calibration process could be enhanced by incorporating additional data points of macroscopic volume loss over time, which would help mitigate numerical overfitting and underfitting, as well as increasing sample sizes at each time point to reduce deviations.

Utilizing *in vitro* models for Mg-5Gd and Mg-10Gd bone implant screws, the Kriging surrogate models accurately predict *in vivo* bio-corrosion and material degradation behavior. These models can simulate the bio-corrosion of Mg-based implants for over 100 days in both *in vitro* and *in vivo* conditions, though further experimental validation is required. Figure 5.13(b) illustrates that the DR calculated for Mg-5Gd and Mg-10Gd in both environments closely match experimental data. While traditional CCM methods suggest that the ratio of *in vitro* to *in vivo* DR varies with degradation time [109], our computational modeling provides a consistent, time-independent ratio based on the diffusivity of Mg ions. For Mg-5Gd, the mean ratio of $D_{\text{int}}$ and $D_{\text{liq}}$ between *in vitro* and *in vivo* experiments was 0.5, and for Mg-10Gd, it was 0.46. Establishing these ratios for various materials allows for the prediction of *in vivo* degradation from *in vitro* observations, reducing the need for extensive experiments and demonstrating the utility and relevance of peridynamic models in designing implant materials for clinical applications.

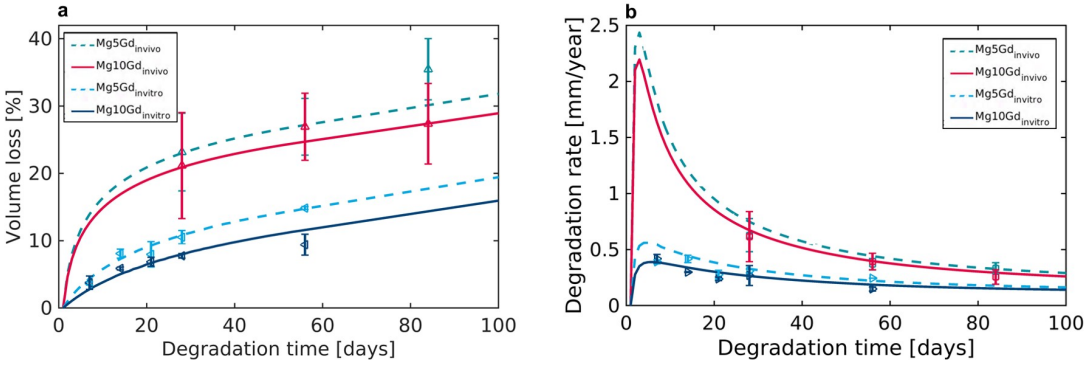


Figure 5.13: (**a**) Experimental data and Kriging-based surrogate model simulations of *in vitro* and *in vivo* volume loss for Mg-5Gd and Mg-10Gd, depicting the mean $\pm$ standard deviation. (**b**) DR calculated from volume loss, determined from $\mu$CT measurements as provided in [74, 76]. Reproduced from [2].

## 5.4 Corrosion-Induced Mechanical Damage Plasticity Simulation

In this section, we aim to predict the impact of bio-corrosion on the mechanical strength of headless bone implant screws, treating the implant as a mechanically isolated object without considering the surrounding electrolyte environment. We use damage plasticity analysis based on a CCM approach and FEM to perform mechanical simulations following corrosion-induced damage. This damage field is obtained either from the peridynamic bi-material bio-corrosion model (Section 5.2) or the full NNPP model of electromigration (Section 5.2.4). The CCM approach is employed for two main reasons: first, appropriate material models for the peridynamic description of Mg-based implants are not yet established, thus necessitating a correspondence approach with a CCM model, particularly in the non-ordinary state-based formalism. Second, since peridynamic modeling currently requires a CCM correspondence approach, it provides an opportunity to demonstrate the supplementary value of peridynamic diffusion-type corrosion models alongside a CCM approach using FEM simulations in bio-corrosion and bio-degradable implant material design. This highlights that the peridynamic approach can serve as a complementary method for obtaining *in vitro* or *in vivo* corrosion-induced damage fields, which can be seamlessly integrated into subsequent FEM simulations, showcasing the versatility of peridynamic models in the implant material design process.

The implant material (Mg-5Gd and Mg-10Gd) is modeled using a constitutive model that includes plasticity and a damage variable $f$, representing the loss of mechanical strength due to prior bio-corrosion. The corrosion-induced material loss, simulated via a peridynamic corrosion model before the mechanical analysis, can be mapped to the damage variable $f$ at any point in the solid metallic implant screw domain. Using this pre-damaged configuration, a FEM simulation of a tensile test is conducted to analyze the remaining mechanical strength of the implant after a specific period of simulated immersion. For the FEM simulations, the initial bone implant screw geometry from the peridynamic corrosion simulation is spatially discretized. For the headless and slotted $M2 \times 4\,\mathrm{mm}$ screw, this results in $773,005$ tetrahedral 4-node elements, with a total of $412,017$ degrees of freedom. Axial Dirichlet boundary conditions were applied, with zero displacement on one end and a prescribed displacement on the opposite end to simulate a tensile load corresponding to a global strain of 0.1, requiring a displacement of 0.4 mm for the bone implant screw. Reaction forces in the axial direction were recorded to mimic a quasi-static tensile test of the isolated implant screw. The FEM analyses were performed using an updated Lagrangian formalism accounting for finite deformations.

In the FEM simulations of tensile tests, aimed at determining the residual mechanical strength of Mg-based bone implant screws following bio-corrosion over a specified immersion period, a classical elasto-plastic material model with damage is utilized. This model defines the yield surface using a plastic potential $\Phi$ as

$$\Phi\left(\boldsymbol{\sigma}, f, \sigma_y(\varepsilon_{\mathrm{eq}}^{\mathrm{pl}})\right) = 0. \tag{5.38}$$

where $\boldsymbol{\sigma}$ is the Cauchy stress tensor, $f$ is the internal damage variable, and $\sigma_y$ is the yield stress of the undamaged material, which varies with accumulated plastic strain. The accumulated plastic strain over the time interval $[t_1, t_2]$, denoted as $\varepsilon_{\mathrm{eq}}^{\mathrm{pl}}$, is given by

$$\varepsilon_{\mathrm{eq}}^{\mathrm{pl}} = \int_{t_1}^{t_2} \sqrt{\frac{2}{3}\dot{\boldsymbol{\varepsilon}}^{\mathrm{pl}} : \dot{\boldsymbol{\varepsilon}}^{\mathrm{pl}}}\, dt \tag{5.39}$$

where the colon represents the double contraction of two second-order tensors, capturing matrix

hardening. The employed damage model is based on [52] and extended for strain hardening materials [138], with the plastic potential defined as

$$\Phi = \left(\frac{\sigma_{\text{eq}}}{\sigma_y}\right)^2 + 2\, q_1 f \cosh\left(\frac{tr(\boldsymbol{\sigma})}{2\sigma_y}\right) - \left(1 + q_1^2 f^2\right), \tag{5.40}$$

where $q_1$ is a model parameter. An increasing $f$ reduces the yield stress. The equivalent stress $\sigma_{\text{eq}}$ follows the von Mises definition

$$\sigma_{\text{eq}} = \sqrt{\frac{3}{2}\boldsymbol{\sigma}' : \boldsymbol{\sigma}'}, \tag{5.41}$$

with $\boldsymbol{\sigma}'$ being the deviatoric part of $\boldsymbol{\sigma}$. The evolution of the damage variable $f$ is governed by

$$\dot{f} = (1 - f)\, tr(\dot{\boldsymbol{\varepsilon}}^{\text{pl}}). \tag{5.42}$$

Simulations were conducted using the FEM implementation of ABAQUS/EXPLICIT, capturing the reduction in ductility with increasing stress triaxiality [55]. The material model parameters, including Young's modulus $E$ and Poisson's ratio $\nu$, are provided in Section 5.1. Additionally, Fig. 5.2 in that section defines the hardening functions $\sigma_y(\varepsilon_{\text{eq}}^{\text{pl}})$ for Mg-10Gd and Mg-5Gd. Consistent with [138], $q_1$ was set to 1.5 for both materials.

In the next step, the corrosion progress and corrosion-induced damage from prior peridynamic bio-corrosion simulations must be mapped to the damage variable $f$ in the mechanical damage plasticity FEM model. Literature, such as [50], proposed a continuum damage mechanics approach where the Cauchy stress is scaled by a corrosion damage variable $D_e$ that evolves due to Mg dissolution in uniform and pitting corrosion. Elements were removed from the FEM model when $D_e = 1$. However, these studies, including follow-ups [49, 18, 19], did not consider additional damage evolution due to mechanical loading. The approach used in this section aims to overcome this limitation, allowing for a more realistic computational assessment of residual strength post-corrosion. The peridynamic bio-corrosion simulations use a concentration variable $C \in [C_{\text{sat}}, C_{\text{solid}}]$ to represent the metallic phase, where $C_{\text{solid}}$ is the initial intact material concentration (Mg-5Gd or Mg-10Gd) and $C_{\text{sat}}$ is the corresponding saturation concentration in the liquid electrolyte medium. To convert this concentration drop into mechanical damage, we define a normalized concentration $\bar{C} = C/C_{\text{solid}} \in [\varepsilon, 1]$, with $\bar{C} = 1$ representing uncorroded Mg-alloy and $\bar{C} = \varepsilon := C_{\text{sat}}/C_{\text{solid}}$ representing fully corroded material. Thus, $\bar{C} = 1$ corresponds to an undamaged state with $f = 0$, and $\bar{C} = \varepsilon$ corresponds to the maximum damage value $f_{\text{max}}$, where yielding occurs at $\boldsymbol{\sigma} = \mathbf{0}$. Assuming $q_1 = \frac{2}{3}$, we get $f_{\text{max}} = \frac{2}{3}$. We assume a linear transition between no damage and maximum damage, resulting in the piecewise linear corrosion-to-damage mapping as

$$f_0 = \begin{cases} 1 - \bar{C}, & \bar{C} > 1 - f_{\text{max}} \\ f_{\text{max}} & \bar{C} \leq 1 - f_{\text{max}} \end{cases}, \tag{5.43}$$

where $f_0$ represents the damage variable after a given period of corrosion and prior the mechanical tensile test simulation, serving as the initial value of $f$ for the evolution equation in (5.42) during tensile tests. This approach captures both the direct material loss from bio-corrosion and indirect effects like stress corrosion cracking near the corrosion surface [145]. Due to the lack of stress transfer data at the interface, we opted for a simple piecewise linear relation in (5.43). This can be refined with more realistic functions as experimental data becomes available. Fig.5.14 shows $f_0$, the internal damage variable before tensile loading of the bone implant screws, following different periods of *in vitro* bio-corrosion as determined by the peridynamic bi-material bio-corrosion model described in Section 5.2.3.

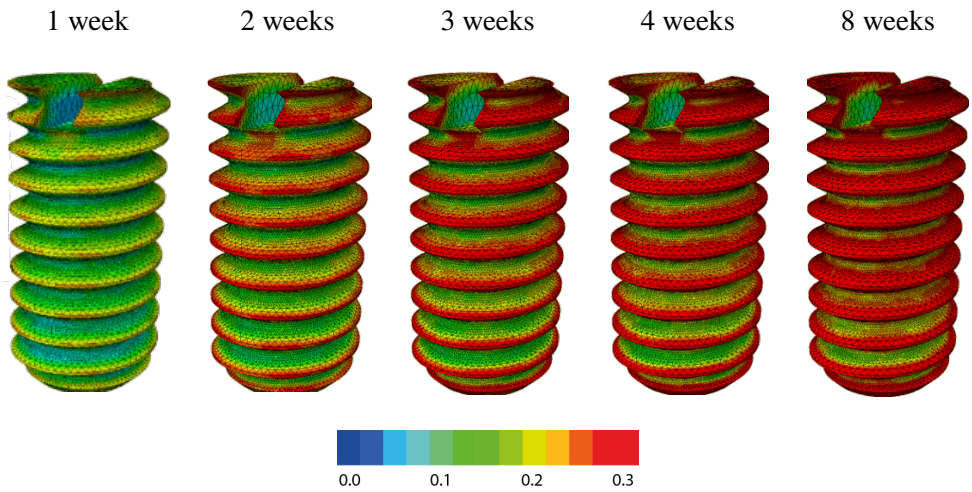


Figure 5.14: Initial internal damage variable $f$ after 1, 2, 3, 4, and 8 weeks of simulated immersion for a Mg-10Gd bone implant screw, before tensile loading. Reproduced from [60].

The results in Fig. 5.15 show force-elongation curves from 14 simulations of bone implant screws made from Mg-5Gd and Mg-10Gd, following various simulated *in vitro* immersion durations. Longer immersion times result in a reduced force transmission capacity of the bone implant screws. Except for Mg-5Gd after one week, all degraded samples exhibit decreased ductility due to damage growth. This reduction is due to the coupling of the internal damage variable and stress state, where damage evolves during loading, reducing the stress-carrying capacity on the screw's surface. This highlights the progressive nature of *in vitro* corrosion damage under mechanical loading. Notably, after 24 weeks, the strength of the Mg-5Gd implant is nearly zero, while the Mg-10Gd implant retains 20% of its initial strength, demonstrating significant differences in the long-term durability of the two alloys.

Fig. 5.16 summarizes the predicted normalized maximum force for Mg-5Gd and Mg-10Gd materials. Both alloys show a similar reduction in strength during the initial weeks of simulated immersion. Interestingly, Mg-5Gd experiences a less pronounced decrease in strength over time compared to Mg-10Gd, despite a higher volume loss as shown in Fig. 5.1. This counterintuitive result stems from the realistic consideration of material hardening (*cf.* Fig. 5.2), which is crucial in determining mechanical strength loss. For longer corrosion periods (8 to 24 weeks), the trend reverses, with the superior corrosion resistance of Mg-10Gd playing a more significant role in implant strength. A thorough investigation of the predicted two-phase decrease in mechanical strength, initially influenced by strain hardening and later by mass loss due to corrosion, will be instrumental in validating the proposed computational models and advancing future research.

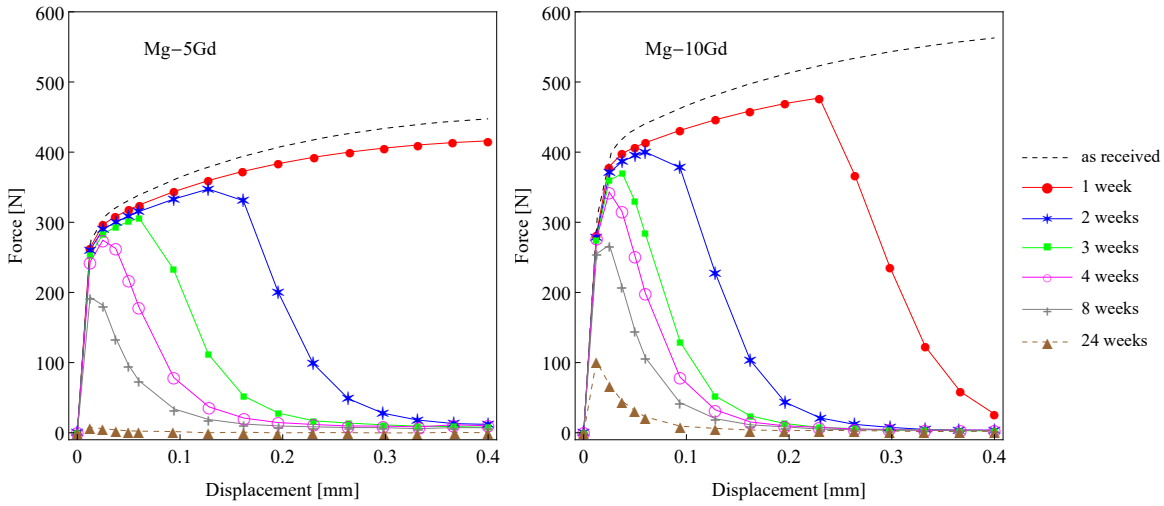


Figure 5.15: Simulated mechanical strength of Mg-5Gd (left) and Mg-10Gd (right) bone implant screws after 1, 2, 3, 4, 8, and 24 weeks of simulated *in vitro* immersion compared to the intact screw. Reproduced from [60].

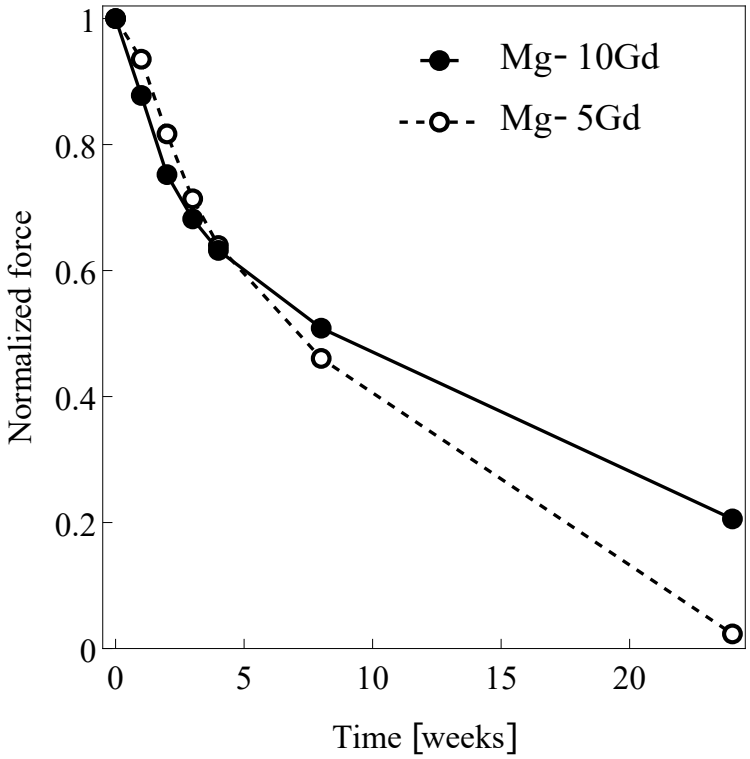


Figure 5.16: Maximum normalized tensile force of Mg-5Gd and Mg-10Gd bone implant screws over varying immersion times. Reproduced from [60].

# Chapter 6

# Conclusions

This dissertation aimed to enhance the applicability of peridynamic models by developing, exploring, and rigorously testing various numerical models, thereby preparing peridynamic models for a broader range of real-world problems in engineering, structural and material design, and biomedical and biomechanical applications. Over nearly three decades, PD theory has provided a fully consistent nonlocal multi-scale framework. However, efficient numerical solution techniques offering accurate and robust discretization and integration methods for solving the integro-differential governing equations are just now emerging. Additionally, applying peridynamic models to unbounded domain problems remained challenging due to the presence of nonlocal integral operators, limiting the use of conventional ABCs and those based on Fourier and Laplace transforms, like Perfectly Matched Layer (PML).

First, we review peridynamic elasticity equations, starting with the general state-based formulation and focusing on the original bond-based formulation and the GPBM constitutive model. We also cover nonlocal scalar wave fields and transport equations, proposing a consistent system of nonlocal diffusion-advection-electromigration-reaction equations, the NNPP system, which generalizes the standard peridynamic bi-material corrosion model. We demonstrate the convergence of the NNPP system to classical local counterparts as nonlocal interactions vanish. An effective diffusive corrosion layer is defined, where material properties change and metal ions transfer into the liquid electrolyte. Constitutive models for the NNPP system based on diffusion-electromigration-reaction are established, providing a framework for peridynamic corrosion modeling and facilitating the integration of existing peridynamic corrosion models into the NNPP system.

This work further explores various efficient numerical solution techniques for peridynamic models in elasticity and nonlocal scalar field equations, using both explicit and implicit time discretization methods. An asymptotically convergent meshfree scheme for bond-based PD governing equations was detailed, using a WLS scheme that is truly meshfree, unlike the standard modified one-point Gaussian quadrature rule. This scheme accurately computes quadrature points and weights without needing partial volumes, outperforming the standard scheme in efficiency by using a smaller subset of family nodes for spatial integrations. The meshfree WLS collocation scheme works well for linear peridynamic models and smooth basis functions, but to handle dynamic fracture and corrosion, it is combined with the standard discretization scheme using an adaptive hybrid approach. This hybrid approach optimizes computational resources by combining the WLS scheme in regions of smooth varying fields with a multi-grid approach that refines the grid only in areas of interest, such as near discontinuities or domain boundaries. The hybrid scheme's ability to balance computational cost and accuracy is demonstrated through numerical examples, including the

Kalthoff-Winkler experiment and the bio-corrosion of Mg-based headless bone implant screws. The multi-adaptive scheme reproduces solutions obtained with the standard scheme and fine grid spacing at significantly lower computational costs, showing enhanced efficiency in large-scale, complex 3D problems with millions of degrees of freedom. This improves the general applicability of peridynamic models for real-world applications and facilitates their incorporation into existing commercial and research PD codes.

A major focus of this work is exploring time domain techniques to derive ABCs for efficiently approximating solutions in unbounded domain problems, which are crucial for various multi-physics applications but have been particularly challenging for 3D models operating directly in the time domain. Many existing techniques rely on Fourier and Laplace methods, which are cumbersome for peridynamic models. We proposed a new strategy for constructing nonlocal ABCs suitable for peridynamic diffusion-type, scalar wave equation, and bond-based PD problems in unbounded domains. The developed nonlocal ABCs, constructed as an efficient extrapolation scheme based on semi-analytical and residual-free EBFs modes, can be employed for both local CCM-based models and PD for all governing equations, with an appropriate implementation at discrete levels. This method applies to available peridynamic discretizations as well as standard FEM models for local counterparts. The proposed Dirichlet-type ABCs are advantageous because their implementation does not depend on differentiation procedures or auxiliary variables, which are challenging even for classical (local) equations. We demonstrated that peridynamic modes recover the local counterpart equations corresponding to CCM in the limit of vanishing nonlocality. Developed entirely in the time and space domains, the proposed ABCs offer significant advantages over existing methods: they are free from Fourier or Laplace transforms, can be easily applied to problems with material nonlinearity, dynamic fracture, and corrosion, and are efficient to implement as time-dependent Dirichlet-type boundary conditions with minimal computational overhead. Moreover, the proposed ABCs do not introduce surface effects, unlike numerical bounded-domain simulations. At the discrete level, the modes satisfy the numerical dispersion relations of waves using the same standard discretization scheme as the near field, ensuring consistency and avoiding numerical instabilities due to the combination of different numerical techniques.

As a challenging multi-physics example, we explored the practical use of peridynamic transport-based corrosion equations, specifically the peridynamic bi-material corrosion equation and the NNPP system of diffusion-electromigration-reaction, for designing bio-corrosive and bio-degradable bone implant materials in physiological environments. We focused on modeling the bio-corrosion behavior of two binary Mg alloys, Mg-5Gd and Mg-10Gd, with either 5% or 10% Gd, using headless M2 $\times$ 4 mm bone implant screws in both *in vitro* and *in vivo* simulated physiological environments. The goal was to assess the mechanical strength loss of the bone implant screws. We developed a 3D peridynamic bi-material bio-corrosion model with appropriate constitutive kinetics assumptions based on semi-empirical descriptions of macroscopic volume loss, capturing corrosion-induced mass loss over several weeks. The numerical model employed an implicit Euler time-stepping method for efficient simulation over large timescales, a multi-grid approach to refine the computational grid around the corrosion surface near the screw threads, and nonlocal ABCs to mimic regular electrolyte exchange in the *in vitro* setup and hydrodynamic *in vivo* bio-degradation. Additionally, we demonstrated that peridynamic models could be calibrated using evolutionary parameter optimization schemes like PSO, effectively reproducing experimentally obtained macroscopic volume losses. The generalized NNPP corrosion formalism provided additional insights into the distribution of ionic components, chemical reactions, precipitation formations, and pH values around the corrosion surface, which are crucial for corrosion science and implant mate-

rial design. Transitioning from the full NNPP formalism to the peridynamic bi-material corrosion model allows for higher abstraction, improving computational efficiency while preserving essential corrosion indicators like the 3D damage field and volume loss over time. We further employed Kriging surrogate modeling to simulate *in vivo* systems based on *in vitro* bio-corrosion simulations, offering efficient predictions of macroscopic volume loss and the DR, though it omits detailed 3D damage distributions. This surrogate modeling can efficiently explore the parameter space and fit experimental data. Moreover, we combined peridynamic corrosion simulations with subsequent FEM analysis to assess residual mechanical strength after simulated immersion. This approach demonstrates that peridynamic models can seamlessly integrate into digital implant material design methodologies, mapping corrosion effects to internal damage variables in FEM codes and combining corrosion simulations with mechanical strength analyses, providing a useful framework for designing future bio-degradable Mg-based implants.

Overall, the hope remains that this dissertation has advanced the field of peridynamic models by addressing their numerical efficiency and applicability to a wide range of practical real-world applications. The novel methods developed and validated through this work demonstrate the potential of peridynamic models to enhance engineering, structural, and biomedical applications. For further refinement and expansion of the capabilities of peridynamic models in complex, multi-physics environments, please refer to the next section on ongoing work and future prospects.

# Chapter 7

# Ongoing Research and Future Prospects

After almost three decades of research, PD has established itself as a fully consistent multi-scale theory, achieving significant progress across various fields, including foundational mathematics, nonlocal calculus, numerical methods, and coupling schemes to CCM. It has been applied in material systems modeling and industrial applications [35]. Peridynamic models of elasticity began with the original bond-based formulation and expanded to ordinary and non-ordinary state-based models, each addressing specific issues in material failure simulations [130]. Furthermore, PD theory has advanced in transport, migration, and diffusion-based systems, as well as nonlocal scalar fields on computational domains involving sharp discontinuities and crack propagation [113, 38]. The development of efficient numerical algorithms has facilitated the practical implementation of peridynamic models in complex multi-physics and multi-scale problems [68]. The future of PD looks promising, with ongoing research focused on broadening its applications, enhancing the understanding of complex material behaviors, and offering innovative solutions to challenging scientific and engineering problems.

HPC and exascale computing are currently of great interest in the peridynamic research community, particularly for their potential to advance peridynamic simulations towards practical applications through massively parallelized and distributed systems. These systems exploit approaches such as MPI for distributed and OpenMP for shared memory parallelization. Numerous research codes have been developed for peridynamic simulations, utilizing Graphics Processing Unit (GPU) computing through frameworks like OpenCL (e.g., [96]), as well as CPU-based implementations that leverage parallel processing capabilities (e.g., [94]) or employ fast convolution-based formulations of PD [66, 141]. Additionally, some commercial software packages have integrated peridynamic capabilities, such as ABAQUS and ANSYS [88, 54]. These implementations include various advancements like the Peridynamic Finite Element Method (PDFEM) and dual-based coupling approaches, enabling efficient simulations of fracture and material behavior [12]. Open-source implementations of peridynamic models are widely available and actively developed, with notable projects focusing on dynamic fracture modeling, parallel optimization, and client-server integration techniques [51, 30, 158]. These developments have significantly improved the computational efficiency and applicability of peridynamic models, facilitating their use in solving complex engineering problems and fostering trust in their reliability for broader academic and industrial applications.

Recent advances in Machine Learning (ML) and Deep Learning (DL) have shown significant potential for enhancing peridynamic models, especially in establishing constitutive relations. In CCM approaches, ML techniques, such as Constitutive Artificial Neural Networks (CANNs), have

successfully provided constitutive models for elastic and viscoelastic materials [84, 1]. These methods can be used as data-driven approaches to learn nonlocal constitutive laws for peridynamic models. For example, novel nonlocal neural operator architectures have been developed to derive constitutive laws from full-field spatial measurements, capturing complex material responses with minimal model-form error [67]. These architectures leverage the expressivity of neural networks while adhering to fundamental physics principles, such as balance laws and objectivity, derived from the peridynamic governing equations [147, 87]. As research in this area progresses, integrating ML and DL approaches into peridynamic frameworks will be crucial for advancing the accuracy and efficiency of constitutive model development in PD.

A promising avenue for future research lies in the coupling of Smoothed Particle Hydrodynamics (SPH) with PD to address multi-physics and multi-scale applications, particularly Fluid-Structure Interaction (FSI) problems. SPH, which employs a particle-based discretization method similar to the formulation of peridynamic equations, is widely used in fluid mechanics. By integrating SPH with PD, it becomes feasible to efficiently formulate and describe FSI problems within a unified nonlocal framework. To date, numerical examples in the literature utilizing this methodology include hybrid PD-SPH approaches for soil fragmentation caused by explosive blast loads [44], as well as coupled approaches in FSI that address large deformations and fractures [146]. Integrated PD-SPH approaches can utilize HPC computing and efficient neighborhood search algorithms to simulate the interactions between fluids and solid structures through short-range forces. Leveraging various peridynamic formulations to describe thin structures, thermo-mechanics, and dynamic crack propagation, the combined strengths of SPH and PD in a single framework could provide nonlocal descriptions of complex multi-physics systems, significantly benefiting practical engineering applications.

In conclusion, ongoing advancements in computational techniques and novel approaches underscore the potential of peridynamic models to efficiently address complex multi-physics and multi-scale problems. Current developments pave the way for broader applications in engineering, material and structural design, as well as biomedical fields, highlighting the promising future of PD research. As the field continues to evolve, peridynamic models are set to become increasingly accurate, efficient, and widely accepted in both scientific and industrial contexts.

# Bibliography


[1] Kian P Abdolazizi, Kevin Linka, and Christian J Cyron. Viscoelastic constitutive artificial neural networks (vcanns)–a framework for data-driven anisotropic nonlinear finite viscoelasticity. *Journal of Computational Physics*, 499:112704, 2024.

[2] Tamadur Al Baraghtheh, Alexander Hermann, Arman Shojaei, Regine Willumeit-Römer, Christian J Cyron, and Berit Zeller-Plumhoff. Utilizing computational modelling to bridge the gap between in vivo and in vitro degradation rates for mg-xgd implants. *Corrosion and Materials Degradation*, 4(2):274–283, 2023.

[3] Bacim Alali, Kuo Liu, and Max Gunzburger. A generalized nonlocal vector calculus. *Zeitschrift für angewandte Mathematik und Physik*, 66(5):2807–2828, 2015.

[4] Holm Altenbach, Oleksiy Larin, Konstantin Naumenko, Olha Sukhanova, and Mathias Würner. Elastic plate under low velocity impact: classical continuum mechanics vs peridynamics analysis. *J. AIMS Mater. Sci*, 9(5):702–718, 2022.

[5] Edward Anderson, Zhaojun Bai, Christian Bischof, L Susan Blackford, James Demmel, Jack Dongarra, Jeremy Du Croz, Anne Greenbaum, Sven Hammarling, Alan McKenney, et al. *LAPACK users' guide*. SIAM, 1999.

[6] Talha Qasim Ansari, Zhihua Xiao, Shenyang Hu, Yulan Li, Jing-Li Luo, and San-Qiang Shi. Phase-field model of pitting corrosion kinetics in metallic materials. *npj Computational Materials*, 4(1):1–9, 2018.

[7] E Askari, F Bobaru, RB Lehoucq, ML Parks, SA Silling, and O Weckner. Peridynamics for multiscale materials modeling. In *Journal of Physics: Conference Series*, volume 125, page 012078. IOP Publishing, 2008.

[8] Herbert Baaser and Dietmar Gross. Remarks on the use of continuum damage models and on the limitations of their applicability in ductile fracture mechanics. In *Deformation and Failure in Metallic Materials*, pages 345–362. Springer, 2003.

[9] Santiago Badia, Michael Parks, Pavel Bochev, Max Gunzburger, and Richard Lehoucq. On atomistic-to-continuum coupling by blending. *Multiscale Modeling & Simulation*, 7(1):381–406, 2008.

[10] José C Bellido and Carlos Mora-Corral. Existence for nonlocal variational problems in peridynamics. *SIAM Journal on Mathematical Analysis*, 46(1):890–916, 2014.

[11] Ted Belytschko and SP Xiao. Coupling methods for continuum model with molecular model. *International Journal for Multiscale Computational Engineering*, 1(1), 2003.

[12] YH Bie, ZM Liu, H Yang, and XY Cui. Abaqus implementation of dual peridynamics for brittle fracture. *Computer methods in applied mechanics and engineering*, 372:113398, 2020.

[13] Florin Bobaru and Monchai Duangpanya. The peridynamic formulation for transient heat conduction. *International Journal of Heat and Mass Transfer*, 53(19-20):4047–4059, 2010.

[14] Florin Bobaru and Monchai Duangpanya. A peridynamic formulation for transient heat conduction in bodies with evolving discontinuities. *Journal of Computational Physics*, 231(7):2764–2785, 2012.

[15] Florin Bobaru, John T Foster, Philippe H Geubelle, and Stewart A Silling. *Handbook of Peridynamic Modeling*. CRC Press, 2016.

[16] Florin Bobaru and Youn Doh Ha. Adaptive refinement and multiscale modeling in 2D peridynamics. *International Journal for Multiscale Computational Engineering*, 9(6):635–660, 2011.

[17] Florin Bobaru, Mijia Yang, Leonardo Frota Alves, Stewart A Silling, Ebrahim Askari, and Jifeng Xu. Convergence, adaptive refinement, and scaling in 1D peridynamics. *International Journal for Numerical Methods in Engineering*, 77(6):852–877, 2009.

[18] Enda L Boland, James A Grogan, Claire Conway, and Peter E Mchugh. *Computer simulation of the mechanical behaviour of implanted biodegradable stents in a remodelling artery*, volume 68. Springer, 2016.

[19] Enda L. Boland, James A. Grogan, and Peter E. McHugh. Computational modeling of the mechanical performance of a magnesium stent undergoing uniform and pitting corrosion in a remodeling artery. *Journal of Medical Devices*, 11(2), 2017.

[20] B Boroomand, AA Tabatabaei, and Eugenio Oñate. Simple modifications for stabilization of the finite point method. *International Journal for Numerical Methods in Engineering*, 63(3):351–379, 2005.

[21] Bijan Boroomand and Sina Parand. Towards a general interpolation scheme. *Computer Methods in Applied Mechanics and Engineering*, 381:113830, 2021.

[22] Michael P. Brady, Gernot Rother, Matthew G. Frith, Anton E. Ievlev, Donovan N. Leonard, Kenneth C. Littrell, Ercan Cakmak, Harry M. Meyer, Lawrence M. Anovitz, and Bruce Davis. Temporal evolution of corrosion film nano-porosity and magnesium alloy hydrogen penetration in NaCl solution. *Journal of The Electrochemical Society*, 167(13):131513, oct 2020.

[23] Sahir N Butt, Jithender J Timothy, and Günther Meschke. Wave dispersion and propagation in state-based peridynamics. *Computational Mechanics*, 60(5):725–738, 2017.

[24] Wanhan Chen, Xin Gu, Qing Zhang, and Xiaozhou Xia. A refined thermo-mechanical fully coupled peridynamics with application to concrete cracking. *Engineering Fracture Mechanics*, 242:107463, 2021.

[25] Ziguang Chen and Florin Bobaru. Peridynamic modeling of pitting corrosion damage. *Journal of the Mechanics and Physics of Solids*, 78:352–381, 2015.

[26] Ziguang Chen and Florin Bobaru. Selecting the kernel in a peridynamic formulation: A study for transient heat diffusion. *Computer Physics Communications*, 197:51–60, 2015.

[27] Ziguang Chen, Siavash Jafarzadeh, Jiangming Zhao, and Florin Bobaru. A coupled mechano-chemical peridynamic model for pit-to-crack transition in stress-corrosion cracking. *Journal of the Mechanics and Physics of Solids*, 146:104203, 2021.

[28] M Dahms, D Höche, N Ahmad Agha, F Feyerabend, and R Willumeit-Römer. A simple model for long-time degradation of magnesium under physiological conditions. *Materials and Corrosion*, 69(2):191–196, 2018.

[29] Rene de Borst. Fracture in quasi-brittle materials: a review of continuum damage-based approaches. *Engineering fracture mechanics*, 69(2):95–112, 2002.

[30] Patrick Diehl, Prashant K Jha, Hartmut Kaiser, Robert Lipton, and Martin Lévesque. An asynchronous and task-based implementation of peridynamics utilizing HPX–the C++ standard library for parallelism and concurrency. *SN Applied Sciences*, 2(12):1–21, 2020.

[31] Daniele Dipasquale, Mirco Zaccariotto, and Ugo Galvanetto. Crack propagation with adaptive grid refinement in 2d peridynamics. *International Journal of Fracture*, 190(1-2):1–22, 2014.

[32] Cagan Diyaroglu, Erkan Oterkus, Erdogan Madenci, Timon Rabczuk, and Amir Siddiq. Peridynamic modeling of composite laminates under explosive loading. *Composite Structures*, 144:14–23, 2016.

[33] Anika Ky-Ja Do. Integration of multi-grid strategies into nonlocal nernst-planck-poisson systems for peridynamic corrosion modeling. Master's thesis, Hamburg University of Technology, Institute of Continuum and Material Mechanics, December 2023.

[34] Matthew Dobson and Mitchell Luskin. Analysis of a force-based quasicontinuum approximation. *ESAIM: Mathematical Modelling and Numerical Analysis*, 42(1):113–139, 2008.

[35] Mehmet Dorduncu, Huilong Ren, Xiaoying Zhuang, Stewart Silling, Erdogan Madenci, and Timon Rabczuk. A review of peridynamic theory and nonlocal operators along with their computer implementations. *Computers & Structures*, 299:107395, 2024.

[36] Qiang Du. Nonlocal calculus of variations and well-posedness of peridynamics. In *Handbook of peridynamic modeling*, pages 101–124. Chapman and Hall/CRC, 2016.

[37] Qiang Du, Max Gunzburger, Richard B Lehoucq, and Kun Zhou. Analysis and approximation of nonlocal diffusion problems with volume constraints. *SIAM review*, 54(4):667–696, 2012.

[38] Qiang Du, Houde Han, Jiwei Zhang, and Chunxiong Zheng. Numerical solution of a two-dimensional nonlocal wave equation on unbounded domains. *SIAM Journal on Scientific Computing*, 40(3):A1430–A1445, 2018.

[39] Etienne Emmrich and Olaf Weckner. The peridynamic equation and its spatial discretisation. *Mathematical Modelling and Analysis*, 12(1):17–27, 2007.

[40] Björn Engquist and Andrew Majda. Absorbing boundary conditions for numerical simulation of waves. *Proceedings of the National Academy of Sciences*, 74(5):1765–1766, 1977.

[41] P Ernst and RC Newman. Pit growth studies in stainless steel foils. i. introduction and pit growth kinetics. *Corrosion Science*, 44(5):927–941, 2002.

[42] P Ernst and RC Newman. Pit growth studies in stainless steel foils. ii. effect of temperature, chloride concentration and sulphate addition. *Corrosion science*, 44(5):943–954, 2002.

[43] Y Fadaei and M Mohseni Moghadam. A greedy sparse meshless method for solving heat conduction problems. *Engineering with Computers*, 33(3):631–645, 2017.

[44] Houfu Fan, Guy Leshem Bergel, and Shaofan Li. A hybrid peridynamics–sph simulation of soil fragmentation by blast loads of buried explosive. *International Journal of Impact Engineering*, 87:14–27, 2016. SI: Experimental Testing and Computational Modeling of Dynamic Fracture.

[45] Gerald S Frankel, Alejandro Samaniego, and Nick Birbilis. Evolution of hydrogen at dissolving magnesium surfaces. *Corrosion Science*, 70:104–111, 2013.

[46] Jan N Fuhg, Amélie Fau, and Udo Nackenhorst. State-of-the-Art and Comparative Review of Adaptive Sampling Methods for Kriging. *Archives of Computational Methods in Engineering*, 28(4):2689–2747, 6 2021.

[47] Tom Gießgen, Andreas Mittelbach, Daniel Höche, Mikhail Zheludkevich, and Karl U Kainer. Enhanced predictive corrosion modeling with implicit corrosion products. *Materials and Corrosion*, 70(12):2247–2255, 2019.

[48] J. Gonzalez, R. Q. Hou, E. P. S. Nidadavolu, R. Willumeit-Römer, and F. Feyerabend. Magnesium degradation under physiological conditions - best practice. *Bioact Mater*, 3(2):174–185, 2018.

[49] J. A. Grogan, S. B. Leen, and P. E. McHugh. A physical corrosion model for bioabsorbable metal stents. *Acta Biomaterialia*, 10(5):2313–2322, 2014.

[50] J. A. Grogan, B. J. O'Brien, S. B. Leen, and P. E. McHugh. A corrosion model for bioabsorbable metallic stents. *Acta Biomaterialia*, 7(9):3523–3533, 2011.

[51] Quan Gu, Lei Wang, and Surong Huang. Integration of peridynamic theory and opensees for solving problems in civil engineering. *Computer Modeling in Engineering & Sciences*, 120(3):471–489, 2019.

[52] A. L. Gurson. Continuum theory of ductile rupture by void nucleation and growth: Part -1 yield criteria and flow rules for porous ductile media. *Journal of Engineering Materials and Technology*, 99:2–15, 1977.

[53] Youn Doh Ha and Florin Bobaru. Characteristics of dynamic brittle fracture captured with peridynamics. *Engineering Fracture Mechanics*, 78(6):1156–1168, 2011.

[54] SW Han, C Diyaroglu, S Oterkus, Erdogan Madenci, E Oterkus, Y Hwang, and H Seol. Peridynamic direct concentration approach by using ansys. In *2016 IEEE 66th Electronic Components and Technology Conference (ECTC)*, pages 544–549. IEEE, 2016.

[55] J.W. Hancock and A.C. Mackenzie. On the mechanisms of ductile failure in high-strength steels subjected to multi-axial stress-states. *J. Mech. Phys. Solids*, 24:147–169, 1976.

[56] J. Harmuth, B. Wiese, J. Bohlen, T. Ebel, and R. Willumeit-Römer. Wide range mechanical customization of mg-gd alloys with low degradation rates by extrusion. *Frontiers in Materials*, 6, 2019.

[57] Y Heider, B Markert, and WJCM Ehlers. Dynamic wave propagation in infinite saturated porous media half spaces. *Computational Mechanics*, 49:319–336, 2012.

[58] Alexander Hermann, Arman Shojaei, Daniel Höche, Siavash Jafarzadeh, Florin Bobaru, and Christian J Cyron. Nonlocal nernst-planck-poisson systems for peridynamic corrosion modeling. *Available at SSRN 4819880*, 2024.

[59] Alexander Hermann, Arman Shojaei, Pablo Seleson, Christian J Cyron, and Stewart A Silling. Dirichlet-type absorbing boundary conditions for peridynamic scalar waves in two-dimensional viscous media. *International Journal for Numerical Methods in Engineering*, 124(16):3524–3553, 2023.

[60] Alexander Hermann, Arman Shojaei, Dirk Steglich, Daniel Höche, Berit Zeller-Plumhoff, and Christian J Cyron. Combining peridynamic and finite element simulations to capture the corrosion of degradable bone implants and to predict their residual strength. *International Journal of Mechanical Sciences*, 220:107143, 2022.

[61] Wenke Hu, Yenan Wang, Jian Yu, Chian-Fong Yen, and Florin Bobaru. Impact damage on a thin glass plate with a thin polycarbonate backing. *International Journal of Impact Engineering*, 62:152–165, 2013.

[62] Siavash Jafarzadeh, Ziguang Chen, and Florin Bobaru. Peridynamic modeling of intergranular corrosion damage. *Journal of The Electrochemical Society*, 165(7):C362, 2018.

[63] Siavash Jafarzadeh, Ziguang Chen, and Florin Bobaru. Peridynamic modeling of repassivation in pitting corrosion of stainless steel. *Corrosion*, 74(4):393, 2018.

[64] Siavash Jafarzadeh, Ziguang Chen, and Florin Bobaru. Computational modeling of pitting corrosion. *Corrosion Reviews*, 37(5):419–439, 2019.

[65] Siavash Jafarzadeh, Ziguang Chen, Shumin Li, and Florin Bobaru. A peridynamic mechano-chemical damage model for stress-assisted corrosion. *Electrochimica Acta*, 323:134795, 2019.

[66] Siavash Jafarzadeh, Farzaneh Mousavi, Longzhen Wang, and Florin Bobaru. Peri-fast/dynamics: a matlab code for explicit fast convolution-based peridynamic analysis of deformation and fracture. *Journal of Peridynamics and Nonlocal Modeling*, 6(1):33–61, 2024.

[67] Siavash Jafarzadeh, Stewart Silling, Ning Liu, Zhongqiang Zhang, and Yue Yu. Peridynamic neural operators: A data-driven nonlocal constitutive model for complex material responses. *arXiv preprint arXiv:2401.06070*, 2024.

[68] Ali Javili, Rico Morasata, Erkan Oterkus, and Selda Oterkus. Peridynamics review. *Mathematics and Mechanics of Solids*, 24(11):3714–3739, 2019.

[69] Joerg F Kalthoff. Modes of dynamic shear failure in solids. *International Journal of Fracture*, 101(1):1–31, 2000.

[70] Amir R Khoei. *Extended finite element method: theory and applications*. John Wiley & Sons, 2014.

[71] Marc Kieke, Frank Feyerabend, Jacques Lemaitre, Peter Behrens, and Regine Willumeit-Römer. Degradation rates and products of pure magnesium exposed to different aqueous media under physiological conditions. *BioNanoMaterials*, 17(3-4):131–143, 2016.

[72] Bahattin Kilic and Erdogan Madenci. Coupling of peridynamic theory and the finite element method. *Journal of mechanics of materials and structures*, 5(5):707–733, 2010.

[73] Diana Krüger, Silvia Galli, Berit Zeller-Plumhoff, DC Florian Wieland, Niccolò Peruzzi, Björn Wiese, Philipp Heuser, Julian Moosmann, Ann Wennerberg, and Regine Willumeit-Römer. High-resolution ex vivo analysis of the degradation and osseointegration of mg-xgd implant screws in 3d. *Bioactive Materials*, 13:37–52, 2022.

[74] Diana Krüger, Silvia Galli, Berit Zeller-Plumhoff, D.C. Florian Wieland, Niccolò Peruzzi, Björn Wiese, Philipp Heuser, Julian Moosmann, Ann Wennerberg, and Regine Willumeit-Römer. High-resolution ex vivo analysis of the degradation and osseointegration of Mg-xGd implant screws in 3D. *Bioactive Materials*, 13:37–52, 7 2022.

[75] Diana Krüger, Berit Zeller-Plumhoff, Björn Wiese, Sangbong Yi, Marcus Zuber, DC Florian Wieland, Julian Moosmann, and Regine Willumeit-Römer. Assessing the microstructure and in vitro degradation behavior of mg-xgd screw implants using $\mu$ct. *Journal of Magnesium and Alloys*, 2021.

[76] Diana Krüger, Berit Zeller-Plumhoff, Björn Wiese, Sangbong Yi, Marcus Zuber, D. C.Florian Wieland, Julian Moosmann, and Regine Willumeit-Römer. Assessing the microstructure and in vitro degradation behavior of Mg-xGd screw implants using µCT. *Journal of Magnesium and Alloys*, 9(6):2207–2222, 11 2021.

[77] Gábor Ladányi and Viktor Gonda. Review of peridynamics: Theory, applications, and future perspectives. *Journal of Mechanical Engineering/Strojniški Vestnik*, 67(12), 2021.

[78] Claude Le Bris. Computational chemistry from the perspective of numerical analysis. *Acta Numerica*, 14:363–444, 2005.

[79] Jooeun Lee, Seong Eun Oh, and Jung-Wuk Hong. Parallel programming of a peridynamics code coupled with finite element method. *International Journal of Fracture*, 203:99–114, 2017.

[80] Eitan Lees, Srujan Rokkam, Sachin Shanbhag, and Max Gunzburger. The electroneutrality constraint in nonlocal models. *The Journal of chemical physics*, 147(12):124102, 2017.

[81] Sylvain Lefebvre and Hugues Hoppe. Perfect spatial hashing. *ACM Transactions on Graphics (TOG)*, 25(3):579–588, 2006.

[82] Yu Leng, Xiaochuan Tian, Nathaniel Trask, and John T Foster. Asymptotically compatible reproducing kernel collocation and meshfree integration for nonlocal diffusion. *SIAM Journal on Numerical Analysis*, 59(1):88–118, 2021.

[83] Yu Leng, Xiaochuan Tian, Nathaniel A Trask, and John T Foster. Asymptotically compatible reproducing kernel collocation and meshfree integration for the peridynamic Navier equation. *Computer Methods in Applied Mechanics and Engineering*, 370:113264, 2020.

[84] Kevin Linka, Markus Hillgärtner, Kian P Abdolazizi, Roland C Aydin, Mikhail Itskov, and Christian J Cyron. Constitutive artificial neural networks: A fast and general approach to predictive data-driven constitutive modeling by deep learning. *Journal of Computational Physics*, 429:110010, 2021.

[85] David John Littlewood, Timothy Shelton, and Jesse David Thomas. Estimation of the critical time step for peridynamic models. Technical report, Sandia National Lab.(SNL-NM), Albuquerque, NM (United States), 2013.

[86] Gui-Rong Liu. *Meshfree methods: moving beyond the finite element method*. CRC Press, 2009.

[87] Ning Liu, Xuxiao Li, Manoj R Rajanna, Edward W Reutzel, Brady Sawyer, Prahalada Rao, Jim Lua, Nam Phan, and Yue Yu. Deep neural operator enabled digital twin modeling for additive manufacturing. *arXiv preprint arXiv:2405.09572*, 2024.

[88] Richard W Macek and Stewart A Silling. Peridynamics via finite element analysis. *Finite Elements in Analysis and Design*, 43(15):1169–1178, 2007.

[89] Stefano Marelli and Bruno Sudret. UQLab: A Framework for Uncertainty Quantification in Matlab. *Vulnerability, Uncertainty, and Risk*, pages 2554–2563, 2014.

[90] Edward McCafferty. *Introduction to corrosion science*. Springer Science & Business Media, 2010.

[91] Tadele Mengesha and Qiang Du. Analysis of a scalar nonlocal peridynamic model with a sign changing kernel. *Discrete and Continuous Dynamical Systems-B*, 18(5):1415–1437, 2013.

[92] Ronald E Miller and Ellad B Tadmor. A unified framework and performance benchmark of fourteen multiscale atomistic/continuum coupling methods. *Modelling and simulation in materials science and engineering*, 17(5):053001, 2009.

[93] Farshid Mossaiby, Pouria Sheikhbahaei, and Arman Shojaei. Multi-adaptive coupling of finite element meshes with peridynamic grids: robust implementation and potential applications. *Engineering with Computers*, May 2022.

[94] Farshid Mossaiby, Pouria Sheikhbahaei, and Arman Shojaei. Multi-adaptive coupling of finite element meshes with peridynamic grids: robust implementation and potential applications. *Engineering with Computers*, 39(4):2807–2828, 2023.

[95] Farshid Mossaiby, Arman Shojaei, Bijan Boroomand, Mirco Zaccariotto, and Ugo Galvanetto. Local dirichlet-type absorbing boundary conditions for transient elastic wave propagation problems. *Computer Methods in Applied Mechanics and Engineering*, 362:112856, 2020.

[96] Farshid Mossaiby, Arman Shojaei, M Zaccariotto, and U Galvanetto. OpenCL implementation of a high performance 3D peridynamic model on graphics accelerators. *Computers & Mathematics with Applications*, 74(8):1856–1870, 2017.

[97] Frédéric Nataf. Absorbing boundary conditions and perfectly matched layers in wave propagation problems. In Ivan Graham, Ulrich Langer, Jens Melenk, and Mourad Sini, editors, *Direct and Inverse Problems in Wave Propagation and Applications*, pages 219–232. ; De Gruyter, 2013.

[98] Eugenio Oñate, Franco Perazzo, and J Miquel. A finite point method for elasticity problems. *Computers & Structures*, 79(22-25):2151–2163, 2001.

[99] Greta Ongaro, Pablo Seleson, Ugo Galvanetto, Tao Ni, and Mirco Zaccariotto. Overall equilibrium in the coupling of peridynamics and classical continuum mechanics. *Computer Methods in Applied Mechanics and Engineering*, 381:113515, 2021.

[100] Greta Ongaro, Arman Shojaei, Farshid Mossaiby, Alexander Hermann, Christian J Cyron, and Patrizia Trovalusci. Multi-adaptive spatial discretization of bond-based peridynamics. *International journal of fracture*, 244(1):1–24, 2023.

[101] Selda Oterkus, Erdogan Madenci, and Abigail Agwai. Peridynamic thermal diffusion. *Journal of Computational Physics*, 265:71–96, 2014.

[102] Sean T O'connell and Peter A Thompson. Molecular dynamics–continuum hybrid computations: a tool for studying complex fluid flows. *Physical Review E*, 52(6):R5792, 1995.

[103] Michael L Parks, Richard B Lehoucq, Steven J Plimpton, and Stewart A Silling. Implementing peridynamics within a molecular dynamics code. *Computer Physics Communications*, 179(11):777–783, 2008.

[104] Michael L Parks, David J Littlewood, John A Mitchell, and Stewart A Silling. Peridigm Users' Guide v1.0.0, Report SAND2012-7800, Sandia National Laboratories. *Albuquerque, New Mexico 87185 and Livermore, California 94550*, 2012.

[105] Michael L Parks, Pablo Seleson, Steven J Plimpton, Richard B Lehoucq, and Stewart A Silling. Peridynamics with LAMMPS: A User Guide v0.2 Beta, Report SAND2010-5549. *Sandia National Laboratories, Albuquerque, New Mexico 87185 and Livermore, California 94550*, 2010.

[106] Marco Pasetto, Yu Leng, Jiun-Shyan Chen, John T. Foster, and Pablo Seleson. A reproducing kernel enhanced approach for peridynamic solutions. *Computer Methods in Applied Mechanics and Engineering*, 340:1044–1078, 2018.

[107] Timon Rabczuk and Huilong Ren. A peridynamics formulation for quasi-static fracture and contact in rock. *Engineering Geology*, 225:42–48, 2017.

[108] Daniel Rabinovich, Dan Givoli, Jacobo Bielak, and Thomas Hagstrom. The double absorbing boundary method for elastodynamics in homogeneous and layered media. *Advanced Modeling and Simulation in Engineering Sciences*, 2(1):1–27, 2015.

[109] Adela Helvia Martinez Sanchez, Bérengère J.C. Luthringer, Frank Feyerabend, and Regine Willumeit. Mg and mg alloys: How comparable are in vitro and in vivo corrosion rates? a review. *Acta Biomaterialia*, 13:16–31, 2015.

[110] Francesco Scabbia, Mirco Zaccariotto, and Ugo Galvanetto. Accurate computation of partial volumes in 3d peridynamics. *Engineering with Computers*, 39(1):959–991, 2023.

[111] Robert Schaback. Greedy sparse linear approximations of functionals from nodal data. *Numerical Algorithms*, 67(3):531–547, 2014.

[112] Pablo Seleson. Improved one-point quadrature algorithms for two-dimensional peridynamic models based on analytical calculations. *Computer Methods in Applied Mechanics and Engineering*, 282:184–217, 2014.

[113] Pablo Seleson, Max Gunzburger, and Michael L Parks. Interface problems in nonlocal diffusion and sharp transitions between local and nonlocal domains. *Computer Methods in Applied Mechanics and Engineering*, 266:185–204, 2013.

[114] Pablo Seleson, Youn Doh Ha, and Samir Beneddine. Concurrent coupling of bond-based peridynamics and the Navier equation of classical elasticity by blending. *International Journal for Multiscale Computational Engineering*, 13(2):91–113, 2015.

[115] Pablo Seleson and David J Littlewood. Convergence studies in meshfree peridynamic simulations. *Computers & Mathematics with Applications*, 71(11):2432–2448, 2016.

[116] Pablo Seleson and Michael Parks. On the role of the influence function in the peridynamic theory. *International Journal for Multiscale Computational Engineering*, 9(6):689–706, 2011.

[117] Pablo Seleson, Michael L Parks, Max Gunzburger, and Richard B Lehoucq. Peridynamics as an upscaling of molecular dynamics. *Multiscale Modeling & Simulation*, 8(1):204–227, 2009.

[118] Pablo D Seleson. *Peridynamic multiscale models for the mechanics of materials: constitutive relations, upscaling from atomistic systems, and interface problems*. PhD thesis, The Florida State University, 2010.

[119] Pouria Sheikhbahaei, Farshid Mossaiby, and Arman Shojaei. An efficient peridynamic framework based on the arc-length method for fracture modeling of brittle and quasi-brittle problems with snapping instabilities. *Computers & Mathematics with Applications*, 136:165–190, 2023.

[120] VB Shenoy, Ronald Miller, EB Tadmor, David Rodney, Rob Phillips, and Michael Ortiz. An adaptive finite element approach to atomic-scale mechanics—the quasicontinuum method. *Journal of the Mechanics and Physics of Solids*, 47(3):611–642, 1999.

[121] A Shojaei, F Mossaiby, M Zaccariotto, and U Galvanetto. An adaptive multi-grid peridynamic method for dynamic fracture analysis. *International Journal of Mechanical Sciences*, 144:600–617, 2018.

[122] Arman Shojaei, Alexander Hermann, Christian J. Cyron, Pablo Seleson, and Stewart A. Silling. A hybrid meshfree discretization to improve the numerical performance of peridynamic models. *Computer Methods in Applied Mechanics and Engineering*, 391:114544, 2022.

[123] Arman Shojaei, Alexander Hermann, Pablo Seleson, and Christian J Cyron. Dirichlet absorbing boundary conditions for classical and peridynamic diffusion-type models. *Computational Mechanics*, 66(4):773–793, 2020.

[124] Arman Shojaei, Alexander Hermann, Pablo Seleson, Stewart A Silling, Timon Rabczuk, and Christian J Cyron. Peridynamic elastic waves in two-dimensional unbounded domains: Construction of nonlocal dirichlet-type absorbing boundary conditions. *Computer methods in applied mechanics and engineering*, 407:115948, 2023.

[125] Arman Shojaei, Farshid Mossaiby, Mirco Zaccariotto, and Ugo Galvanetto. A local collocation method to construct dirichlet-type absorbing boundary conditions for transient scalar wave propagation problems. *Computer Methods in Applied Mechanics and Engineering*, 356:629–651, 2019.

[126] Arman Shojaei, T Mudric, Mirco Zaccariotto, and Ugo Galvanetto. A coupled meshless finite point/peridynamic method for 2d dynamic fracture analysis. *International Journal of Mechanical Sciences*, 119:419–431, 2016.

[127] SA Silling. Peridynamic modeling of the Kalthoff–Winkler experiment. *Submission for the 2001 Sandia Prize in computational science*, 2001.

[128] Stewart A Silling. Reformulation of elasticity theory for discontinuities and long-range forces. *Journal of the Mechanics and Physics of Solids*, 48(1):175–209, 2000.

[129] Stewart A Silling. Linearized theory of peridynamic states. *Journal of Elasticity*, 99(1):85–111, 2010.

[130] Stewart A Silling and Ebrahim Askari. A meshfree method based on the peridynamic model of solid mechanics. *Computers & Structures*, 83(17-18):1526–1535, 2005.

[131] Stewart A Silling, O Weckner, E Askari, and Florin Bobaru. Crack nucleation in a peridynamic solid. *International Journal of Fracture*, 162(1-2):219–227, 2010.

[132] Chin-Teh Sun and Zhihe Jin. *Fracture mechanics*. Academic press, 2011.

[133] Xiaochuan Tian and Qiang Du. Analysis and comparison of different approximations to nonlocal diffusion and linear peridynamic equations. *SIAM Journal on Numerical Analysis*, 51(6):3458–3482, 2013.

[134] Xiaochuan Tian and Qiang Du. Asymptotically compatible schemes and applications to robust discretization of nonlocal models. *SIAM Journal on Numerical Analysis*, 52(4):1641–1665, 2014.

[135] Jeremy Trageser and Pablo Seleson. Bond-based peridynamics: A tale of two Poisson's ratios. *Journal of Peridynamics and Nonlocal Modeling*, 2(3):278–288, 2020.

[136] Nathaniel Trask, Benjamin Huntington, and David Littlewood. Asymptotically compatible meshfree discretization of state-based peridynamics for linearly elastic composite materials. *arXiv preprint arXiv:1903.00383*, 2019.

[137] Nathaniel Trask, Huaiqian You, Yue Yu, and Michael L Parks. An asymptotically compatible meshfree quadrature rule for nonlocal problems with applications to peridynamics. *Computer Methods in Applied Mechanics and Engineering*, 343:151–165, 2019.

[138] V. Tvergaard and A. Needleman. Analysis of the cup-cone fracture in a round tensile bar. *Acta Metall.*, 32(1):157–169, 1984.

[139] Andre E Vellwock and Flavia Libonati. Xfem for composites, biological, and bioinspired materials: A review. *Materials*, 17(3):745, 2024.

[140] Jianqiang Wang, Wei Hu, Xiaobing Zhang, and Wenxiao Pan. Modeling heat transfer subject to inhomogeneous neumann boundary conditions by smoothed particle hydrodynamics and peridynamics. *International Journal of Heat and Mass Transfer*, 139:948–962, 2019.

[141] Longzhen Wang, Siavash Jafarzadeh, Farzaneh Mousavi, and Florin Bobaru. Peri-fast/corrosion: a 3d pseudospectral peridynamic matlab code for corrosion. *Journal of Peridynamics and Nonlocal Modeling*, pages 1–25, 2023.

[142] Yongwei Wang, Fei Han, and Gilles Lubineau. Strength-induced peridynamic modeling and simulation of fractures in brittle materials. *Computer Methods in Applied Mechanics and Engineering*, 374:113558, 2021.

[143] Olaf Weckner, Gerd Brunk, Michael A Epton, Stewart A Silling, and Ebrahim Askari. Comparison between local elasticity and non-local peridynamics. *Sandia National Laboratory Report, SAND2009-1109J, Albuquerque, New Mexico*, 2009.

[144] Raymond A Wildman and George A Gazonas. A finite difference-augmented peridynamics method for reducing wave dispersion. *International Journal of Fracture*, 190(1-2):39–52, 2014.

[145] N. Winzer, A. Atrens, G. Song, E. Ghali, W. Dietzel, K.U. Kainer, N. Hort, and C. Blawert. A critical review of the stress corrosion cracking (scc) of magnesium alloys. *Advanced Engineering Materials*, 7(8):659–693, 2005.

[146] Xuehao Yao and Dan Huang. Coupled pd-sph modeling for fluid-structure interaction problems with large deformation and fracturing. *Computers & Structures*, 270:106847, 2022.

[147] Huaiqian You, Yue Yu, Stewart Silling, and Marta D'Elia. Nonlocal operator learning for homogenized models: From high-fidelity simulations to constitutive laws. *Journal of Peridynamics and Nonlocal Modeling*, 2024.

[148] K Yu, XJ Xin, and KB Lease. A new adaptive integration method for the peridynamic theory. *Modelling and Simulation in Materials Science and Engineering*, 19(4):045003, 2011.

[149] Mirco Zaccariotto, Teo Mudric, Davide Tomasi, Arman Shojaei, and Ugo Galvanetto. Coupling of FEM meshes with Peridynamic grids. *Computer Methods in Applied Mechanics and Engineering*, 330:471–497, 2018.

[150] Berit Zeller-Plumhoff, Tamadur AlBaraghtheh, Daniel Höche, and Regine Willumeit-Römer. Computational modelling of magnesium degradation in simulated body fluid under physiological conditions. *Journal of magnesium and alloys*, 10(4):965–978, 2022.

[151] Berit Zeller-Plumhoff, Melissa Gile, Melissa Priebe, Hanna Slominska, Benjamin Boll, Björn Wiese, Tim Würger, Regine Willumeit-Römer, and Robert Horst Meißner. Exploring key ionic interactions for magnesium degradation in simulated body fluid – a data-driven approach. *Corrosion Science*, 182:109272, 2021.

[152] Berit Zeller-Plumhoff, Heike Helmholz, Frank Feyerabend, Thomas Dose, Fabian Wilde, Alexander Hipp, Felix Beckmann, Regine Willumeit-Römer, and Jörg U. Hammel. Quantitative characterization of degradation processes in situ by means of a bioreactor coupled flow chamber under physiological conditions using time-lapse srμct. *Materials and Corrosion*, 69(3):298–306, 2018.

[153] Berit Zeller-Plumhoff, Daniel Laipple, Hanna Slominska, Kamila Iskhakova, Elena Longo, Alexander Hermann, Silja Flenner, Imke Greving, Malte Storm, and Regine Willumeit-Römer. Evaluating the morphology of the degradation layer of pure magnesium via 3d imaging at resolutions below 40 nm. *Bioactive Materials*, 6(12):4368–4376, 2021.

[154] Berit Zeller-Plumhoff, Daniel Laipple, Hanna Slominska, Kamila Iskhakova, Elena Longo, Alexander Hermann, Silja Flenner, Imke Greving, Malte Storm, and Regine Willumeit-Römer. Evaluating the morphology of the degradation layer of pure magnesium via 3d imaging at resolutions below 40 nm. *Bioactive Materials*, 6(12):4368–4376, 2021.

[155] Berit Zeller-Plumhoff, Domonkos Tolnai, Martin Wolff, Imke Greving, Norbert Hort, and Regine Willumeit-Römer. Utilizing synchrotron radiation for the characterization of biodegradable magnesium alloys—from alloy development to the application as implant material. *Advanced Engineering Materials*, 23(11):2100197, 2021.

[156] Berit Zeller-Plumhoff, Domonkos Tolnai, Martin Wolff, Imke Greving, Norbert Hort, and Regine Willumeit-Römer. Utilizing Synchrotron Radiation for the Characterization of Biodegradable Magnesium Alloys—From Alloy Development to the Application as Implant Material. *Advanced Engineering Materials*, 23(11):2100197, 11 2021.

[157] Berit Zeller-Plumhoff, Domonkos Tolnai, Martin Wolff, Imke Greving, Norbert Hort, and Regine Willumeit-Römer. Utilizing Synchrotron Radiation for the Characterization of Biodegradable Magnesium Alloys—From Alloy Development to the Application as Implant Material. *Advanced Engineering Materials*, 23(11):2100197, 11 2021.

[158] Haoran Zhang, Yaxun Liu, Lisheng Liu, Xin Lai, Qiwen Liu, and Hai Mei. Implementation of openmp parallelization of rate-dependent ceramic peridynamic model. *CMES-Computer Modeling in Engineering & Sciences*, 133(1), 2022.

[159] Wohua Zhang and Yuanqiang Cai. *Continuum damage mechanics and numerical applications*. Springer Science & Business Media, 2010.

[160] Yuan Zhang, Guoyang Zhang, Longbin Tao, Chao Wang, Liyu Ye, Shuai Sun, and Kang Han. Study and discussion on computational efficiency of ice–structure interaction by peridynamic. *Journal of Marine Science and Engineering*, 11(6):1154, 2023.

[161] Jiangming Zhao, Ziguang Chen, Javad Mehrmashhadi, and Florin Bobaru. Construction of a peridynamic model for transient advection-diffusion problems. *International Journal of Heat and Mass Transfer*, 126:1253–1266, 2018.

[162] Jiangming Zhao, Siavash Jafarzadeh, Ziguang Chen, and Florin Bobaru. Enforcing local boundary conditions in peridynamic models of diffusion with singularities and on arbitrary domains. *Engineering with Computers*, pages 1–20, 2024.

[163] Liang Zhao, Kyung Choi, and Ikjin Lee. Metamodeling Method Using Dynamic Kriging for Design Optimization. *Aiaa Journal*, 49:2034–2046, 2011.

[164] Ning Zhu, Cemal Kochan, Erkan Oterkus, and Selda Oterkus. Fatigue analysis of polycrystalline materials using peridynamic theory with a novel crack tip detection algorithm. *Ocean Engineering*, 222:108572, 2021.